

# **MOLECULAR DYNAMICS AND CONTINUUM SIMULATIONS OF FLUID FLOWS WITH SLIP BOUNDARY CONDITIONS**

By

Anoosheh NiavaraniKheiri

A DISSERTATION

Submitted to  
Michigan State University  
in partial fulfillment of the requirements  
for the degree of

DOCTOR OF PHILOSOPHY

Mechanical Engineering

2011

## ABSTRACT

# MOLECULAR DYNAMICS AND CONTINUUM SIMULATIONS OF FLUID FLOWS WITH SLIP BOUNDARY CONDITIONS

By

Anoosheh NiavaraniKheiri

Microfluidics is a rapidly developing field with applications ranging from molecular biology, environmental monitoring, and clinical diagnostics. Microfluidic systems are characterized by large surface-to-volume ratios, and, therefore, fluid flows are significantly influenced by boundary conditions. The fundamental assumption in fluid mechanics is the no-slip boundary condition, which states that the tangential fluid velocity is equal to the adjacent wall speed. Although this assumption is successful in describing fluid flows on macroscopic length scales, recent experimental and numerical studies have shown that it breaks down at microscopic scales due to the possibility of slip of the fluid relative to the wall. The effect of slip is more pronounced for highly viscous liquids like polymer melts or in the region near the moving contact line due to the large gradient in shear stress at the liquid/solid interface. The measure of slip is the so-called slip length, which is defined as a distance between the real interface and imaginary plane where the extrapolated velocity profile vanishes. The slip length value is sensitive to several key parameters, such as surface energy, surface roughness, fluid structure, and shear rate.

In this dissertation, the slip phenomena in thin liquid films confined by either flat or structured surfaces are investigated by molecular dynamics (MD) and continuum simulations. It is found that for flows of both monatomic and polymeric fluids over smooth surfaces, the slip length depends nonlinearly on shear rate at sufficiently high rates. The laminar flow

away from a curved boundary is usually described by means of the effective slip length, which is defined with respect to the mean roughness height. MD simulations show that for corrugated surfaces with wavelength larger than the size of polymer chains, the effective slip length decreases monotonically with increasing corrugation amplitude. A detailed comparison between the solution of the Navier-Stokes equation with the local rate-dependent slip condition and results of MD simulations indicates that there is excellent agreement between the velocity profiles and the effective slip lengths at low shear rate and small-scale surface roughness. It was found that the main cause of the slight discrepancy between MD and continuum results at high shear rates is the reduction of the local slip length in the higher pressure regions where the boundary slope becomes relatively large with respect to the mainstream flow. It was further shown that for the Stokes flow with the local no-slip boundary condition, the effective slip length decreases with increasing corrugation amplitude and a flow circulation is developed in sufficiently deep grooves. Analysis of a numerical solution of the Navier-Stokes equation with the local slip condition shows that the inertial effects promote the asymmetric vortex flow formation and reduce the effective slip length.

# TABLE OF CONTENTS

<b>LIST OF TABLES</b>	<b>vi</b>
<b>LIST OF FIGURES</b>	<b>vii</b>
<b>1 Introduction</b>	<b>1</b>
<b>2 Rheological study of polymer flow past rough surfaces with slip boundary conditions</b>	<b>4</b>
2.1 Introduction . . . . .	4
2.2 The details of the numerical simulations . . . . .	7
2.2.1 Molecular dynamics model . . . . .	7
2.2.2 Continuum method . . . . .	8
2.3 MD results for flat walls . . . . .	10
2.4 Results for periodically corrugated walls: large wavelength . . . . .	11
2.4.1 MD simulations . . . . .	11
2.4.2 Comparison between MD and continuum simulations . . . . .	12
2.5 Results for periodically corrugated walls: small wavelengths . . . . .	14
2.5.1 Comparison between MD and continuum simulations . . . . .	14
2.5.2 The polymer chain configuration and dynamics near rough surfaces .	15
2.6 Conclusions . . . . .	17
<b>3 Slip boundary conditions for shear flow of polymer melts past atomically flat surfaces</b>	<b>31</b>
3.1 Introduction . . . . .	31
3.2 Details of molecular dynamics simulations . . . . .	33
3.3 Results . . . . .	36
3.3.1 Fluid density and velocity profiles . . . . .	36
3.3.2 Rate dependence of the slip length and shear viscosity . . . . .	36
3.3.3 Analysis of the fluid structure in the first layer . . . . .	39
3.4 Conclusions . . . . .	41
<b>4 The effective slip length and vortex formation in laminar flow over a rough surface</b>	<b>54</b>
4.1 Introduction . . . . .	54
4.2 Details of numerical simulations . . . . .	57
4.3 Results . . . . .	60
4.3.1 Analytical solution of the Stokes equation for viscous flow over a wavy wall . . . . .	60

4.3.2	Flow over a rough surface with the local no-slip boundary condition . . . . .	60
4.3.3	Effect of the local slip on the flow pattern near the rough surface . . . . .	63
4.3.4	Effect of the Reynolds number on the effective slip length . . . . .	65
4.4	Conclusions . . . . .	67
<b>5</b>	<b>Modeling the combined effect of surface roughness and shear rate on slip flow of simple fluids</b>	<b>86</b>
5.1	Introduction . . . . .	86
5.2	The details of numerical methods . . . . .	89
5.2.1	Molecular dynamics simulations . . . . .	89
5.2.2	Continuum simulations . . . . .	91
5.3	Results . . . . .	93
5.3.1	MD simulations: the intrinsic and effective slip lengths . . . . .	93
5.3.2	Comparison between MD and continuum simulations . . . . .	95
5.3.3	A detailed analysis of the flow near the curved boundary . . . . .	96
5.4	Conclusions . . . . .	100
<b>6</b>	<b>Slip boundary conditions for the moving contact line in molecular dynamics and continuum simulations</b>	<b>116</b>
6.1	Introduction . . . . .	116
6.2	Molecular dynamics (MD) simulations . . . . .	118
6.2.1	Equilibrium case . . . . .	118
6.2.2	Shear flow . . . . .	121
6.3	Details of continuum simulations . . . . .	123
6.3.1	Fixed grid method for immersed objects . . . . .	123
6.3.2	Continuum Results . . . . .	127
6.4	Conclusions . . . . .	128
<b>BIBLIOGRAPHY</b>		<b>145</b>

## LIST OF TABLES

2.1	Averaged $\hat{x}$ , $\hat{y}$ , and $\hat{z}$ components of the radius of gyration at equilibrium and in the shear flow. The $R_g$ values are reported in the bulk, near the flat upper wall, above the peaks, and inside the grooves. The wavelength of the lower wall is $\lambda = 7.5\sigma$ . The size of the averaging region above the peaks and inside the grooves is $\sigma \times 12.5\sigma \times 1.5\sigma$ . The estimate of the error bars is $0.03\sigma$ . . . . .	27
2.2	Averaged $\hat{x}$ , $\hat{y}$ , and $\hat{z}$ components of the radius of gyration at equilibrium and in the shear flow. The $R_g$ values are reported in the bulk, near the flat upper wall, above the peaks, and inside the grooves. The wavelength of the lower is $\lambda = 3.75\sigma$ . The dimensions of the averaging region are the same as in the Table 2.1. . . . .	28
3.1	The fluid pressure $P$ at equilibrium, i.e., with the stationary upper wall, and the channel height $h$ (defined as a distance between the inner FCC planes) as a function of the fluid density. . . . .	34

## LIST OF FIGURES

2.1 For interpretation of the references to color in this and all other figures, the reader is referred to the electronic version of this dissertation. A snapshot of the fluid monomers (open circles) confined between solid walls (closed circles) obtained from the MD simulations. The atoms of the stationary lower wall are distributed along the sinusoidal curve with the wavelength $\lambda$ and amplitude $a$ . The flat upper wall is moving with a constant velocity $U$ in the $\hat{x}$ direction. The effective slip length $L_{\text{eff}}$ is determined by the linear extrapolation of the velocity profile to $u_x = 0$ . . . . .	18
2.2 Averaged velocity profiles in the cell with flat upper and lower walls. The solid lines are the best linear fit to the data. The vertical axes indicate the location of the <i>FCC</i> lattice planes. The velocities of the upper wall are tabulated in the inset. . . . .	19
2.3 Viscosity of the polymer melt $\mu/\varepsilon\tau\sigma^{-3}$ as a function of shear rate. The dashed line with the slope $-0.33$ is plotted for reference. . . . .	20
2.4 Variation of the slip length as a function of shear rate in the cell with flat upper and lower walls. The solid line is a fourth-order polynomial fit to the data given by Eq. (2.9). . . . .	21
2.5 Averaged density profiles near the stationary upper wall (a), above the peak and in the groove of the lower wall with amplitude $a = 8.16\sigma$ and wavelength $\lambda = 66.60\sigma$ (b). . . . .	22
2.6 Averaged velocity profiles for the indicated values of the corrugation amplitude $a$ . The vertical dashed line denotes a reference plane for calculation of the effective slip length at the corrugated lower wall. The velocity of the flat upper wall is $U = 0.5\sigma/\tau$ . . . . .	23
2.7 The effective slip length as a function of wavenumber $ka$ obtained from the MD simulations ( $\blacklozenge$ ), the solution of the Stokes equation with rate-independent slip length $L_0$ ( $\circ$ ) and with $L_0(\dot{\gamma}\tau)$ given by Eq. (2.9) ( $\times$ ), the solution of the Navier-Stokes equation with $L_0$ ( $\Delta$ ). . . . .	24
2.8 Averaged fluid density profiles near flat upper wall (a) and corrugated lower wall with amplitude $a = 1.4\sigma$ and wavelength $\lambda = 7.5\sigma$ (b). The velocity of the upper wall is $U = 0.5\sigma/\tau$ . . . . .	25

2.9	The effective slip length as a function of wavenumber $ka$ for the indicated values of wavelength $\lambda$ . Continuum results are denoted by the dashed lines and open symbols, while the MD results are shown by straight lines and filled symbols. The inset shows the same data for $ka \leq 0.25$ .	26
2.10	A snapshot of four polymer chains near the lower corrugated wall for wavelength $\lambda = 7.5\sigma$ and amplitude $a = 1.4\sigma$ . The velocity of the upper wall is $U = 0.5\sigma/\tau$ .	29
2.11	A snapshot of five polymer chains near the lower corrugated wall for the wavelength $\lambda = 3.75\sigma$ and amplitude $a = 1.0\sigma$ . The figure shows the side view (top) and the top view (bottom). The velocity of the upper wall is $U = 0.5\sigma/\tau$ .	30
3.1	A schematic representation of the steady-state shear flow in the Couette cell. The upper wall is translated with a constant velocity $U$ in the $\hat{x}$ direction. The fluid slip velocity is determined from the relation $V_s = \dot{\gamma}L_s$ , where $\dot{\gamma}$ is the slope of the velocity profile and $L_s$ is the slip length.	43
3.2	Averaged fluid density profiles near the stationary thermal wall with $\kappa = 1200\varepsilon/\sigma^2$ and $\varepsilon_{wf}/\varepsilon = 0.9$ . The velocities of the upper wall are tabulated in the inset. The fluid density in the center of the cell is $\rho = 0.91\sigma^{-3}$ . The left vertical axis denotes the position of the liquid/solid interface at $z = -14.74\sigma$ .	44
3.3	Average normalized velocity profiles, $V_x/U$ , for the indicated values of the upper wall velocity $U$ and the fluid density $\rho = 0.91\sigma^{-3}$ . Vertical axes denote the position of the FCC lattice planes at $z = -15.24\sigma$ and $z = 12.03\sigma$ . The dashed lines indicate the location of liquid/solid interfaces at a distance $0.5\sigma_w$ away from the FCC lattice planes, i.e., $z = -14.74\sigma$ and $z = 11.53\sigma$ . The inset shows the same data near the lower wall.	45
3.4	Behavior of the fluid viscosity $\mu/\varepsilon\tau\sigma^{-3}$ as a function of shear rate for the tabulated values of the polymer density. The straight dashed line with a slope $-0.37$ is shown for reference. Solid curves are a guide for the eye.	46
3.5	Slip length $L_s/\sigma$ as a function of the shear rate for the polymer melt with linear chains $N = 20$ . Solid curves are a guide for the eye.	47
3.6	Log-log plot of the friction coefficient, $k = \mu/L_s$ , as a function of the slip velocity for the indicated values of the fluid density. The dashed curve is the best fit to Eq.(3.10) with $C_1 = 1.77m\sigma^{-3}$ and $C_2 = 0.71\sigma^2\tau^{-2}$ . Solid curves are a guide for the eye.	48

3.7	Master curve for the friction coefficient as a function of the slip velocity. The same data as in Fig. 3.6. The values of the friction coefficient $k^* [\varepsilon\tau\sigma^{-4}]$ and the slip velocity $V_s^* [\sigma/\tau]$ used for normalization of the data are shown in the inset. The dashed line $y = [1 + (4x)^2]^{-0.35}$ is plotted for reference. . . . .	49
3.8	Structure factor $S(k_x, k_y)$ in the first fluid layer for the fluid density $\rho = 0.91 \sigma^{-3}$ . The upper wall velocity is $U = 0.05 \sigma/\tau$ (a) and $U = 5.0 \sigma/\tau$ (b). The same flow conditions as in Fig. 3.3. . . . .	50
3.9	Temperature profiles for the indicated values of the upper wall speed $U$ and the fluid density $\rho = 0.91 \sigma^{-3}$ . Vertical dashed lines denote the position of the liquid/solid interface. The inset shows the $\hat{x}$ , $\hat{y}$ and $\hat{z}$ components of the temperature profile near the stationary lower wall when the velocity of the upper wall is $U = 5.0 \sigma/\tau$ . . . . .	51
3.10	Log-log plot of $L_s/\mu$ as a function of the ratio $T_1 k_B / \varepsilon [S(\mathbf{G}_1) \rho_c \sigma^3]^{-1}$ for the indicated values of the polymer density. The solid line with a slope 0.9 is plotted for reference. . . . .	52
3.11	Log-log plot of the ratio $L_s/\mu$ as a function of the variable $S(0)/[S(\mathbf{G}_1) \rho_c \sigma^3]$ . The values of the fluid density are tabulated in the inset. The same data as in Fig. 3.10. The straight solid line with a slope 1.15 is plotted as a reference. . . . .	53
4.1	Schematic diagram of the steady-state Couette flow over a rough surface. The upper flat wall is moving with a constant velocity $U$ in the $\hat{x}$ direction. The lower stationary wall is modeled as a sinusoidal wave with amplitude $a$ and wavelength $\lambda$ . The wavenumber $ka = 2\pi a/\lambda$ varies in the range $0 \leq ka \leq 1.26$ . . . . .	68
4.2	Diagram of a bilinear element in (a) the <i>physical</i> coordinate system $(x, z)$ and (b) a transformed element in the <i>natural</i> coordinate system $(\xi, \eta)$ . . . . .	69
4.3	The effective slip length as a function of wavenumber $ka$ computed from the solution of the Stokes equation with the no-slip boundary condition. The primary vortex is formed at the bottom of the valley for $ka \geq 0.79$ (see the vertical arrow at $ka = 0.79$ ). The solid line is calculated using Eq. (4.18). The inset shows the normalized velocity profiles obtained from the Stokes solution for the selected values of $ka$ . The dashed line located at $a = 0$ is the reference for calculating the effective slip length. . . . .	70
4.4	Shear stress along the lower wavy wall computed from the Stokes solution with no-slip boundary condition ( $L_0 = 0$ ) for the indicated values of wavenumber $ka$ . The value $\tau_w^*$ used for normalization is the shear stress at the flat wall. The intersection of the curves with the dashed line determines the location of the flow separation and attachment inside the valley. . . . .	71

4.5	The normalized pressure along the lower corrugated boundary extracted from the Stokes solution with no-slip boundary condition for the same values of $ka$ as in Fig. 4.4. The maximum pressure $P^*$ for $ka = 1.12$ and $L_0 = 0$ is located in the bulk region at $(x/\lambda, z/\lambda) \simeq (0.07, 0.23)$ . . . . .	72
4.6	Pressure contours and streamlines for the wavenumber $ka = 1.12$ and the slip length at the lower wall $L_0 = 0$ (a), $L_0/h = 0.03$ (b), $L_0/h = 0.06$ (c), and $L_0/h = 0.08$ (d). The pressure contours are normalized by the maximum value $P^*$ located on the left side of the peak $(x/\lambda, z/\lambda) \simeq (0.07, 0.23)$ in the case of $L_0 = 0$ . The horizontal dashed line denotes the location of the effective no-slip boundary plane. The vertical dashed line inside the valley at $x/\lambda = 0.75$ indicates the cross-section used to compute the velocity profiles shown in the inset. . . . .	73
4.7	Normalized pressure along the lower wavy wall extracted from the solution of the Stokes equation for the tabulated values of $L_0$ and $ka = 1.12$ . The maximum pressure $P^*$ for $L_0 = 0$ is located above the lower surface at $(x/\lambda, z/\lambda) \simeq (0.07, 0.23)$ . . . . .	77
4.8	Shear stress along the corrugated lower wall ( $ka = 1.12$ ) for the indicated values of the local slip length $L_0$ . The intersection of the dashed line with the shear stress profiles shows the location of the flow separation and attachment inside the valley. . . . .	78
4.9	The effective slip length, extracted from the Stokes solution as a function of $L_0$ for $ka = 0.28$ (top) and $ka = 1.12$ (bottom). The dashed line is computed from Eq. (4.18). For $ka = 1.12$ and $L_0/h \leq 0.067$ , the vortex is formed in the valley (see the vertical arrow at $L_0/h = 0.067$ ). The error bars are smaller than the symbol size. . . . .	79
4.10	The intrinsic slip length $L_0$ above which there is no vortex at the bottom of the valley (top) and the corresponding effective slip length $L_{eff}$ (bottom) computed from the Stokes solution and plotted as a function of wavenumber $ka$ . The increment in the slip length used to determine the threshold values is about the symbol size (top). The dashed lines are quadratic fits to guide the eye. . . . .	80
4.11	The normalized pressure (top) and shear stress (bottom) along the lower wavy wall as a function of the Reynolds number for $ka = 1.12$ and no-slip boundary conditions. The value $P^*$ is the maximum pressure located above the lower boundary on the left side of the peak $(x/\lambda, z/\lambda) \simeq (0.07, 0.23)$ for $L_0 = 0$ and $Re = 4.0$ . . . . .	81
4.12	Pressure contours and streamlines extracted from the solution of the Navier-Stokes equation for $ka = 1.12$ and $L_0 = 0$ (a) and $L_0/h = 0.25$ (b). The value $P^*$ is the maximum pressure located at $(x/\lambda, z/\lambda) \simeq (0.07, 0.23)$ for $ka = 1.12$ , $L_0 = 0$ , and $Re = 4.0$ . The horizontal dashed line denotes the effective no-slip boundary plane. The vertical dashed line inside the valley indicates the cross-section used to compute the velocity profiles shown in the inset. . . . .	82

4.13 The normalized pressure (top) and shear stress (bottom) along the lower wavy wall as a function of the Reynolds number for $ka = 1.12$ and $L_0/h = 0.25$ . The normalization value $P^*$ is the maximum pressure located above the surface on the left side of the peak $(x/\lambda, z/\lambda) \simeq (0.07, 0.23)$ for $L_0 = 0$ and $Re = 4.0$ .	84
4.14 The effective slip length computed from the solution of the Navier-Stokes equation as a function of the Reynolds number for $ka = 1.12$ and $L_0 = 0$ ( $\triangleright$ ), $L_0/h = 0.09$ ( $\blacktriangle$ ), $L_0/h = 0.12$ ( $\triangleleft$ ), and $L_0/h = 0.25$ ( $\blacktriangledown$ ). The dashed line indicates the upper bound of the region where a vortex is present in the groove of a rough surface. The error bars associated with the threshold values of the Reynolds number are about the symbol size.	85
5.1 The projection of $x$ and $z$ coordinates of the fluid monomers (open circles) confined between solid walls (filled circles). The atoms of the lower stationary wall are uniformly distributed along the sinusoidal curve with wavelength $\lambda$ , amplitude $a$ , and density $\rho_w = 3.1 \sigma^{-3}$ . The shear flow is induced by the flat upper wall with the density $0.67 \sigma^{-3}$ moving with a constant velocity $U$ in the $\hat{x}$ direction. The effective slip length $L_{\text{eff}}$ is computed by extrapolation of the velocity profile to $u_x = 0$ .	102
5.2 Averaged velocity profiles for the tabulated upper wall speeds in the cell with flat upper and lower walls. The solid lines are the best linear fits to the data. The vertical axes indicate the location of the <i>FCC</i> lattice planes.	103
5.3 Shear viscosity in the cell with flat upper and lower walls when the temperature of the Langevin thermostat is set to $T = 1.1 \varepsilon/k_B$ ( $\square$ ). Fluid viscosity as a function of the thermostat temperature $1.1 \leq T k_B/\varepsilon \leq 1.4$ for the upper wall speed $U = 1.0 \sigma/\tau$ ( $\triangle$ ) and $1.1 \leq T k_B/\varepsilon \leq 1.35$ for $U = 3.5 \sigma/\tau$ ( $\diamond$ ).	104
5.4 The intrinsic slip length $L_0/\sigma$ as a function of shear rate for atomically flat walls ( $\square$ ). The blue solid curve is a ninth-order polynomial fit to the data. The effective slip length $L_{\text{eff}}/\sigma$ as a function of shear rate for the flow over the corrugated wall with wavenumber $ka = 0.27$ ( $\circ$ ). The effective slip length computed from the solution of the Navier-Stokes equation with the local rate-dependent slip length ( $\bullet$ ).	105
5.5 Temperature of the first fluid layer $T(x)$ (in units of $\varepsilon/k_B$ ) along the lower corrugated wall ( $ka = 0.27$ ) for the indicated upper wall speeds. The vertical dashed lines denote the location of the crest ( $x/\lambda = 0.25$ ) and the bottom of the valley ( $x/\lambda = 0.75$ ).	106
5.6 The normal pressure $P_n$ (in units of $\varepsilon/\sigma^3$ ) along the lower corrugated wall ( $ka = 0.27$ ) for the selected upper wall speeds. The vertical dashed lines indicate the location of the crest ( $x/\lambda = 0.25$ ) and the bottom of the valley ( $x/\lambda = 0.75$ ).	107

5.7	A snapshot of the fluid monomers (open circles) near the lower corrugated wall (filled circles) with wavenumber $ka = 0.27$ . The rectangular boxes denote averaging regions on the left side of the peak (I) ( $x/\lambda \simeq 0.05$ ), above the crest (II) ( $x/\lambda \simeq 0.25$ ), on the right side of the peak (III) ( $x/\lambda \simeq 0.45$ ), and at the bottom of the valley (IV) ( $x/\lambda \simeq 0.75$ ). The unit vectors $\vec{t}$ and $\vec{n}$ indicate the tangential and normal directions at the boundary. . . . .	108
5.8	Fluid density profiles averaged inside regions I–IV (shown in Fig. 5.7) near the corrugated lower wall with wavenumber $ka = 0.27$ . The upper wall speeds are $U = 0$ (a) and $U = 6.0 \sigma/\tau$ (b). . . . .	109
5.9	Averaged tangential velocity profiles inside regions I–IV obtained from MD simulations (open symbols) and the solution of the Navier-Stokes equation (filled symbols). The location of the averaging regions near the lower corrugated wall is shown in Fig. 5.7. The upper wall speed is $U = 1.0 \sigma/\tau$ . . . . .	110
5.10	Averaged normal velocity profiles inside regions I–IV (shown in Fig. 5.7) for the upper wall speed $U = 1.0 \sigma/\tau$ . The profiles are extracted from MD simulations (open symbols) and the solution of the Navier-Stokes equation (filled symbols). The horizontal dashed lines indicate the location of the minima in density profiles (see text for details). . . . .	111
5.11	Tangential velocity profiles averaged inside regions I–IV (shown in Fig. 5.7) near the lower corrugated wall. The upper wall speed is $U = 6.0 \sigma/\tau$ . The velocity profiles are extracted from MD simulations (open symbols) and the solution of the Navier-Stokes equation (filled symbols). . . . .	112
5.12	The intrinsic slip length along the lower corrugated wall ( $ka = 0.27$ ) for the upper wall speed $U = 6.0 \sigma/\tau$ . The data are obtained from MD simulations (open symbols) and the solution of the Navier-Stokes equation (filled symbols). The vertical dashed lines denote the position of the crest ( $x/\lambda = 0.25$ ) and the bottom of the valley ( $x/\lambda = 0.75$ ). . . . .	113
5.13	Averaged normal velocity profiles inside regions I–IV obtained from MD simulations (open symbols) and the solution of the Navier-Stokes equation (filled symbols). The upper wall speed is $U = 6.0 \sigma/\tau$ . The horizontal arrows indicate the location of the minima in density profiles between the first and second fluid layers in regions I and III. . . . .	114
5.14	The intrinsic slip length $L_0/\sigma$ as a function of the bulk pressure $P$ (in units of $\varepsilon/\sigma^3$ ) in the cell with flat upper and lower walls. The temperature of the Langevin thermostat is varied in the range $1.1 \leq T k_B/\varepsilon \leq 1.35$ for the upper wall speed $U = 3.5 \sigma/\tau$ (a) and $1.1 \leq T k_B/\varepsilon \leq 1.4$ for $U = 1.0 \sigma/\tau$ (b). . . . .	115
6.1	The schematic representation of the contact line and the shape of the fluid/fluid interface for the static (left) and dynamic (right) cases. . . . .	130

6.2	The schematic picture of the moving contact line problem where the slip velocity and the friction coefficient far from the contact line are denoted by $u_{\text{slip}}$ and $\beta_{\text{slip}}$ and in the contact region by $u_{\text{contact}}$ and $\beta_{\text{contact}}$ . . . . .	131
6.3	Initial arrangement of fluid molecules and wall atoms in the system that consists of two immiscible fluids confined between flat walls. . . . .	131
6.4	The modified Lennard-Jones potential Eq. (6.1) as a function of monomer monomer distance for different values of the parameter $\delta$ . . . . .	132
6.5	A snapshot of an equilibrated system with two immiscible fluids when both walls are at rest. . . . .	132
6.6	The averaged density profiles for fluid 1 across the channel width in the $\hat{z}$ direction (a) and density profiles for fluids 1 and 2 parallel to the walls in the $\hat{x}$ direction (b). . . . .	133
6.7	The normal stress distributions in the $\hat{x}$ , $\hat{y}$ , and $\hat{z}$ directions in equilibrium case ( $U = 0$ ) calculated from the Irving-Kirkwood relation. The normal stresses are measured in units of $\varepsilon/\sigma^3$ . . . . .	134
6.8	(a) The snapshot of the fluid molecules near the solid wall within $5\sigma$ from the contact line at equilibrium. The horizontal arrows near the contact line indicate the direction of the tangential forces on each fluid. (b) The shear stress distribution $\tau_{xz}(x)$ along the wall as a function of the distance from the contact line. . . . .	135
6.9	The shape of the fluid/fluid interfaces as a function of the wall speeds for (a) $U = 0$ , (b) $U = 0.05\sigma/\tau$ , and (c) $U = 0.1\sigma/\tau$ . . . . .	136
6.10	The contact angle averaged in two fluid phases is plotted as a function of the wall speeds $U$ . . . . .	137
6.11	The snapshot of the system near the contact line for $U = 0.1\sigma/\tau$ (top), the averaged velocity vectors (bottom) obtained from MD simulations. . . . .	138
6.12	The slip velocity of the first fluid layer for upper and lower wall speeds $U = 0.1\sigma/\tau$ . The velocity profiles are averaged separately in each fluid phase as shown by symbols. The dashed line is the slip velocity computed regardless of the fluid type. The black solid is a guide for the eye. . . . .	139
6.13	(a) The slip velocity in the first fluid layer as a function of upper/lower wall speeds. (b) The velocity profiles across the channel far from the contact lines in the $\hat{z}$ direction as a function of the upper/lower wall speeds. . . . .	140

6.14 The setup of the continuum simulations where the black solid lines show the fixed Cartesian grids, the red circles are the initial position of the marker points, and the blue circles are the initial location of the contact points. The boundary conditions are applied along the green regions away from the contact point and along blue regions close to the contact point (top). The schematic velocity profile in the bottom figure shows an enlarged view of the velocity profile inside top figure's dashed-boxes. . . . .	141
6.15 The results from the Navier-Stokes solution of the moving contact line as a function of upper/lower wall speeds $U = 0.01$ (a), $U = 0.05$ (b), and $U = 0.1$ (c). The velocity vectors are shown by blue arrows, streamlines by black lines, and fluid/fluid interfaces by red lines. . . .	142
6.16 The filled symbols represent the contact angle extracted from the Navier-Stokes solution as a function of upper/lower wall speeds. The open symbols are the results from the molecular dynamics simulations. Solid and dashed lines are a guide for the eye. . . . .	143
6.17 The symbols and solid lines show the slip velocities near the moving contact line obtained from the Navier-Stokes solution. The dashed lines are the slip velocities from molecular dynamics simulations in the first fluid layer as a function of upper/lower wall speeds. . . . .	144

# CHAPTER 1

## Introduction

Microfluidics is a multidisciplinary research field that bridges between engineering, chemistry, and biology [1]. Microfluidic systems are characterized by high surface to volume ratios and low Reynolds number flows. These features allow precise control and manipulation of fluids, reduced sample volume usage, and fast mixing [2]. As new areas of application are currently being explored and the systems under investigation are becoming more complex, there is an increasing demand to understand the physics of flows on the submicron scale and to develop more efficient numerical modeling techniques.

In the interfacial region of about a few molecular diameters from the solid wall, the fluid flow has very different physical properties than in the bulk region. One of the classical assumptions in the fluid mechanics textbooks is the *no-slip boundary condition*, which proved to be very successful in describing flows on large scales. However, recent experimental and molecular dynamics simulation studies have shown that this condition needs revision for microscopic scales due to the possibility of slip of the fluid relative to the wall. The breakdown of the no-slip condition, the so-called *slip boundary condition*, refers to a situation where the fluid tangential velocity adjacent to the wall is different from the wall speed. The measure of slip is the slip length, which is defined as a distance from the real liquid-solid interface to an imaginary plane where an extrapolated velocity profile vanishes. There are several key factors that influence the degree of slippage including surface roughness, surface energy, fluid structure, relative size of fluid molecules with respect to the wall atoms, the ratio of the fluid and wall densities, and the rate of shear.

In this dissertation, we investigate fluid flows and the slip phenomena in confined systems using molecular dynamics (MD) and continuum simulations. The molecular dynamics technique, despite its computational cost, provides a detailed information about the structure, dynamics, and thermodynamics of complex flows, especially near the solid/liquid interface. On the other hand, the continuum modeling is computationally more affordable but requires specification of the proper boundary conditions. One of the main themes in this dissertation is a comparative analysis of fluid flows using both atomistic and continuum descriptions. In particular, we numerically solve the Navier-Stokes equation for flows in various geometries using the slip boundary conditions obtained from MD studies. The continuum predictions are compared with the results of MD simulations for a wide range of parameters describing liquid-solid interfaces, i.e., fluid structure (monatomic and polymeric liquids), wall structure (wall density and topological roughness), and flow conditions (low/high shear rates, low/high Reynolds numbers, and single/two phase flows). The results are categorized as follows.

In chapter II, molecular dynamics simulations are carried out to investigate the dynamic behavior of the slip length for polymeric liquids confined between either atomically flat or periodically corrugated surfaces. The MD results show that for atomically flat walls the slip length depends non-linearly on shear rate. In contrast to the description of the flow over smooth boundaries (with microscopic surface roughness) by the intrinsic slip length, it is more appropriate to characterize the flow away from macroscopically rough surfaces by the *effective slip length*, which is usually defined with respect to the location of the mean roughness height. For periodically corrugated surfaces, the effective slip length gradually decreases as a function of wavenumber. The polymer chain configuration and dynamics are studied near rough surfaces. For flows over periodically corrugated surfaces, the solution of the Stokes equation is compared with the results of MD simulations in a wide range of wavelengths and amplitudes.

The effects of shear rate and fluid density on slip boundary conditions for polymer melt flows past flat crystalline walls are investigated by molecular dynamics simulations in chapter III. It is shown that the rate-dependent slip length exhibits a local minimum and then it increases rapidly at higher shear rates. The friction coefficient at the liquid/solid interface

follows a power law decay as a function of the slip velocity. The ratio of the viscosity to the slip length (i.e., friction coefficient at the liquid-solid interface) is determined by the surface induced structure in the first fluid layer.

In chapter IV, we investigate the effects of local slip boundary conditions and the Reynolds number on the flow structure near periodically corrugated surfaces and the effective slip length. It was shown that for the Stokes flow with the local no-slip boundary condition, the effective slip length decreases with increasing corrugation amplitude and a flow circulation is developed in sufficiently deep grooves. The analysis of numerical solution of the Navier-Stokes equation with the local slip condition shows that the inertial effects promote the asymmetric vortex flow formation and reduce the effective slip length.

In chapter V, the slip flow of monatomic fluids over a periodically corrugated surface is studied in a wide range of shear rates using molecular dynamics and continuum simulations. The effective slip length in both methods is nearly constant at low shear rates and it gradually increases at higher shear rates. The slight discrepancy between the effective slip lengths computed from MD and continuum methods at high shear rates is explained by careful examination of the local pressure, velocity, and density profiles along the wavy surface.

The moving contact line problem is considered in the last chapter VI using molecular dynamics and continuum simulations. The MD simulations are carried out to resolve the flow fields in the vicinity of the moving contact line at the molecular scale. Then, the boundary conditions extracted from MD simulations is implemented in the continuum solution of the Navier-Stokes equations (using finite difference/particle tracking methods) to reproduce velocity profiles and the shape of the fluid/fluid interface.

# CHAPTER 2

## Rheological study of polymer flow past rough surfaces with slip boundary conditions

### 2.1 Introduction

The dynamics of fluid flow in confined geometries has gained renewed interest due to the recent developments in micro- and nanofluidics [3]. The investigations are motivated by important industrial applications including lubrication, coating, and painting processes. The flow behavior at the sub-micron scale strongly depends on the boundary conditions at the liquid/solid interface. A number of experimental studies on fluid flow past nonwetting surfaces have shown that the conditions at the boundary deviate from the no-slip assumption [4]. The most popular Navier model relates the slip velocity (the relative velocity of the fluid with respect to the adjacent solid wall) and the shear rate with the proportionality coefficient, *the slip length*, which is determined by the linear extrapolation of the fluid velocity profile to zero. The magnitude of the slip length depends on several key parameters, such as wettability [5, 6, 8, 7], surface roughness [9, 10, 11, 12, 13, 14], complex fluid structure [15, 16], and shear rate [17, 18, 19]. However, the experimental determination of the slip length as a function of these parameters is hampered by the presence of several factors with competing effects on the wall slip, e.g. surface roughness and wettability [9] or surface

roughness and shear rate [10].

In recent years, molecular dynamics (MD) simulations have been widely used to examine the slip flow past atomically smooth, homogeneous surfaces [20, 21, 125, 23, 24, 25, 26, 28, 27, 29]. The advantage of the MD approach is that the velocity profiles and shear stresses are resolved at the molecular level. The slip length in the shear flow of simple fluids past crystalline walls is a function of the wall-fluid density ratio [21, 23], the relative size of wall atoms and fluid molecules [23, 28], the surface energy [21, 23, 29], and the interfacial shear rate [23, 27, 29]. Weak wall-fluid interactions and incommensurable structures of the solid and fluid phases at the interface usually lead to enhancement of slip [21, 23, 26, 29]. If the slip length at low shear rates is about several molecular diameters then it increases with the shear rate, and the slope of the rate dependence is greater for weaker wall-fluid interactions [23, 29]. The rate dependence of the slip length in the flow of polymer melts is more complicated because of the additional length and time scales associated with the dynamics of polymer chains at the interface and the shear thinning viscosity [125, 30, 31, 27, 32].

In the presence of surface roughness [33, 34, 35, 36, 37] or chemical patterning [38, 39, 40, 41, 42], the fluid flow near the solid boundary is perturbed on the length scales of the surface heterogeneities and its description requires definitions of the effective slip length and the average location of the reference plane. Most commonly, the location of the reference plane is defined as the mean height of the surface asperities, and the shear rate is determined by averaging of the fluid flow over the typical length scale of the surface inhomogeneities. In general, the surface roughness is expected to reduce the effective slip length for wetting liquids [34, 35, 37]. For sufficiently rough surfaces the no-slip boundary condition can be achieved even if the local condition is of zero shear stress [43]. However, in special cases, when the fluid is partially dewetted at the nanostructured, or the so-called “superhydrophobic” surfaces, the slip length might be enhanced up to a few microns [44, 45, 46, 47, 48, 49, 50].

In recent MD studies on shear flow of simple fluids, the behavior of the effective slip length was investigated in the Couette cell with either mixed boundary conditions [40] or periodic surface roughness [35]. In the first study, the lower stationary wall with mixed boundary conditions was patterned with a periodic array of stripes representing alternating regions of

finite slip and zero shear stress. In the other study [35], the periodically roughened surface was modeled by introducing a sinusoidal offset to the position of the wall atoms. At the wavy wall, the local slip length is modified by the presence of curvature and becomes position-dependent along the curved boundary [51, 52]. A detailed comparison between continuum analysis and MD simulations shows an excellent agreement between the velocity profiles and effective slip lengths when the characteristic length scale of substrate inhomogeneities is larger than approximately thirty molecular diameters [40, 35]. In the case of rough surfaces, an additional correction due to variable wall density was incorporated in the analysis [35]. The problem of applicability of the results obtained for monoatomic fluids to polymer melts is important for modeling polymer flows in confined geometries and design of the hybrid continuum-atomistic algorithms.

In this chapter, the MD simulations are carried out to study the dynamic behavior of the slip length at the interface between a polymer melt and atomically flat or periodically corrugated surfaces. The MD results for flat crystalline walls confirm previous findings [32] that the slip length goes through a local minimum at low shear rates and then increases rapidly at higher shear rates. For periodically corrugated surfaces and wetting conditions, the effective slip length decreases gradually with increasing values of the wavenumber. The solution of the Stokes equation with either constant or rate-dependent local slip length is compared with the MD simulations for corrugated surfaces with wavelengths ranging from molecular dimensions to values much larger than the radius of gyration of polymer chains. The orientation and the dynamics of linear polymer chains are significantly affected by surface roughness when the corrugation wavelengths are comparable with the radius of gyration.

The rest of the chapter is organized as follows. The details of molecular dynamics and continuum simulations are described in the next section. The dynamic response of the slip length and shear viscosity in the cell with atomically flat surfaces is presented in Sec. 2.3. The results of MD simulations for corrugated walls with large wavelengths and comparison with continuum predictions are reported in Sec. 2.4. The slip behavior for small wavelengths and the conformational properties of the polymer chains near the rough surfaces are analyzed in Sec. 2.5. The summary is given in the last section.

## 2.2 The details of the numerical simulations

### 2.2.1 Molecular dynamics model

The computational domain consists of a polymeric fluid confined between two atomistic walls. Figure 2.1 shows the MD simulation setup. Any two fluid monomers within a cut-off distance of  $r_c = 2.5 \sigma$  interact through the truncated Lennard-Jones (LJ) potential

$$V_{LJ}(r) = 4\epsilon \left[ \left( \frac{\sigma}{r} \right)^{12} - \left( \frac{\sigma}{r} \right)^6 \right], \quad (2.1)$$

where  $\epsilon$  is the energy scale and  $\sigma$  is the length scale of the fluid phase. The LJ potential was also employed for the wall-fluid interaction with  $\epsilon_{wf} = \epsilon$  and  $\sigma_{wf} = \sigma$ . The wall atoms do not interact with each other, and the wall-fluid parameters are fixed throughout the study. In addition to the LJ potential, the neighboring monomers in a polymer chain ( $N = 20$  beads) interact with the finite extensible nonlinear elastic (FENE) potential

$$V_{FENE}(r) = -\frac{1}{2}kr_o^2 \ln \left[ 1 - \left( \frac{r}{r_o} \right)^2 \right], \quad (2.2)$$

where  $r_o = 1.5 \sigma$  and  $k = 30 \epsilon \sigma^{-2}$  [53]. The MD simulations were performed at a constant density ensemble with  $\rho = 0.88 \sigma^{-3}$ . The total number of fluid monomers is  $N_f = 67200$ .

The motion of the fluid monomers was weakly coupled to an external thermal reservoir [54]. To avoid a bias in the flow direction, the random force and the friction term were added to the equation of motion in the  $\hat{y}$  direction [21]

$$m\ddot{y}_i = - \sum_{i \neq j} \frac{\partial(V_{LJ} + V_{FENE})}{\partial y_i} - m\Gamma y_i + f_i(t), \quad (2.3)$$

where  $\Gamma = 1.0 \tau^{-1}$  is a friction constant that regulates the rate of heat flux between the fluid and the heat bath, and  $f_i(t)$  is the random force with zero mean and variance  $2m\Gamma k_B T \delta(t)$  determined from the fluctuation-dissipation theorem [55]. Temperature of the Langevin thermostat is set to  $T = 1.1 \epsilon / k_B$ , where  $k_B$  is the Boltzmann constant. The equations of motion were integrated using the Verlet algorithm [56] with a time step  $\Delta t = 0.005 \tau$ , where  $\tau = \sqrt{m\sigma^2/\epsilon}$  is the characteristic LJ time.

The dimensions of the system in the  $xy$  plane, unless specified otherwise, were set to  $L_x = 66.60 \sigma$  and  $L_y = 15.59 \sigma$ . The upper wall was composed of two layers of an *FCC*

lattice with density  $\rho_w = 1.94 \sigma^{-3}$ , which corresponds to the nearest-neighbor distance of  $d = 0.9\sigma$  between wall atoms in the (111) plane. The lower wall was constructed of two *FCC* layers of atoms distributed along the sinusoidal curve with the wavelength  $\lambda$  and amplitude  $a$ . For the largest wavelength  $\lambda = 66.60\sigma$ , the density of the lower wall  $\rho_w = 1.94 \sigma^{-3}$  was kept uniform along the sinusoid (by including additional rows of atoms parallel to the  $\hat{y}$  axis) to avoid additional analysis of the effective slip length due to variable wall density [35]. In the present study, the corrugation amplitude was varied in the range  $0 \leq a/\sigma \leq 12.04$ . In the absence of the imposed corrugation ( $a=0$ ) the distance between the inner *FCC* planes is set to  $L_z = 74.15\sigma$  in the  $\hat{z}$  direction. Periodic boundary conditions were imposed in the  $\hat{x}$  and  $\hat{y}$  directions.

The initial velocities of the fluid monomers were chosen from the Maxwell-Boltzmann probability distribution at the temperature  $T = 1.1\varepsilon/k_B$ . After an equilibration period of about  $3 \times 10^4\tau$  with stationary walls, the velocity of the upper wall was gradually increased in the  $\hat{x}$  direction from zero to its final value during the next  $2 \times 10^3\tau$ . Then the system was equilibrated for an additional period of  $6 \times 10^3\tau$  to reach steady-state. Averaging time varied from  $10^5\tau$  to  $2 \times 10^5\tau$  for large and small velocities of the upper wall respectively. The velocity profiles were averaged within horizontal slices of  $L_x \times L_y \times \Delta z$ , where  $\Delta z = 0.2\sigma$ . Fluid density profiles near the walls were computed within slices with thickness  $\Delta z = 0.01\sigma$  [29].

### 2.2.2 Continuum method

A solver based on the finite element method was developed for the two-dimensional steady-state and incompressible Navier-Stokes (NS) equation. The NS equation with these assumptions is reduced to

$$\rho(\mathbf{u} \cdot \nabla \mathbf{u}) = -\nabla p + \mu \nabla^2 \mathbf{u}, \quad (2.4)$$

where  $\mathbf{u}$  is the velocity vector,  $\rho$  is the fluid density, and  $p$  and  $\mu$  are the pressure field and viscosity of the fluid respectively.

The incompressibility condition is satisfied by a divergence-free velocity field  $\mathbf{u}$ . In order to avoid the decoupling of the velocity and the pressure fields in the numerical simulation

of the incompressible flow, the penalty formulation is adopted [57]. This method replaces the continuity equation,  $\nabla \cdot \mathbf{u} = 0$ , with a perturbed equation

$$\nabla \cdot \mathbf{u} = -\frac{p}{\Lambda}, \quad (2.5)$$

where  $\Lambda$  is the penalty parameter. For most practical applications, where computation is performed with double-precision 64 bit words, a penalty parameter between  $10^7$  and  $10^9$  is sufficient to conserve the accuracy [57]. In our simulations the incompressibility constraint was set to  $\Lambda = 10^7$ . The pressure term in Eq. (2.5) is then substituted into the NS equation. The equation Eq. (2.4) can be rewritten as follows:

$$\rho(\mathbf{u} \cdot \nabla \mathbf{u}) = \Lambda \nabla(\nabla \cdot \mathbf{u}) + \mu \nabla^2 \mathbf{u}, \quad (2.6)$$

where the continuity equation is no longer necessary [57]. The NS equation is integrated with the Galerkin method using bilinear rectangular isoparametric elements [57].

Four boundary conditions must be specified for the continuum simulation. Periodic boundary conditions are used for the inlet and outlet along the  $\hat{x}$  direction. A slip boundary condition is applied at the upper and lower walls. In the local coordinate system (spanned by the tangential vector  $\vec{t}$  and the normal vector  $\vec{n}$ ), the fluid velocity along the curved boundary is calculated as

$$u_t = L_0[(\vec{n} \cdot \nabla) u_t + u_t/R], \quad (2.7)$$

where  $u_t$  is the tangential component of  $\mathbf{u} = u_t \vec{t} + u_n \vec{n}$ ,  $L_0$  is the slip length at the flat liquid/solid interface, the term in the brackets is the local shear rate, and  $R$  is the local radius of curvature [52]. The radius of curvature is positive for the concave and negative for the convex regions. For a flat surface,  $R \rightarrow \infty$ , the boundary condition given by Eq. (2.7) simply becomes the Navier slip law.

The simulation is started by applying the no-slip boundary condition as the initial guess. Once the equations of motion are solved implicitly, the local slip velocities at the lower and upper boundaries are updated using Eq. (2.7). In the next step, the equations of motion are solved with the updated slip velocities used as a new boundary condition. The iterative procedure is repeated until the solution converges to a desired accuracy. The convergence rate of the iterative solution remains under control with the under-relaxation value about

0.001 for the boundary nodes. In all continuum simulations, the grids at the lower boundary have an aspect ratio of about one. The computational cost is reduced by increasing the aspect ratio of the grids in the bulk region.

The normalized average error value in the simulation is defined as

$$\text{error} = \left[ \sum_{i=1}^{N_p} \frac{|\mathbf{u}_i^n - \mathbf{u}_i^{n+1}|}{|\mathbf{u}_i^{n+1}|} \right] / N_p, \quad (2.8)$$

where  $N_p$  is the number of nodes in the system,  $\mathbf{u}_i^n$  is the velocity at the node  $i$  and time step  $n$ , and  $\mathbf{u}_i^{n+1}$  is the velocity in the next time step. The typical error in the converged solution is less than  $10^{-9}$ . At the boundaries the solution satisfies  $u_t = L_{\text{local}} \frac{\partial u_t}{\partial n}$ , where the local slip length is  $L_{\text{local}} = (L_0^{-1} - R^{-1})^{-1}$  [52].

## 2.3 MD results for flat walls

The averaged velocity profiles for selected values of the upper wall speed  $U$  are presented in Fig. 2.2. The profiles are linear throughout the cell, except for  $U \geq 6.0 \sigma/\tau$  where a slight curvature appears in the region of about  $4\sigma$  near the walls. Note that the relative slip velocity at the upper and lower walls increases with increasing upper wall speed. The shear rate was determined from the linear fit to the velocity profiles across the whole width of the channel (see Fig. 2.2). The uncertainty in the estimated value of shear rate is due to the thermal fluctuations and the slight curvature in the velocity profiles near the walls. The typical error bars for the shear rate are about  $2 \times 10^{-5} \tau^{-1}$  and  $6 \times 10^{-4} \tau^{-1}$  for small and large upper wall speeds respectively (not shown).

In this study, the shear stress in steady-state flow was computed from the Irving-Kirkwood relation [58]. The dynamic response of the fluid viscosity with increasing shear rate is presented in Fig. 2.3. At higher shear rates, the fluid exhibits shear thinning behavior with the slope of about  $-0.33$ . Although the power law coefficient is larger than the reported values in experimental studies [59], the results are consistent with previous MD simulations of polymer melts for similar flow conditions [60, 61, 32].

The slip length was calculated by the linear extrapolation of the fluid velocity profile to zero with respect to a reference plane, which is located  $0.5\sigma$  away from the *FCC* lattice

plane [29, 32]. Figure 2.4 shows the rate dependence of the slip length in the same range of shear rates as in Fig. 2.3. The slip length goes through a shallow minimum at low shear rates and then increases rapidly at higher rates. The error bars are larger at low shear rates because the thermal fluid velocity  $v_T^2 = k_B T/m$  is greater than the average flow velocity. The nonmonotonic behavior of the slip length in sheared polymer films with atomically flat surfaces can be interpreted in terms of the friction coefficient at the liquid/solid interface, which undergoes a gradual transition from a nearly constant value to the power law decay as a function of the slip velocity [32]. The data for the slip length shown in Fig. 2.4 are well fitted by the fourth-order polynomial

$$L_0(x)/\sigma = 16.8 - 72.0 \times 10 x + 44.0 \times 10^3 x^2 - 97.3 \times 10^4 x^3 + 80.5 \times 10^5 x^4, \quad (2.9)$$

where  $x = \dot{\gamma}\tau$  is the shear rate. The polynomial fit will be used to specify the boundary conditions for the continuum solution described in the next section.

## 2.4 Results for periodically corrugated walls: large wavelength

### 2.4.1 MD simulations

The monomer density profiles were computed in the averaging regions located in the grooves and above the peaks of the corrugated lower wall with wavelength  $\lambda = L_z = 66.60 \sigma$ . The dimensions of the averaging regions are set to  $0.5 \sigma$  and  $L_y = 15.59 \sigma$  in the  $\hat{x}$  and  $\hat{y}$  directions respectively. Figure 2.5 shows the monomer density profiles near the upper and lower walls at equilibrium. The pronounced density oscillations are attributed to the successive layering of the fluid monomers near the walls. These oscillations decay within a few molecular diameters from the walls to a uniform profile characterized by the bulk density of  $\rho = 0.88 \sigma^{-3}$ . Note that the height of the first peak in the density profile inside the groove is slightly larger than its value above the crest [see Fig. 2.5(b)]. The fluid monomers experience stronger net surface potential in the groove than above the crest because of the closer spatial arrangement of the wall atoms around the location of the first density peak in the groove. This effect

is amplified when the local radius of curvature at the bottom of the grooves is reduced at smaller wavelengths (see below).

The averaged velocity profiles in the cell with periodically corrugated lower and flat upper walls are presented in Fig. 2.6. The fluid velocity profiles were averaged within horizontal slices of thickness  $\Delta z = 0.2\sigma$  distributed uniformly from the bottom of the grooves to the upper wall. With increasing corrugation amplitude, the slip velocity decreases and the profiles acquire a curvature near the lower wall. Note also that the relative slip velocity at the upper wall increases with the shear rate. The linear part of the velocity profiles,  $30 \leq z/\sigma \leq 60$ , was used to determine the effective slip length  $L_{\text{eff}}$  at the corrugated lower wall. The variation of the effective slip length as a function of wavenumber  $ka = 2\pi a/\lambda$  is shown in Fig. 2.7. The slip length decreases monotonically with increasing wavenumber and becomes negative at  $ka \gtrsim 0.7$ . The results of comparison between the MD and continuum simulations for three different cases are presented in the next section.

#### 2.4.2 Comparison between MD and continuum simulations

In continuum simulations, the length, time and energy scales are normalized by the LJ parameters  $\sigma$ ,  $\tau$  and  $\varepsilon$  respectively. The continuum nondimensional parameters are denoted by the  $(\sim)$  sign. The size of the two-dimensional domain is fixed to  $66.60 \times 73.15$  in the  $\hat{x}$  and  $\hat{z}$  directions, respectively. The following three cases were examined: the Stokes solution with constant slip length in Eq. (2.7), the Stokes solution with shear-rate-dependent slip length given by Eq. (2.9), and the Navier-Stokes solution with constant slip length in Eq. (2.7). For all cases considered, the flat upper wall is translated with a constant velocity  $\tilde{U} = 0.5$  in the  $\hat{x}$  direction. Similarly to the MD method, the effective slip length is defined as a distance from the reference plane at  $a = 0$  to the point where the linearly extrapolated velocity profile vanishes.

In the first case, the finite element method was implemented to solve the Stokes equation with boundary conditions at the upper and lower walls specified by Eq. (2.7) with  $\tilde{L}_0 = 14.1$ . This value corresponds to the slip length  $L_0 = 14.1 \pm 0.5\sigma$  extracted from the MD simulations in the cell with flat walls and the velocity of the upper wall  $U = 0.5\sigma/\tau$ . Note that at large amplitudes  $\tilde{a} \geq 8.16$ , the normal derivative of the tangential velocity  $\partial u_t / \partial n$  at the

bottom of the grooves is negative, while the  $\hat{x}$  component of the slip velocity is positive everywhere along the corrugated lower wall. The dependence of the effective slip length on the corrugation amplitude is shown in Fig. 2.7. The continuum results agree well with the approximate analytical solution [52] for  $ka \lesssim 0.5$  (not shown). For larger amplitudes,  $ka > 0.5$ , where the analytical solution is not valid, our results were tested to be grid independent. There is an excellent agreement between slip lengths obtained from the MD and continuum simulations for  $ka \lesssim 0.3$ . With further increasing the amplitude, the slip length obtained from the continuum solution overestimates its MD value. The results presented in Fig. 2.7 are consistent with the analysis performed earlier for simple fluids [35], although a better agreement between MD and continuum solutions was expected at  $ka > 0.5$  because of the larger system size considered in the present study.

As discussed in the previous section, the slip length for atomically flat walls is rate-dependent even at low shear rates (see Fig. 2.4). In the second case, we include the effect of shear rate in the analysis of the effective slip length at the corrugated lower wall and flat upper wall. The Stokes equation is solved with boundary conditions given by Eq. (2.7), where the slip length Eq. (2.9) is a function of the local shear rate at the curved and flat boundaries. The results obtained from the Stokes solution with constant and rate-dependent slip lengths are almost indistinguishable (see Fig. 2.7). This behavior can be attributed to a small variation of the intrinsic slip length Eq. (2.9) at low shear rates. For example, at the largest amplitude,  $\tilde{a} = 12.04$ , the local shear rate at the corrugated wall is position-dependent and bounded by  $|\partial u_t / \partial n + u_t / R| \leq 0.0035$ . In this range of shear rates, the normalized value of the slip length in Eq. (2.9) varies between  $14.7 \leq \tilde{L}_0 \leq 16.6$ . It is expected, however, that the effect of shear rate will be noticeable at larger values of the top wall speed  $\tilde{U}$ .

In the third case, the Navier-Stokes equation is solved with a constant slip length  $\tilde{L}_0 = 14.1$  in Eq. (2.7) at the flat upper and corrugated lower walls. The upper estimate of the Reynolds number based on the fluid density  $\tilde{\rho} = 0.88$ , viscosity  $\tilde{\mu} = 20.0$ , and the fluid velocity difference across the channel is  $Re \approx 1.3$ . It was previously shown by Tuck and Kouzoubov [63] that at small  $ka$  and  $\tilde{L}_0 = 0$  the magnitude of the apparent slip velocity at the mean surface increases due to finite Reynolds number effects for  $Re \gtrsim 30$ . In our study, the difference

between the slip lengths extracted from the Stokes and Navier-Stokes solutions is within the error bars (see Fig. 2.7). These results confirm that the slip length is not affected by the inertia term in the Navier-Stokes equation for  $Re \lesssim 1.3$ . To check how sensitive the boundary conditions are to higher Reynolds number flows, we have also repeated the continuum simulations for larger velocity of the upper wall  $\tilde{U} = 50$ , which corresponds to  $Re \approx 130$ . For the largest corrugation amplitude  $\tilde{a} = 12.04$ , the backflow appears inside the groove and the effective slip length becomes smaller than its value for  $\tilde{U} = 0.5$  by about 0.7 (not shown).

## 2.5 Results for periodically corrugated walls: small wavelengths

### 2.5.1 Comparison between MD and continuum simulations

The MD simulations described in this section were performed at corrugation wavelengths ( $\lambda/\sigma = 3.75, 7.5$  and  $22.5$ ) comparable with the size of a polymer coil. Periodic surface roughness of the lower wall was created by displacing the *FCC* wall atoms by  $\Delta z = a \sin(2\pi x/\lambda)$  in the  $\hat{z}$  direction [35]. In order to reduce the computational time the system size was restricted to  $N_f = 8580$  fluid monomers and  $L_x = 22.5\sigma$ ,  $L_y = 12.5\sigma$  and  $L_z = 35.6\sigma$ . All other system parameters were kept the same as in the previous section.

The representative density profiles near the upper and lower walls are shown in Fig. 2.8 for the wavelength  $\lambda = 7.5\sigma$ . The height of the first peak in the density profile is larger in the grooves than near the flat wall or above the crests of the corrugated surface. The effective slip length as a function of wavenumber  $ka$  is plotted in Fig. 2.9. For all wavelengths, the slip length decreases monotonically with increasing values of  $ka$ . At the smallest wavelength  $\lambda = 3.75\sigma$ , the slip length rapidly decays to zero at  $ka \approx 0.4$  and weakly depends on the corrugation amplitude at larger  $ka$ . Inspection of the local velocity profiles for  $\lambda = 3.75\sigma$  and  $ka \gtrsim 1.0$  indicates that the flow is stagnant inside the grooves [62].

In the continuum analysis, the Stokes equation with a constant slip length  $\tilde{L}_0 = 14.1$  in Eq. (2.7) is solved for the three wavelengths. The comparison between the MD results and the solution of the Stokes equation is presented in Fig. 2.9. The error bars are larger for the

smallest wavelength because of the fine grid resolution required near the lower boundary at  $ka \lesssim 0.2$  (see inset in Fig. 2.9). The results shown in Fig. 2.9 confirm previous findings for simple fluids [35] that the slip length obtained from the Stokes flow solution overestimates its MD value and the agreement between the two solutions becomes worse at smaller wavelengths. It is interesting to note that the curves for different wavelengths intersect each other at  $ka \approx 0.63$  in the MD model and at  $ka \approx 1.02$  in the continuum analysis. The same trend was also observed in the previous study on slip flow of simple fluids past periodically corrugated surfaces [35].

### 2.5.2 The polymer chain configuration and dynamics near rough surfaces

In this section, the properties of polymer chains are examined in the bulk and near the corrugated boundary with wavelengths  $\lambda = 3.5\sigma$  and  $\lambda = 7.5\sigma$ . The radius of gyration  $R_g$  was computed as

$$R_g^2 = \frac{1}{N} \sum_{i=1}^N (R_i - R_{cm})^2, \quad (2.10)$$

where  $R_i$  is the three-dimensional position vector of a monomer,  $N = 20$  is the number of monomers in the chain, and  $R_{cm}$  is center of mass vector defined as

$$R_{cm} = \frac{1}{N} \sum_{i=1}^N R_i. \quad (2.11)$$

The chain statistics were collected in four different regions at equilibrium ( $U = 0$ ) and in the shear flow induced by the upper wall moving with velocity  $U = 0.5\sigma/\tau$  in the  $\hat{x}$  direction. Averaging regions were located above the peaks, in the grooves, near the flat upper wall and in the bulk (see Fig. 2.10 for an example). The dimensions of the averaging regions above the peaks and in the grooves of the lower wall are  $\sigma \times 12.5\sigma \times 1.5\sigma$ , and near the upper wall and in the bulk are  $22.5\sigma \times 12.5\sigma \times 1.5\sigma$ . Three components of the radius of gyration were computed for polymer chains with the center of mass inside the averaging regions.

In the bulk region, the components of the radius of gyration remain the same for both wavelengths, indicating that the chain orientation is isotropic at equilibrium and is not

affected by the confining walls. In the steady-state flow, the effective slip length is suppressed by the surface roughness and, therefore, the shear rate in the bulk increases with the corrugation amplitude. This explains why the  $\hat{x}$  component of the radius of gyration  $R_{gx}$  increases slightly at larger amplitudes (see Tables 2.1 and 2.2). Near the upper wall, the polymer chains become flattened parallel to the surface and slightly stretched in the presence of shear flow. These results are consistent with the previous MD simulations of polymer melts confined between atomically flat walls [65, 30, 64].

In the case of a rough surface with the wavelength  $\lambda = 7.5\sigma$ , a polymer chain can be accommodated inside a groove (see Fig. 2.10 for an example). With increasing corrugation amplitude, the polymer chains inside the grooves elongate along the  $\hat{y}$  direction and contract in the  $\hat{x}$  direction (see Table 2.1). The tendency of the trapped molecules to orient parallel to the grooves was observed previously in MD simulations of hexadecane [34]. In the presence of shear flow, polymer chains are highly stretched in the  $\hat{x}$  direction above the crests of the wavy wall. A snapshot of the unfolded chains during migration between neighboring valleys is shown in Fig. 2.10. The flow conditions in Fig. 2.10 correspond to a negative effective slip length  $L_{\text{eff}} \approx -2\sigma$ .

For the smallest corrugation wavelength  $\lambda = 3.75\sigma$ , polymer chains cannot easily fit in the grooves unless highly stretched. Therefore, the  $\hat{y}$  component of the radius of gyration is relatively large when the center of mass is located in the deep grooves (see Table 2.2). Figure 2.11 shows a snapshot of several polymer chains in contact with the lower corrugated wall. The chain segments are oriented parallel to the grooves and stretched above the crests of the surface corrugation. Visual inspection of the consecutive snapshots reveals that the chains near the corrugated wall move, on average, in the direction of shear flow; however, their tails can be trapped for a long time because of the strong net surface potential inside the grooves. For large wavenumbers  $ka \gtrsim 0.5$ , the magnitude of the negative effective slip length is approximately equal to the sum of the corrugation amplitude and  $R_{gz}$  of the polymer chains above the crests of the wavy wall.

## 2.6 Conclusions

In this chapter the effects of the shear rate and surface roughness on slip flow of a polymer melt was studied using molecular dynamics and continuum simulations. The linear part of the velocity profiles in the steady-state flow was used to calculate the effective slip length and shear rate. For atomically flat walls, the slip length passes through a shallow minimum at low shear rates and then increases rapidly at higher shear rates. In the case of periodic surface heterogeneities with the wavelength larger than the radius of gyration, the effective slip length decays monotonically with increasing the corrugation amplitude. For small wavenumbers, the effective slip length obtained from the solution of the Stokes equation with constant and shear-dependent local slip length is in a good agreement with its values computed from the MD simulations, in accordance with the previous analysis for simple fluids [35]. At low Reynolds numbers, the inertial effects on slip boundary conditions are negligible. When the corrugation wavelengths are comparable to the radius of gyration, polymer chains stretch in the direction of shear flow above the crests of the surface corrugation, while the chains located in the grooves elongate perpendicular to the flow. In this regime the continuum approach fails to describe accurately the rapid decay of the effective slip length with increasing wavenumber.

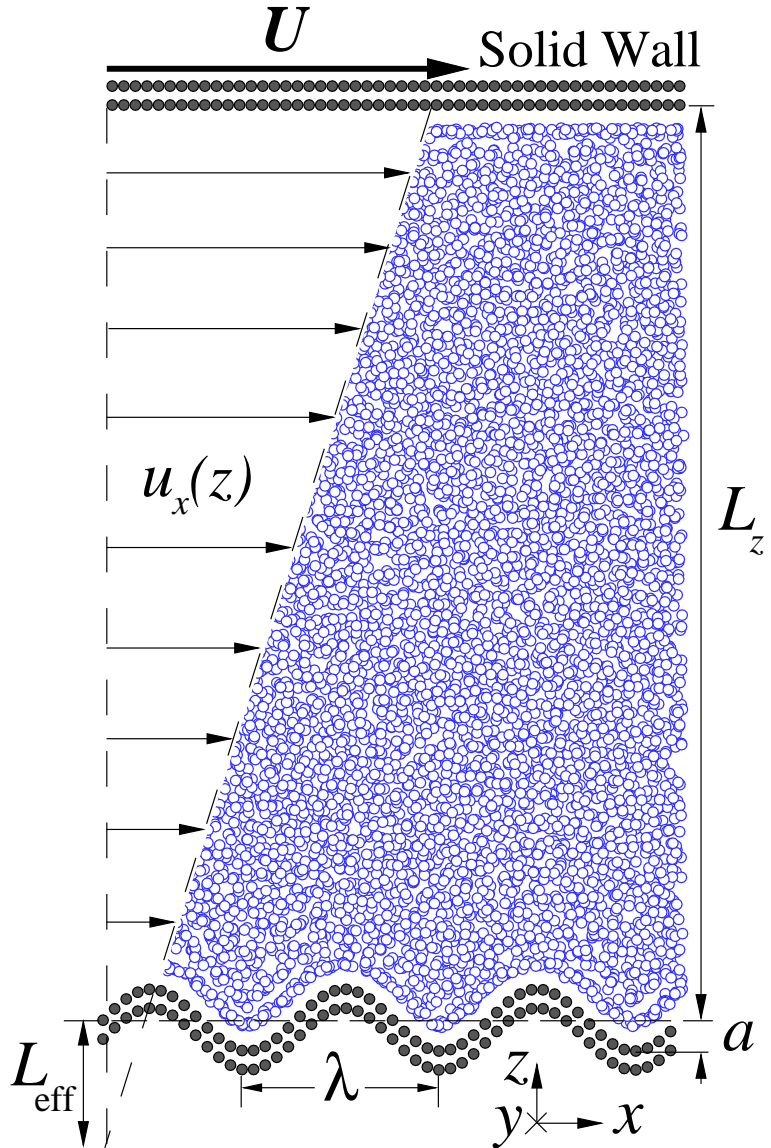


Figure 2.1. For interpretation of the references to color in this and all other figures, the reader is referred to the electronic version of this dissertation. A snapshot of the fluid monomers (open circles) confined between solid walls (closed circles) obtained from the MD simulations. The atoms of the stationary lower wall are distributed along the sinusoidal curve with the wavelength  $\lambda$  and amplitude  $a$ . The flat upper wall is moving with a constant velocity  $U$  in the  $\hat{x}$  direction. The effective slip length  $L_{\text{eff}}$  is determined by the linear extrapolation of the velocity profile to  $u_x = 0$ .

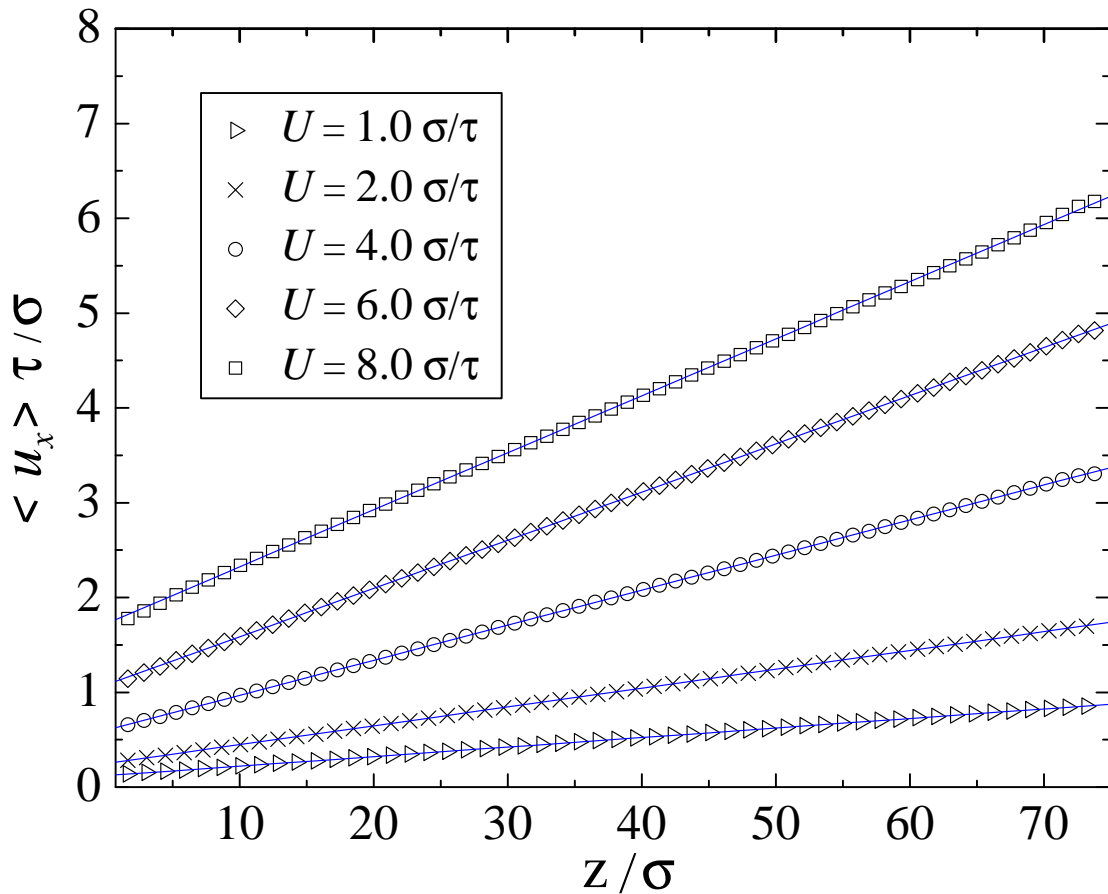


Figure 2.2. Averaged velocity profiles in the cell with flat upper and lower walls. The solid lines are the best linear fit to the data. The vertical axes indicate the location of the *FCC* lattice planes. The velocities of the upper wall are tabulated in the inset.

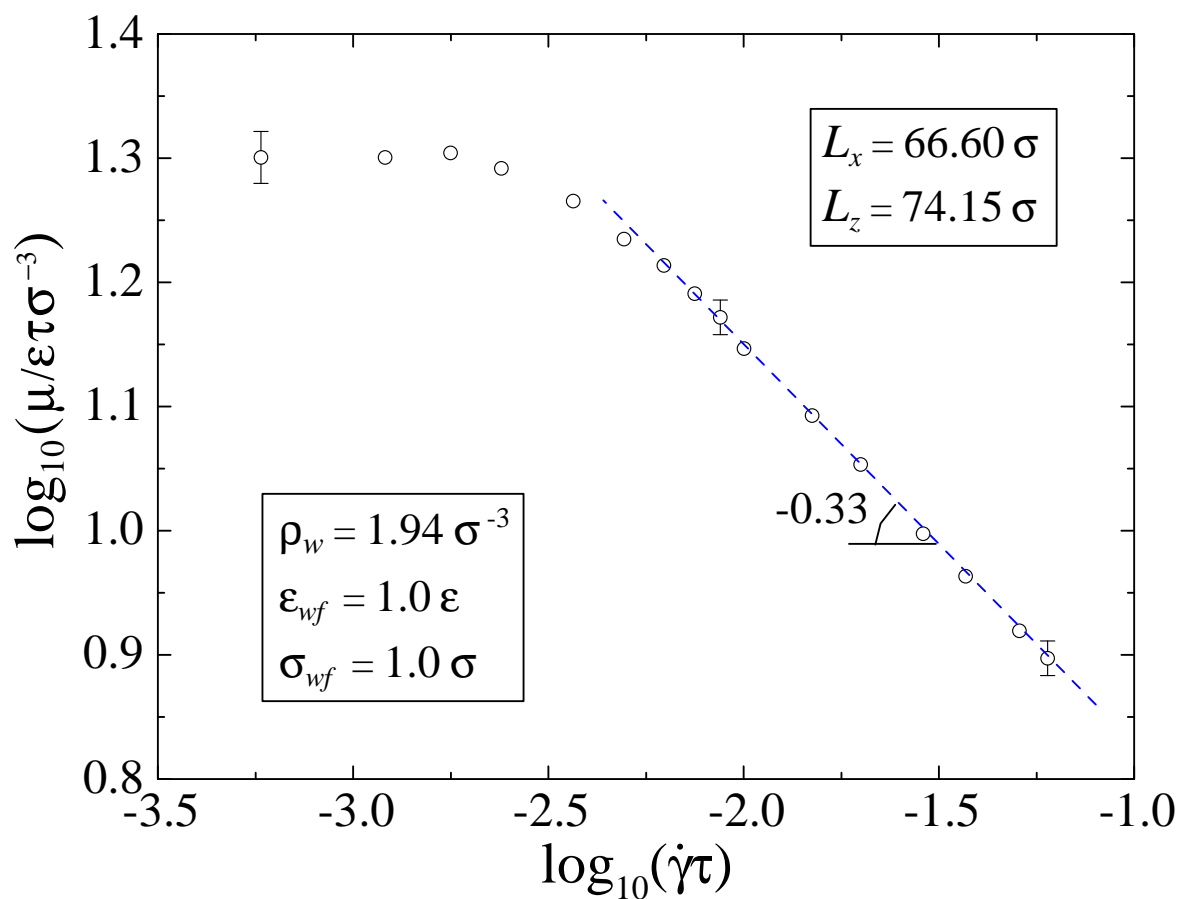


Figure 2.3. Viscosity of the polymer melt  $\mu/\varepsilon\tau\sigma^{-3}$  as a function of shear rate. The dashed line with the slope  $-0.33$  is plotted for reference.

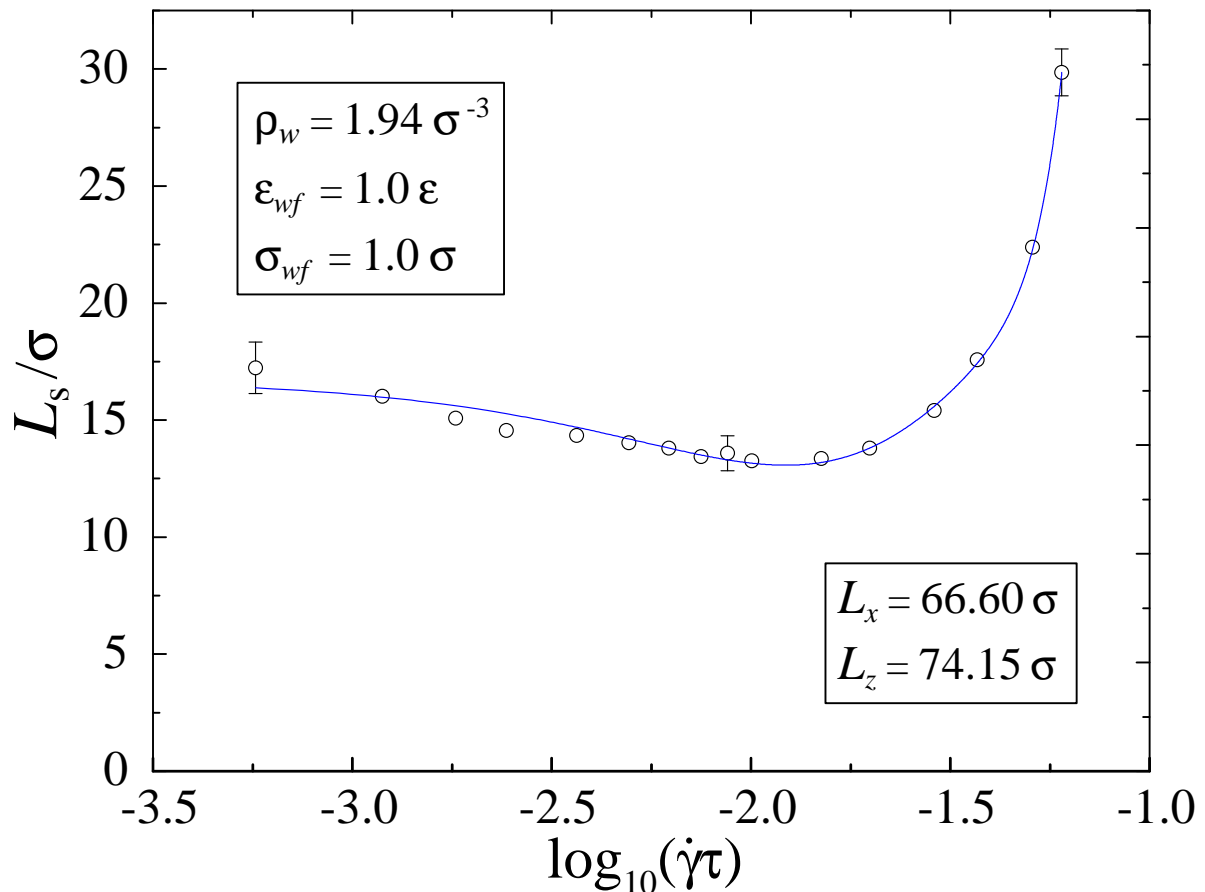


Figure 2.4. Variation of the slip length as a function of shear rate in the cell with flat upper and lower walls. The solid line is a fourth-order polynomial fit to the data given by Eq. (2.9).

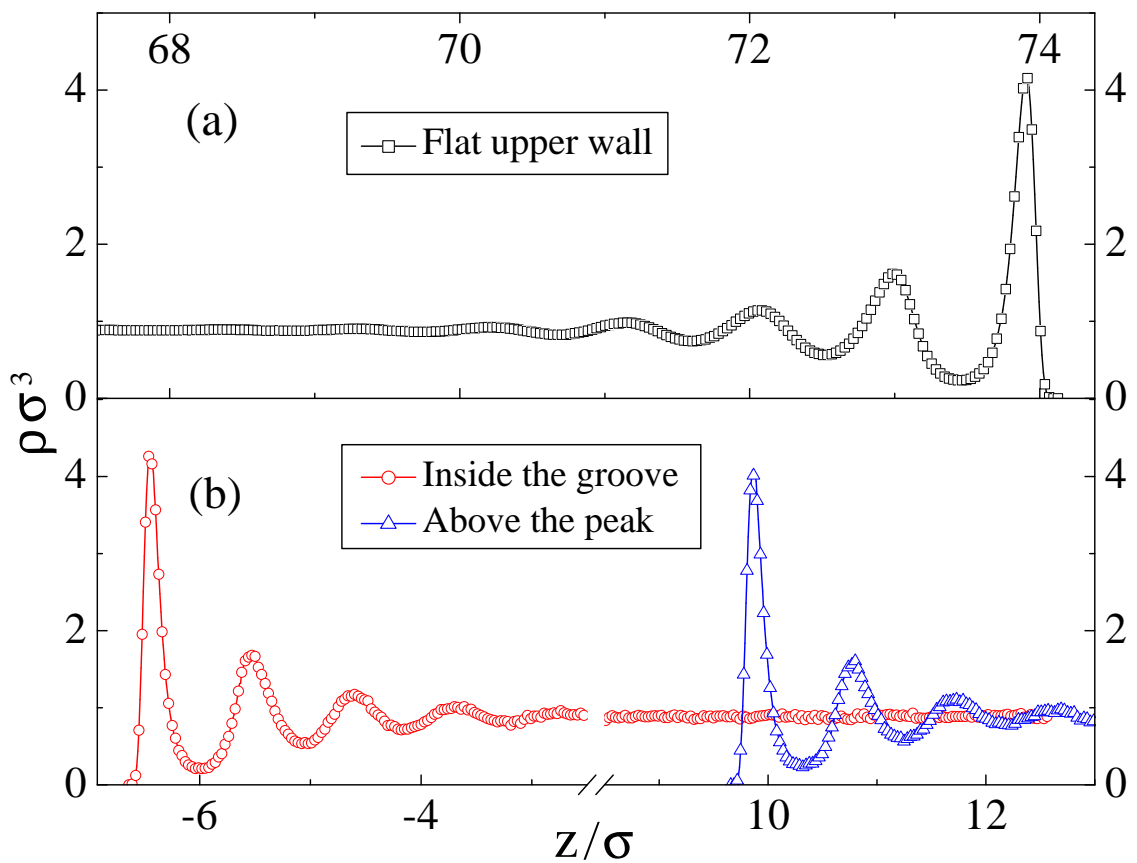


Figure 2.5. Averaged density profiles near the stationary upper wall (a), above the peak and in the groove of the lower wall with amplitude  $a = 8.16\sigma$  and wavelength  $\lambda = 66.60\sigma$  (b).

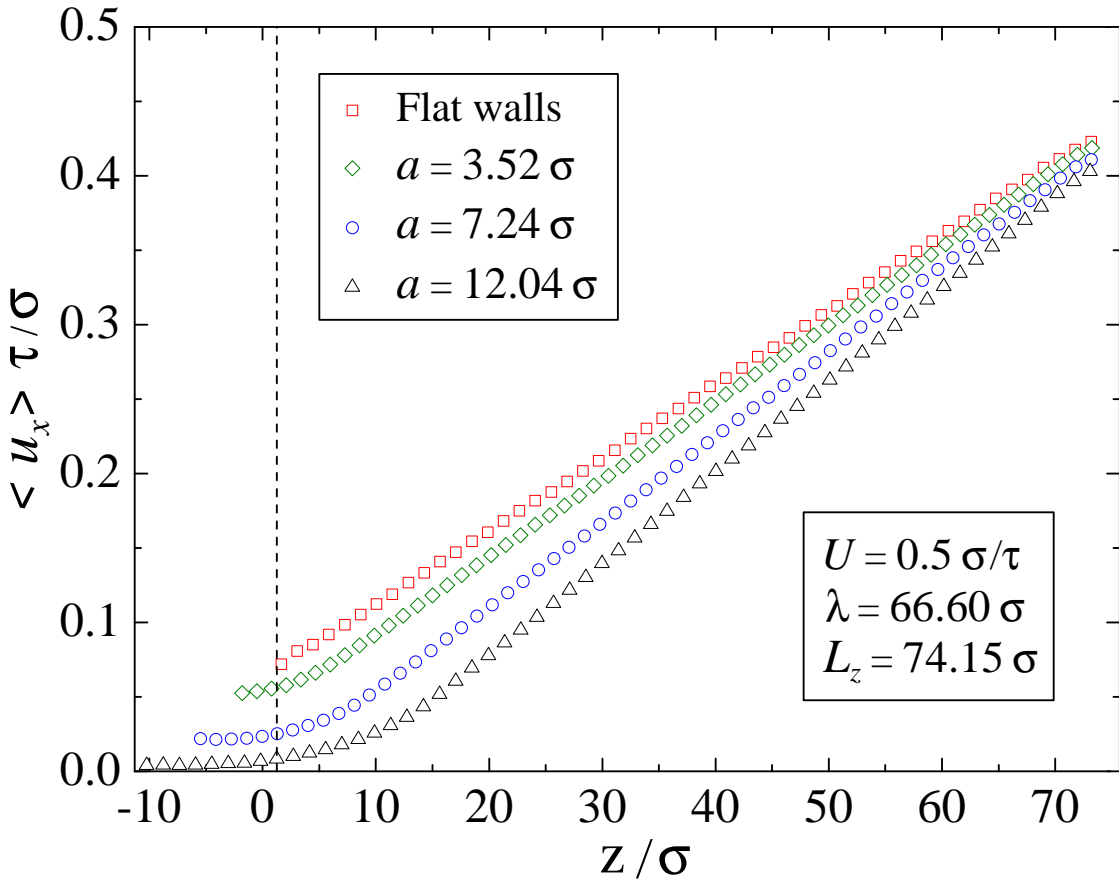


Figure 2.6. Averaged velocity profiles for the indicated values of the corrugation amplitude  $a$ . The vertical dashed line denotes a reference plane for calculation of the effective slip length at the corrugated lower wall. The velocity of the flat upper wall is  $U = 0.5 \sigma/\tau$ .

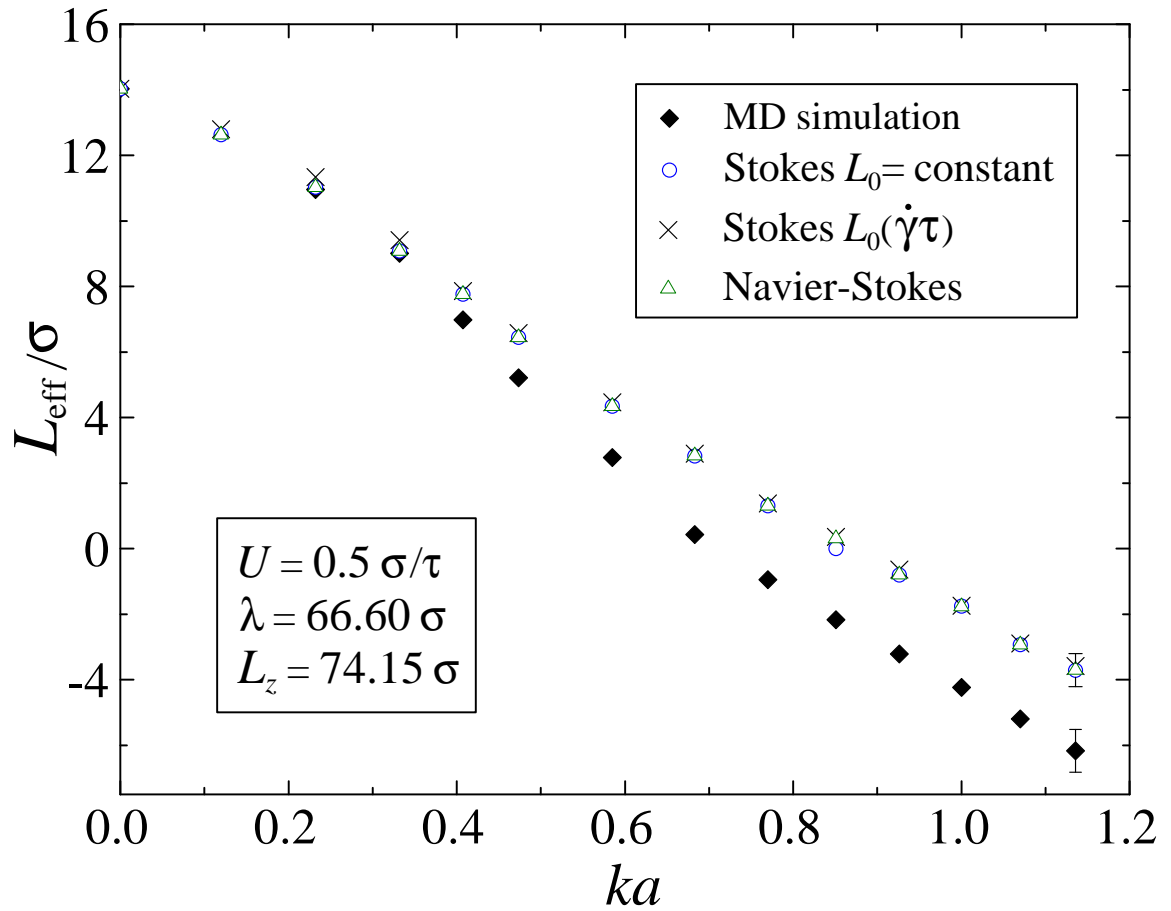


Figure 2.7. The effective slip length as a function of wavenumber  $ka$  obtained from the MD simulations (♦), the solution of the Stokes equation with rate-independent slip length  $L_0$  (○) and with  $L_0(\dot{\gamma}\tau)$  given by Eq. (2.9) (×), the solution of the Navier-Stokes equation with  $L_0$  (△).

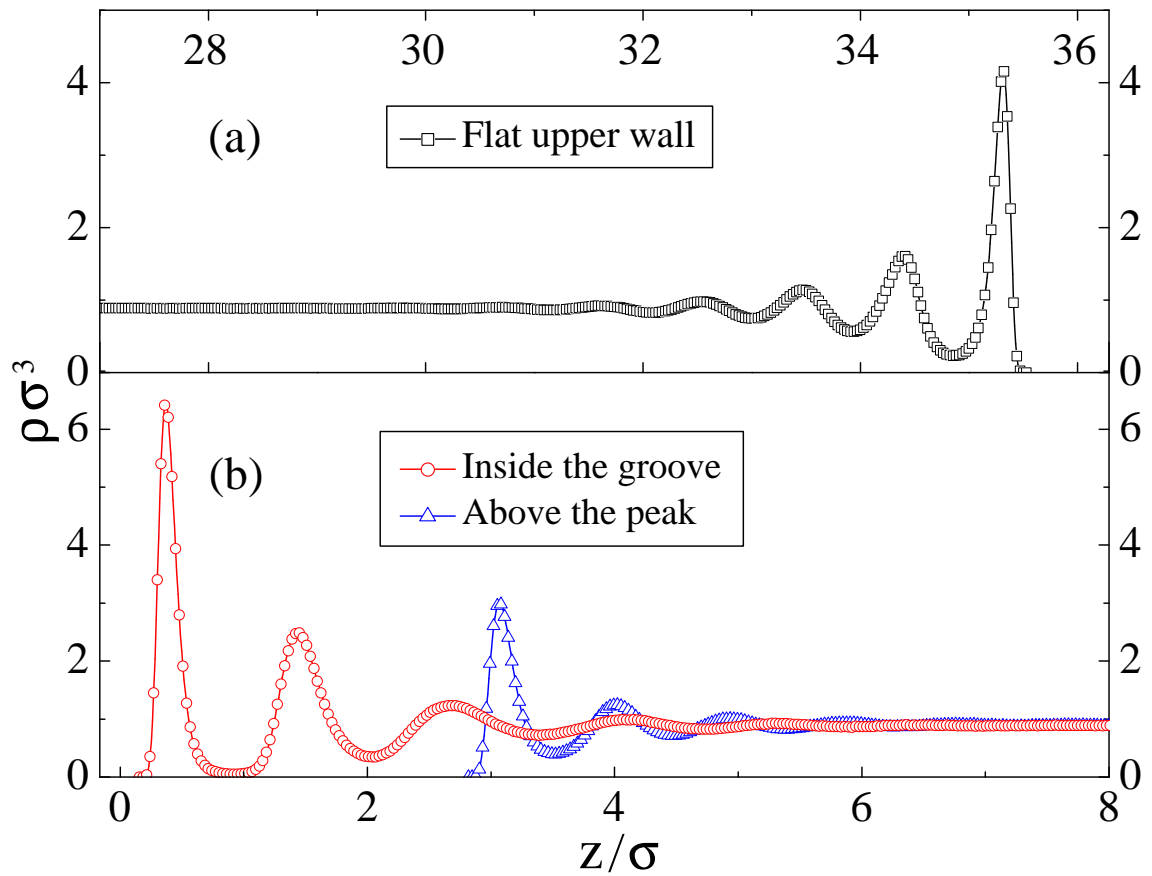


Figure 2.8. Averaged fluid density profiles near flat upper wall (a) and corrugated lower wall with amplitude  $a = 1.4 \sigma$  and wavelength  $\lambda = 7.5 \sigma$  (b). The velocity of the upper wall is  $U = 0.5 \sigma/\tau$ .

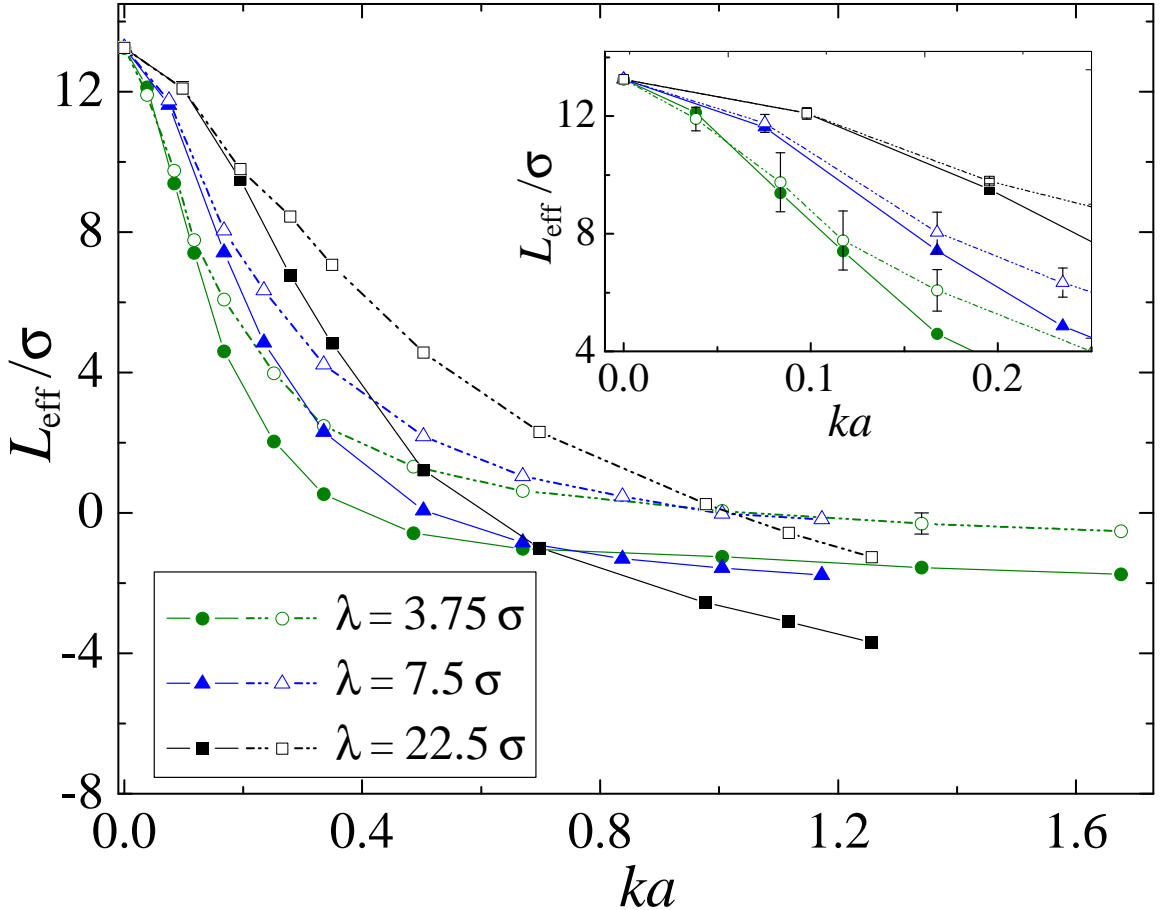


Figure 2.9. The effective slip length as a function of wavenumber  $ka$  for the indicated values of wavelength  $\lambda$ . Continuum results are denoted by the dashed lines and open symbols, while the MD results are shown by straight lines and filled symbols. The inset shows the same data for  $ka \leq 0.25$ .

$\lambda = 7.5 \sigma$		$a = 0.2 \sigma$			$a = 0.6 \sigma$			$a = 1.4 \sigma$		
		$R_{gx}$	$R_{gy}$	$R_{gz}$	$R_{gx}$	$R_{gy}$	$R_{gz}$	$R_{gx}$	$R_{gy}$	$R_{gz}$
Bulk	Equilibrium	1.18	1.18	1.18	1.18	1.18	1.18	1.18	1.18	1.18
	Shear flow	1.70	1.11	1.04	1.76	1.10	1.02	1.79	1.10	1.01
Upper wall	Equilibrium	1.34	1.37	0.66	1.35	1.36	0.66	1.35	1.35	0.66
	Shear flow	1.63	1.29	0.63	1.64	1.29	0.63	1.67	1.29	0.63
Peak	Equilibrium	1.35	1.36	0.69	1.40	1.31	0.76	1.46	1.27	0.84
	Shear flow	1.65	1.28	0.67	1.85	1.21	0.75	2.17	1.10	0.93
Groove	Equilibrium	1.31	1.37	0.63	1.10	1.47	0.61	0.77	1.69	0.61
	Shear flow	1.50	1.34	0.62	1.19	1.44	0.60	0.75	1.89	0.59

Table 2.1. Averaged  $\hat{x}$ ,  $\hat{y}$ , and  $\hat{z}$  components of the radius of gyration at equilibrium and in the shear flow. The  $R_g$  values are reported in the bulk, near the flat upper wall, above the peaks, and inside the grooves. The wavelength of the lower wall is  $\lambda = 7.5 \sigma$ . The size of the averaging region inside the grooves and above the peaks is  $\sigma \times 12.5 \sigma \times 1.5 \sigma$ . The estimate of the error bars is  $\pm 0.03 \sigma$ .

$\lambda = 3.75 \sigma$		$a = 0.07 \sigma$			$a = 0.2 \sigma$			$a = 1.0 \sigma$		
		$R_{gx}$	$R_{gy}$	$R_{gz}$	$R_{gx}$	$R_{gy}$	$R_{gz}$	$R_{gx}$	$R_{gy}$	$R_{gz}$
Bulk	Equilibrium	1.18	1.18	1.18	1.18	1.18	1.18	1.18	1.18	1.18
	Shear flow	1.70	1.12	1.03	1.76	1.10	1.02	1.78	1.10	1.01
Upper wall	Equilibrium	1.33	1.36	0.66	1.36	1.34	0.66	1.37	1.34	0.65
	Shear flow	1.60	1.32	0.63	1.64	1.29	0.63	1.65	1.27	0.63
Peak	Equilibrium	1.38	1.33	0.67	1.42	1.30	0.71	1.41	1.25	0.92
	Shear flow	1.61	1.27	0.65	1.66	1.26	0.69	1.78	1.17	0.84
Groove	Equilibrium	1.33	1.36	0.64	1.25	1.42	0.61	0.48	2.64	0.55
	Shear flow	1.60	1.29	0.61	1.60	1.33	0.59	0.47	2.70	0.54

Table 2.2. Averaged  $\hat{x}$ ,  $\hat{y}$ , and  $\hat{z}$  components of the radius of gyration at equilibrium and in the shear flow. The  $R_g$  values are reported in the bulk, near the flat upper wall, above the peaks, and inside the grooves. The wavelength of the lower wall is  $\lambda = 3.75 \sigma$ . The dimensions of the averaging region are the same as in Table 2.1.

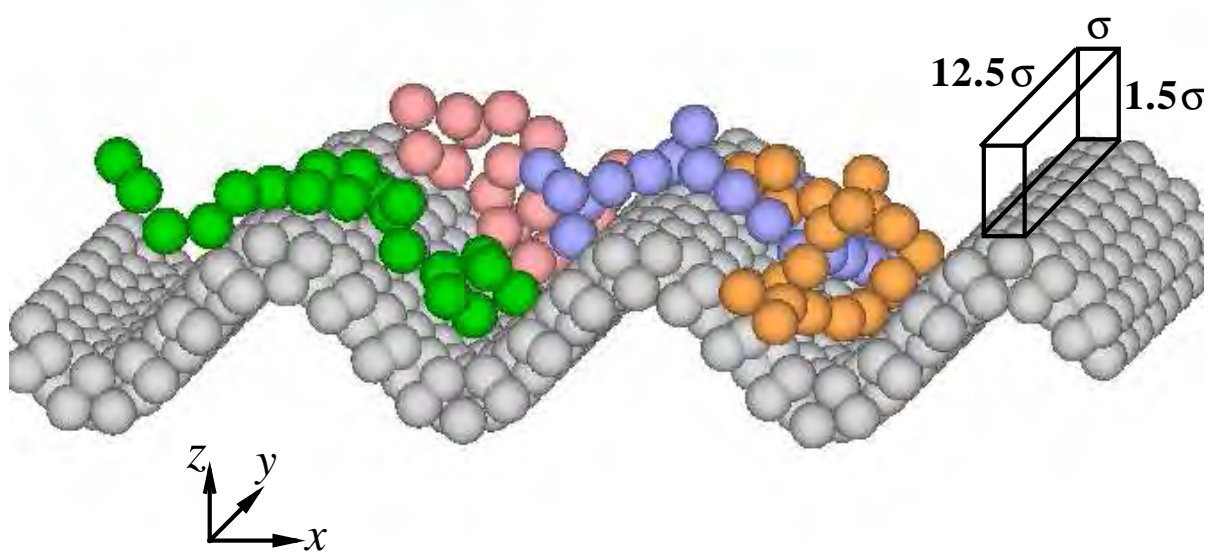


Figure 2.10. A snapshot of four polymer chains near the lower corrugated wall for wavelength  $\lambda = 7.5\sigma$  and amplitude  $a = 1.4\sigma$ . The velocity of the upper wall is  $U = 0.5\sigma/\tau$ .

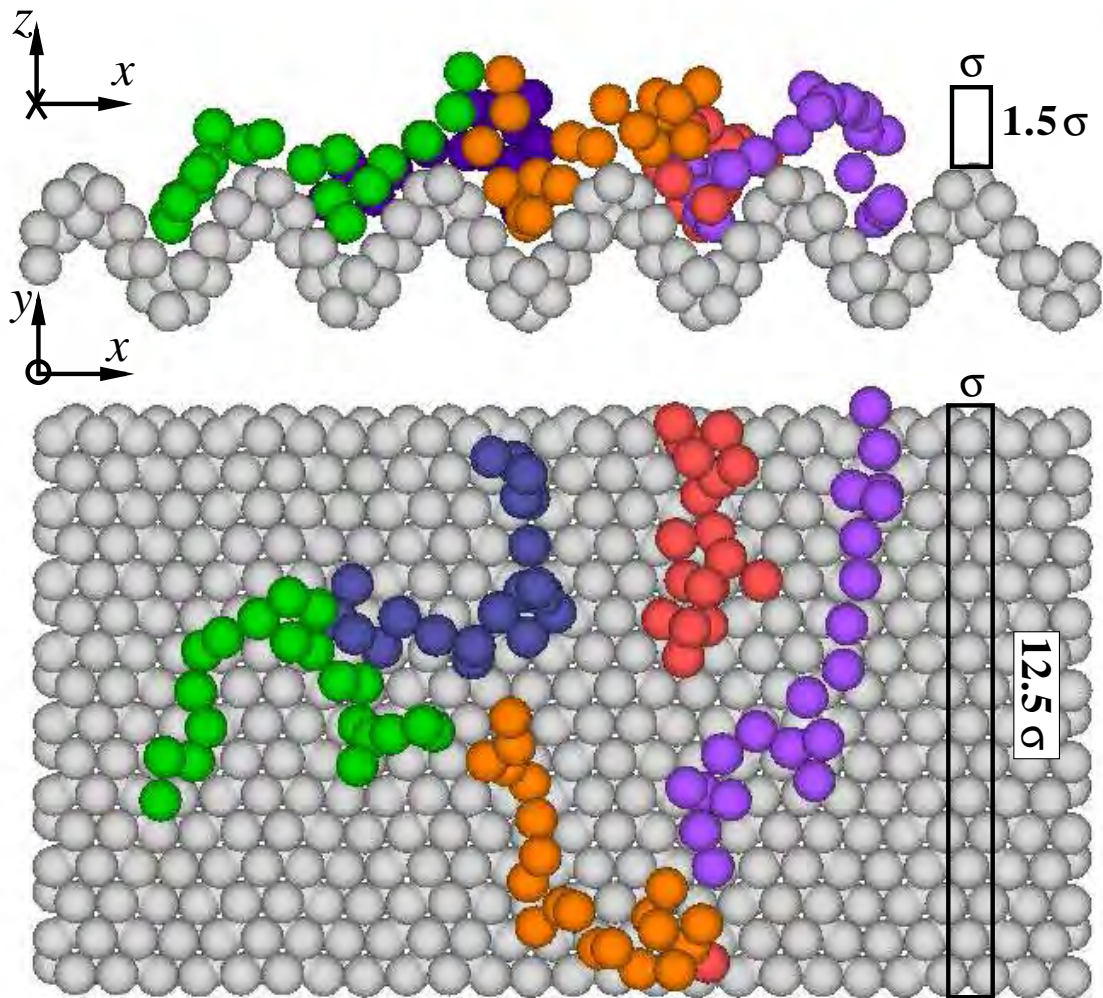


Figure 2.11. A snapshot of five polymer chains near the lower corrugated wall for the wavelength  $\lambda = 3.75 \sigma$  and amplitude  $a = 1.0 \sigma$ . The figure shows the side view (top) and the top view (bottom). The velocity of the upper wall is  $U = 0.5 \sigma/\tau$ .

# CHAPTER 3

## Slip boundary conditions for shear flow of polymer melts past atomically flat surfaces

### 3.1 Introduction

The fluid flow in microfluidic channels can be significantly influenced by liquid slip at the solid boundary because of the large surface to volume ratio [67]. The Navier model for the partial slip boundary conditions relates the fluid slip velocity to the tangential viscous stress at the wall via the friction coefficient, which is defined as the ratio of the shear viscosity to the slip length. Geometrically, the slip length is determined as a distance from the solid wall where the linearly extrapolated fluid velocity profile vanishes. Experimental studies have demonstrated that for atomically smooth surfaces the slip length is relatively large for non-wetting liquid/solid interfaces [5, 15, 117], polymeric fluids [68, 16] and high shear rates [69, 17, 19]. By contrast, surface roughness even on the submicron length scale strongly reduces the degree of slip for both polymeric [12] and Newtonian [10, 14, 13] fluids. However, experimentally it is often difficult to isolate and, consequently, to analyze the effects of wettability, surface roughness and shear rate on slip boundary conditions because of the small scales involved.

During the past two decades, a number of molecular dynamics (MD) simulations [20,

21, 121, 25, 24, 26, 27, 28, 40, 29] have been performed to investigate the dependence of the slip length on the structure of dense fluids near atomically flat surfaces. For simple fluids, it has been well established that the slip length correlates inversely with the wall-fluid interaction energy and the surface induced order in the first fluid layer [21, 121, 29]. The strong wall-fluid coupling and commensurate structures of the liquid/solid interface lead to the no-slip boundary condition for monoatomic fluids [21, 28]. The interfacial slip is enhanced in the flow of polymer melts due to the higher shear viscosity and reduced molecular ordering near the flat wall [125, 30, 31, 27]. The magnitude of the slip length in the flow of polycarbonate blends past atomically smooth nickel surfaces is determined by the competition between the apparent slip of the adsorbed polymer layer and its thickness [70]. The slip boundary conditions for the polymer melt flow over the brush can be controlled by changing the density of the end-grafted polymer layer [71]. Finally, the degree of slip at the interface between immiscible polymers is larger for longer chain molecules and greater repulsion between unlike species [72].

Until ten years ago, the slip length in the Navier model was assumed to be independent of shear rate. In the seminal MD study by Thompson and Troian [23] on shear flow of simple fluids past atomically flat rigid walls, it was found that the slip length increases nonlinearly with the shear rate. Upon increasing the surface energy, a gradual transition from the power law behavior [23] to the linear rate dependence was recently reported for weak wall-fluid interactions and incommensurate structures of the liquid/solid interface [29]. In a wide range of shear rates and surface energies, the slip length in simple fluids is determined by a function of the in-plane structure factor, contact density and temperature of the first fluid layer near the wall [29]. The rate-dependent slip length at the interface between a polymer melt composed of short linear chains and a crystalline substrate is also well described by the power law function used to fit the data for simple fluids [27, 23]. Whether these boundary conditions hold for higher molecular weight polymers or rough surfaces is an open question that has to be addressed for the correct interpretation of the experimental results and modeling fluid flows in microfluidic channels.

In this chapter, the effects of shear rate and fluid density on slip boundary conditions for the flow of a polymer melt past a crystalline wall are investigated by molecular dynamics

simulations. We will show that the rate-dependent slip length reaches a local minimum and then increases rapidly at higher shear rates. In the shear thinning regime, the friction coefficient at the liquid/solid interface follows a power law decay as a function of the slip velocity. In a wide range of shear rates and polymer densities, the ratio of the slip length to the shear viscosity is determined by the surface induced structure in the first fluid layer. These results suggest that the correlation between the fluid structure near the flat wall and the slip length is determined by a universal combination of parameters for both polymer melts and simple fluids [29].

This chapter is organized as follows. The molecular dynamics simulation model and parameter values are described in the next section. The results for the rate dependence of the slip length and the analysis of the fluid structure near the solid wall are presented in Section 5.3. The conclusions are given in the last section.

## 3.2 Details of molecular dynamics simulations

The polymer melt is confined between two atomically flat walls and is subject to planar shear in the  $\hat{x}$  direction (see Fig. 3.1 for a schematic representation). The fluid monomers interact through the pairwise Lennard-Jones (LJ) potential

$$V_{LJ}(r) = 4\epsilon \left[ \left(\frac{\sigma}{r}\right)^{12} - \left(\frac{\sigma}{r}\right)^6 \right], \quad (3.1)$$

with a cutoff distance  $r_c = 2.5\sigma$ , where  $\epsilon$  and  $\sigma$  represent the energy and length scales of the fluid phase. The total number of monomers is  $N_f = 6000$ . The wall-fluid interaction parameters of the LJ potential are set to  $\epsilon_{wf} = 0.9\epsilon$  and  $\sigma_{wf} = \sigma$  throughout the study. The polymer melt is modeled as a collection of bead-spring chains of  $N = 20$  LJ monomers interacting through the FENE (finitely extensible nonlinear elastic) potential [59]

$$V_{FENE}(r) = -\frac{k}{2} r_o^2 \ln[1 - r^2/r_o^2], \quad (3.2)$$

with Kremer and Grest parameters  $k = 30\epsilon\sigma^{-2}$  and  $r_o = 1.5\sigma$  [53]. This choice of parameters prevents polymer chains from unphysical crossing or bond breaking [54].

The system was coupled to an external heat bath through a Langevin thermostat [54] with a random force and a damping term with a small value of the friction coefficient

$\Gamma = 1.0 \tau^{-1}$  [73]. The thermostat was only applied to the equation of motion for a fluid monomer along the  $\hat{y}$  axis to avoid a bias in the shear flow direction [21]. The equations of motion for the  $\hat{x}$ ,  $\hat{y}$  and  $\hat{z}$  components are given by

$$m\ddot{x}_i = - \sum_{i \neq j} \frac{\partial V_{ij}}{\partial x_i}, \quad (3.3)$$

$$m\ddot{y}_i + m\Gamma\dot{y}_i = - \sum_{i \neq j} \frac{\partial V_{ij}}{\partial y_i} + f_i, \quad (3.4)$$

$$m\ddot{z}_i = - \sum_{i \neq j} \frac{\partial V_{ij}}{\partial z_i}, \quad (3.5)$$

where  $f_i$  is a random force with zero mean and variance  $\langle f_i(0)f_j(t) \rangle = 2mk_B T \Gamma \delta(t) \delta_{ij}$ , the temperature is  $T = 1.1 \varepsilon / k_B$  and  $k_B$  is the Boltzmann constant. The equations of motion for fluid monomers and wall atoms were integrated using the fifth-order gear-predictor algorithm [56] with a time step  $\Delta t = 0.002 \tau$ , where  $\tau = \sqrt{m\sigma^2/\varepsilon}$  is the characteristic time of the LJ potential.

Each wall was constructed out of 576 LJ atoms, which formed two (111) layers of the face-centered cubic (*FCC*) lattice with the density  $\rho_w = 1.40 \sigma^{-3}$ . The corresponding nearest-neighbor distance between equilibrium positions of the wall atoms in the  $xy$  plane is  $d = 1.0 \sigma$ . The dimensions of the Couette cell ( $xyz$ ) were held fixed to  $20.86 \sigma \times 12.04 \sigma \times h$ , where  $h$  is the channel height (see Table 3.1). The MD simulations were performed at a constant density ensemble. The fluid density is defined as a ratio of the total number of monomers to the volume accessible to the fluid, i.e.,  $0.5 \sigma_w$  away from the *FCC* lattice planes in the  $\hat{z}$  direction. The range of fluid densities considered in this study is  $0.86 \leq \rho \sigma^3 \leq 1.02$ . The pressures of the system at equilibrium are given in Table 3.1 for each value of the fluid density. Periodic boundary conditions were employed along the  $\hat{x}$  and  $\hat{y}$  directions parallel to the confining walls.

$\rho [\sigma^{-3}]$	0.86	0.88	0.91	0.94	1.00	1.02
$P [\varepsilon \sigma^{-3}]$	0.0	0.5	1.0	2.0	4.0	5.0
$h [\sigma]$	28.93	28.18	27.27	26.32	24.85	24.36

Table 3.1. The fluid pressure  $P$  at equilibrium, i.e., with the stationary upper wall, and the channel height  $h$  (defined as a distance between the inner *FCC* planes) as a function of the fluid density.

The wall atoms were attached to their equilibrium *FCC* lattice positions by the harmonic spring with the potential  $V_{sp} = \frac{1}{2} \kappa r^2$ . The spring stiffness  $\kappa = 1200 \varepsilon/\sigma^2$  is large enough so that the mean-square displacement of the wall atoms is less than the Lindemann criterion for melting, i.e.,  $\langle \delta u^2 \rangle/d^2 \lesssim 0.023$  (see Ref. [74]). In a recent paper on shear flow of simple fluids [37], it was shown that the slope of the rate-dependent slip length remains approximately the same for the thermal walls with  $\kappa = 1200 \varepsilon/\sigma^2$  and rigid *FCC* walls. The friction term and the random force were also added to the  $\hat{x}$ ,  $\hat{y}$  and  $\hat{z}$  components of the wall atoms equations of motion

$$m_w \ddot{x}_i + m_w \Gamma \dot{x}_i = - \sum_{i \neq j} \frac{\partial V_{ij}}{\partial x_i} - \frac{\partial V_{sp}}{\partial x_i} + f_i, \quad (3.6)$$

$$m_w \ddot{y}_i + m_w \Gamma \dot{y}_i = - \sum_{i \neq j} \frac{\partial V_{ij}}{\partial y_i} - \frac{\partial V_{sp}}{\partial y_i} + f_i, \quad (3.7)$$

$$m_w \ddot{z}_i + m_w \Gamma \dot{z}_i = - \sum_{i \neq j} \frac{\partial V_{ij}}{\partial z_i} - \frac{\partial V_{sp}}{\partial z_i} + f_i, \quad (3.8)$$

where the mass of the wall atoms is  $m_w = 10m$  and the summation is performed only over the fluid monomers within the cutoff distance  $r_c = 2.5\sigma$ .

The simulations began with an equilibration period of about  $5 \times 10^4 \tau$  with both walls being at rest. Then, the steady-state shear flow was generated by translating the upper wall with a constant velocity  $U$  in the  $\hat{x}$  direction, while the lower wall always remained stationary (see Fig. 3.1). The fluid velocity profiles were computed by averaging the instantaneous monomer velocities in the  $\hat{x}$  direction within bins of thickness  $\Delta z = 0.2\sigma$  for a time interval up to  $4 \times 10^5 \tau$  at the lowest shear rates. The density profiles were averaged for a time period  $5 \times 10^4 \tau$  within bins of thickness of only  $\Delta z = 0.01\sigma$  to accurately resolve the fluid structure near the walls [29]. The maximum value of the Reynolds number is  $Re \approx 10.5$ , which was estimated from the maximum fluid velocity difference across the channel, the shear viscosity, and the channel height. The small values of the Reynolds number correspond to laminar flow conditions even at the highest shear rates considered in this study.

### 3.3 Results

#### 3.3.1 Fluid density and velocity profiles

The fluid structure in the direction perpendicular to a flat surface usually consists of several distinct layers on the molecular scale [75]. Examples of the averaged monomer density profiles near the lower thermal wall are presented in Fig. 3.2 for three values of the upper wall velocity. The highest peak is associated with a layer of fluid monomers (each connected to a polymer chain) in contact with the wall atoms. The contact density  $\rho_c$  corresponds to the maximum value of the peak. The density oscillations gradually decay away from the wall to a uniform profile with bulk density  $\rho = 0.91 \sigma^{-3}$ . The amplitude of the density oscillations is reduced at higher values of the slip velocity.

Figure 3.3 shows the averaged velocity profiles for the same values of the upper wall speed as in Fig. 3.2 and the fluid density  $\rho = 0.91 \sigma^{-3}$ . For a given  $U$ , the relative slip velocity is the same at the upper and lower walls. Surprisingly, the scaled slip velocity is smaller at the intermediate speed of the upper wall  $U = 1.0 \sigma/\tau$ . Because of the thermal fluctuations, longer averaging times (up to  $4 \times 10^5 \tau$ ) were required to accurately resolve the fluid velocity profile for  $U = 0.05 \sigma/\tau$ . A small curvature in the velocity profile is evident for the largest velocity of the upper wall  $U = 5.0 \sigma/\tau$ . The deviation from the linearity might be related to the heating up of the fluid near the walls (see discussion below). The slope of the velocity profile (used for calculation of the slip length and the shear rate) was computed from the central part of the velocity profile excluding the data from the region of about  $2\sigma$  near the walls.

We comment that at small shear rates,  $\dot{\gamma}\tau \lesssim 0.01$ , and higher fluid densities,  $\rho \gtrsim 1.04 \sigma^{-3}$ , the fluid velocity profiles acquired a pronounced curvature within a distance of about  $4\sigma$  from the walls. The linearity of the fluid velocity profiles is restored at higher shear rates. This effect will be examined in a separate study.

#### 3.3.2 Rate dependence of the slip length and shear viscosity

In the MD study by Thompson and Troian [23] on shear flow of Newtonian liquids past atomically flat surfaces, the slip length was found to increase nonlinearly with the shear

rate. The data for different wall densities and weak wall-fluid interactions were fitted well by the power law function

$$L_s(\dot{\gamma}) = L_s^0 (1 - \dot{\gamma}/\dot{\gamma}_c)^{-0.5}, \quad (3.9)$$

where  $\dot{\gamma}_c$  and  $L_s^0$  are the parameters used for normalization. The rate-dependent slip length in the Poiseuille flow of simple fluids was also well described by the function [Eq. (3.9)] for incommensurate structures of the liquid/solid interface and weak surface energy [29].

The nonlinear behavior of the slip length can be interpreted in terms of the velocity-dependent shear stress at the wall [76]. By definition, the fluid slip velocity  $V_s$  is related to the slip length as  $V_s = \dot{\gamma}L_s$ . On the other hand, the shear stress through any plane parallel to the walls is the same in the steady-state shear flow, and it is equal to the fluid viscosity multiplied by the shear rate, i.e.,  $\sigma_{xz} = \mu\dot{\gamma}$ . At the liquid/solid interface the viscous shear stress becomes  $\sigma_{xz} = kV_s$ , where  $k$  is the friction coefficient per unit area. The functional form given by Eq. (3.9) implies that the friction coefficient,  $k = \mu/L_s$ , can be expressed as a function of the slip velocity as follows:

$$k(V_s) = C_1(\sqrt{C_2 + V_s^2} - V_s), \quad (3.10)$$

where  $C_1 = \mu/2\dot{\gamma}_c(L_s^0)^2$  and  $C_2 = (2L_s^0\dot{\gamma}_c)^2$ , and  $\mu$  is the shear-independent viscosity [23, 27].

In the previous MD study [27], it was shown that the slip length increases monotonically with shear rate for polymer melts with short linear chains  $N \leq 16$ . The data for the slip length were well fitted by the power law function given by Eq. (3.9) for shear rates exceeding  $\dot{\gamma} \gtrsim 5 \times 10^{-3} \tau^{-1}$ . Although the fluid viscosity exhibited a slight shear thinning behavior for chain lengths  $N \geq 8$ , no minimum in the rate dependence of the slip length was observed. In the present study, the shear thinning effect is more pronounced because the polymer melt consists of longer chains and the simulations are performed at higher fluid densities.

Figure 3.4 shows the rate behavior of the fluid viscosity, which was computed from the Kirkwood relation for the shear stress [59] in steady-state shear flow. In the range of accessible shear rates, the transition from the Newtonian regime to the shear thinning is more evident at lower fluid densities. At higher shear rates, the bulk viscosity approximately follows a power law decay with the exponent  $-0.37$  (see Fig. 3.4). A similar shear thinning

behavior of polymer melts was reported in the previous MD studies [60, 61]. The error bars are larger at lower shear rates because of an increasing role of thermal fluctuations [77].

The dynamic response of the slip length with increasing shear rate is shown in Fig. 3.5 for the indicated values of the polymer density. The rate dependence of the slip length exhibits a distinct local minimum, which is followed by a rapid increase at higher shear rates. The minimum is shifted to lower shear rates and becomes more shallow at higher fluid densities. The slip length tends to saturate to a constant value at the lowest shear rates for the fluid density  $\rho = 0.86 \sigma^{-3}$ . Typical error bars are included for three points corresponding to the fluid velocity profiles shown in Fig. 3.3. In the range of shear rates from the local minimum up to the highest  $\dot{\gamma}$ , the data for the slip length (as well as the ratio  $L_s/\mu$ ) cannot be fitted by the power law function given by Eq. (3.9). For each value of the fluid density, the highest shear rate corresponds to the maximum sustainable shear stress at the interface [29].

The data for the rate-dependent slip length and fluid viscosity are replotted in Fig. 3.6 in terms of the friction coefficient at the liquid/solid interface and the slip velocity. The constant value of the friction coefficient at small slip velocities indicates that the ratio of the slip length and viscosity is rate-independent. At higher fluid densities (or pressures), the friction coefficient is larger, and the transition to the power law regime is shifted to smaller slip velocities. The transition point approximately corresponds to the location of the minimum in the shear rate dependence of the slip length shown in Fig. 3.5. The data for the lowest fluid density  $\rho = 0.86 \sigma^{-3}$  can be fairly well fitted by Eq. (3.10) [see Fig. 3.6], but the fit becomes worse at higher fluid densities (not shown). The simulation results indicate that the nonmonotonic rate behavior of the slip length for polymer melts can be ascribed to the velocity dependence of the friction coefficient, which undergoes a transition from a nearly constant value to a decreasing function of the slip velocity.

Furthermore, the data for different fluid densities can be collapsed onto a single master curve by scaling both axes (see Fig. 3.7). The values of the normalization parameters for the friction coefficient and the slip velocity are listed in the inset. The decay at large slip velocities approximately follows the power law function with the exponent  $-0.7$  (see Fig. 3.7). The onset of the power law decay depends on the polymer density and might occur when the time scale of the in-plane diffusion of the fluid monomers over the lattice spacing

$d$  is comparable to  $d/V_s$ . We also note that the data for the viscosity and slip length at the interface between a polymer melt (with linear chains  $N=20$  and density  $\rho=0.88\sigma^{-3}$ ) and a rigid *FCC* wall (with density  $\rho_w=1.94\sigma^{-3}$  and  $\varepsilon_{wf}=\varepsilon$ ) can be normalized to follow the master curve shown in Fig. 3.7 [93].

### 3.3.3 Analysis of the fluid structure in the first layer

The surface induced order in the adjacent fluid layer is described by the structure factor at the reciprocal lattice vectors of the crystal wall [21]. The structure factor is defined as

$$S(\mathbf{k}) = \frac{1}{N_\ell} \left| \sum_j e^{i\mathbf{k}\cdot\mathbf{r}_j} \right|^2, \quad (3.11)$$

where  $\mathbf{r}_j = (x_j, y_j)$  is the position vector of the  $j$ -th monomer and the summation is performed over  $N_\ell$  monomers within the first layer. The friction force between a layer of adsorbed monomers and a solid substrate is proportional to the peak value of the in-plane structure factor estimated at the first reciprocal lattice vector [78, 79]. Previous MD studies of simple fluids have also reported a strong correlation between the slip length (which is inversely proportional to the friction coefficient at the liquid/solid interface) and the surface induced order in the first fluid layer [21, 121, 29].

Figure 3.8 shows the averaged structure factor in the first fluid layer moving with a constant velocity against the stationary lower wall. The circular ridge at the wavevector  $|\mathbf{k}| \approx 2\pi/\sigma$  is attributed to the short-range ordering of the fluid monomers. The periodic potential of the crystalline substrate induces several sharp peaks in the fluid structure factor, which are reduced at higher slip velocities. The first reciprocal lattice vector in the direction of shear flow is  $\mathbf{G}_1 = (7.23\sigma^{-1}, 0)$ . Although the nearest-neighbor distance between equilibrium lattice sites in the  $xy$  plane is equal to the diameter of the LJ monomers, the surface induced order in the first fluid layer is frustrated by the topological constraints associated with packing of polymer chains near the surface.

In the recent MD study on shear flow of simple fluids past rigid *FCC* walls [29], it was shown that the slip length scales according to

$$L_s \sim [T_1/S(\mathbf{G}_1)\rho_c]^{1.44}, \quad (3.12)$$

where  $\mathbf{G}_1$  is the the first reciprocal lattice vector,  $T_1$  and  $\rho_c$  are the temperature and the contact density of the first fluid layer respectively. This relation was found to hold in a wide range of shear rates and for weak wall-fluid interactions  $0.3 \leq \varepsilon_{\text{wf}}/\varepsilon \leq 1.1$ . It is expected, however, that the scaling relation given by Eq. (3.12) is not valid at higher surface energies because the first fluid layer is locked to the solid wall and, as a consequence, the slip length is negative [21]. Note that the surface induced peaks in the structure factor are much higher for polymers (see Fig. 3.8) than for simple fluid [29]. Since the viscosity is independent of shear rate for simple fluids, the scaling relation Eq. (3.12) also predicts the dependence of the friction coefficient on microscopic parameters of the adjacent fluid layer.

We computed the parameters entering Eq. (3.12) in the first fluid layer for the polymer melt. The fluid temperature was estimated from the kinetic energy

$$k_B T = \frac{m}{3N} \sum_{i=1}^N [\dot{\mathbf{r}}_i - \mathbf{v}(\mathbf{r}_i)]^2, \quad (3.13)$$

where  $\dot{\mathbf{r}}_i$  is the instantaneous velocity of the fluid monomer and  $\mathbf{v}(\mathbf{r}_i)$  is the local average flow velocity. Averaged temperature profiles are shown in Fig. 3.9 for the same flow conditions as in Figs. 3.2 and 3.3. At low shear rates  $\dot{\gamma} \lesssim 0.01 \tau^{-1}$ , the fluid temperature is equal to its equilibrium value of  $T = 1.1 \varepsilon / k_B$  determined by the Langevin thermostat. As in the case of simple fluids [29, 37], with further increase of the shear rate, the polymer melt heats up and the temperature profile becomes non-uniform across the channel. The fluid temperature is higher near the walls because of the large slip velocity, which is comparable to the thermal velocity,  $v_T^2 = k_B T / m$ , at high shear rates. The non-uniform temperature distribution might be related to the slight curvature in the velocity profile for the top wall speed  $U = 5.0 \sigma / \tau$  shown in Fig. 3.3. We can also notice that at high shear rates, the temperature in the  $\hat{y}$  direction, in which the Langevin thermostat is applied, is slightly smaller than its value in the  $\hat{x}$  and  $\hat{z}$  directions (see inset of Fig. 3.9). This difference implies that the kinetic energy in the  $\hat{y}$  direction dissipates faster than the energy transfer from the other directions. In principle, it is important to investigate whether the choice of the thermostat, e.g. dissipative particle dynamics thermostat, has an effect on the velocity and temperature profiles at high shear rates [80]. In the present study, the temperature in the first fluid layer was computed

from

$$T_1 = \int_{z_0}^{z_1} T(z)\rho(z)dz / \int_{z_0}^{z_1} \rho(z)dz, \quad (3.14)$$

where the limits of integration ( $z_0 = -14.4\sigma$  and  $z_1 = -13.8\sigma$ ) are given by the width of the first peak in the density profile (e.g. see Fig. 3.2).

The ratio of the slip length to viscosity is plotted in Fig. 3.10 as a function of  $T_1/[S(\mathbf{G}_1)\rho_c]$  for different fluid densities and shear rates. Except for higher densities at low shear rates, the data collapse onto a single curve, which approximately follows the power law function with a slope of 0.9 (see Fig. 3.10). Although the slope is different from the value 1.44 reported for simple fluids [29], it is remarkable that the same combination of parameters determines the boundary conditions for both polymer melts and simple fluids. The simulation results also show that for each value of the fluid density, the number of fluid monomers in the first layer  $N_\ell = S(0)$  decreases by about 4% at the highest shear rates. The same data for the slip length and viscosity are replotted as a function of the variable  $S(0)/[S(\mathbf{G}_1)\rho_c]$  in Fig. 3.11. The collapse of the data is consistent with the previous results for the rate-independent slip length at the interface between simple fluids and crystalline walls [21]. The correlation between the friction coefficient and the fluid structure in the adjacent layer presented in Figs. 3.10 and 3.11 suggests a possible existence of a general functional relation between the slip length, shear rate and polymer density.

### 3.4 Conclusions

In this chapter, the rate dependence of the slip length in the shear flow of polymer melts past atomically smooth, thermal surfaces was studied using molecular dynamics simulations. For weak wall-fluid interactions, the slip length passes through a minimum as a function of shear rate and then increases rapidly at higher shear rates. The nonlinear rate dependence of the slip length was analyzed in terms of the dynamic friction at the liquid/solid interface. In a wide range of fluid densities, the friction coefficient (the ratio of the shear viscosity and the slip length) undergoes a universal transition from a constant value to the power law decay as a function of the slip velocity. The simulation results for polymer melts confirm the previous findings for simple fluids [29] that the surface induced structure and the contact

density of the adjacent fluid layer are crucial factors for determining the value of the friction coefficient.

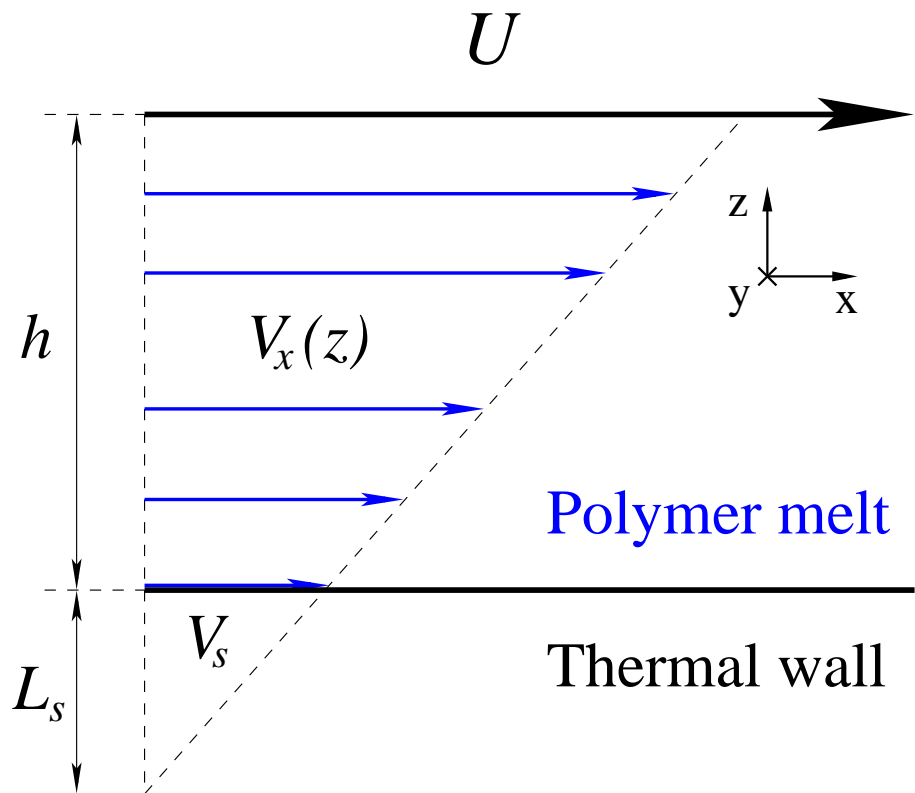


Figure 3.1. A schematic representation of the steady-state shear flow in the Couette cell. The upper wall is translated with a constant velocity  $U$  in the  $\hat{x}$  direction. The fluid slip velocity is determined from the relation  $V_s = \dot{\gamma}L_s$ , where  $\dot{\gamma}$  is the slope of the velocity profile and  $L_s$  is the slip length.

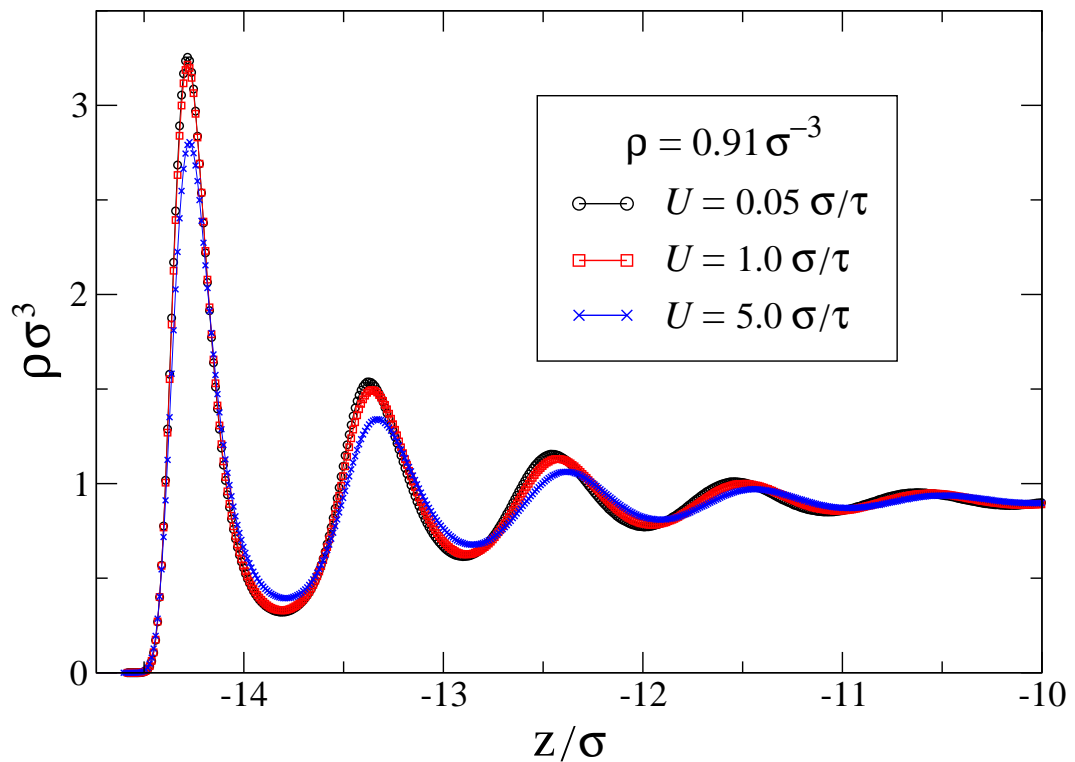


Figure 3.2. Averaged fluid density profiles near the stationary thermal wall with  $\kappa = 1200 \varepsilon/\sigma^2$  and  $\varepsilon_{\text{wf}}/\varepsilon = 0.9$ . The velocities of the upper wall are tabulated in the inset. The fluid density in the center of the cell is  $\rho = 0.91 \sigma^{-3}$ . The left vertical axis denotes the position of the liquid/solid interface at  $z = -14.74 \sigma$ .

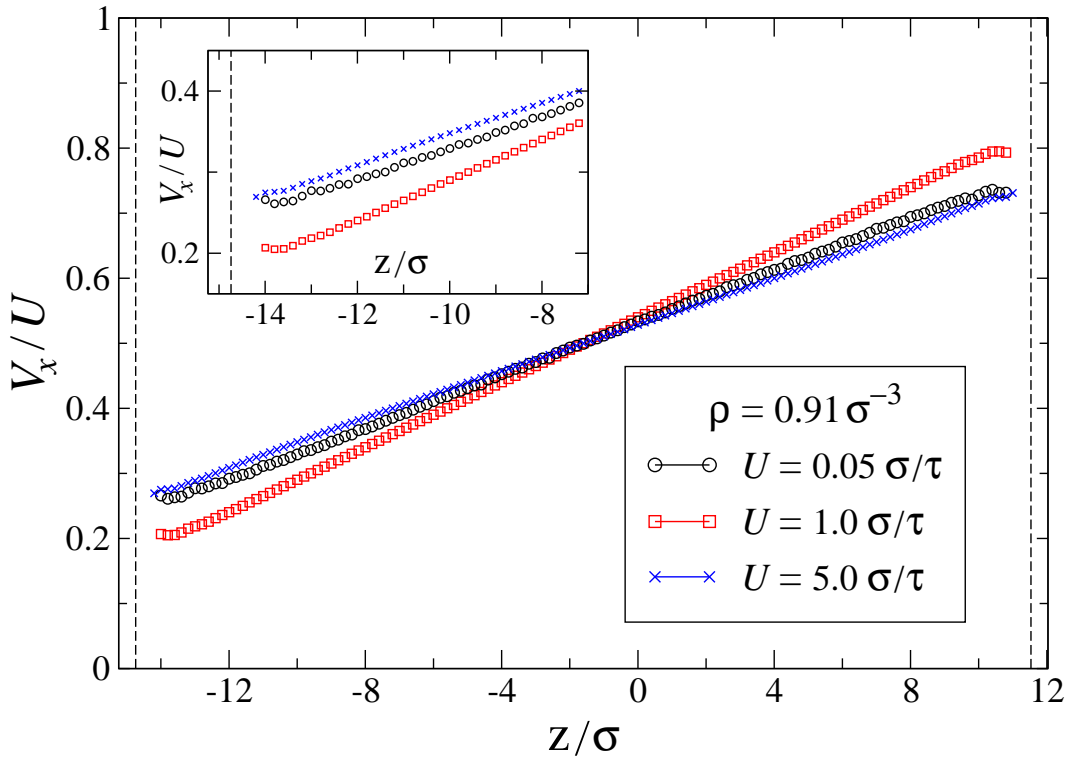


Figure 3.3. Average normalized velocity profiles,  $V_x/U$ , for the indicated values of the upper wall velocity  $U$  and the fluid density  $\rho = 0.91 \sigma^{-3}$ . Vertical axes denote the position of the FCC lattice planes at  $z = -15.24\sigma$  and  $z = 12.03\sigma$ . The dashed lines indicate the location of liquid/solid interfaces at a distance  $0.5\sigma_w$  away from the FCC lattice planes, i.e.,  $z = -14.74\sigma$  and  $z = 11.53\sigma$ . The inset shows the same data near the lower wall.

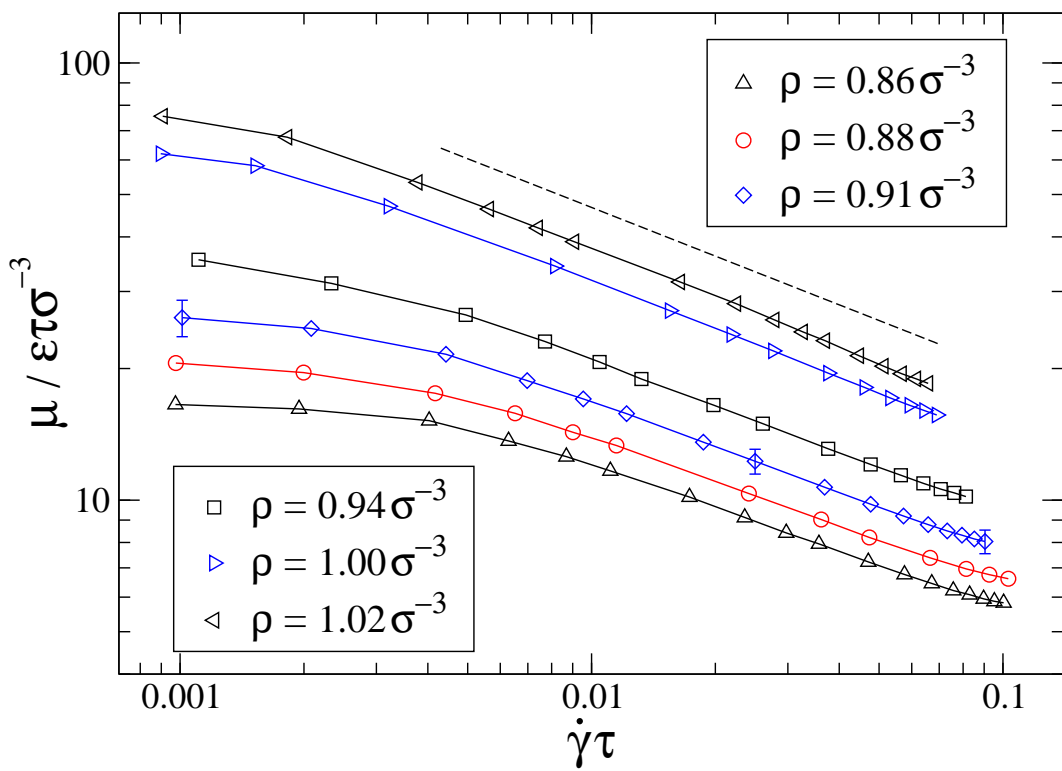


Figure 3.4. Behavior of the fluid viscosity  $\mu / \varepsilon \tau \sigma^{-3}$  as a function of shear rate for the tabulated values of the polymer density. The straight dashed line with a slope  $-0.37$  is shown for reference. Solid curves are a guide for the eye.

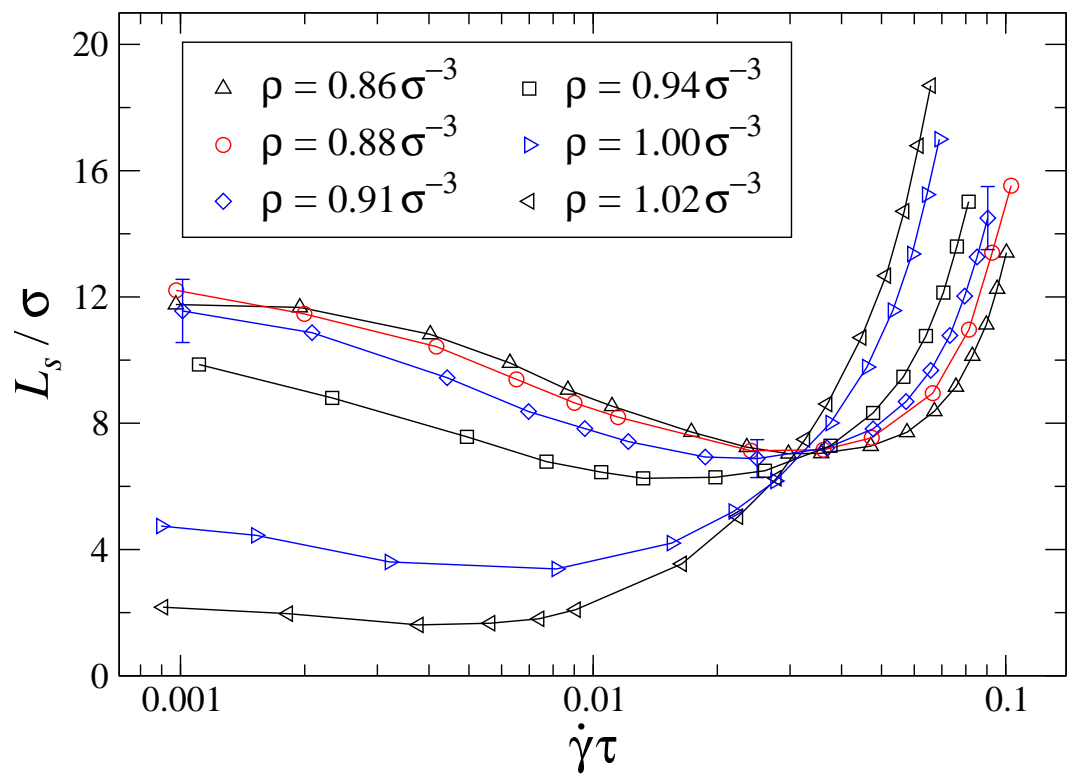


Figure 3.5. Slip length  $L_s/\sigma$  as a function of the shear rate for the polymer melt with linear chains  $N = 20$ . Solid curves are a guide for the eye.

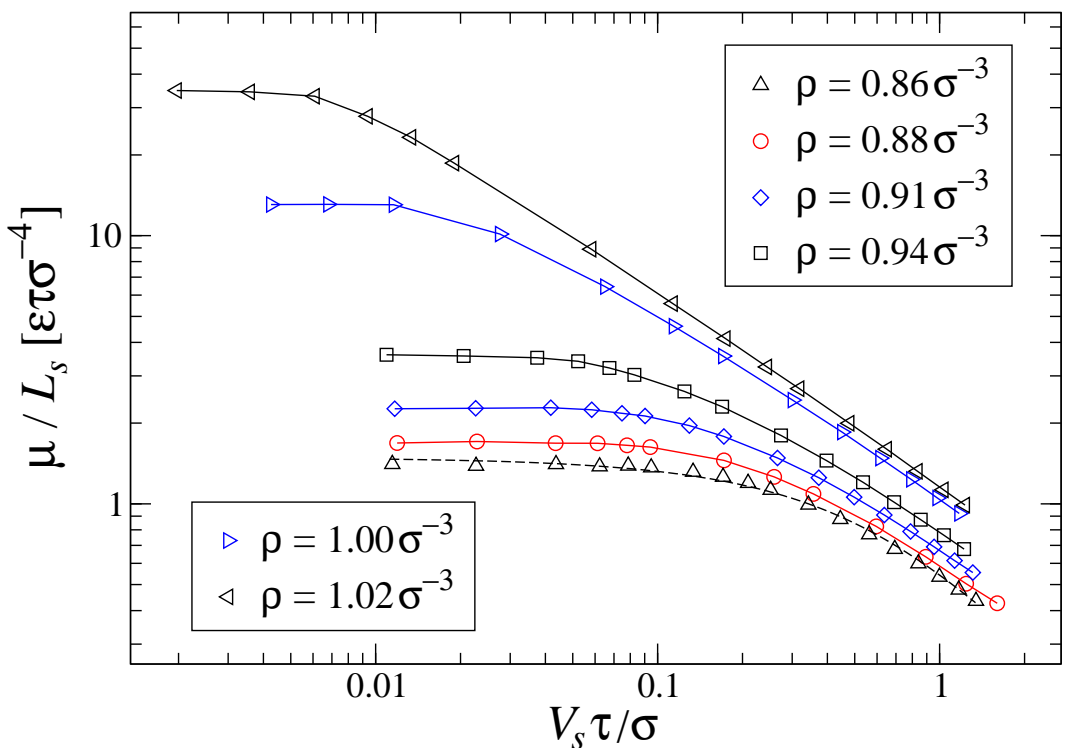


Figure 3.6. Log-log plot of the friction coefficient,  $k = \mu/L_s$ , as a function of the slip velocity for the indicated values of the fluid density. The dashed curve is the best fit to Eq. (3.10) with  $C_1 = 1.77 m\sigma^{-3}$  and  $C_2 = 0.71 \sigma^2\tau^{-2}$ . Solid curves are a guide for the eye.

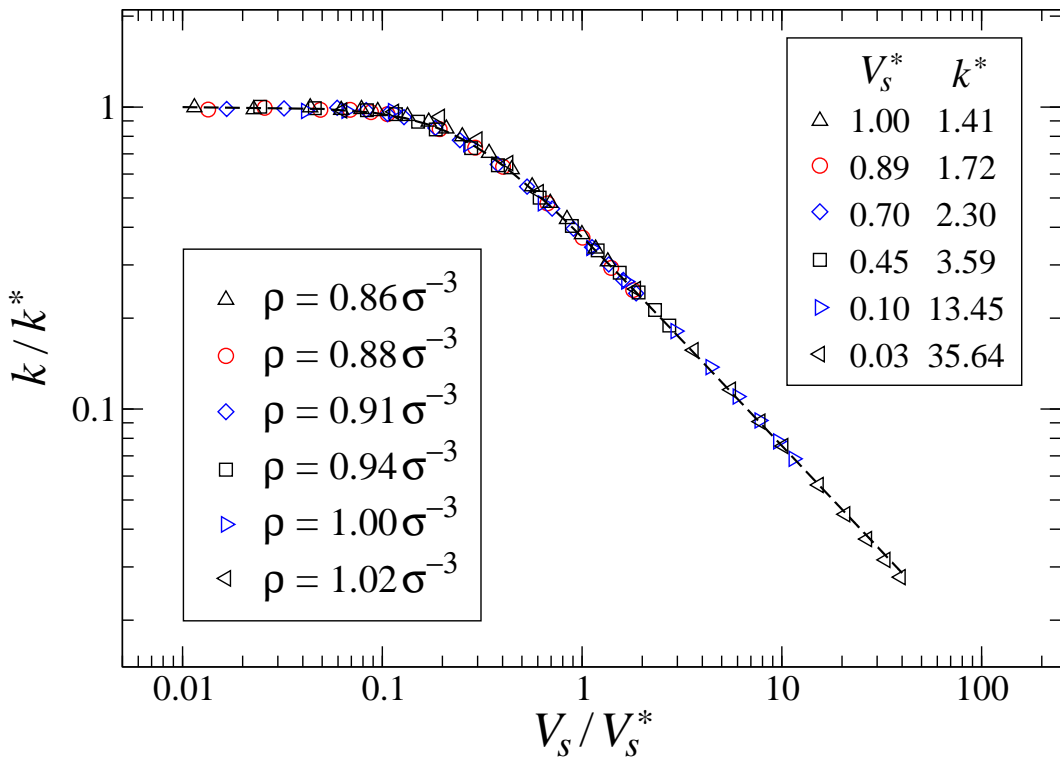


Figure 3.7. Master curve for the friction coefficient as a function of the slip velocity. The same data as in Fig. 3.6. The values of the friction coefficient  $k^* [\varepsilon\tau\sigma^{-4}]$  and the slip velocity  $V_s^* [\sigma/\tau]$  used for normalization of the data are shown in the inset. The dashed line  $y = [1 + (4x)^2]^{-0.35}$  is plotted for reference.

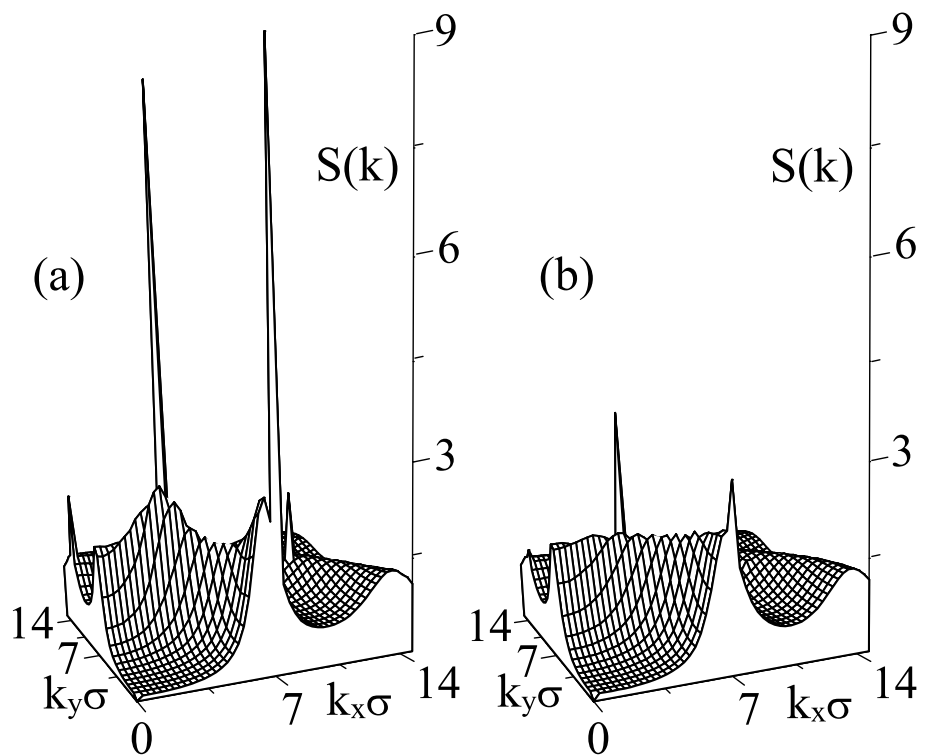


Figure 3.8. Structure factor  $S(k_x, k_y)$  in the first fluid layer for the fluid density  $\rho = 0.91 \sigma^{-3}$ . The upper wall velocity is  $U = 0.05 \sigma/\tau$  (a) and  $U = 5.0 \sigma/\tau$  (b). The same flow conditions as in Fig. 3.3.

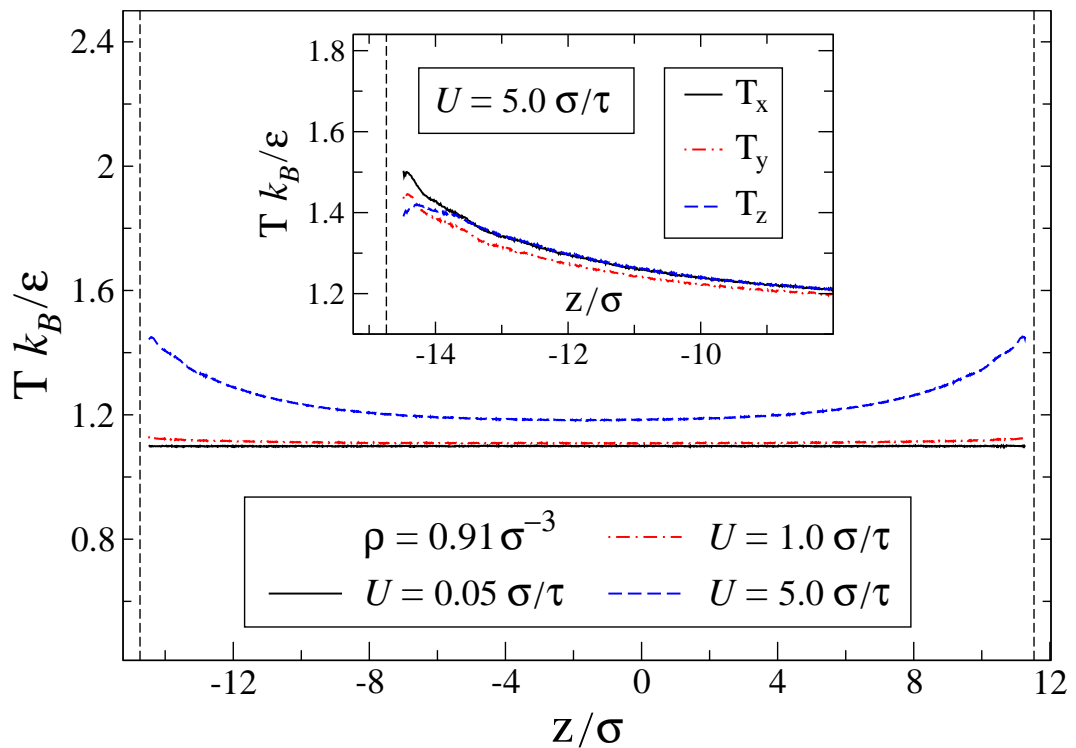


Figure 3.9. Temperature profiles for the indicated values of the upper wall speed  $U$  and the fluid density  $\rho = 0.91 \sigma^{-3}$ . Vertical dashed lines denote the position of the liquid/solid interface. The inset shows the  $\hat{x}$ ,  $\hat{y}$  and  $\hat{z}$  components of the temperature profile near the stationary lower wall when the velocity of the upper wall is  $U = 5.0 \sigma/\tau$ .

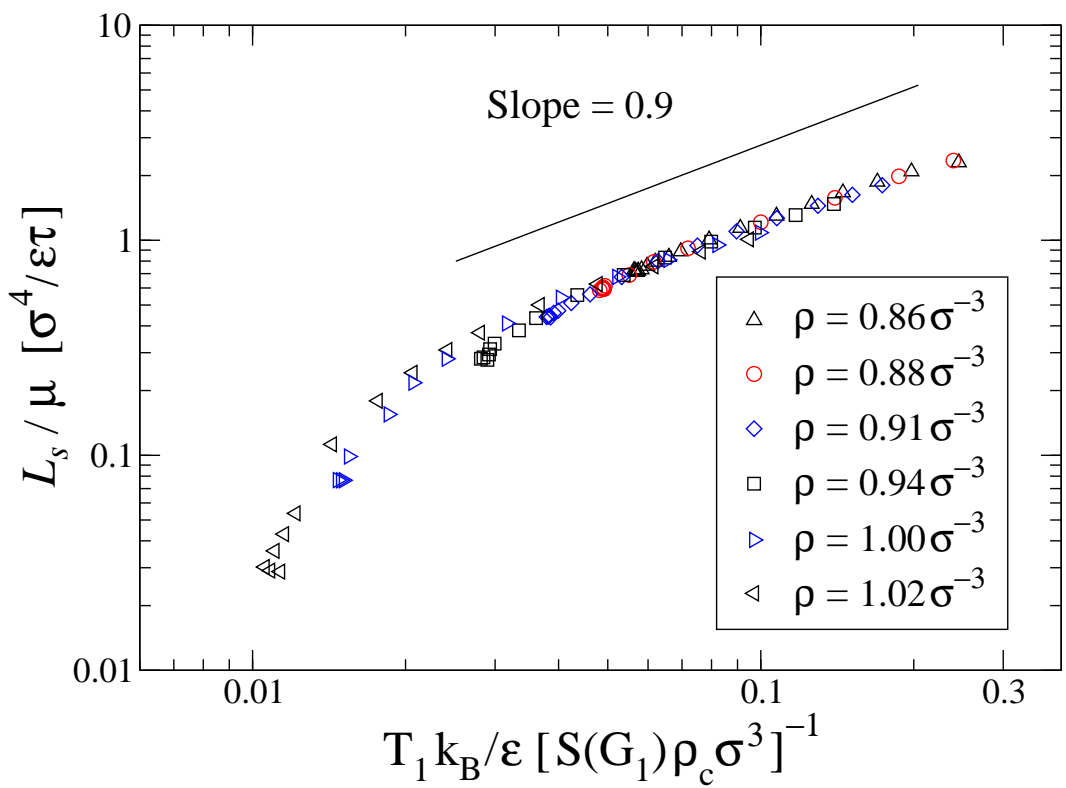


Figure 3.10. Log-log plot of  $L_s/\mu$  as a function of the ratio  $T_1 k_B/\varepsilon [S(G_1) \rho_c \sigma^3]^{-1}$  for the indicated values of the polymer density. The solid line with a slope 0.9 is plotted for reference.

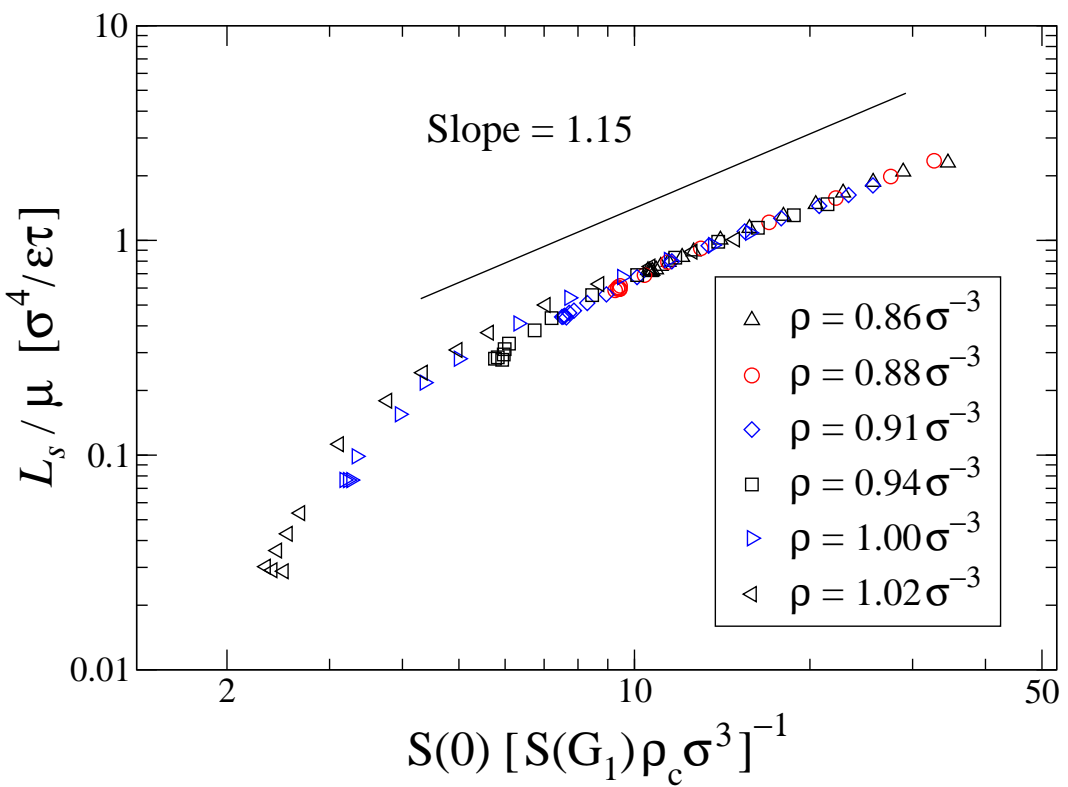


Figure 3.11. Log-log plot of the ratio  $L_s/\mu$  as a function of the variable  $S(0)/[S(\mathbf{G}_1)\rho_c\sigma^3]$ . The values of the fluid density are tabulated in the inset. The same data as in Fig. 3.10. The straight solid line with a slope 1.15 is plotted as a reference.

# CHAPTER 4

## The effective slip length and vortex formation in laminar flow over a rough surface

### 4.1 Introduction

An accurate flow prediction in micro-channels is important for the optimal design and fabrication of microfluidic devices whose applications range from medicine to biotechnology [81, 82]. The boundary conditions and the surface topology are major factors affecting the flow pattern near the solid boundary and the formation of recirculation zones. The flow separation at rough surfaces can modify the wall shear stress distribution or initiate instability towards turbulence. In microfluidic channels, the vortex flow enhances the mixing efficiency [83, 84] and promotes convective heat transfer [85, 86, 87]. In cardiovascular systems, the separation region at the entrance of branching vessels may trap lipid particles which could lead to arterial diseases [88, 89, 90]. In the present study we examine the role of slip boundary condition in determining the flow properties near rough surfaces including the separation phenomena, and distribution of pressure and shear stress along the surface.

Although the validity of the no-slip boundary condition is well accepted at the macroscopic level, recent experiments [5, 16, 9, 19, 91, 14] and molecular dynamics (MD) simulations [21, 23, 25, 92, 27, 29] reported the existence of a boundary slip in microflows. The

model first proposed by Navier relates the slip velocity to the rate of shear via the proportionality coefficient, the so-called slip length. The MD simulations are particularly suitable for examining the influence of molecular parameters on the microscopic slip length at the liquid/solid interface. The advantage of the MD simulations is that a detailed flow analysis can be performed at the molecular level while the explicit specification of the boundary conditions is not required. In contrast to description of the flow near boundary by means of microscopic slip length, it is convenient to characterize the flow over macroscopically rough surfaces by the effective slip length, which is defined as a distance from the level of the mean height of the surface roughness to the point where linearly extrapolated bulk velocity profile vanishes. Recent MD studies have demonstrated that the effective slip length in a flow of simple fluids [35] and polymer melts [93] over a wavy surface agrees well with hydrodynamic predictions [51, 52] when the corrugation wavelength is larger than approximately thirty molecular diameters.

The influence of surface roughness on fluid flow with either local no-slip or zero shear stress (i.e. perfect slip) boundary conditions has been extensively studied in the past decades [43, 62, 94, 95, 63, 96, 97], see also a review section in [35]. Analytical calculations have shown that in a shear flow over a corrugated surface with microscopic no-slip or zero shear stress conditions, the effective boundary slip is insignificant macroscopically [43, 94]. The effective no-slip boundary plane is located at the intermediate position between crests and valleys of the rough surface when the no-slip condition is imposed along the solid boundary [62, 63, 98, 14, 36]. For an arbitrary surface roughness with small amplitudes, the slip coefficient in the Navier model is proportional to the average amplitude of the wall roughness and depends on the position of the origin of the coordinate system [95]. Applying the no-slip boundary condition along the wavy surface, Tuck and Kouzoubov [63] have demonstrated that the effective slip length is inversely proportional to the corrugation wavelength and quadratically proportional to the amplitude of the surface roughness. However, the series expansion method used in [63] fails at large wavenumbers,  $ka \gtrsim 0.5$ , when a backflow appears inside the grooves of the substrate. The effective slip length for a flow above the surface with deep corrugations only weakly depends on the depth of the grooves [62, 97, 93]. Despite considerable analytical efforts, the relation between the vortex flow structure in

deep grooves and the effective slip length has not yet been systematically investigated.

The laminar flow separation at the corrugated surface with the local no-slip boundary conditions depends on the depth of the grooves and the Reynolds number [99, 100, 101, 102, 103, 104, 105, 106]. In a creeping flow over a sinusoidal surface, the flow circulation appears in sufficiently deep grooves and, as the corrugation amplitude increases, the vortex grows and remains symmetric [104, 107, 108]. With increasing Reynolds number, the vortex flow forms even in shallow grooves, the circulation region expands, and the center of vorticity is displaced upstream [99, 102, 103, 105]. In the limit of small-scale surface roughness and for no-slip boundary conditions, the apparent slip velocity at the mean surface becomes more negative as the Reynolds number increases [63]. A noticeable change in the effective slip length was also observed at  $Re \gtrsim 100$  for laminar flow over deep grooves when the local slip length is comparable to the corrugation amplitude [93]. However, the influence of the local slip condition at the curved boundary on the vortex flow formation has not been considered at finite Reynolds numbers.

This chapter is focused on investigation of the effects of local slip boundary conditions and the Reynolds number on the flow structure near periodically corrugated surfaces and the effective slip length. We will show that for the Stokes flow with the local no-slip boundary condition, the effective slip length decreases with increasing corrugation amplitude and the flow circulation develops in sufficiently deep grooves. In the presence of the local slip boundary condition along the rough surface, the effective slip length increases and the size of the vortex is reduced but its structure remains symmetrical. The analysis of the numerical solution of the Navier-Stokes equation with the local slip condition shows that the inertial effects promote the asymmetric vortex flow formation and reduce the effective slip length.

This chapter is organized as follows. The details of a continuum model and the implementation of the local slip boundary conditions are described in the next section. The analytical results for the Stokes flow over a wavy surface by Panzer *et al.* [52] are summarized in Sec. 4.3.1. The analysis of the effective slip length and the flow structure is presented in Sec. 4.3.2 for the no-slip case and in Sec. 4.3.3 for the finite microscopic slip. The effect of Reynolds number on the effective slip flow over a periodically corrugated surface is studied in Sec. 4.3.4. A brief summary is given in the last section.

## 4.2 Details of numerical simulations

The two-dimensional incompressible and steady Navier-Stokes (NS) equation is solved using the finite element method. The computational setup consists of a viscous fluid confined between an upper flat wall and a lower sinusoidal wall (see Fig. 4.1). The corrugation wavelength of the lower wall is set to  $\lambda$  and is equal to the system size in the  $\hat{x}$  direction. The upper wall is located at  $h = \lambda$  above the reference line at  $a = 0$ , which is defined as the mean height of the surface roughness. The continuity and NS equations are

$$\nabla \cdot \mathbf{u} = 0, \quad (4.1)$$

$$\rho (\mathbf{u} \cdot \nabla \mathbf{u}) = -\nabla p + \mu \nabla^2 \mathbf{u}, \quad (4.2)$$

where  $\mathbf{u} = u \hat{i} + v \hat{j}$  is the velocity vector in the cartesian coordinate system,  $p$  is the pressure field,  $\rho$  is the fluid density, and  $\mu$  is the Newtonian viscosity.

The penalty formulation is employed to avoid decoupling between the pressure and velocity fields [109]. In this method, the continuity equation is replaced with a perturbed equation

$$\nabla \cdot \mathbf{u} = -\frac{p}{\Lambda}, \quad (4.3)$$

where  $\Lambda$  is the penalty parameter, which ensures the incompressibility condition. Thus, the modified momentum equations in the  $\hat{x}$  and  $\hat{z}$  directions are

$$\rho (\mathbf{u} \cdot \nabla u) = \Lambda \nabla (\nabla \cdot \mathbf{u}) + \mu \nabla^2 u, \quad (4.4)$$

$$\rho (\mathbf{u} \cdot \nabla v) = \Lambda \nabla (\nabla \cdot \mathbf{u}) + \mu \nabla^2 v. \quad (4.5)$$

The advantage of the penalty formulation is the elimination of pressure and the continuity equation. The penalty parameter  $\Lambda$  must be large enough so that compressibility errors are minimal. The upper bound of  $\Lambda$  is determined from the condition that the viscous effects are not destroyed by the machine precision [109, 110]. The penalty parameter  $\Lambda$  should be chosen according to the rule

$$\Lambda = c \max\{\mu, \mu Re\}, \quad (4.6)$$

where  $Re$  is the Reynolds number and the constant  $c$  is recommended to be about  $10^7$  for computations with double-precision 64 bit words [110].

The Galerkin formulation of Eq. (4.4) and Eq. (4.5) can be explicitly rewritten as

$$\left[ \int_{\Omega} \rho N_i \left( \bar{u}_i u_j \frac{\partial N_j}{\partial x} + \bar{v}_i v_j \frac{\partial N_j}{\partial z} \right) \right] + \left[ \int_{\Omega} \Lambda \frac{\partial N_i}{\partial x} \left( \frac{\partial N_j}{\partial x} u_j + \frac{\partial N_j}{\partial z} v_j \right) d\Omega \right] + \left[ \int_{\Omega} \mu \left( \frac{\partial N_i}{\partial x} \frac{\partial N_j}{\partial x} + \frac{\partial N_i}{\partial z} \frac{\partial N_j}{\partial z} \right) u_j d\Omega \right] = RHS_x, \quad (4.7)$$

$$\left[ \int_{\Omega} \rho N_i \left( \bar{u}_i v_j \frac{\partial N_j}{\partial x} + \bar{v}_i v_j \frac{\partial N_j}{\partial z} \right) \right] + \left[ \int_{\Omega} \Lambda \frac{\partial N_i}{\partial z} \left( \frac{\partial N_j}{\partial x} u_j + \frac{\partial N_j}{\partial z} v_j \right) d\Omega \right] + \left[ \int_{\Omega} \mu \left( \frac{\partial N_i}{\partial x} \frac{\partial N_j}{\partial x} + \frac{\partial N_i}{\partial z} \frac{\partial N_j}{\partial z} \right) v_j d\Omega \right] = RHS_z, \quad (4.8)$$

where  $N_i$  is the weight function,  $N_j$ ,  $u_j$ ,  $v_j$  are the node shape function and the velocities in each element,  $\bar{u}_i$  and  $\bar{v}_i$  are the lagged velocities, and the right hand side ( $RHS_x$ ,  $RHS_z$ ) terms include the boundary velocities.

In our simulation, the bilinear quadrilateral elements ( $i, j = 1, 2, 3, 4$ ) with non-orthogonal edges are transformed to straight-sided orthogonal elements by introducing the natural coordinates  $\xi = \xi(x, z)$  and  $\eta = \eta(x, z)$ . The shape functions  $N_i$  in the natural coordinate system are defined as

$$N_i = \frac{(1 + \xi_i \xi)(1 + \eta_i \eta)}{4} \quad i = 1, \dots, 4 \quad (4.9)$$

where  $\xi_i$  and  $\eta_i$  are the corner points of each element (see Fig. 4.2).

In the next step, Eq. (4.7) and Eq. (4.8) are integrated numerically using four-point Gaussian quadrature [57]. The final system of equations is constructed as follows:

$$\left[ \rho[K_1] + \Lambda[K_2] + \mu[K_3] \right] \begin{bmatrix} u \\ v \end{bmatrix} = \begin{bmatrix} RHS_x \\ RHS_z \end{bmatrix}, \quad (4.10)$$

where the terms  $RHS_x$  and  $RHS_z$  contain the velocities at the boundary nodes.

The boundary conditions must be specified at the inlet, outlet and upper and lower walls of the Couette cell. The periodic boundary conditions are imposed at inlet and outlet along the  $\hat{x}$  direction. A finite slip is allowed along the lower wall while the boundary condition at the upper wall is always no-slip. In the local coordinate system (spanned by the tangential  $\vec{t}$  and normal  $\vec{n}$  vectors), the fluid velocity along the lower wavy wall is computed from

$$u_t = L_0[(\vec{n} \cdot \nabla) u_t + u_t/R(x)], \quad (4.11)$$

where  $u_t$  is the tangential component of  $\mathbf{u} = u_t \vec{t} + u_n \vec{n}$ ,  $L_0$  is the intrinsic (or microscopic) slip length at the flat surface, and  $R(x)$  is the local radius of curvature [52]. The radius of

curvature is positive for concave and negative for convex regions. The Navier slip condition for a flat wall is recovered from Eq. (4.11) when  $R(x) \rightarrow \infty$ . The effective slip length  $L_{eff}$  at the corrugated lower wall is obtained by extrapolating the linear part of the velocity profile ( $0.45 \leq z/h \leq 0.9$ ) to zero velocity with respect to the reference line  $a = 0$ .

The simulation begins by setting the no-slip boundary condition at the upper and lower walls as an initial guess. Once Eq. (4.10) is solved, the fluid velocities at the lower boundary are updated using Eq. (4.11). This iteration is repeated until the solution is converged to a desired accuracy. The convergence rate of the solution remains under control by using the under-relaxation value 0.001 for the boundary nodes. The results presented in this chapter are obtained with the grid resolution  $150 \times 150$  in the  $\hat{x}$  and  $\hat{z}$  directions, respectively. In order to check the accuracy of the results, several sets of simulations were also carried out with a finer grid  $180 \times 180$ . The maximum relative error of the effective slip length due to the grid size is  $L_{eff}/h = 0.003$ . The converged solution of the Navier-Stokes equation satisfies the following boundary condition:

$$u_t = L_s(x) \frac{\partial u_t}{\partial n}, \quad \frac{1}{L_s(x)} = \frac{1}{L_0} - \frac{1}{R(x)}, \quad (4.12)$$

where  $L_s(x)$  is the local slip length in the presence of surface curvature [52].

The accuracy of the numerical solution is checked by the normalized average error, which is defined as

$$\text{error} = \left[ \sum_{i=1}^{N_p} \frac{|u_i^n - u_i^{n+1}|}{|u_i^{n+1}|} \right] / N_p, \quad (4.13)$$

where  $N_p$  is the total number of computational nodes,  $u_i^n$  is the velocity at the node  $i$  and time step  $n$ , and  $u_i^{n+1}$  is the velocity in the next time step. The typical value of the error in the converged solution is less than  $10^{-9}$ . Throughout the study, the results are presented in the non-dimensional form. The length scale, shear rate, shear stress, and velocity are normalized by  $h$ ,  $\dot{\gamma}^*$ ,  $\tau_w^*$ , and  $U^*$ , respectively, where  $\dot{\gamma}^*$  is the shear rate in the case of no-slip boundary condition at the flat upper and lower walls, and  $\tau_w^* = \mu \dot{\gamma}^*$  and  $U^* = h \dot{\gamma}^*$ .

## 4.3 Results

### 4.3.1 Analytical solution of the Stokes equation for viscous flow over a wavy wall

The effect of small periodic surface roughness on the effective slip length has been previously investigated for pressure-driven flows in a Couette geometry [51, 52]. The analytical solution of the Stokes equation with boundary conditions Eq. (4.12) at the wavy wall with amplitude  $a$  and wavelength  $\lambda$  was obtained for two limiting cases and small  $ka$ . For  $L_0/\lambda \ll 1$  the effective slip length is given by

$$\lim_{kL_0 \rightarrow 0} L_{eff} = L_0 - ka^2 \omega_o(ka), \quad (4.14)$$

while in the limit of  $L_0/\lambda \gg 1$  it reduces to

$$\lim_{kL_0 \rightarrow \infty} L_{eff} = \left( \frac{1}{L_0} + \frac{k^3 a^2}{\omega_\infty(ka)} \right)^{-1}, \quad (4.15)$$

where the functions  $\omega_o(ka)$  and  $\omega_\infty(ka)$  are defined as

$$\omega_o(ka) = \frac{1 - 1/4(ka)^2 + 19/64(ka)^4 + O[(ka)^6]}{1 + (ka)^2 - 1/2(ka)^4 + O[(ka)^6]}, \quad (4.16)$$

and

$$\omega_\infty(ka) = \frac{1 - 5/4(ka)^2 + 61/64(ka)^4 + O[(ka)^6]}{1 + (ka)^2 - 1/2(ka)^4 + O[(ka)^6]}. \quad (4.17)$$

An approximate analytical expression for the effective slip length that interpolates between the two bounds Eq. (4.14) and Eq. (4.15) is given by

$$L_{eff} = \frac{L_0 \omega_\infty(ka) - ka^2 \omega_o(ka)/(1 + 2kL_0)}{1 + k^3 a^2 L_0}, \quad (4.18)$$

with the range of applicability  $ka \lesssim 0.5$ . For larger wavenumbers  $ka > 0.5$ , the function  $\omega_\infty(ka)$  overestimates the numerical solution and the interpolated formula Eq. (4.18) does not apply [52].

### 4.3.2 Flow over a rough surface with the local no-slip boundary condition

In this section, the Stokes equation with the local no-slip condition at the upper and lower walls is solved numerically to study the effect of corrugation amplitude on the effective

slip length. The velocity profiles, averaged over the period of corrugation  $\lambda$ , are plotted in the inset of Fig. 4.3 for several values of wavenumber  $ka = 2\pi a/\lambda$ . As  $ka$  increases, the normalized velocity profiles remain linear in the bulk region and become curved near the lower corrugated wall. The linear part of the velocity profiles is used to compute the effective slip length, which is plotted as a function of wavenumber in Fig. 4.3. With increasing corrugation amplitude of the lower wall, the effective slip length decays monotonically and becomes negative, indicating that the effective no-slip boundary is shifted into the fluid domain. For  $ka \lesssim 1$ , the numerical results agree well with the analytical solution Eq. (4.18) denoted by the solid line in Fig. 4.3. The deviation from the analytical solution becomes significant at larger wavenumbers where the streamlines extracted from the Stokes solution indicate the presence of backflow at the bottom of the valley.

In order to investigate the flow behavior above the sinusoidal surface, the shear stress and pressure along the lower wall were computed from the solution of the Stokes equation. In the presence of surface curvature the wall shear stress  $\tau_w$  has two components

$$\tau_w = \mu \left( \frac{\partial u_t}{\partial n} + u_t/R(x) \right) \Big|_w, \quad (4.19)$$

where  $\partial u_t / \partial n$  is the normal derivative of the tangential velocity  $u_t$ , and  $R(x)$  is the local radius of curvature. In the case of no-slip boundary condition ( $u_t = 0$ ), the local shear stress at the wall is reduced to  $\tau_w = \mu \frac{\partial u_t}{\partial n}$ . The normalized shear stress along the lower corrugated wall is plotted in Fig. 4.4 for different corrugation amplitudes. The maximum value of the shear stress is located at the peak of the surface corrugation ( $x/\lambda = 0.25$ ) and it increases with increasing amplitude, which is consistent with the results of previous analytical studies of a laminar flow over a wavy wall [111, 100]. The fluid tangential velocity near the boundary is proportional to the wall shear stress shown in Fig. 4.4. Therefore, the tangential velocity is also maximum above the peak and, as the flow moves downstream, it decelerates and the velocity becomes zero inside the valley at sufficiently large amplitudes. For  $ka \geq 0.79$ , the shear stress profiles intersect the dashed line ( $\tau_w = 0$ ) at two points and a clockwise flow circulation develops inside the valley. As the corrugation amplitude increases, the intersection points move away from each other and the flow recirculation region becomes larger. These results are in agreement with previous estimates of the critical wavenumber

$ka \approx 0.77$  for the onset of flow separation in sufficiently thick films [107, 108].

The pressure along the lower wavy wall is plotted in Fig. 4.5 for the same amplitudes as in Fig. 4.4. The value  $P^*$  used for normalization is the maximum pressure, which is located above the wavy surface with  $ka = 1.12$  on the left side of the peak. For each wavenumber, the pressure along the surface is maximum on the left side of the peak, where the surface faces the mainstream flow. The surface pressure reaches its minimum value on the right side of the peak (see Fig. 4.5). As the flow moves further downstream into the valley, it encounters an adverse pressure gradient, which becomes larger as  $ka$  increases. At large wavenumbers  $ka \geq 0.83$ , the flow near the surface cannot overcome the combined resistance of the viscous forces and the adverse pressure gradient, and separates from the surface at the point where  $\tau_w = 0$ .

The pressure contours and streamlines near the corrugated surface with wavenumber  $ka = 1.12$  are depicted in Fig. 4.6(a). The pressure contours indicate the presence of an adverse pressure gradient in the region  $0.3 \lesssim x/\lambda \lesssim 0.6$  on the right side of the peak (see also Fig. 4.5). The streamlines illustrate the flow separation inside the valley at  $x/\lambda \simeq 0.52$ . After the separation point the flow near the wall reverses direction and moves against the mainstream. The local velocity profile inside the valley is shown in the inset of Fig. 4.6(a). As the flow cross-section decreases towards the peak, the flow attaches to the surface at the point where the shear stress is zero again. Note also that for  $ka \geq 0.83$  in Fig. 4.5, the pressure profiles along the lower surface exhibit a slight drop inside the valley where the vortex is present. After the attachment point, due to the periodic boundary condition in the  $\hat{x}$  direction, the surface pressure increases up to its maximum value, which is located on the left side of the peak. The nonlinearity due to inertia is absent in the Stokes flow and the vortex in the valley remains symmetrical.

We also comment that a secondary vortex is formed inside a deeper cavity ( $ka \approx 2.33$ ), which is counter-rotating with respect to the primary vortex (not shown). Previous analytical study of a creeping flow over a wavy wall demonstrated that a secondary vortex appears at  $ka \gtrsim 2.28$  when the channel width is larger than the corrugation wavelength [108]. In the limiting case, when the cavity consists of two parallel walls, an infinite sequence of counter-rotating vortices appears between the walls [112, 113].

### 4.3.3 Effect of the local slip on the flow pattern near the rough surface

Next, we present the results of the numerical solution of the Stokes equation with the local slip condition at the lower wavy wall while the boundary condition at the upper wall remains no-slip. The pressure contours and the streamlines are plotted in Fig. 4.6 for several values of the intrinsic slip length  $L_0$  and the wavenumber  $ka = 1.12$ . The streamline patterns indicate that with increasing slip length  $L_0$ , the size of vortex inside the valley is progressively reduced and the vortex eventually disappears. Similar to the analysis in the previous section, the pressure and shear stress along the lower wall are computed in the presence of the local boundary slip.

The normalized pressure along the lower wavy wall is plotted in Fig. 4.7 as a function of the slip length  $L_0$ . Similar to the case of no-slip boundary condition, the profiles exhibit a maximum and a minimum in pressure on the right and left sides on the peak, respectively. In a wide range of  $L_0$ , the difference between the locations and the magnitudes of the extrema is barely noticeable. As the flow moves down a slope ( $0.3 \lesssim x/\lambda \lesssim 0.5$  region in Fig. 4.7), the pressure gradient along the surface becomes positive and its magnitude decreases with increasing values of  $L_0$ . The separation and attachment points are located at the intersection of the shear stress profiles with the horizontal line ( $\tau_w = 0$ ) shown in Fig. 4.8. In comparison to the no-slip case, the smaller combined effect of the adverse pressure gradient and the wall shear stress causes a shift of the separation point deeper into the valley (e.g. see Fig. 4.6). As the slip length  $L_0$  increases, the separation and attachment points move closer to each other, the vortex becomes smaller and eventually vanishes. We also note that at the separation point both components of the shear stress  $\partial u_t / \partial n$  and  $u_t / R(x)$  become zero in agreement with the MRS criterion for the flow separation of the boundary layer at a moving substrate [114].

The influence of the local slip on the shape of the velocity profile and the normal derivative of the tangential velocity at the bottom of the valley is illustrated in the insets of Fig. 4.6. The local slip length  $L_s(x)$  in Eq. (4.12) is a function of the radius of curvature  $R(x)$  and the intrinsic slip length  $L_0$ . For all cases considered in Fig. 4.6, the condition  $L_0 < |R(x)|$

holds and the local slip length  $L_s$  remains positive everywhere along the lower wall, which means that the slip velocity  $u_t$  and the normal derivative  $\partial u_t / \partial n$  carry the same sign. It is expected, however, that for the opposite condition,  $L_0 > |R(x)|$ , the values  $u_t$  and  $\partial u_t / \partial n$  would have different signs at the bottom of the valley, and the corresponding velocity profile will be qualitatively similar to the profile shown in the inset of Fig. 4.6(d) but shifted by a negative slip velocity (see next section).

The effective slip length computed from the numerical solution of the Stokes equation and Eq. (4.18) is plotted in Fig. 4.9 as a function of the intrinsic slip length  $L_0$  for wavenumbers  $ka = 0.28$  ( $a/h = 0.04$ ) and  $ka = 1.12$  ( $a/h = 0.18$ ). For small values of  $L_0$ , the effective slip length approaches a negative value previously reported in Fig. 4.3 for the no-slip case. As  $L_0$  increases,  $L_{eff}$  grows monotonically and appears to saturate to a constant value. The transition of the effective slip length from a growing function of  $L_0$  to a nearly constant value occurs at larger  $L_0$  when  $ka$  decreases. For the small wavenumber  $ka = 0.28$ , the effective slip length computed from Eq. (4.18) is in a good agreement with the numerical solution of the Stokes equation. Visual inspection of the streamline patterns indicates that there is no backflow at any  $L_0$ . In the saturation regime,  $L_0 \rightarrow \infty$ , the wall shear stress becomes zero everywhere along the lower boundary, the streamlines near the lower wall follow the boundary curvature, and the effective slip length in Eq. (4.15) approaches  $L_{eff}/\lambda \simeq 1/[2\pi(ka)^2] - 9/8\pi$ . For the large wavenumber  $ka = 1.12$ , the analytical results Eq. (4.18) overestimate  $L_{eff}$  computed from the numerical solution at  $L_0/h \gtrsim 0.02$  and the flow circulation is developed in the valley at  $L_0/h \leq 0.067$ . The vortex vanishes at the bottom of the valley at sufficiently large values of  $L_0$  (denoted by the vertical arrow in Fig. 4.9), and the flow streamlines are deformed to follow the boundary curvature [e.g. see Fig. 4.6(d)]. The results for the intrinsic slip length, which determines the threshold for the onset of the flow circulation at the bottom of the groove, are summarized in Fig. 4.10. For the wavenumbers examined in this study,  $ka \leq 1.26$ , the numerical simulations indicate that if the flow circulation is present in the valley then the effective slip length is negative and  $L_{eff}$  increases with decreasing vortex size.

#### 4.3.4 Effect of the Reynolds number on the effective slip length

The analysis of the Stokes equation discussed in the previous section demonstrated that increasingly large local slip at the lower wavy wall eliminates the flow circulation in the valley and leads to a larger effective slip. In this section, the influence of the inertia term in the Navier-Stokes equation on the flow pattern and the effective slip length is investigated. For the shear flow with slip condition at the lower corrugated wall  $L_0$ , the Reynolds number is defined as

$$Re = \frac{\rho U^* h (1 + L_{eff}/h)}{\mu}, \quad (4.20)$$

where  $\rho$  is the fluid density,  $U^*$  is the upper wall velocity, and  $h (1 + L_{eff}/h)$  is the distance between the upper flat wall and the effective no-slip boundary plane. In the case of no-slip boundary condition at the lower flat wall,  $L_{eff}$  is zero and the standard definition of the Reynolds number is recovered, i.e.,  $Re = \rho U^* h / \mu$ .

The pressure and shear stress along the lower wavy wall are plotted in Fig. 4.11 for the selected values of the Reynolds number and no-slip boundary conditions. As  $Re$  increases, the adverse pressure gradient along the right side of the corrugation peak ( $0.3 \lesssim x/\lambda \lesssim 0.5$ ) becomes larger and the pressure drop inside the valley ( $0.5 \lesssim x/\lambda \lesssim 0.9$ ) increases. For each value of the Reynolds number in Fig. 4.11(b), similar to the Stokes flow case, the shear stress above the peak is maximum and, as the flow moves downstream along the right side of the peak, it decelerates and eventually separates from the surface when  $\tau_w = 0$ . With increasing upper wall velocity, the shear stress above the peak increases and causes the flow to decelerate faster along the right side of the peak. The separation and attachment points (determined from the condition  $\tau_w = 0$ ) move further apart from each other and the circulation region inside the valley expands [see Fig. 4.11(b)].

The effect of the inertia term in the Navier-Stokes equation on the shape of the wall shear stress and pressure profiles can be seen in Fig. 4.11. The shear stress profiles above the peak are not symmetric with respect to  $x/\lambda = 0.25$ , which means that the flow decelerates faster on the right side of the corrugation peak than it accelerates on the left side. Also, the average adverse pressure gradient on the left side of the peak is larger than its value on the right side of the peak ( $0.3 \lesssim x/\lambda \lesssim 0.5$ ). By increasing the upper wall velocity,

the separation point moves further upstream than the attachment point downstream. The formation of asymmetric vortex flow at finite Reynolds numbers is consistent with previous findings for a flow in an undulated tube [103, 99, 102, 105]. The pressure contours and streamlines extracted from the NS equation with the no-slip boundary condition are plotted in Fig. 4.12(a) for  $ka = 1.12$  and  $Re = 79$ . The flow streamlines in the valley indicate an asymmetric clockwise circulation, which is larger than the flow circulation region shown in Fig. 4.6(a) for the Stokes case.

In the presence of the local slip condition along the lower corrugated wall, the size of the vortex becomes smaller while the flow structure remains asymmetric (see Fig. 4.12). The decrease of the vortex size is similar to the case of the Stokes flow shown in Fig. 4.6 and can also be described in terms of the pressure and shear stress along the lower wall. In Fig. 4.13 the pressure and shear stress profiles are plotted for the same values of the upper wall velocity as in Fig. 4.11 but with the slip boundary condition ( $L_0/h = 0.25$ ) along the lower wall. Note that the Reynolds numbers in Fig. 4.13 are slightly larger than the values reported in Fig. 4.11 for the same  $U^*$  because of the larger effective slip length entering the definition of the Reynolds number [see Eq. (4.20)]. For each value of the upper wall velocity, the adverse pressure gradient and the wall shear stress on the right side of the peak are smaller than in the case of the no-slip boundary condition, and, as a result, the vortex either becomes smaller or vanishes (see Figs. 4.11 and 4.13). As the Reynolds number increases, however, the vortex forms and expands asymmetrically to fill the bottom of the groove. The inset of the Fig. 4.12(b) demonstrates that the slip velocity at the bottom of the valley is negative while its normal derivative  $\partial u_t / \partial n$  is positive, in contrast to the velocity profiles shown in Fig. 4.6 for the same  $ka = 1.12$  and smaller slip lengths  $L_0/h \leq 0.08$ .

The effective slip length is plotted in Fig. 4.14 as a function of the Reynolds number for the selected values of the intrinsic slip length  $L_0$  and  $ka = 1.12$ . With increasing Reynolds number, the flow streamlines move away from the lower boundary and straighten out, the slope of the normalized velocity profiles increases and the effective no-slip boundary plane is shifted into the fluid domain. For  $L_0/h \leq 0.067$ , the circulation is always present in the valley and the flow streamlines in the bulk of the fluid do not penetrate deep into the valley [e.g. see Fig. 4.12(b)]. For larger slip lengths  $L_0/h > 0.067$ , the flow streamlines show

that there is no backflow at low  $Re$ , and the vortex is formed at the bottom of the valley only at sufficiently large Reynolds numbers indicated by the dashed line in Fig. 4.14. The numerical results obtained from the solution of the Navier-Stokes equation demonstrate that the growth or decay of the vortex as a function of the Reynolds number or the intrinsic slip length is accompanied by the decrease or increase of the effective slip length.

## 4.4 Conclusions

In this chapter the effects of local slip boundary condition and the Reynolds number on the flow structure near sinusoidally corrugated surfaces and the effective slip length were investigated numerically by solving the Stokes and Navier-Stokes equations. The effective slip length was defined with respect to the mean height of the surface roughness by extrapolating the linear part of the velocity profile averaged over the corrugation period. In the case of the Stokes flow with the local no-slip boundary condition, the effective slip length decreases with increasing corrugation amplitude and the vortex flow develops in the groove of the rough surface for  $ka \geq 0.79$ . In the presence of the local slip boundary condition along the wavy wall, the effective slip length increases and the size of the recirculation zone is reduced. The vortex vanishes at sufficiently large values of the intrinsic slip length. The analysis of the pressure and wall shear stress computed from the Navier-Stokes equation shows that the asymmetric vortex flow develops in the groove due to the inertia term even when the local slip boundary condition is applied. The effective slip length decreases with increasing Reynolds number. The numerical simulations suggest that the variation of the vortex size as a function of either the Reynolds number or the intrinsic slip length correlates with the magnitude of the effective slip length.

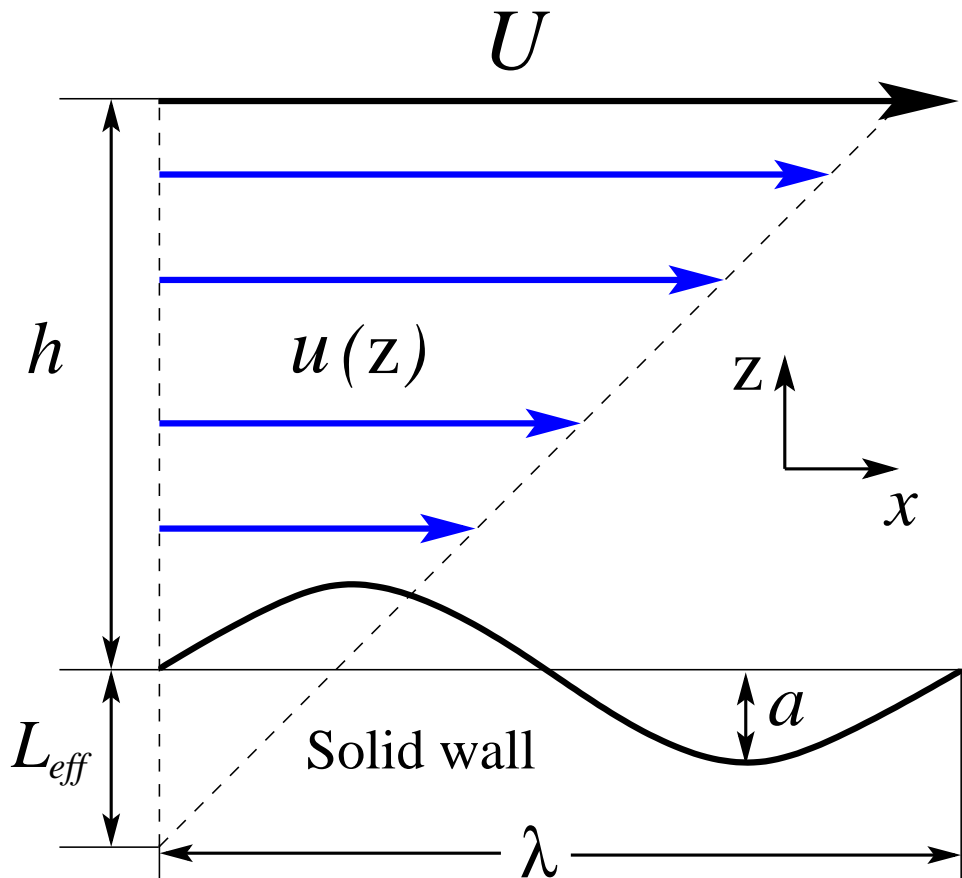


Figure 4.1. Schematic diagram of the steady-state Couette flow over a rough surface. The upper flat wall is moving with a constant velocity  $U$  in the  $\hat{x}$  direction. The lower stationary wall is modeled as a sinusoidal wave with amplitude  $a$  and wavelength  $\lambda$ . The wavenumber  $ka = 2\pi a/\lambda$  varies in the range  $0 \leq ka \leq 1.26$ .

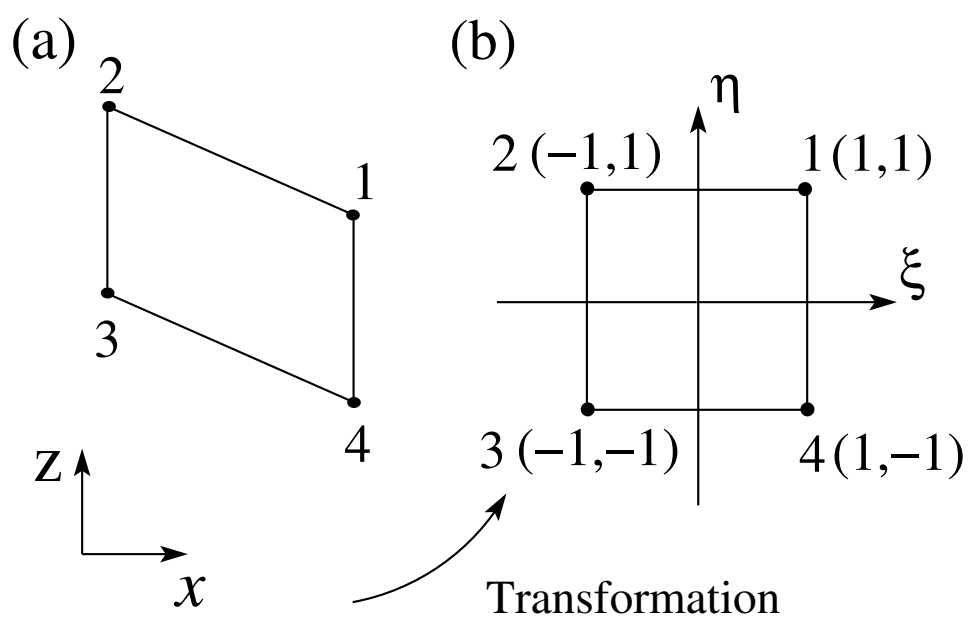


Figure 4.2. Diagram of a bilinear element in (a) the *physical* coordinate system ( $x, z$ ) and (b) a transformed element in the *natural* coordinate system ( $\xi, \eta$ ).

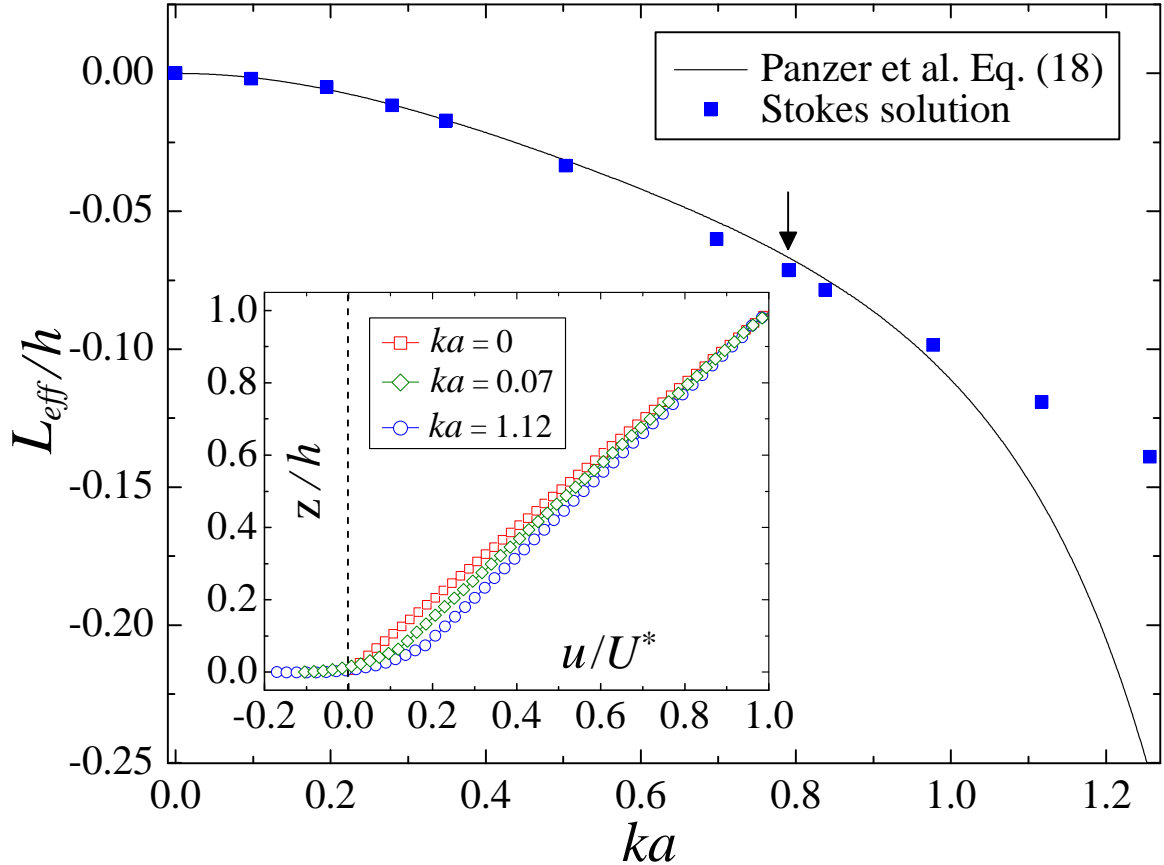


Figure 4.3. The effective slip length as a function of wavenumber  $ka$  computed from the solution of the Stokes equation with the no-slip boundary condition. The primary vortex is formed at the bottom of the valley for  $ka \geq 0.79$  (see the vertical arrow at  $ka = 0.79$ ). The solid line is calculated using Eq. (4.18). The inset shows the normalized velocity profiles obtained from the Stokes solution for the selected values of  $ka$ . The dashed line located at  $a = 0$  is the reference for calculating the effective slip length.

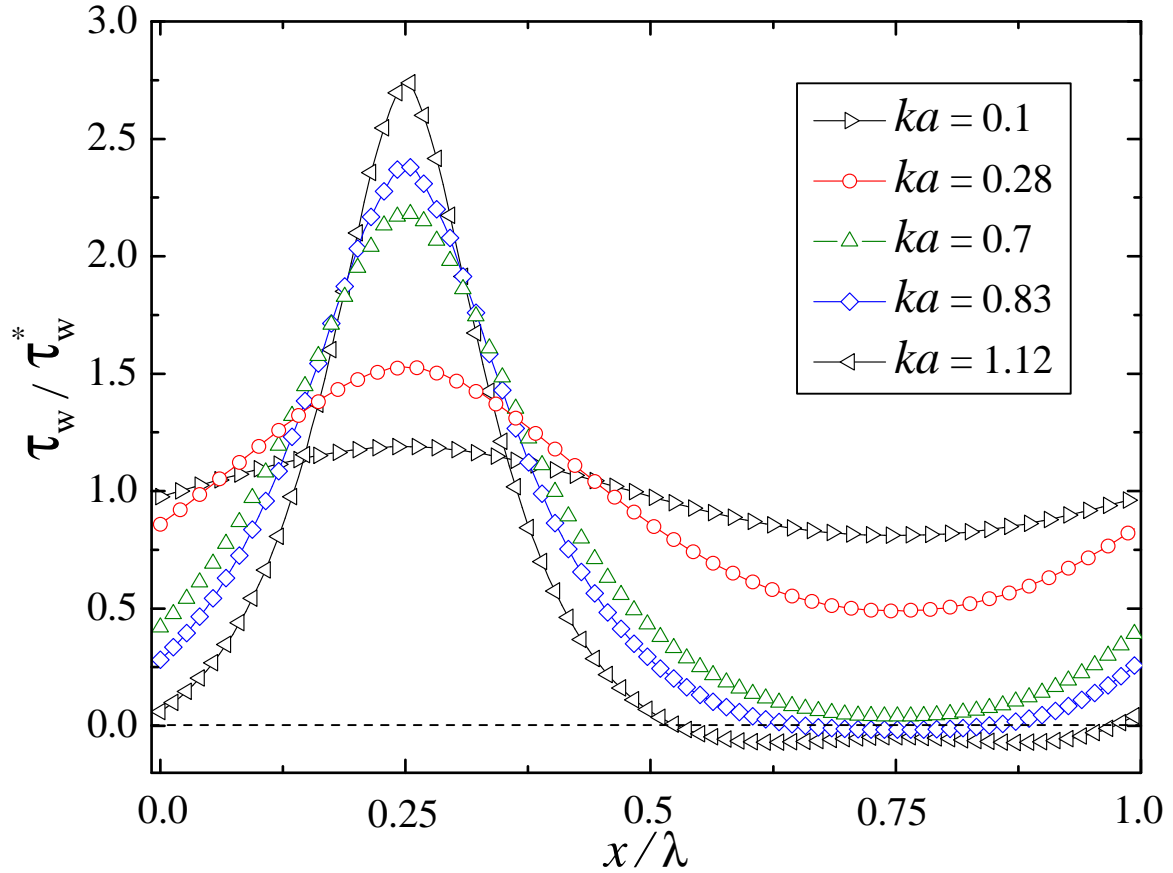


Figure 4.4. Shear stress along the lower wavy wall computed from the Stokes solution with no-slip boundary condition ( $L_0 = 0$ ) for the indicated values of wavenumber  $ka$ . The value  $\tau_w^*$  used for normalization is the shear stress at the flat wall. The intersection of the curves with the dashed line determines the location of the flow separation and attachment inside the valley.

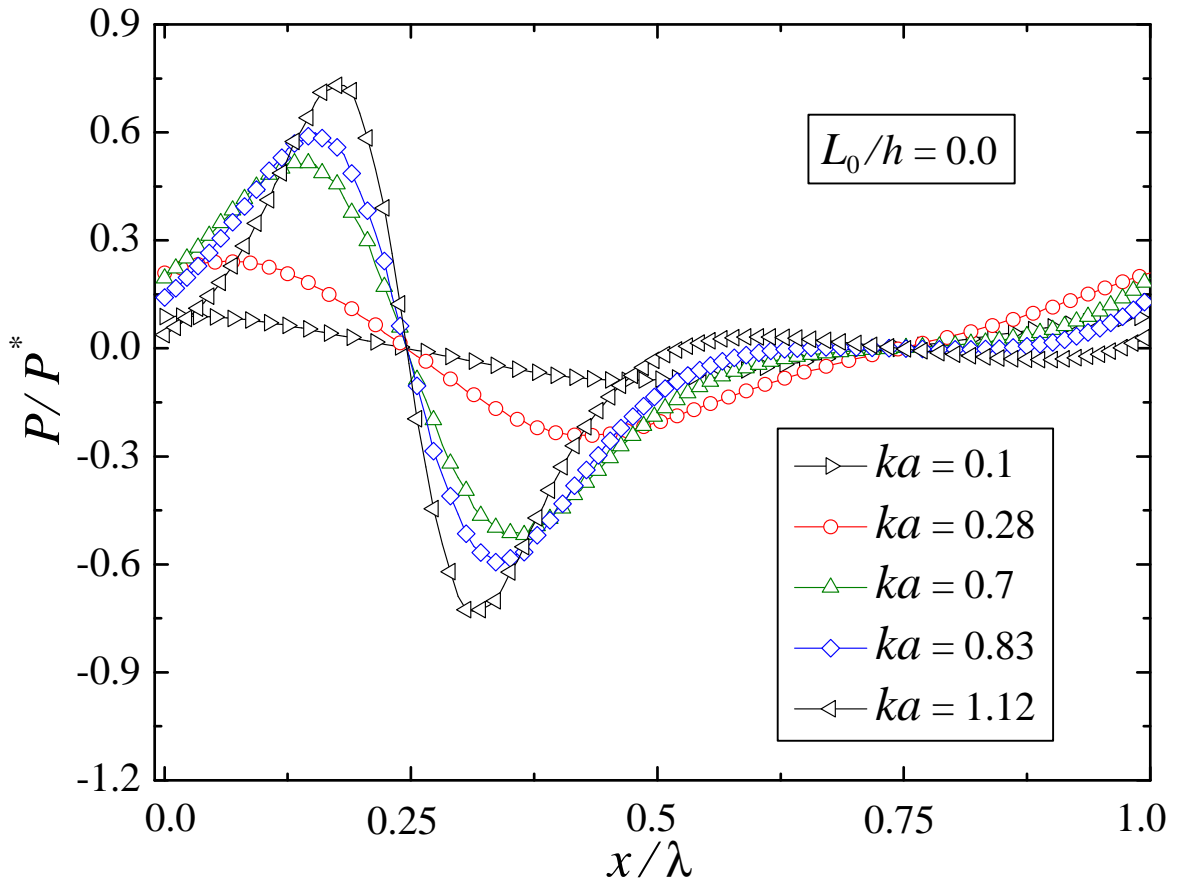


Figure 4.5. The normalized pressure along the lower corrugated boundary extracted from the Stokes solution with no-slip boundary condition for the same values of  $ka$  as in Fig. 4.4. The maximum pressure  $P^*$  for  $ka = 1.12$  and  $L_0 = 0$  is located in the bulk region at  $(x/\lambda, z/\lambda) \simeq (0.07, 0.23)$ .

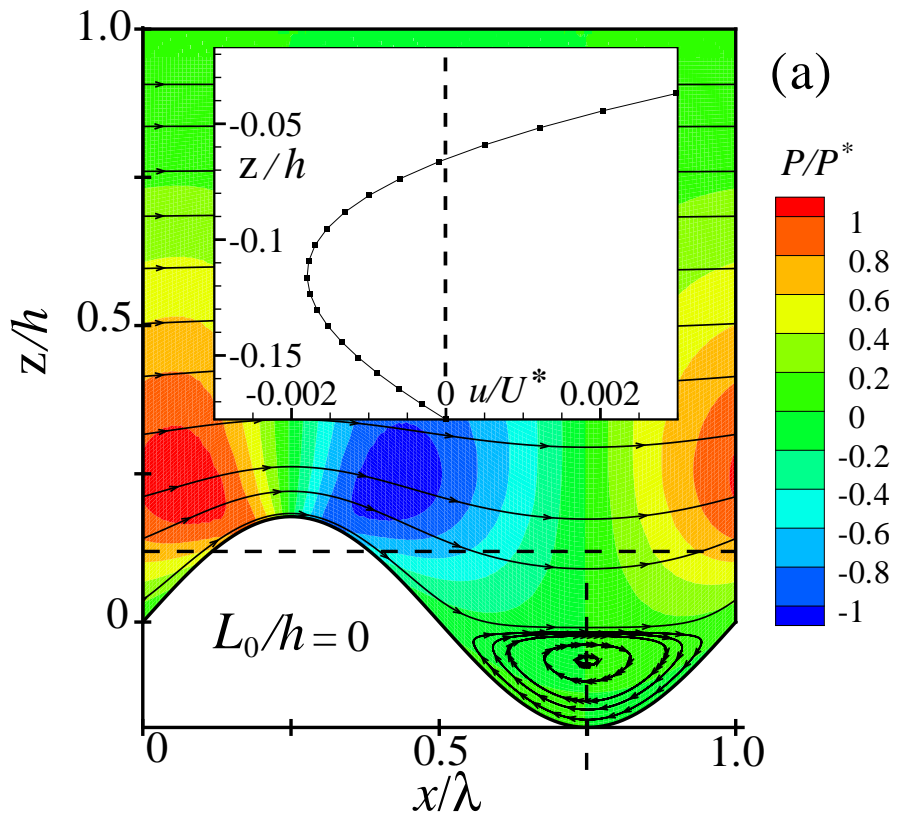


Figure 4.6. Pressure contours and streamlines for the wavenumber  $ka = 1.12$  and the slip length at the lower wall  $L_0 = 0$  (a),  $L_0/h = 0.03$  (b),  $L_0/h = 0.06$  (c), and  $L_0/h = 0.08$  (d). The pressure contours are normalized by the maximum value  $P^*$  located on the left side of the peak  $(x/\lambda, z/\lambda) \simeq (0.07, 0.23)$  in the case of  $L_0 = 0$ . The horizontal dashed line denotes the location of the effective no-slip boundary plane. The vertical dashed line inside the valley at  $x/\lambda = 0.75$  indicates the cross-section used to compute the velocity profiles shown in the inset.

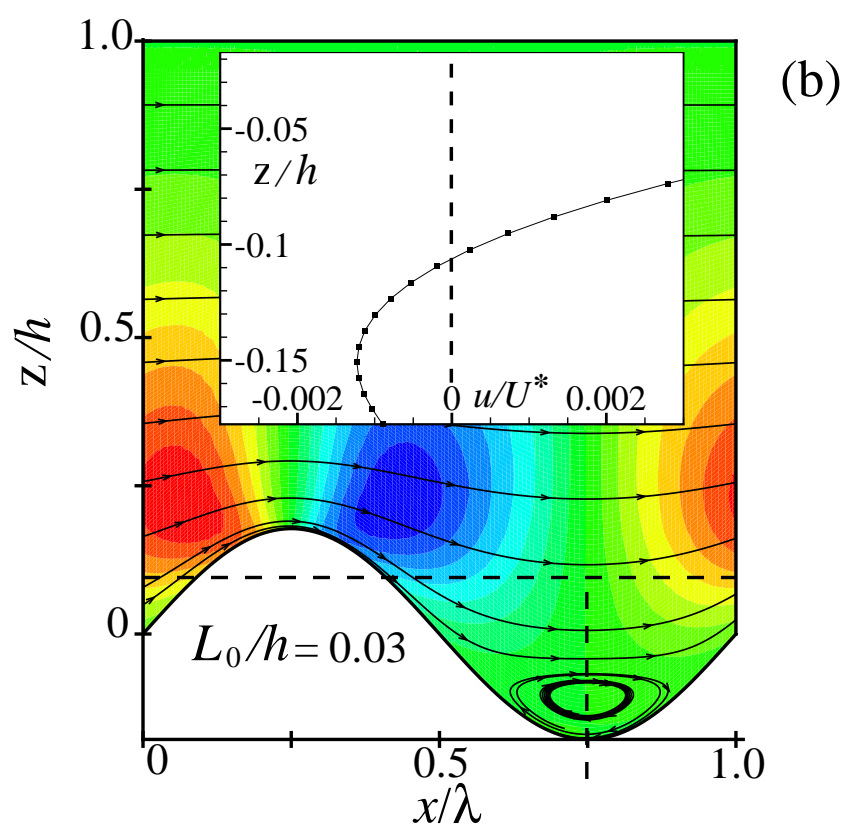


Figure 4.6. continued.

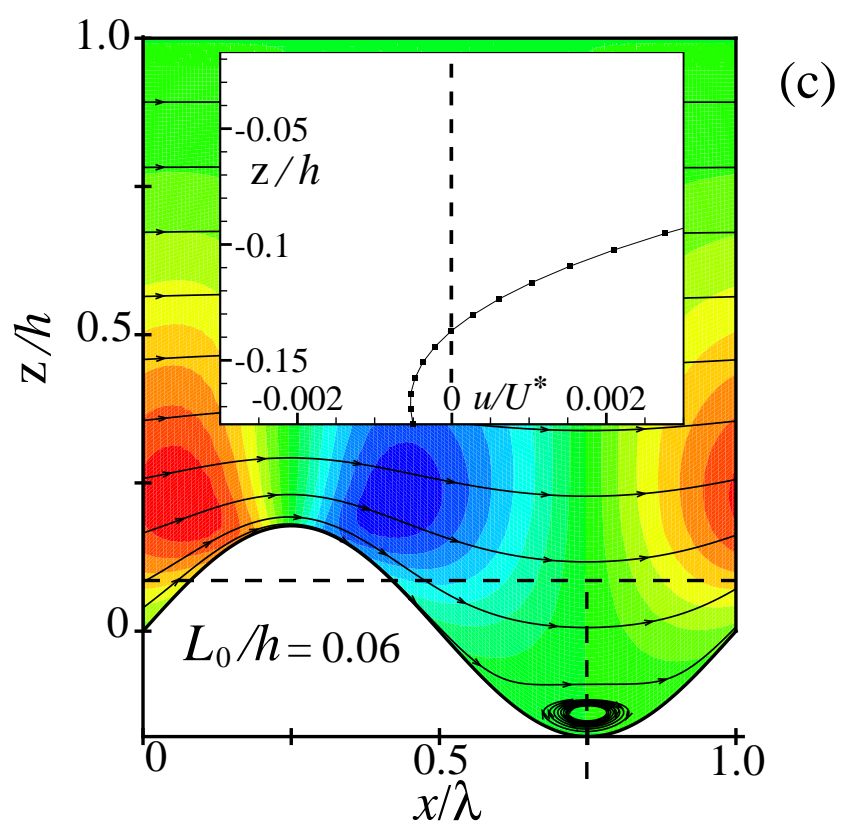


Figure 4.6. continued.

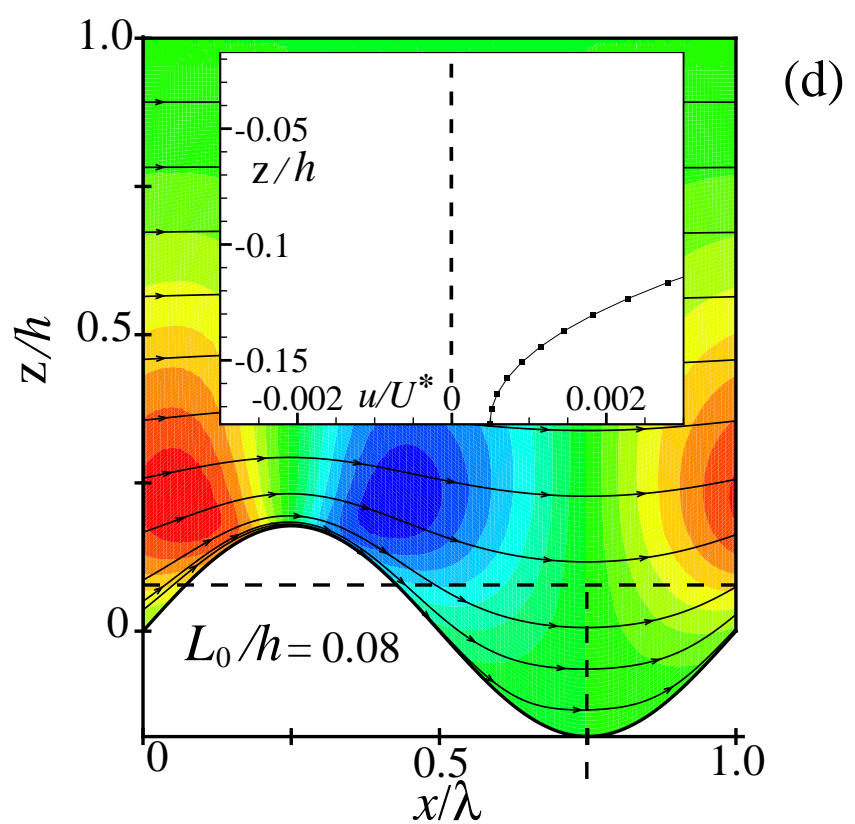


Figure 4.6. continued.

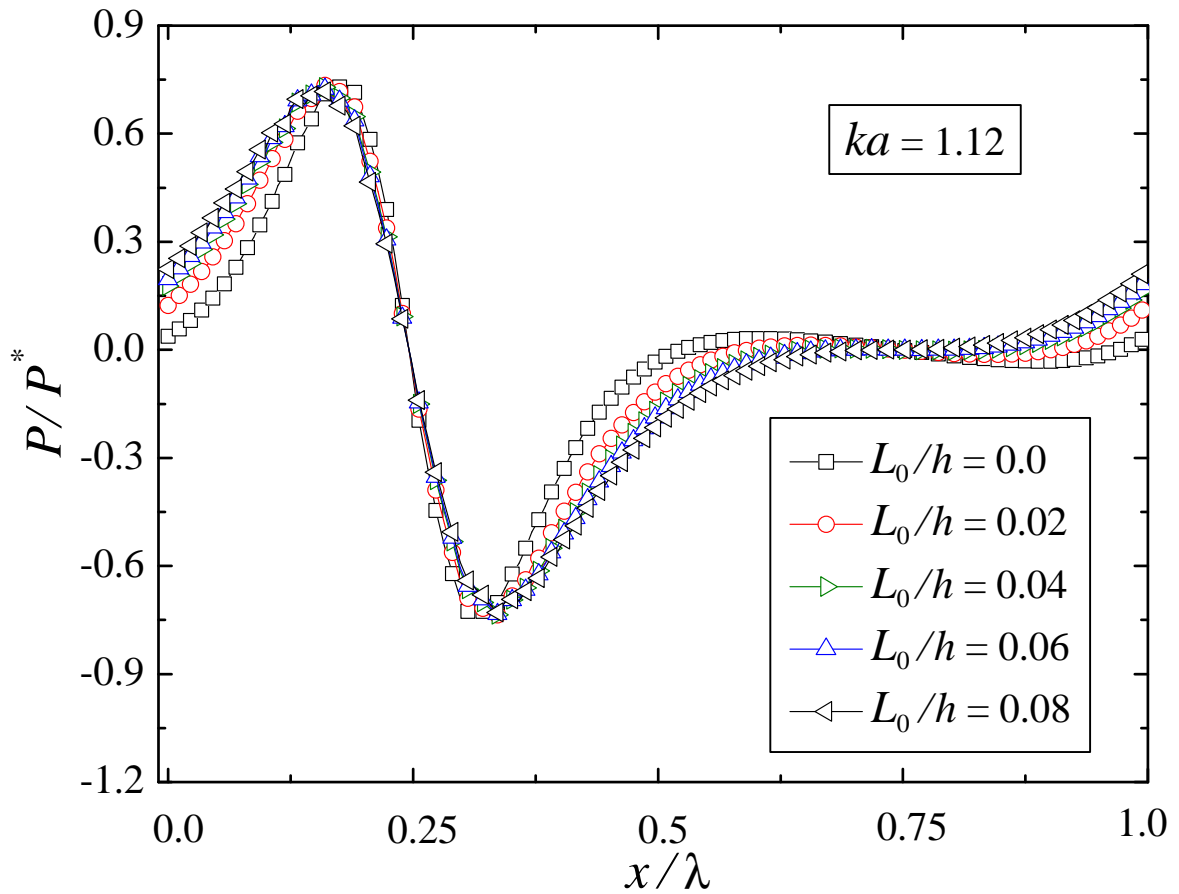


Figure 4.7. Normalized pressure along the lower wavy wall extracted from the solution of the Stokes equation for the tabulated values of  $L_0$  and  $ka = 1.12$ . The maximum pressure  $P^*$  for  $L_0 = 0$  is located above the lower surface at  $(x/\lambda, z/\lambda) \simeq (0.07, 0.23)$ .

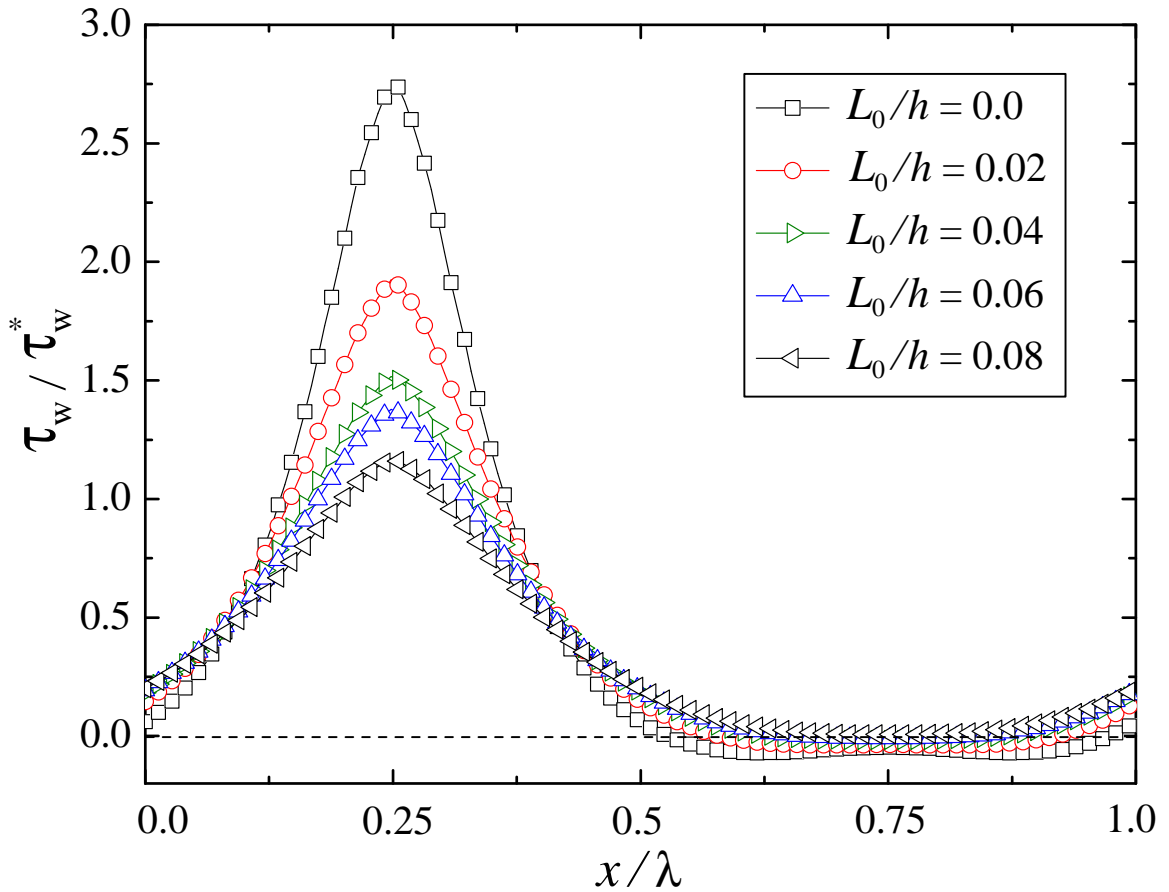


Figure 4.8. Shear stress along the corrugated lower wall ( $ka = 1.12$ ) for the indicated values of the local slip length  $L_0$ . The intersection of the dashed line with the shear stress profiles shows the location of the flow separation and attachment inside the valley.

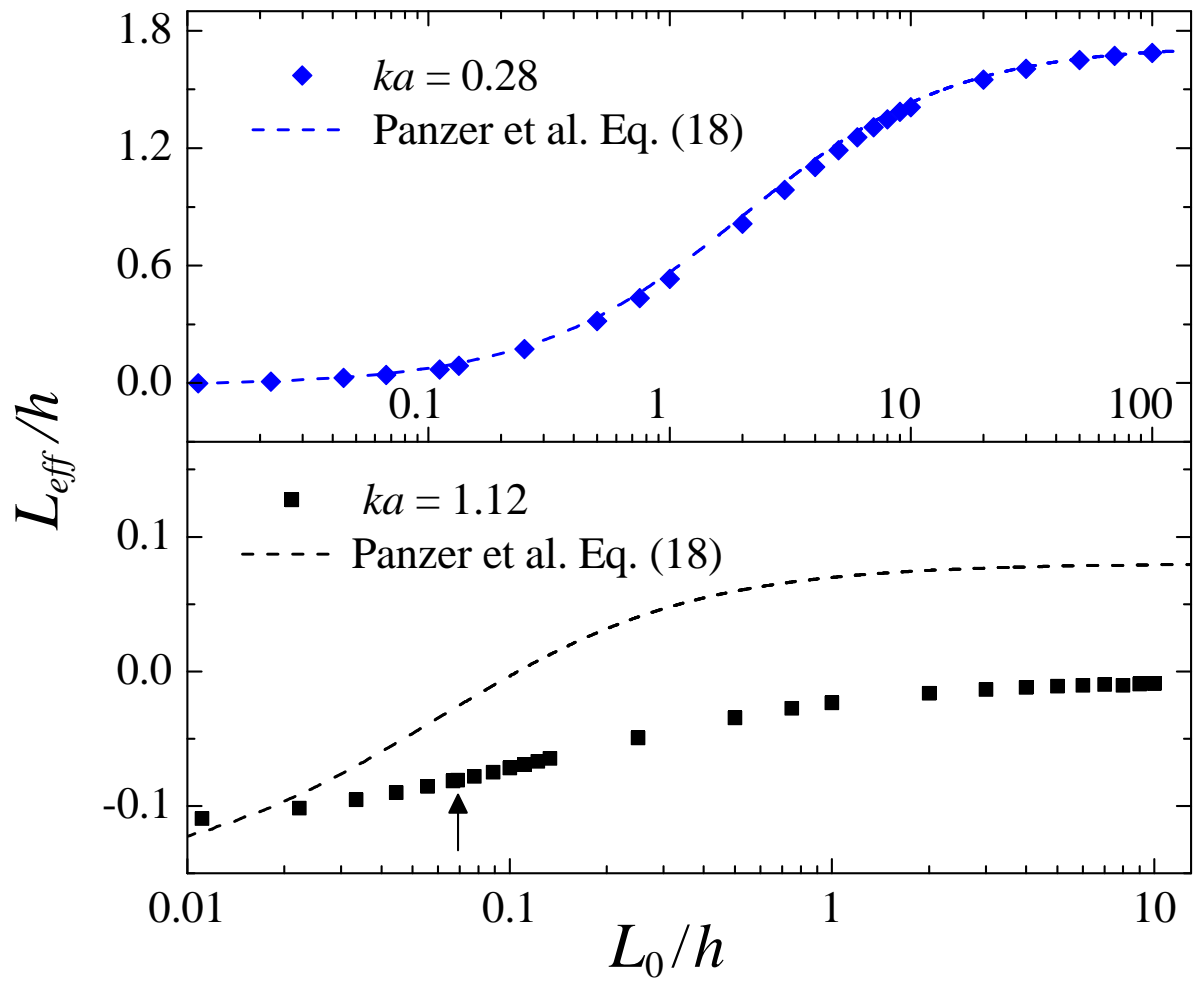


Figure 4.9. The effective slip length, extracted from the Stokes solution as a function of  $L_0$  for  $ka = 0.28$  (top) and  $ka = 1.12$  (bottom). The dashed line is computed from Eq. (4.18). For  $ka = 1.12$  and  $L_0/h \leq 0.067$ , the vortex is formed in the valley (see the vertical arrow at  $L_0/h = 0.067$ ). The error bars are smaller than the symbol size.

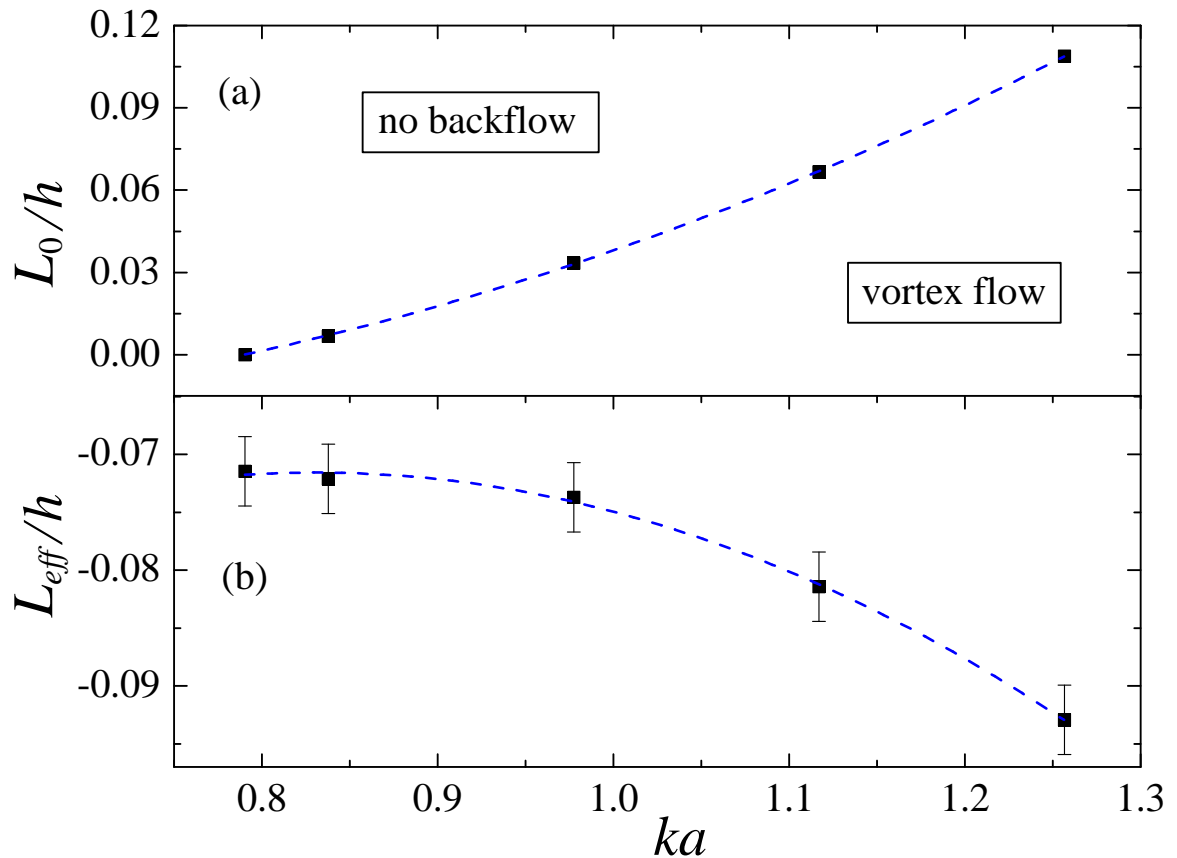


Figure 4.10. The intrinsic slip length  $L_0$  above which there is no vortex at the bottom of the valley (top) and the corresponding effective slip length  $L_{eff}$  (bottom) computed from the Stokes solution and plotted as a function of wavenumber  $ka$ . The increment in the slip length used to determine the threshold values is about the symbol size (top). The dashed lines are quadratic fits to guide the eye.

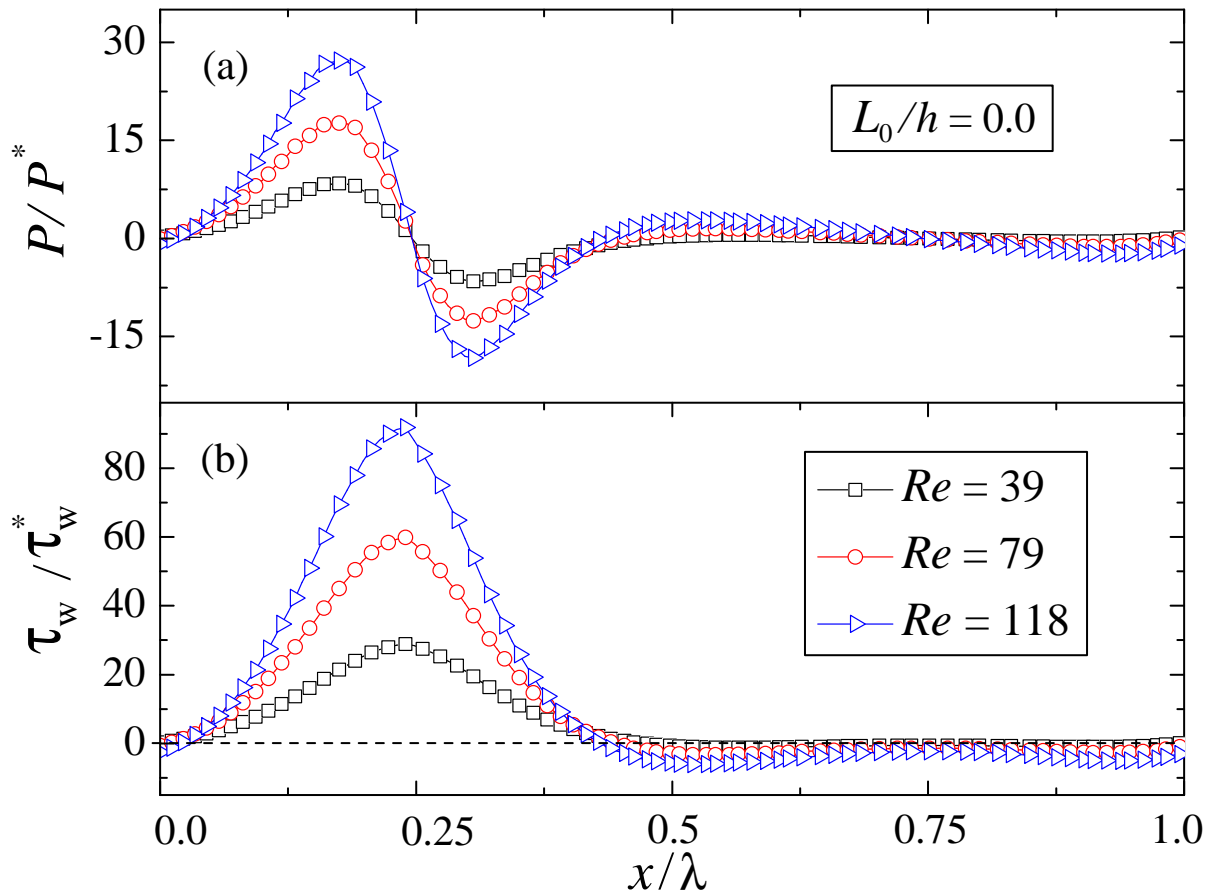


Figure 4.11. The normalized pressure (top) and shear stress (bottom) along the lower wavy wall as a function of the Reynolds number for  $ka = 1.12$  and no-slip boundary conditions. The value  $P^*$  is the maximum pressure located above the lower boundary on the left side of the peak ( $x/\lambda, z/\lambda \simeq (0.07, 0.23)$  for  $L_0 = 0$  and  $Re = 4.0$ ).

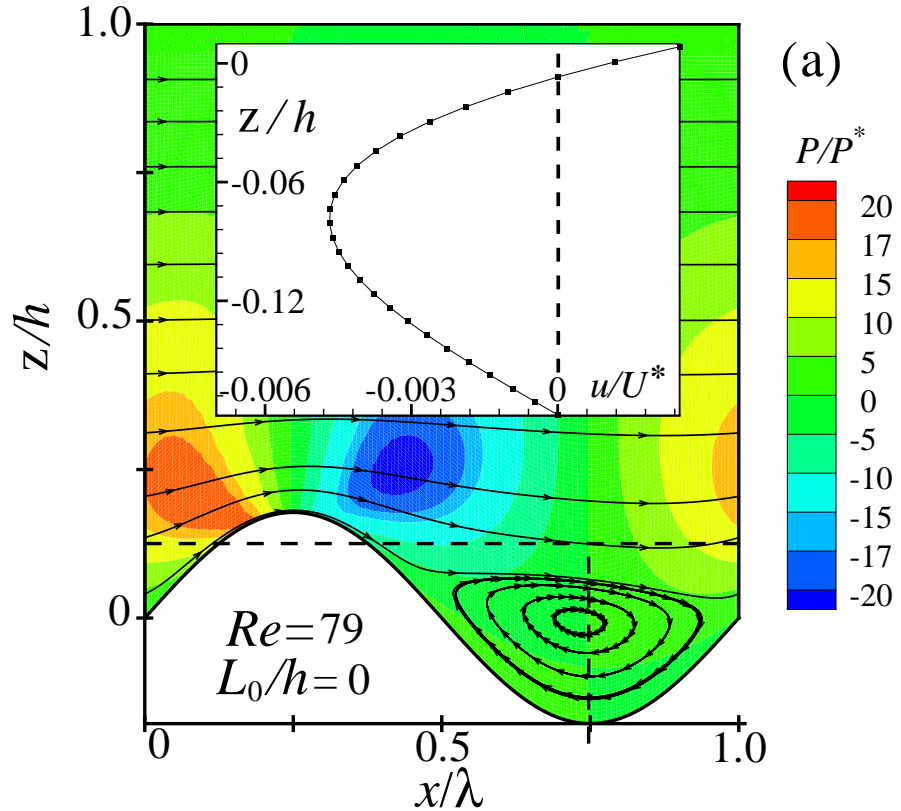


Figure 4.12. Pressure contours and streamlines extracted from the solution of the Navier-Stokes equation for  $ka = 1.12$  and  $L_0 = 0$  (a) and  $L_0/h = 0.25$  (b). The value  $P^*$  is the maximum pressure located at  $(x/\lambda, z/\lambda) \simeq (0.07, 0.23)$  for  $ka = 1.12$ ,  $L_0 = 0$ , and  $Re = 4.0$ . The horizontal dashed line denotes the effective no-slip boundary plane. The vertical dashed line inside the valley indicates the cross-section used to compute the velocity profiles shown in the inset.

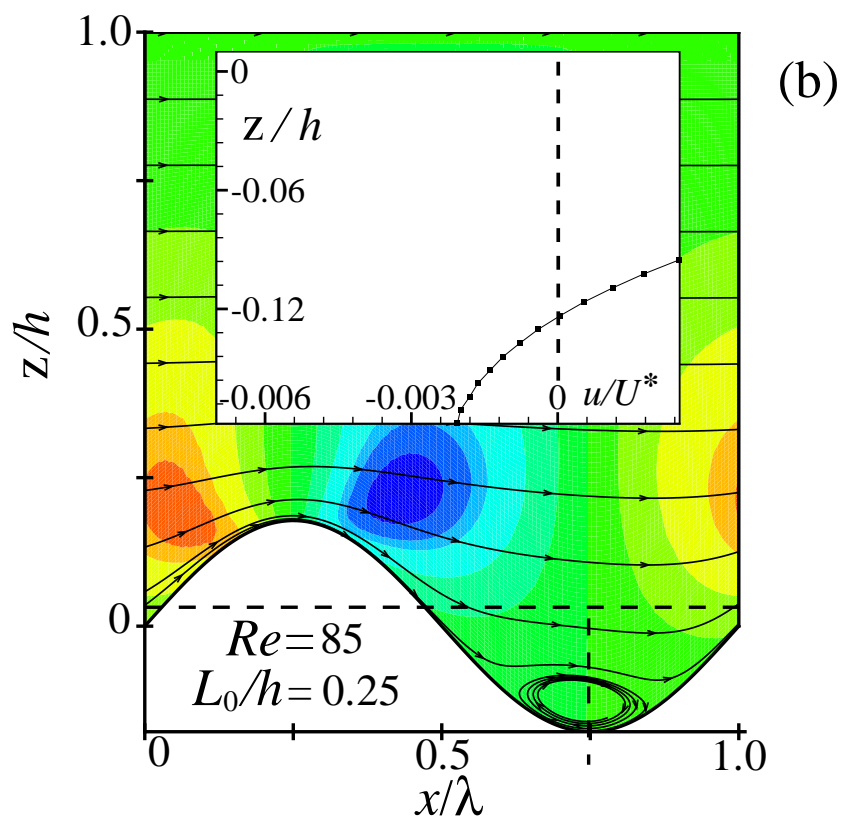


Figure 4.12. continued.

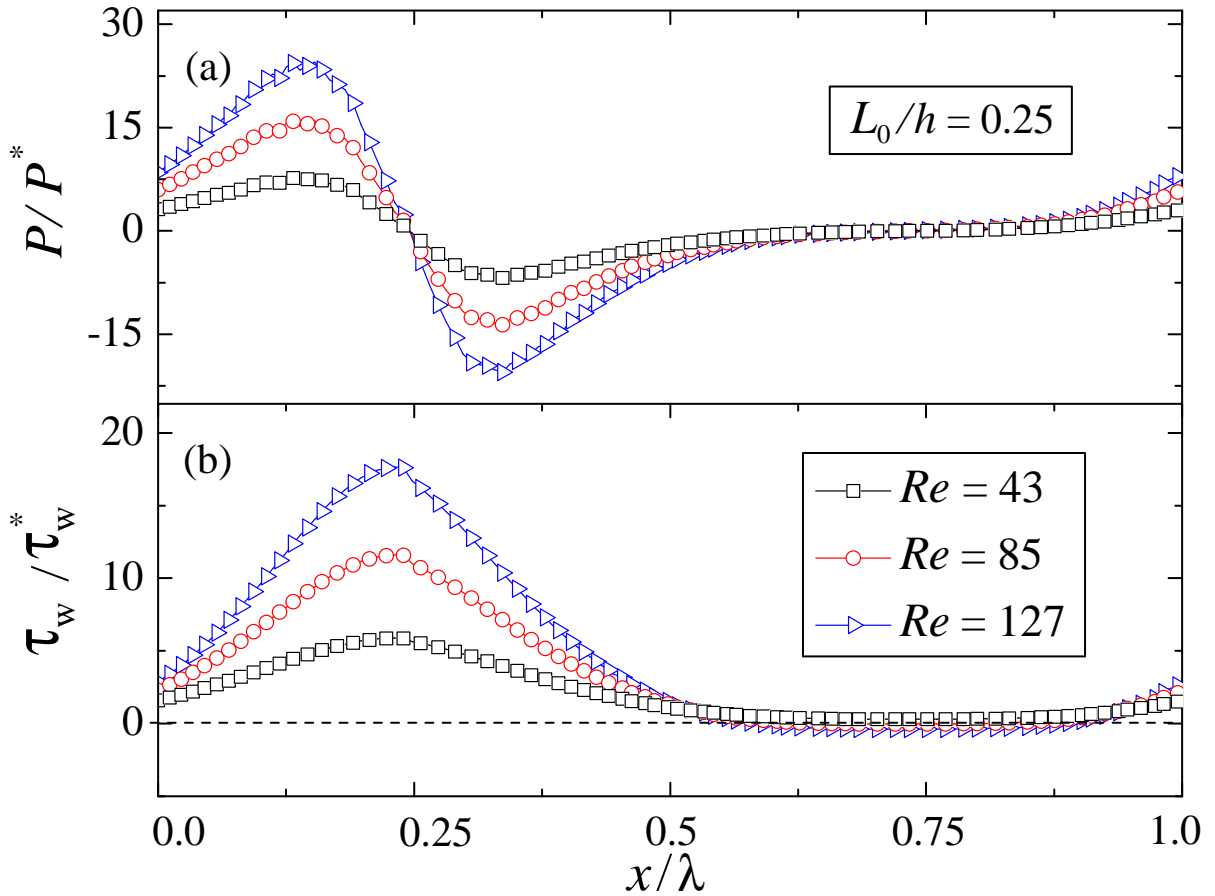


Figure 4.13. The normalized pressure (top) and shear stress (bottom) along the lower wavy wall as a function of the Reynolds number for  $ka = 1.12$  and  $L_0/h = 0.25$ . The normalization value  $P^*$  is the maximum pressure located above the surface on the left side of the peak  $(x/\lambda, z/\lambda) \simeq (0.07, 0.23)$  for  $L_0 = 0$  and  $Re = 4.0$ .

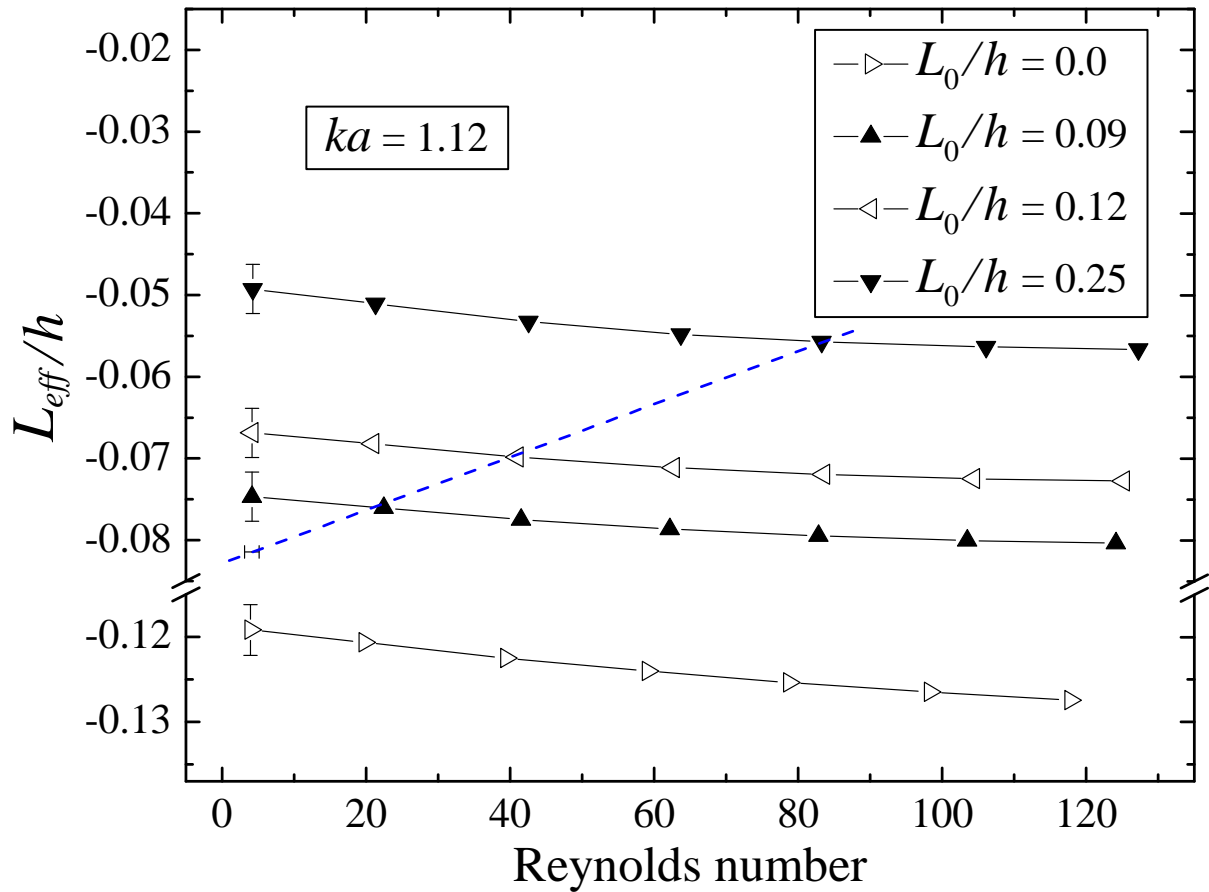


Figure 4.14. The effective slip length computed from the solution of the Navier-Stokes equation as a function of the Reynolds number for  $ka = 1.12$  and  $L_0 = 0$  ( $\diamond$ ),  $L_0/h = 0.09$  ( $\blacktriangle$ ),  $L_0/h = 0.12$  ( $\triangleleft$ ), and  $L_0/h = 0.25$  ( $\blacktriangledown$ ). The dashed line indicates the upper bound of the region where a vortex is present in the groove of a rough surface. The error bars associated with the threshold values of the Reynolds number are about the symbol size.

# CHAPTER 5

## Modeling the combined effect of surface roughness and shear rate on slip flow of simple fluids

### 5.1 Introduction

An adequate description of fluid flow over a solid boundary with surface roughness on multiple length scales often requires resolution of fine microscopic details of the flow structure while retaining peculiarities of a macroscopic picture [115]. The most popular and practically important example is the problem of transport through heterogeneous porous media, which is an inherently multiscale system [116]. Modeling fluid flow at multiple scales is a nontrivial problem itself; however, it becomes much more difficult if one also needs to incorporate slip boundary conditions into equations of motion. Typically, a local slip appears if the wall-fluid interaction is sufficiently low, but the value of slip length (an extrapolated distance of the velocity profile to zero) generally depends not only on the surface energy and structure [5, 117, 10, 13, 14] but on shear rate as well [17, 10, 118, 19, 119]. Therefore, a correct form of the Navier-Stokes equation can be obtained only if the combined effect of surface roughness and shear rate on the slip length is taken properly into account. It is intuitively clear that the surface roughness and shear rate have an opposite impact on the slip length. A precise evaluation of relative contributions of these two factors is the subject

of the present study.

The boundary conditions for the flow of monatomic fluids over atomically flat surfaces can be described in terms of the *intrinsic* slip length, which is defined as the ratio of the shear viscosity to the friction coefficient at the liquid/solid interface. The friction is determined by the strength of the interaction potential and molecular-scale corrugations of the crystalline wall. Recent MD studies [120, 20, 21, 23, 25, 121, 28, 40, 29, 37] have reported values of the intrinsic slip length up to about a hundred molecular diameters for weak wall-fluid interaction energies. It is well established that the formation of commensurate structures of liquid and solid phases at the interface leads to stick boundary conditions [21, 28]. The slip length decreases with increasing bulk pressure in the flow of nonwetting simple fluids over a smooth substrate [25]. The MD simulations have also demonstrated that, depending on the wall-fluid interaction energy and the ratio of wall and fluid densities, the slip length is either relatively small (below a couple of molecular diameters) and shear-rate-independent [21] or larger than several molecular diameters and increases with shear rate [23, 29]. Although several functional forms for the rate-dependent intrinsic slip length have been suggested for monatomic fluids [23, 122, 29, 37], as well as for polymer melts [27, 32, 93, 123, 124], the rate-dependent boundary conditions were not used for modeling slip flows in complex geometries.

In contrast to the description of the flow over smooth boundaries (with microscopic surface roughness) by the intrinsic slip length, it is more appropriate to characterize the flow away from macroscopically rough surfaces by the *effective* slip length, which is usually defined with respect to the location of the mean roughness height. Recently, we investigated the behavior of the effective slip length in laminar flow over periodically corrugated surfaces for simple fluids [35] and polymer melts [93]. Both MD and continuum simulations have shown that the effective slip length decreases with increasing amplitude of the surface roughness. In the continuum analysis, the local (rate-independent) slip length is modified by the presence of boundary curvature [51, 52] and, therefore, becomes position-dependent along the wavy wall. A direct comparison between MD and continuum simulations at low shear rates demonstrated that there is an excellent agreement between the effective slip lengths for large wavelengths (above approximately 30 molecular diameters) and small wavenumbers

$ka \lesssim 0.3$  [35, 93]. In the present chapter, the analysis of the flow over a periodically corrugated surface is extended to higher shear rates and to the situation where the local slip length at the curved boundary is a function of both the radius of curvature and shear rate.

In the last decade, a number of studies have focused on the development of the hybrid continuum-atomistic methods to simulate fluid flows near smooth solid boundaries [125, 126], rough walls [127], superhydrophobic surfaces [128], corner flows [129], and flows near a moving contact line [130, 131]. In multiscale algorithms, the time and length scales accessible in molecular simulations are considerably extended by employing the continuum method in the bulk region and applying the MD technique only near the interfaces. The two methods are coupled via constrained dynamics in an overlap region by matching mass, momentum and energy fluxes or velocity fields. The full MD simulations are then performed to validate the hybrid scheme. The drawback of the hybrid methods, however, is the cumbersome procedure for coupling of the two methods in the overlap region. The approach pursued in the present chapter is different from that in the hybrid schemes. We first compute by MD simulations the intrinsic slip length as a function of shear rate in the flow over an atomically smooth surface. The Navier-Stokes equation is then solved numerically (in the whole computational domain) for the flow over a rough surface with the rate-dependent intrinsic slip length used as a local boundary condition. We found that the full MD simulations recover the continuum results at low and intermediate shear rates and small-scale surface roughness.

In this chapter, the dynamic behavior of the effective slip length is investigated in steady shear flow over a periodically corrugated surface using molecular dynamics and continuum simulations. Both methods show that the effective slip length is nearly constant at low shear rates and it gradually increases at higher shear rates. The slight discrepancy between the effective slip lengths obtained from MD and continuum simulations at high shear rates is analyzed by examination of the local velocity and density profiles, as well as pressure and temperature distributions along the wavy surface. It is also shown by MD simulations that the singular behavior of the intrinsic slip length (in a flow over a smooth wall) at high shear rates is suppressed by the surface roughness.

The rest of this chapter is organized as follows. The details of molecular dynamics and continuum simulations are described in the next section. The shear rate dependence of the intrinsic and effective slip lengths and the results of the comparative analysis are presented in Sec. 5.3. The results are briefly summarized in the last section.

## 5.2 The details of numerical methods

### 5.2.1 Molecular dynamics simulations

The system geometry and the definition of the effective slip length are illustrated in Fig. 5.1. The total number of fluid monomers in the cell is fixed to  $N_f = 16\,104$ . The fluid monomers interact through the truncated pairwise Lennard-Jones (LJ) potential

$$V_{LJ}(r) = 4\varepsilon \left[ \left( \frac{\sigma}{r} \right)^{12} - \left( \frac{\sigma}{r} \right)^6 \right], \quad (5.1)$$

where  $\varepsilon$  is the energy scale and  $\sigma$  is the length scale of the fluid phase. The cutoff radius for the LJ potential is set to  $r_c = 2.5\sigma$  for both fluid/fluid and wall/fluid interactions. The size of the wall atoms is the same as fluid monomers. Wall atoms are fixed at the lattice sites and do not interact with each other.

The motion of the fluid monomers was weakly coupled to a thermal reservoir via the Langevin thermostat [54]. To avoid bias in the shear flow direction, the random force and friction terms were added to the equations of motion in the  $\hat{y}$  direction, perpendicular to the plane of shear [21]. The equations of motion for fluid monomers in all three directions are as follows:

$$m\ddot{x}_i = - \sum_{i \neq j} \frac{\partial V_{ij}}{\partial x_i}, \quad (5.2)$$

$$m\ddot{y}_i + m\Gamma\dot{y}_i = - \sum_{i \neq j} \frac{\partial V_{ij}}{\partial y_i} + f_i, \quad (5.3)$$

$$m\ddot{z}_i = - \sum_{i \neq j} \frac{\partial V_{ij}}{\partial z_i}, \quad (5.4)$$

where  $\Gamma = 1.0\tau^{-1}$  is a friction coefficient that regulates the rate of heat flux between the fluid and the heat bath, and  $f_i(t)$  is the random force with zero mean and variance  $2m\Gamma k_B T\delta(t)$

determined from the fluctuation-dissipation relation. Unless otherwise specified, the temperature of the Langevin thermostat is set to  $T = 1.1 \varepsilon/k_B$ , where  $k_B$  is the Boltzmann constant. The equations of motion were integrated using the Verlet algorithm [56] with a time step  $\Delta t = 0.002 \tau$ , where  $\tau = \sqrt{m\sigma^2/\varepsilon}$  is the characteristic time of the LJ potential.

The intrinsic slip length was computed at the lower flat wall composed out of two layers of the *FCC* lattice with density  $\rho_w = 3.1 \sigma^{-3}$  and nearest-neighbor distance  $d = 0.77 \sigma$  between atoms in the  $xy$  plane. The partial slip is permitted along the lower boundary due to relatively low wall-fluid interaction energy  $\varepsilon_{wf} = 0.5 \varepsilon$ . The no-slip boundary condition is enforced at the flat upper wall with a lower density  $0.67 \sigma^{-3}$  by allowing the formation of commensurate structures of liquid and solid phases at the interface. The nearest-neighbor distance between wall atoms is  $1.28 \sigma$  in the (111) plane of the *FCC* lattice. The wall-fluid interaction energy  $\varepsilon$  ensures the no-slip condition at the upper wall holds even at high shear rates. The cell dimensions are set to  $L_x = 42.34 \sigma$  and  $L_y = 10.0 \sigma$  parallel to the confining walls. The MD simulations were performed at a constant fluid density ( $\rho = 0.81 \sigma^{-3}$ ) ensemble, i.e., the relative distance between the walls was always fixed to  $L_z = 41.41 \sigma$  in the  $\hat{z}$  direction. Periodic boundary conditions were applied along the  $\hat{x}$  and  $\hat{y}$  directions.

The effect of surface roughness on slip flow was investigated in the cell with a lower sinusoidal wall with wavelength  $\lambda = L_x$  and amplitude  $a = 1.82 \sigma$  (see Fig. 5.1). Special care was taken to make the lower corrugated wall with a uniform density  $\rho_w = 3.1 \sigma^{-3}$  (by including additional rows of atoms along the  $\hat{y}$  direction) so that the lattice spacing along the sinusoidal curve remained  $d = 0.77 \sigma$ .

The fluid monomer velocities were initialized using the Maxwell-Boltzmann probability distribution at the temperature  $T = 1.1 \varepsilon/k_B$ . After an equilibration period of about  $2 \times 10^4 \tau$ , the velocity and density profiles across the channel were averaged for about  $2 \times 10^5 \tau$  within bins of  $L_x \times L_y \times \Delta z$ , where  $\Delta z = 0.01 \sigma$ . The location and dimensions of the averaging regions for the computation of the local velocity and density profiles will be specified in Sec. 5.3.3.

### 5.2.2 Continuum simulations

The two-dimensional, steady-state and incompressible Navier-Stokes (NS) equation is solved numerically using the finite element method. The equation of motion based on these assumptions is written as follows:

$$\rho \mathbf{u} \cdot \nabla \mathbf{u} = -\nabla p + \mu \nabla^2 \mathbf{u}, \quad (5.5)$$

where  $\mathbf{u} = u \hat{i} + v \hat{j}$  is the velocity vector,  $\rho$  is the density of the fluid, and  $p$  and  $\mu$  are the pressure field and fluid viscosity, respectively.

The penalty formulation was implemented for the incompressible solution to avoid decoupling of the velocity and pressure terms [57]. In the penalty formulation, the continuity equation,  $\nabla \cdot \mathbf{u} = 0$ , is replaced with a perturbed equation

$$\nabla \cdot \mathbf{u} = -\frac{p}{\Lambda}, \quad (5.6)$$

where  $\Lambda$  is the penalty parameter, which enforces the incompressibility condition. For most practical situations, where computation is performed with double-precision 64 bit words, a penalty parameter ( $\Lambda$ ) between  $10^7$  and  $10^9$  is sufficient to conserve the accuracy [57]. After substitution of the pressure term in Eq. (5.6) into Eq. (5.5), the modified momentum equation can be rewritten as follows:

$$\rho \mathbf{u} \cdot \nabla \mathbf{u} = \Lambda \nabla (\nabla \cdot \mathbf{u}) + \mu \nabla^2 \mathbf{u}. \quad (5.7)$$

The Galerkin method with rectangular bilinear isoparametric elements is used to integrate the Navier-Stokes equation [57, 132].

The boundary conditions are applied at the inlet, outlet, and upper and lower walls. The periodic boundary conditions are implemented along the  $\hat{x}$  direction for the inlet and outlet. The boundary condition at the upper wall is always no-slip. A partial slip boundary condition is applied at the lower wall. In addition to the global coordinate system  $(\hat{x}, \hat{z})$ , a local coordinate system  $(\vec{t}, \vec{n})$  is defined along the lower curved boundary with unit vectors  $\vec{t}$  and  $\vec{n}$  representing the tangential and normal directions, respectively. The tangential component of the fluid velocity in the local coordinate system can be computed as

$$u_t = L_0[(\vec{n} \cdot \nabla) u_t + u_t/R], \quad (5.8)$$

where  $R$  is the local radius of curvature and  $L_0$  is the *intrinsic* slip length at the flat liquid/solid interface [52]. The radius of curvature  $R$  is positive and negative for concave and convex regions, respectively. The second-order forward-differencing scheme was used to compute accurately the normal derivative of the tangential velocity  $(\vec{n} \cdot \nabla) u_t$  at the lower boundary.

At the beginning of the simulation procedure, the boundary conditions at the upper and lower walls are set to no-slip. Then, the equations of motion are solved implicitly and the tangential velocities at the lower boundary are updated according to Eq. (5.8). In the next step, the updated velocities at the lower boundary are used as a new boundary condition and the equations of motion are solved again. The iterative process is repeated until a desired accuracy is achieved. The convergence rate of the solution was controlled by applying an under-relaxation factor of 0.001 for the boundary nodes. For all results reported in the present chapter, the continuum simulations were performed with  $150 \times 150$  grid resolution. However, the accuracy of the results was also checked by performing a set of simulations using a finer grid  $180 \times 180$ . The maximum error in the effective slip length due to the grid resolution is  $L_{\text{eff}}/L_z = 0.003$ . The same error bars were reported in the previous study of laminar flow over a periodically corrugated surface with either no-slip or (rate-independent) slip boundary conditions [132].

The averaged error of the solution is defined as

$$\text{error} = \left[ \sum_{i=1}^{N_p} \frac{|\mathbf{u}_i^n - \mathbf{u}_i^{n+1}|}{|\mathbf{u}_i^{n+1}|} \right] / N_p, \quad (5.9)$$

where  $N_p$  is the number of nodes in the computational domain,  $\mathbf{u}_i^n$  is the magnitude of the velocity at node  $i$  and time step  $n$ , and  $\mathbf{u}_i^{n+1}$  is the magnitude of the velocity in the next time step. The solution is converged when  $\text{error} \leq 10^{-9}$  and the tangential velocities along the lower boundary satisfy  $u_t = L_{\text{local}} \frac{\partial u_t}{\partial n}$ , where the local slip length is  $L_{\text{local}} = (L_0^{-1} - R^{-1})^{-1}$  [52].

## 5.3 Results

### 5.3.1 MD simulations: the intrinsic and effective slip lengths

We first consider flow in the cell with flat upper and lower walls. The averaged velocity profiles are plotted in Fig. 5.2 for the selected upper wall speeds. The profiles are linear throughout the channel except for a slight curvature near the lower wall at  $U = 5.0 \sigma/\tau$ . Note that with increasing upper wall speed, the slip velocity at the lower wall increases monotonically up to about  $2\sigma/\tau$  at  $U = 5.0 \sigma/\tau$ . The flow velocity at the top boundary remains equal to the upper wall speed due to the commensurability of liquid and solid structures at the interface and sufficiently high wall-fluid interaction energy. The shear rate was estimated from the linear slope of the velocity profiles across the entire cell.

The fluid viscosity computed from the Kirkwood relation [58] is plotted in Fig. 5.3 as a function of shear rate in the cell with flat walls. In agreement with the results of previous MD studies on shear flow of simple fluids [23, 29, 37], the shear viscosity  $\mu = 2.15 \pm 0.15 \varepsilon \tau \sigma^{-3}$  remains rate-independent up to  $\dot{\gamma}\tau \simeq 0.072$ , which corresponds to the upper wall speed  $U = 5.375 \sigma/\tau$ . It is also known that at high shear rates the fluid temperature profiles become nonuniform across the cell and the heating up is larger near the interfaces [29, 37, 32]. To ensure that the fluid viscosity is not affected by the heating up, we performed two additional sets of simulations at the upper wall speeds  $U = 1.0 \sigma/\tau$  and  $U = 3.5 \sigma/\tau$  and increased the temperature of the Langevin thermostat with an increment of  $0.05 \varepsilon/k_B$ . In the range of the thermostat temperatures and error bars reported in Fig. 5.3, the shear viscosity is independent of temperature for both upper wall speeds. In Sec. 5.3.3, the results of simulations performed at higher temperatures will be used to estimate the effect of pressure on the slip length.

The intrinsic slip length  $L_0$  in the flow over a flat lower wall was determined from the linear extrapolation of velocity profiles to zero with respect to the reference plane located  $0.5\sigma$  above the *FCC* lattice plane. The variation of the intrinsic slip length as a function of shear rate is presented in Fig. 5.4. At low shear rates  $\dot{\gamma}\tau \lesssim 0.005$ , the slip length is nearly constant. The leftmost data point reported in Fig. 5.4 is  $\dot{\gamma}\tau \simeq 1.7 \times 10^{-4}$  at the upper wall speed  $U = 0.01 \sigma/\tau$ . At higher shear rates, the intrinsic slip length first gradually increases

and then grows rapidly as it approaches  $\dot{\gamma}\tau \simeq 0.072$  when  $U = 5.375\sigma/\tau$ . The behavior of the slip length in the flow over a flat wall can not be well described by the power law function suggested in Ref. [23]. Instead, a ninth-order polynomial function was used to fit the data (see the blue curve in Fig. 5.4). In the continuum analysis presented in the next section, the polynomial function will be used as a local (rate-dependent) boundary condition, Eq. (5.8), for the flow over a periodically corrugated wall.

When the upper wall speed becomes greater than  $U = 5.375\sigma/\tau$ , the rate-dependence of the intrinsic slip length passes through a turning point at the maximum shear rate  $\dot{\gamma}\tau \simeq 0.072$ , and the slip length increases ( $L_0 \gg L_z$ ) while the shear rate decreases, leading to a negative slope of the rate-dependent curve (not shown). In this regime the slip velocity at the lower flat wall is greater than the fluid thermal velocity  $v_T^2 = k_B T/m$ . The behavior of the intrinsic slip length at very large slip velocities was not considered further in the present study.

Next, the influence of surface roughness on the effective slip length is investigated in the flow over the lower corrugated wall with wavenumber  $ka = 2\pi a/\lambda = 0.27$ . The velocity profiles, averaged over the period of corrugation  $\lambda = L_x$ , are linear in the bulk of the film and curved near the lower wall within about  $2a$  from the bottom of the valley (e.g., see [93, 132]). Therefore, the effective slip length and shear rate were extracted from a linear fit to the velocity profiles inside the bulk region  $10 \leq z/\sigma \leq 30$ . The effective slip length as a function of shear rate is also plotted in Fig. 5.4. Both the magnitude and slope of the rate-dependence of the effective slip length are reduced in comparison with the results for the flat wall. Following the rate-independent regime at  $\dot{\gamma}\tau \lesssim 0.01$ , the effective slip length increases monotonically up to a maximum value  $L_{\text{eff}}(0.14\tau^{-1}) \simeq 16.6\sigma$  at  $U = 8.0\sigma/\tau$ .

At higher shear rates  $\dot{\gamma}\tau \gtrsim 0.14$ , the effective slip length starts to decrease with further increase in shear rate (see Fig. 5.4). We found, however, that the fluid temperature (density) becomes anomalously high (low) on the right side of the corrugation peak. For example, the fluid temperature in the region  $0.5 \lesssim x/\lambda \lesssim 0.9$  varies up to  $Tk_B/\varepsilon \simeq 1.6 - 1.85$  at  $U = 12.0\sigma/\tau$  (the rightmost point in Fig. 5.4). Also, the amplitude of the characteristic density oscillations normal to the curved boundary at  $x/\lambda \simeq 0.43$  is reduced by about 40% at  $U = 12.0\sigma/\tau$  in comparison with the fluid layering at equilibrium conditions (not shown).

In the next section, the comparison between the effective slip lengths estimated from MD and continuum simulations is studied at shear rates  $\dot{\gamma}\tau \lesssim 0.14$ .

### 5.3.2 Comparison between MD and continuum simulations

In this section, we describe the behavior of the rate-dependent effective slip length computed from the solution of the Navier-Stokes equation. All variables in continuum simulations are normalized by the LJ length  $\sigma$ , time  $\tau$ , and energy  $\varepsilon$  scales. The system is designed to mimic the MD setup. All nondimensional parameters in continuum simulations are marked by the ( $\sim$ ) sign. The cell dimensions are set to  $\tilde{L}_x = 42.34$  and  $\tilde{L}_z = 40.41$  in the  $\hat{x}$  and  $\hat{z}$  directions, respectively. Similar to the MD setup, the wavenumber of the lower corrugated wall is fixed to  $ka = 0.27$ . This value was chosen based on the previous analysis of the effective slip length in laminar flow of simple [35] and polymeric [93] fluids over a rough surface. It was shown [35] that at low shear rates there is an excellent agreement between the effective slip lengths extracted from MD and continuum simulations when a local (rate-independent) intrinsic slip length is used as a boundary condition along the wavy wall with  $\lambda \gtrsim 30\sigma$  and  $ka \lesssim 0.3$ .

It is important to emphasize that in continuum simulations the intrinsic slip length in Eq. (5.8) is a function of the total shear rate at the curved boundary. The total shear rate is computed as a sum of the normal derivative of the tangential velocity  $\partial u_t / \partial n$  and the ratio of the slip velocity to the radius of curvature  $u_t/R$ . The effective slip length is extracted from a linear part of the velocity profiles in the bulk region  $10 \leq \tilde{z} \leq 30$ .

Figure 5.4 shows the effective slip length extracted from the continuum solution with the local rate-dependent intrinsic slip length at the lower corrugated boundary. The upper wall speed is varied in the range  $0.025 \leq \tilde{U} \leq 6$ . As expected, the effective slip length obtained from the continuum simulations agrees well with the MD results at low shear rates  $\dot{\gamma}\tau \lesssim 0.01$  where  $L_0$  is nearly constant. With increasing shear rate up to  $\dot{\gamma}\tau \lesssim 0.1$ , the effective slip length increases monotonically. There is an excellent agreement between the two methods at intermediate shear rates  $0.01 \lesssim \dot{\gamma}\tau \lesssim 0.04$ . At higher shear rates,  $0.04 \lesssim \dot{\gamma}\tau \lesssim 0.1$ , the continuum predictions slightly overestimate the MD results. The maximum discrepancy in the effective slip length is about  $2.5\sigma$  at  $\dot{\gamma}\tau \simeq 0.1$ , which corresponds to the upper wall

speed  $\tilde{U} = 6.0$ . For  $\tilde{U} > 6.0$ , the local shear rate at the crest of the lower boundary,  $[(\vec{n} \cdot \nabla) u_t + u_t/R]$ , becomes larger than the highest shear rate,  $\dot{\gamma}\tau \simeq 0.072$ , achieved in the MD simulations for the intrinsic slip length (see Fig. 5.4), and, therefore, the local boundary condition, Eq. (5.8), cannot be applied.

### 5.3.3 A detailed analysis of the flow near the curved boundary

In order to determine what factors cause the discrepancy between the effective slip lengths obtained from MD and continuum simulations at high shear rates, we performed a detailed analysis of the fluid temperature, pressure, density and velocity profiles near the lower boundary. The fluid temperature in the first fluid layer along the lower wall is plotted in Fig. 5.5 for the indicated upper wall speeds. The temperature was computed by subtracting the mean flow in the  $\hat{x}$  and  $\hat{z}$  directions and averaging the kinetic energy in all three directions. As expected, at low shear rates  $\dot{\gamma}\tau \lesssim 0.019$  ( $U \lesssim 1.0\sigma/\tau$ ), the fluid temperature remains equal to the value  $T = 1.1\varepsilon/k_B$  set in the Langevin thermostat. With increasing upper wall speed, the temperature increases and eventually becomes nonuniformly distributed along the curved boundary (see Fig. 5.5). Somewhat surprisingly, we find that at high upper wall speeds  $U \geq 5.0\sigma/\tau$  the fluid temperature is lowest above the crest even though the slip velocity in this region is expected to be higher than in the other locations.

The normal pressure distribution along the lower corrugated wall is shown in Fig. 5.6 for the selected upper wall speeds. Each data point represents the ratio of the averaged normal force on the wall atoms from the fluid monomers (within the cutoff radius) to the surface area  $0.77\sigma \times 10.0\sigma$  in the  $ty$  plane. The small variation of the pressure at equilibrium is due to the boundary curvature, i.e., the number of fluid monomers within the cutoff distance from the wall atoms is on average slightly larger above the peak than inside the valley. With increasing upper wall speed, the normal pressure increases in the valley ( $x/\lambda \lesssim 0.12$  and  $x/\lambda \gtrsim 0.54$ ) while it becomes smaller than the equilibrium pressure on the right slope of the peak (see Fig. 5.6). The normal pressure distribution extracted from the solution of the NS equation (not shown) is qualitatively similar to the profiles presented in Fig. 5.6. However, in the region  $x/\lambda \gtrsim 0.54$  the MD data overestimate the continuum predictions for the pressure distribution at  $U \gtrsim 3.0\sigma/\tau$  due to the increase in fluid temperature (see

Fig. 5.5). It is clear from Fig. 5.6 that at higher upper wall speeds there is a considerable deviation from the equilibrium pressure, which can affect the local intrinsic slip length along the curved boundary (see discussion below). We finally comment that the normal pressure on the flat lower wall ( $ka = 0$ ) at equilibrium is equal to  $P \simeq 2.36 \varepsilon/\sigma^3$  (which agrees well with the pressure on the locally flat surface at  $x/\lambda \simeq 0.5$  for  $U = 0$  in Fig. 5.6) and it increases up to  $P \simeq 2.52 \varepsilon/\sigma^3$  at the highest upper wall speed  $U = 5.375 \sigma/\tau$ .

A snapshot of the flow near the lower corrugated wall is shown in Fig. 5.7, where the rectangular boxes illustrate the location of the averaging regions along the surface. The dimensions of the boxes are  $d = 0.77 \sigma$ ,  $5.0 \sigma$ , and  $L_y = 10.0 \sigma$  along the curved boundary ( $xz$  plane), normal to the curved boundary ( $xz$  plane), and in the  $\hat{y}$  direction, respectively. The velocity and density profiles discussed below were averaged inside the boxes within bins of thickness  $0.01 \sigma$  in the direction normal to the surface.

In Figure 5.8 the averaged density profiles are plotted in regions I–IV for  $U = 0$  and  $6.0 \sigma/\tau$ . In both cases, a pronounced fluid layering is developed near the lower wall. In the stationary case, Fig. 5.8(a), the density profiles are almost the same in all four regions. Similar to the results of previous MD studies on slip flow over smooth surfaces [29, 37], when the upper wall speed increases, the contact density (magnitude of the first peak) is reduced due to a finite slip velocity along the curved boundary [see Fig. 5.8(b)]. Among regions I–IV, it is expected that the local slip velocity is highest above the crest (region II) and lowest at the bottom of the valley (region IV), and, therefore, it is not surprising that the contact density in the region IV is larger than in the region II [see Fig. 5.8(b)]. However, this correlation does not hold in regions I and III, where it is expected that at finite  $Re$  the slip velocity in the region I would be larger than in the region III; but, as shown in Fig. 5.8(b), the contact density in the region I is slightly larger than in the region III. Instead, we correlate this behavior with the nonuniform pressure distribution along the curved boundary where the local normal pressure in the region I is higher than in the region III (see Fig. 5.6). Note also that the location of the second and third fluid layers in regions II and III is slightly shifted away from the surface and the magnitude of the peaks is reduced due to the lower pressure in the region  $0.2 \lesssim x/\lambda \lesssim 0.5$  at  $U = 6.0 \sigma/\tau$  in Fig. 5.6.

The local tangential velocity profiles normal to the curved boundary are presented in

Fig. 5.9 for the upper wall speed  $U = 1.0 \sigma/\tau$ . Note that the profiles are almost linear away from the surface except for a slight curvature in the MD velocity profiles near the wall. The slip velocity above the crest (region II) is larger than in the other regions and  $u_t$  at the bottom of the valley (region IV) is the lowest, as expected. The tangential velocity on the left side of the peak (region I) is larger than on the right side (region III) due to the inertial effects [132]. The tangential velocity  $u_t$  and its normal derivative  $\partial u_t / \partial n$  extracted from MD simulations in regions I, III, and IV agree rather well with the continuum results. Despite a slight overestimation of the continuum velocity with respect to the MD results above the crest (region II), the effective slip length is essentially the same in both methods for the upper wall speed  $U = 1.0 \sigma/\tau$  (see the data at  $\dot{\gamma}\tau \simeq 0.019$  in Fig. 5.4).

Figure 5.10 shows local profiles of the velocity component normal to the curved boundary for the upper wall speed  $U = 1.0 \sigma/\tau$ . Within statistical uncertainty, the normal velocities at the boundary are zero in both MD and continuum simulations. In regions I and IV the normal velocity is negative, while in regions II and III the velocity is positive away from the boundary. The negative and positive signs of the normal velocity are expected in regions I and III because of the positive and negative slopes of the boundary with respect to the shear flow direction. Although the boundary slope at the crest and at the bottom of the valley is parallel to the upper wall, the local symmetry of the flow with respect to  $x/\lambda = 0.25$  and  $0.75$  is broken at finite Reynolds numbers ( $Re \approx 15.6$  for  $U = 1.0 \sigma/\tau$  in Fig. 5.10), and, as a result, the normal velocity in regions II and IV is not zero. Furthermore, the MD velocity profiles exhibit an unexpected oscillatory pattern away from the surface. These oscillations correlate well with the locations of the minima among the first three fluid layers [e.g., see Fig. 5.8(a)]. Visual inspection of the individual molecule trajectories indicates that the fluid monomers mostly undergo thermal motion within the moving layers but occasionally jump back and forward between the layers. The net flux between the layers, however, is not zero and its sign is determined by the direction of the flow near the boundary.

The tangential velocity profiles averaged in regions I–IV at a higher upper wall speed  $U = 6.0 \sigma/\tau$  are shown in Fig. 5.11. The flow pattern near the lower boundary is similar to that described in Fig. 5.9 for  $U = 1.0 \sigma/\tau$ , but the relative difference between the MD and continuum velocities is larger in each region which results in a maximum discrepancy

between the effective slip lengths of about  $2.5\sigma$  at  $\dot{\gamma}\tau \simeq 0.1$  in Fig. 5.4. We tried to estimate the local intrinsic slip length from the MD velocity profiles in regions I–IV and to compare  $L_0$  with the continuum predictions. However, the normal derivative of the tangential velocity cannot be computed accurately because of the curvature in the velocity profiles and ambiguity in determining the range for the best linear fit. The resulting error bars associated with the linear extrapolation of the MD velocity profiles in Fig. 5.11 are greater than the maximum difference between MD and continuum results for  $L_{\text{eff}}$  at high shear rates in Fig. 5.4. Instead, a more reliable data for the local intrinsic slip length (see Fig. 5.12) are obtained by computing the friction coefficient ( $k_f = \mu/L_0$ ), which is the ratio of the wall shear stress to the slip velocity. The agreement between the MD and continuum results is quite good on the right side of the peak in Fig. 5.12. The intrinsic slip length computed from MD simulations is about  $3 - 4\sigma$  smaller than the continuum  $L_0$  on the left side of the peak due to higher fluid pressure in that region (see also discussion below).

The normal velocity profiles averaged in regions I–IV along the lower boundary are displayed in Fig. 5.13 for the upper wall speed  $U = 6.0\sigma/\tau$ . In each region, the amplitude of oscillations in the MD velocity profiles is increased with respect to the mean flow predicted by the continuum analysis. Similar to the correlation between density and velocity profiles observed in Fig. 5.10 for  $U = 1.0\sigma/\tau$ , the locations of the maxima in the normal velocity profiles in Fig. 5.13 correspond to the minima in the density profiles shown in Fig. 5.8(b). At the higher upper wall speed,  $U = 6.0\sigma/\tau$ , however, the location of the first peak in the velocity profile above the crest (region II) and on the right side of the peak (region III) is slightly displaced away from the boundary due to a small shift in the position of the second and third fluid layers in regions II and III [see Fig. 5.8(b)].

The effect of pressure variation along the curved boundary is not included in the rate-dependent intrinsic slip length, Eq. (5.8), used in continuum simulations. It was shown in Fig. 5.6 that at higher upper wall speeds,  $U \gtrsim 3.0\sigma/\tau$ , the fluid pressure along the lower corrugated wall deviates significantly from the equilibrium pressure. Next, we estimate the influence of pressure on the intrinsic slip length in shear flow over a flat wall by increasing the temperature of the Langevin thermostat. The MD simulations described in Sec. 5.3.1 were repeated at the upper wall speeds  $U = 1.0\sigma/\tau$  and  $3.5\sigma/\tau$  to examine  $L_0$  at low ( $\dot{\gamma}\tau \approx 0.018$ )

and high ( $\dot{\gamma}\tau \approx 0.055$ ) shear rates. The results are presented in Fig. 5.14 for the indicated temperatures of the Langevin thermostat. As the bulk pressure increases, the intrinsic slip length is reduced by about  $3\sigma$  at  $U = 3.5\sigma/\tau$  and about  $\sigma$  at  $U = 1.0\sigma/\tau$ . Note, however, that under these flow conditions the shear viscosity remains nearly constant (see Fig. 5.3), and the variation of the friction coefficient ( $k_f = \mu/L_0$ ) is determined only by the intrinsic slip length.

The maximum increase in pressure and the difference in  $L_0$  reported in Fig. 5.14(a) correlate well with the variation of pressure in Fig. 5.6 and the intrinsic slip length in Fig. 5.12 on the left side of the peak at  $U = 6.0\sigma/\tau$ . We conclude, therefore, that the discrepancy between the effective slip lengths computed from MD and continuum simulations at high shear rates (shown in Fig. 5.4) is caused by the increase in fluid pressure on the left side of the peak (where the solid boundary faces the mainstream flow) and, as a result, the local intrinsic slip length is reduced. Thus, a more accurate continuum description of the slip flow over a curved boundary can be achieved by including the effect of pressure and temperature on the rate-dependent intrinsic slip length.

## 5.4 Conclusions

In this chapter, molecular dynamics simulations were used to determine the intrinsic slip length as a function of shear rate in steady flow over an atomically flat surface. It was found, in agreement with previous MD studies, that the intrinsic slip length is nearly constant (rate-independent) at low shear rates and it grows rapidly as the shear rate approaches a critical value. In the presence of periodic surface roughness, the magnitude of the effective slip length is significantly reduced and its dependence on shear rate becomes less pronounced.

For the same surface roughness, the Navier-Stokes equation was solved numerically with the rate-dependent boundary conditions specified by the intrinsic slip length obtained from MD simulations. The continuum simulations reproduce accurately the MD results for the effective slip length at low and intermediate shear rates. The small difference between the effective slip lengths at high shear rates was analyzed by performing a detailed analysis of the local velocity fields and pressure distribution along the curved boundary. We found

that the main cause of the discrepancy between MD and continuum results at high shear rates is the reduction of the local intrinsic slip length in the region of higher pressure where the boundary slope becomes relatively large with respect to the mainstream flow. These findings suggest that the continuum analysis of the flow over a rough surface at high shear rates should take into account the effect of pressure on the rate-dependent intrinsic slip length. One way to include pressure in the numerical analysis is to perform an additional set of MD simulations (for flat walls) at different values of the constant normal load and vary the upper wall speed. Thus, the intrinsic slip length as a function pressure and shear rate can be obtained from interpolation of the MD data and then used as a local boundary condition in the continuum simulation.

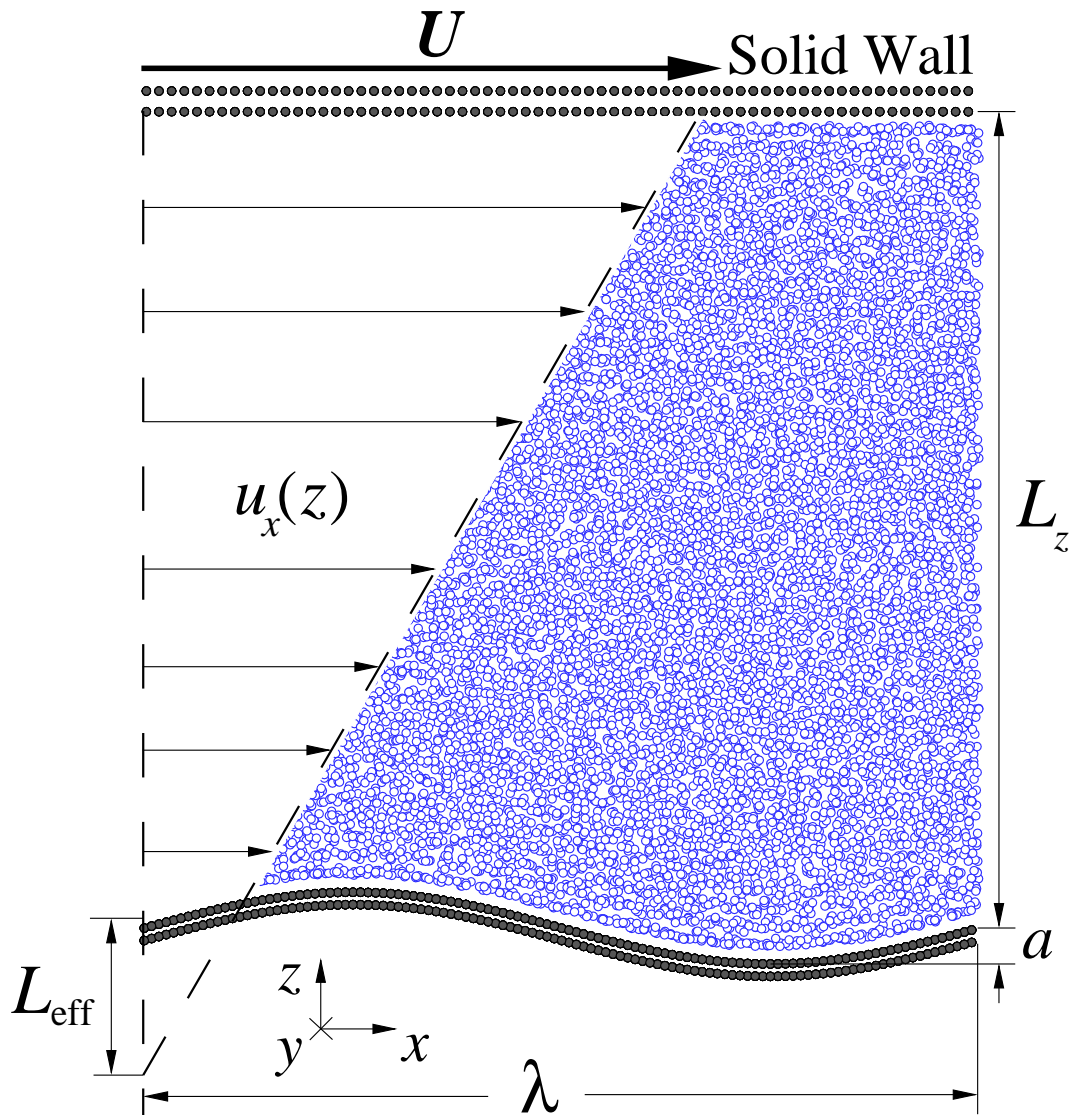


Figure 5.1. The projection of  $x$  and  $z$  coordinates of the fluid monomers (open circles) confined between solid walls (filled circles). The atoms of the lower stationary wall are uniformly distributed along the sinusoidal curve with wavelength  $\lambda$ , amplitude  $a$ , and density  $\rho_w = 3.1 \sigma^{-3}$ . The shear flow is induced by the flat upper wall with the density  $0.67 \sigma^{-3}$  moving with a constant velocity  $U$  in the  $\hat{x}$  direction. The effective slip length  $L_{\text{eff}}$  is computed by extrapolation of the velocity profile to  $u_x = 0$ .

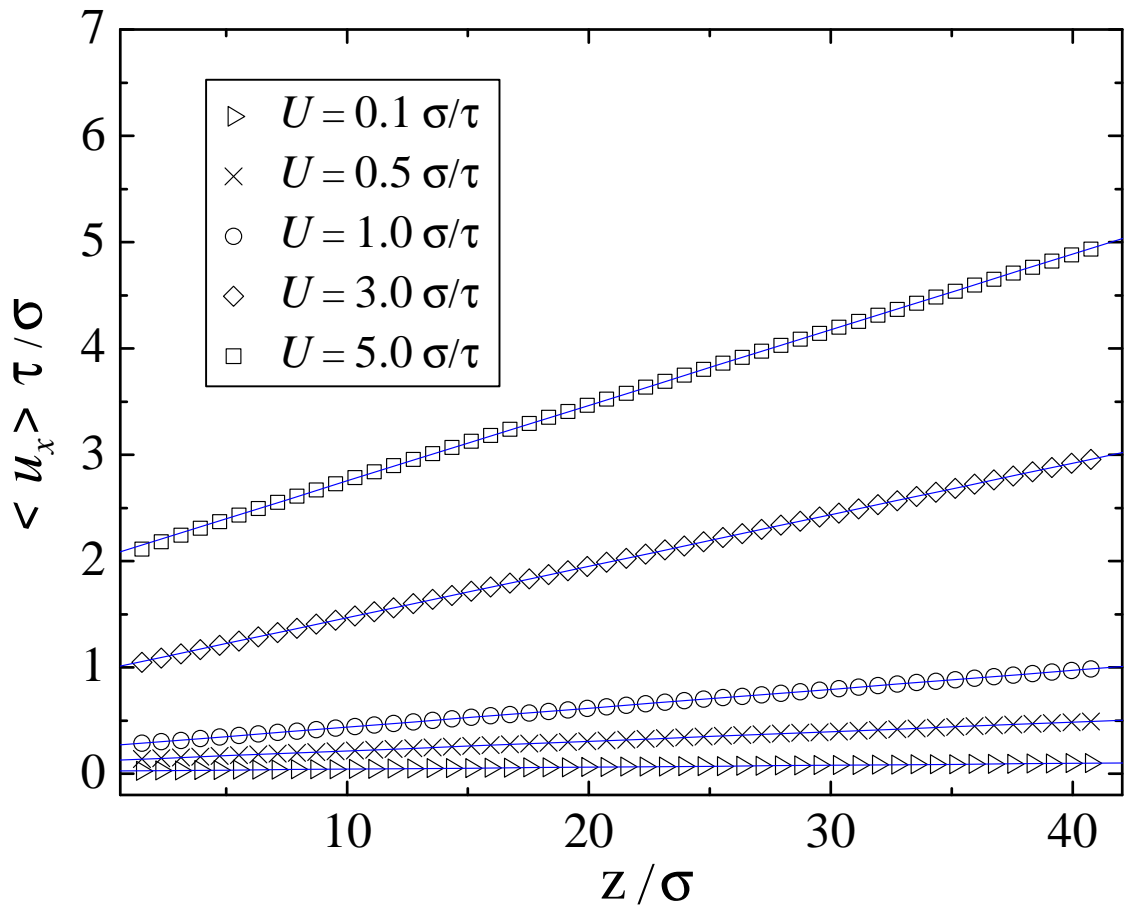


Figure 5.2. Averaged velocity profiles for the tabulated upper wall speeds in the cell with flat upper and lower walls. The solid lines are the best linear fits to the data. The vertical axes indicate the location of the *FCC* lattice planes.

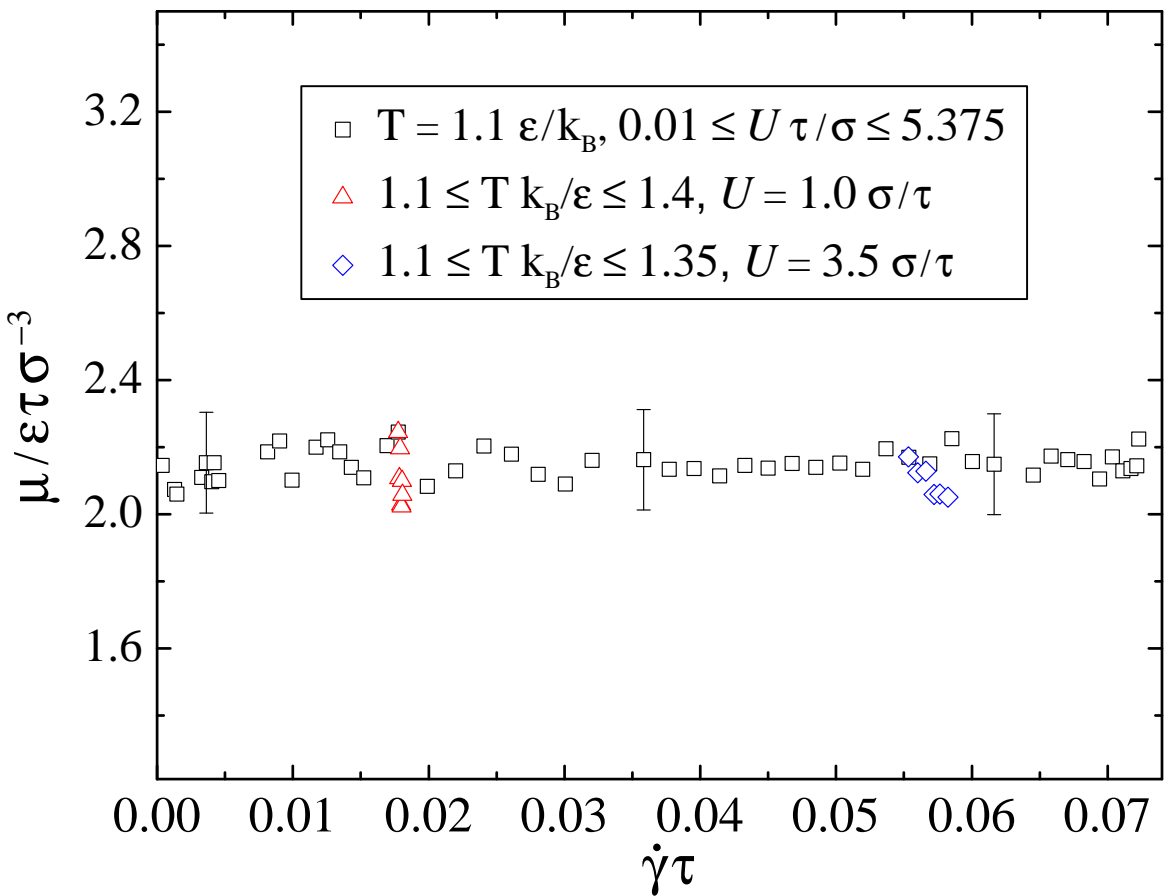


Figure 5.3. Shear viscosity in the cell with flat upper and lower walls when the temperature of the Langevin thermostat is set to  $T = 1.1 \varepsilon/k_B$  ( $\square$ ). Fluid viscosity as a function of the thermostat temperature  $1.1 \leq T k_B/\varepsilon \leq 1.4$  for the upper wall speed  $U = 1.0 \sigma/\tau$  ( $\triangle$ ) and  $1.1 \leq T k_B/\varepsilon \leq 1.35$  for  $U = 3.5 \sigma/\tau$  ( $\diamond$ ).

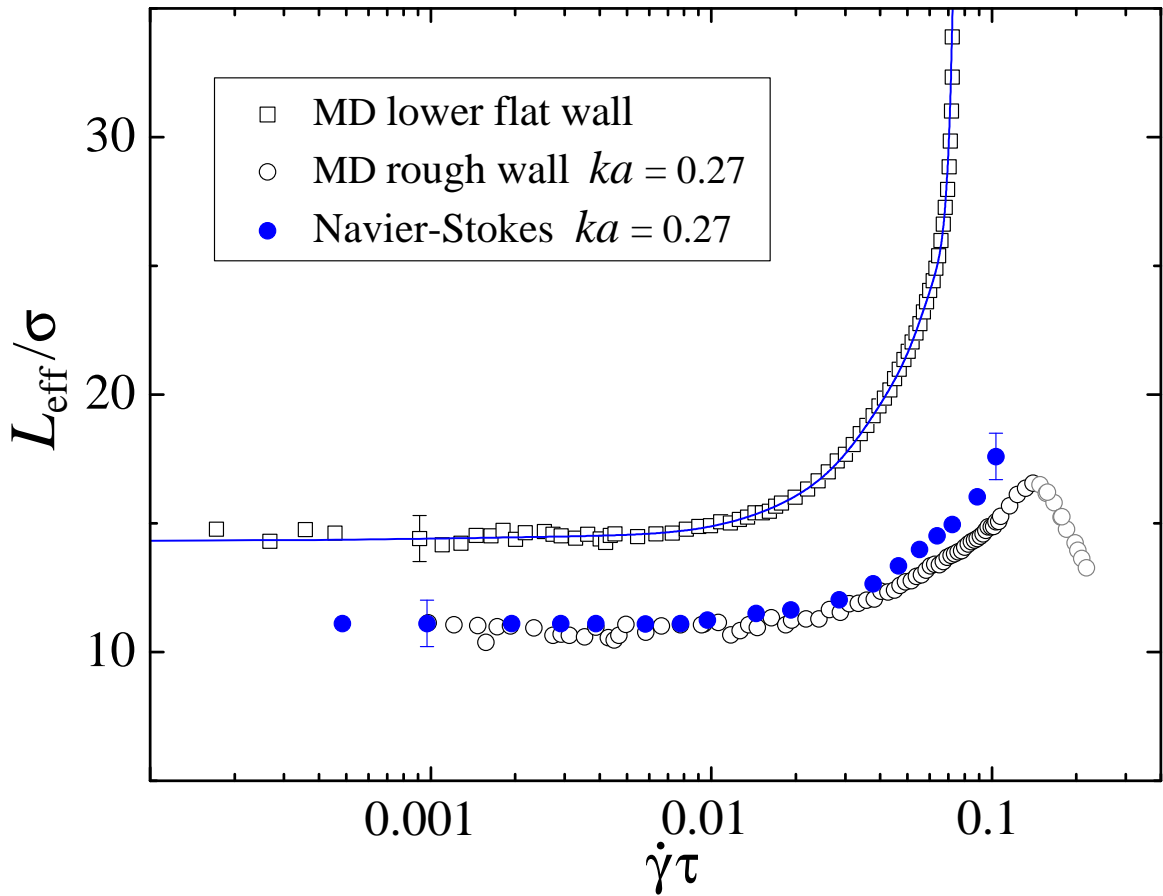


Figure 5.4. The intrinsic slip length  $L_0/\sigma$  as a function of shear rate for atomically flat walls ( $\square$ ). The blue solid curve is a ninth-order polynomial fit to the data. The effective slip length  $L_{\text{eff}}/\sigma$  as a function of shear rate for the flow over the corrugated wall with wavenumber  $ka = 0.27$  ( $\circ$ ). The effective slip length computed from the solution of the Navier-Stokes equation with the local rate-dependent slip length ( $\bullet$ ).

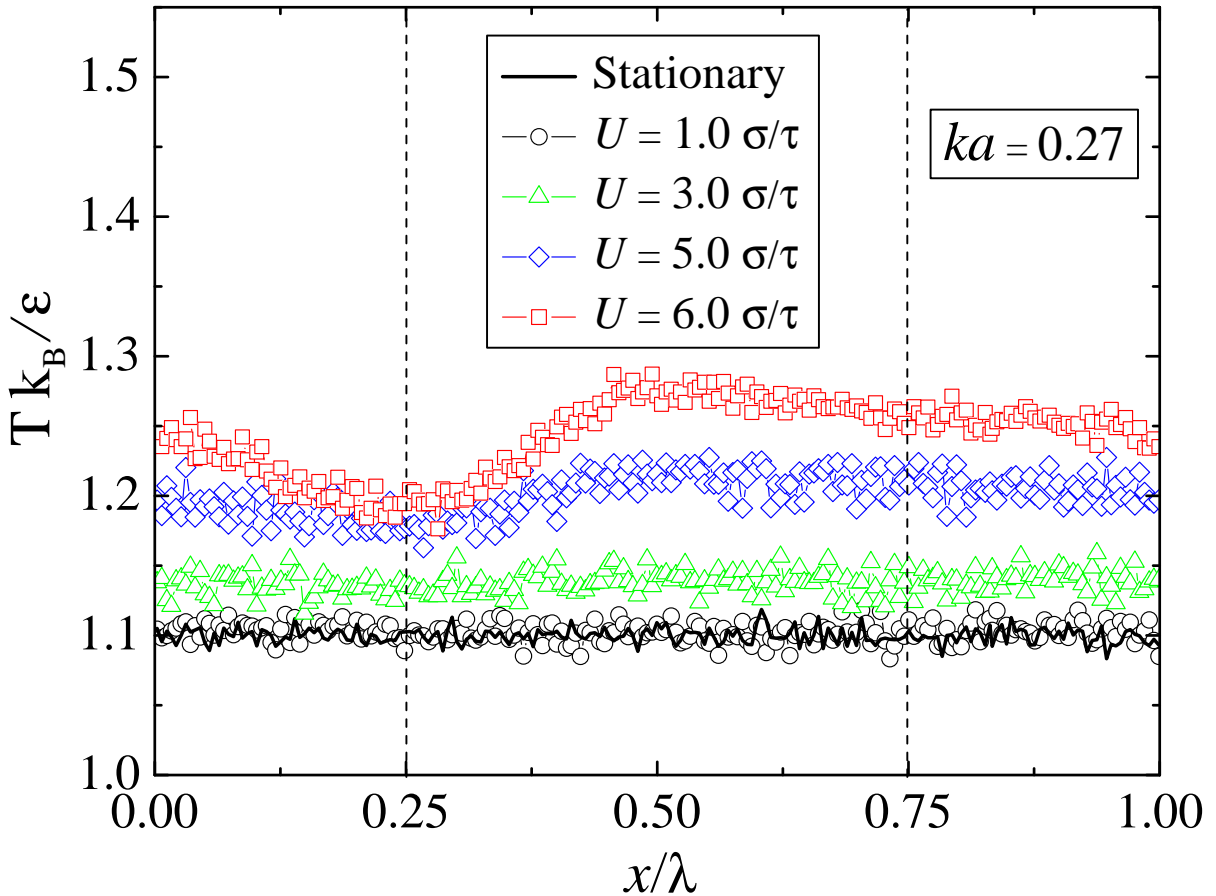


Figure 5.5. Temperature of the first fluid layer  $T(x)$  (in units of  $\varepsilon/k_B$ ) along the lower corrugated wall ( $ka = 0.27$ ) for the indicated upper wall speeds. The vertical dashed lines denote the location of the crest ( $x/\lambda = 0.25$ ) and the bottom of the valley ( $x/\lambda = 0.75$ ).

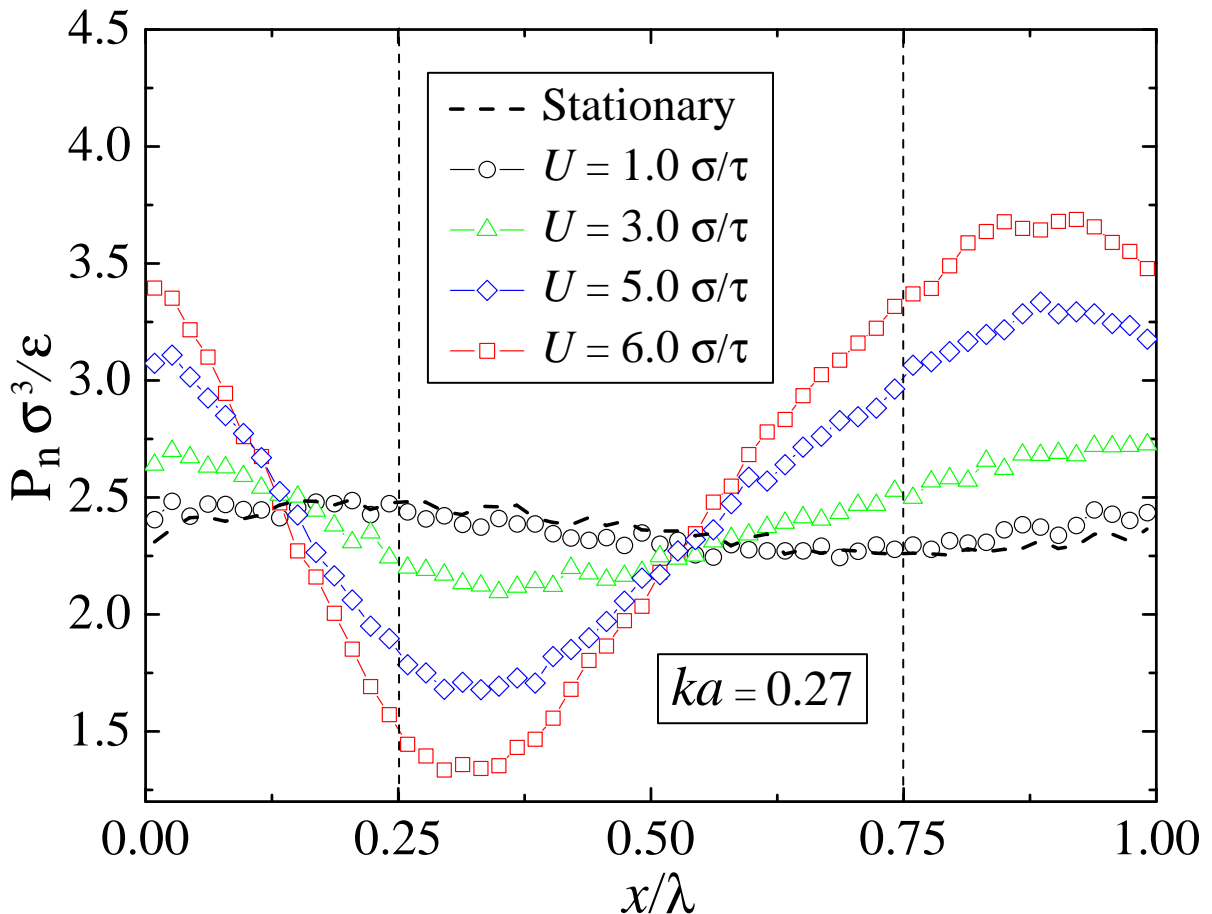


Figure 5.6. The normal pressure  $P_n$  (in units of  $\varepsilon/\sigma^3$ ) along the lower corrugated wall ( $ka = 0.27$ ) for the selected upper wall speeds. The vertical dashed lines indicate the location of the crest ( $x/\lambda = 0.25$ ) and the bottom of the valley ( $x/\lambda = 0.75$ ).

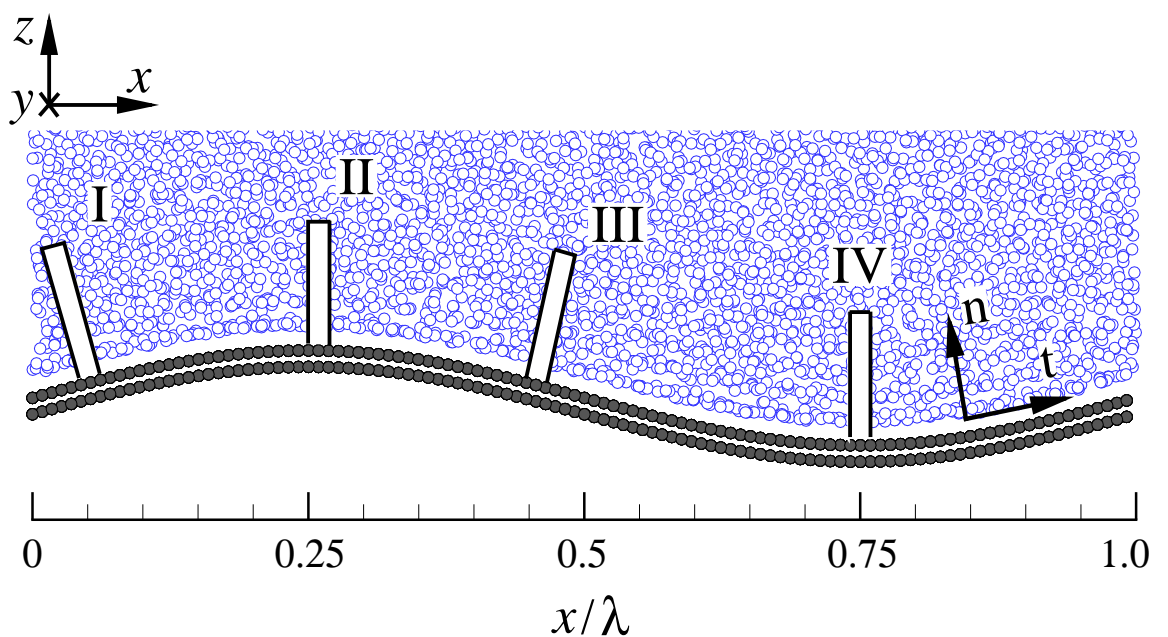


Figure 5.7. A snapshot of the fluid monomers (open circles) near the lower corrugated wall (filled circles) with wavenumber  $ka = 0.27$ . The rectangular boxes denote averaging regions on the left side of the peak (I) ( $x/\lambda \simeq 0.05$ ), above the crest (II) ( $x/\lambda \simeq 0.25$ ), on the right side of the peak (III) ( $x/\lambda \simeq 0.45$ ), and at the bottom of the valley (IV) ( $x/\lambda \simeq 0.75$ ). The unit vectors  $\vec{t}$  and  $\vec{n}$  indicate the tangential and normal directions at the boundary.

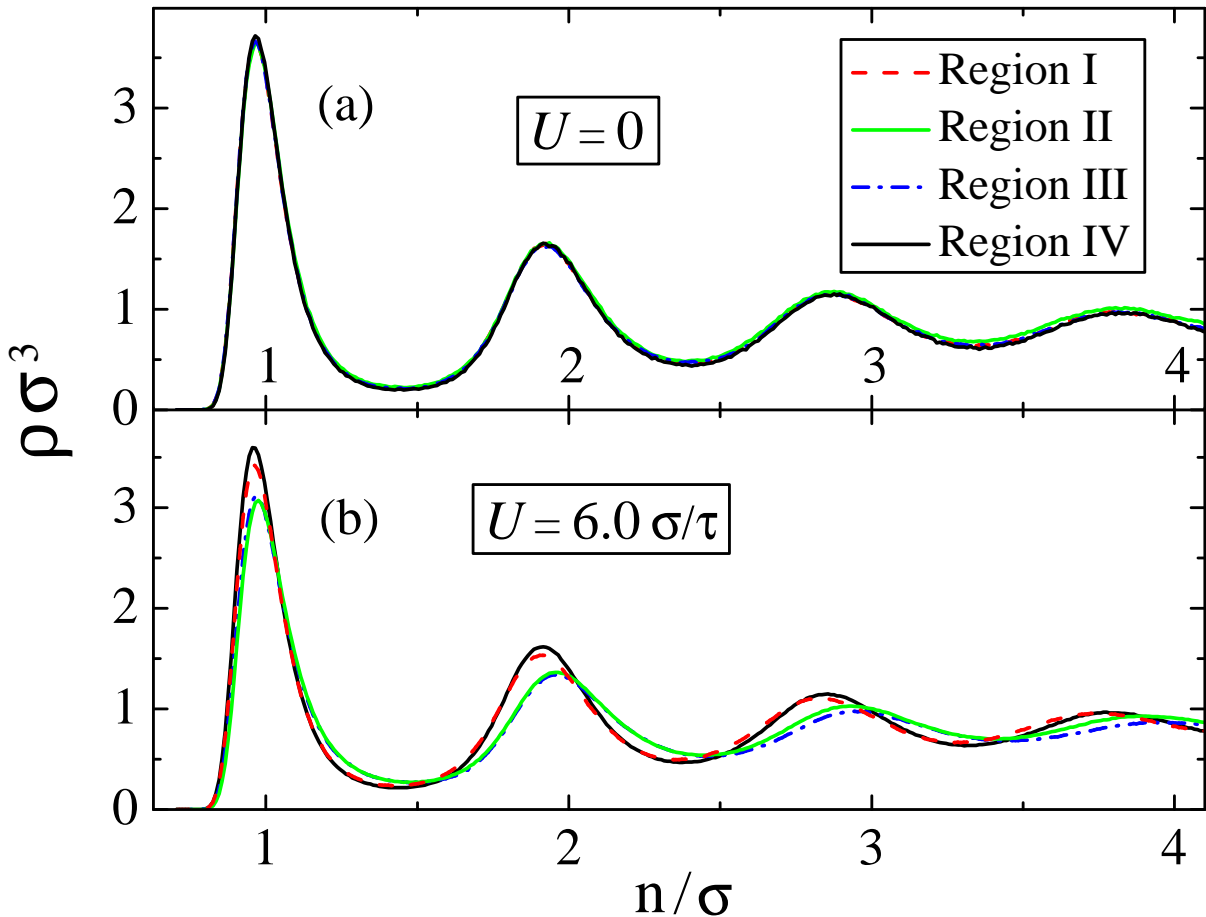


Figure 5.8. Fluid density profiles averaged inside regions I–IV (shown in Fig. 5.7) near the corrugated lower wall with wavenumber  $ka = 0.27$ . The upper wall speeds are  $U = 0$  (a) and  $U = 6.0 \sigma/\tau$  (b).

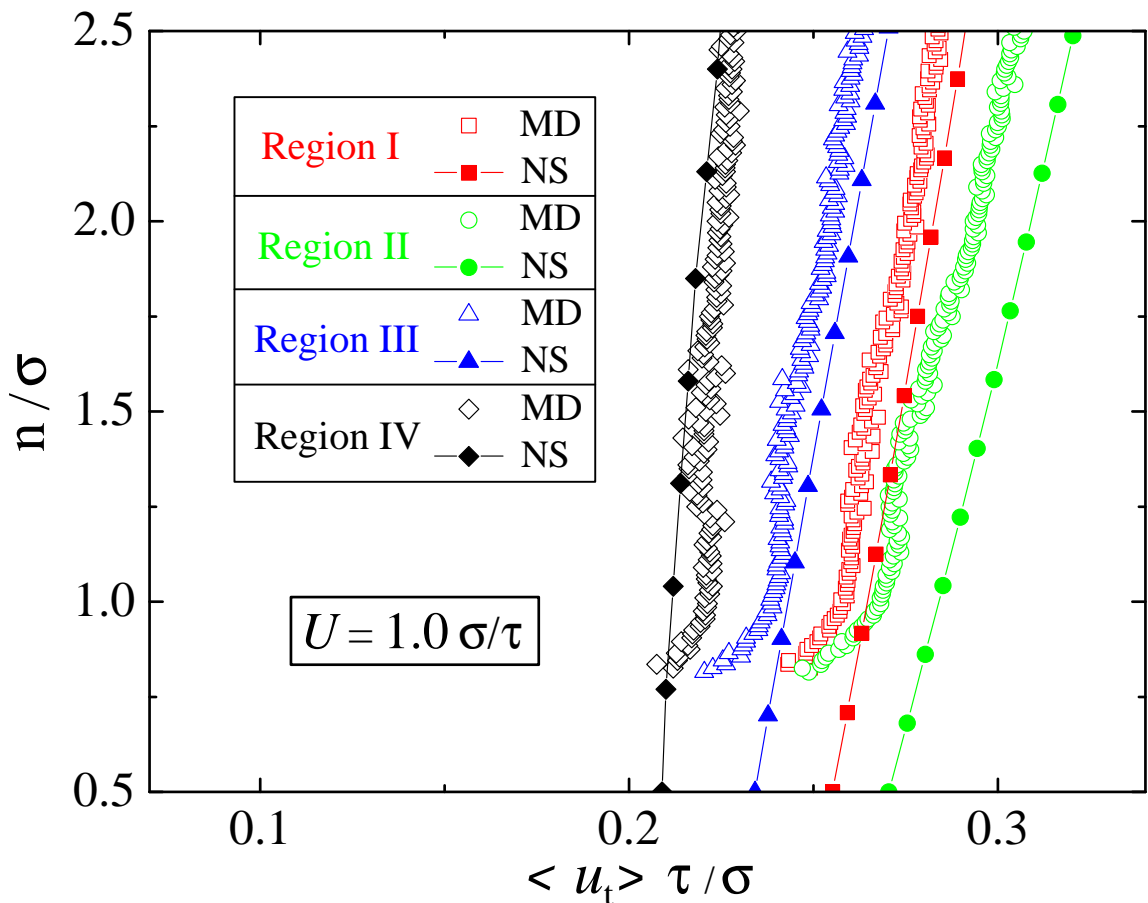


Figure 5.9. Averaged tangential velocity profiles inside regions I-IV obtained from MD simulations (open symbols) and the solution of the Navier-Stokes equation (filled symbols). The location of the averaging regions near the lower corrugated wall is shown in Fig. 5.7. The upper wall speed is  $U = 1.0 \sigma/\tau$ .

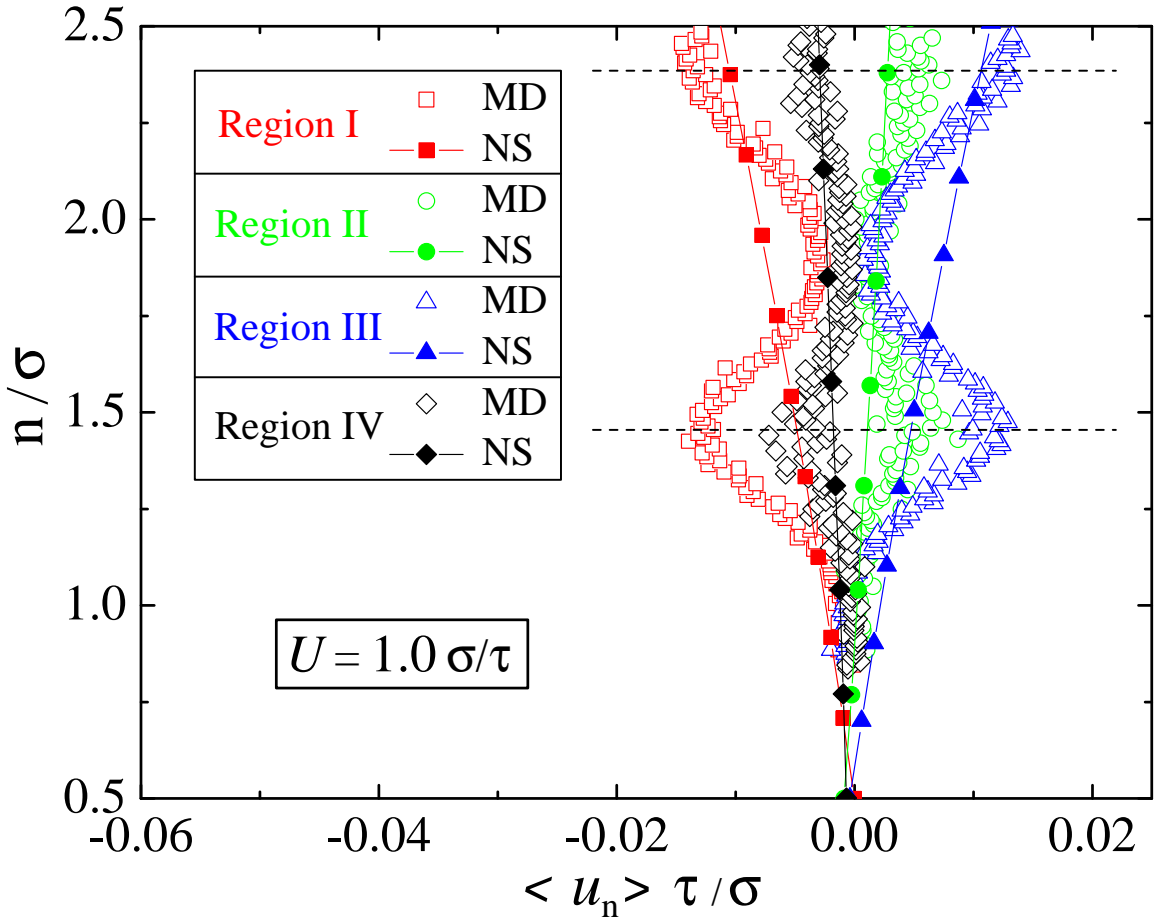


Figure 5.10. Averaged normal velocity profiles inside regions I–IV (shown in Fig. 5.7) for the upper wall speed  $U = 1.0 \sigma/\tau$ . The profiles are extracted from MD simulations (open symbols) and the solution of the Navier-Stokes equation (filled symbols). The horizontal dashed lines indicate the location of the minima in density profiles (see text for details).

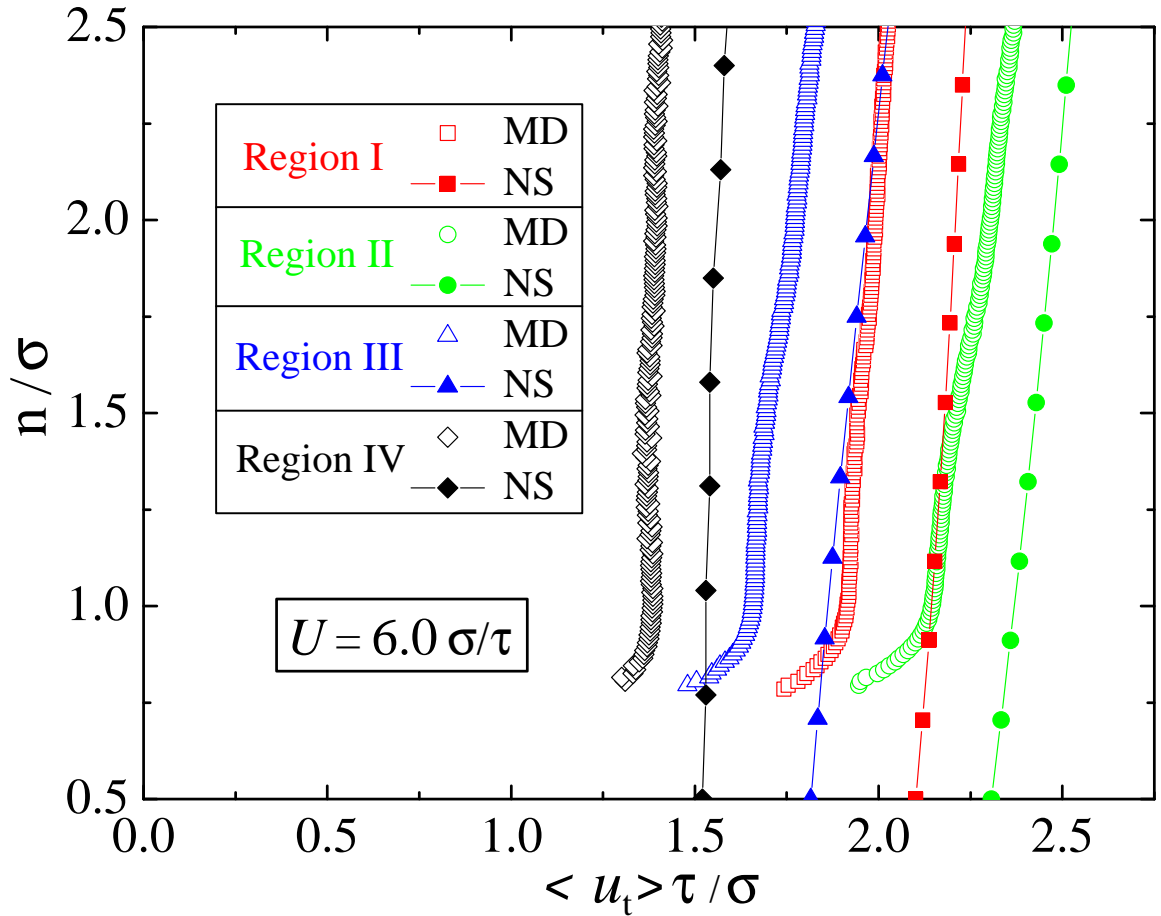


Figure 5.11. Tangential velocity profiles averaged inside regions I–IV (shown in Fig. 5.7) near the lower corrugated wall. The upper wall speed is  $U = 6.0 \sigma/\tau$ . The velocity profiles are extracted from MD simulations (open symbols) and the solution of the Navier-Stokes equation (filled symbols).

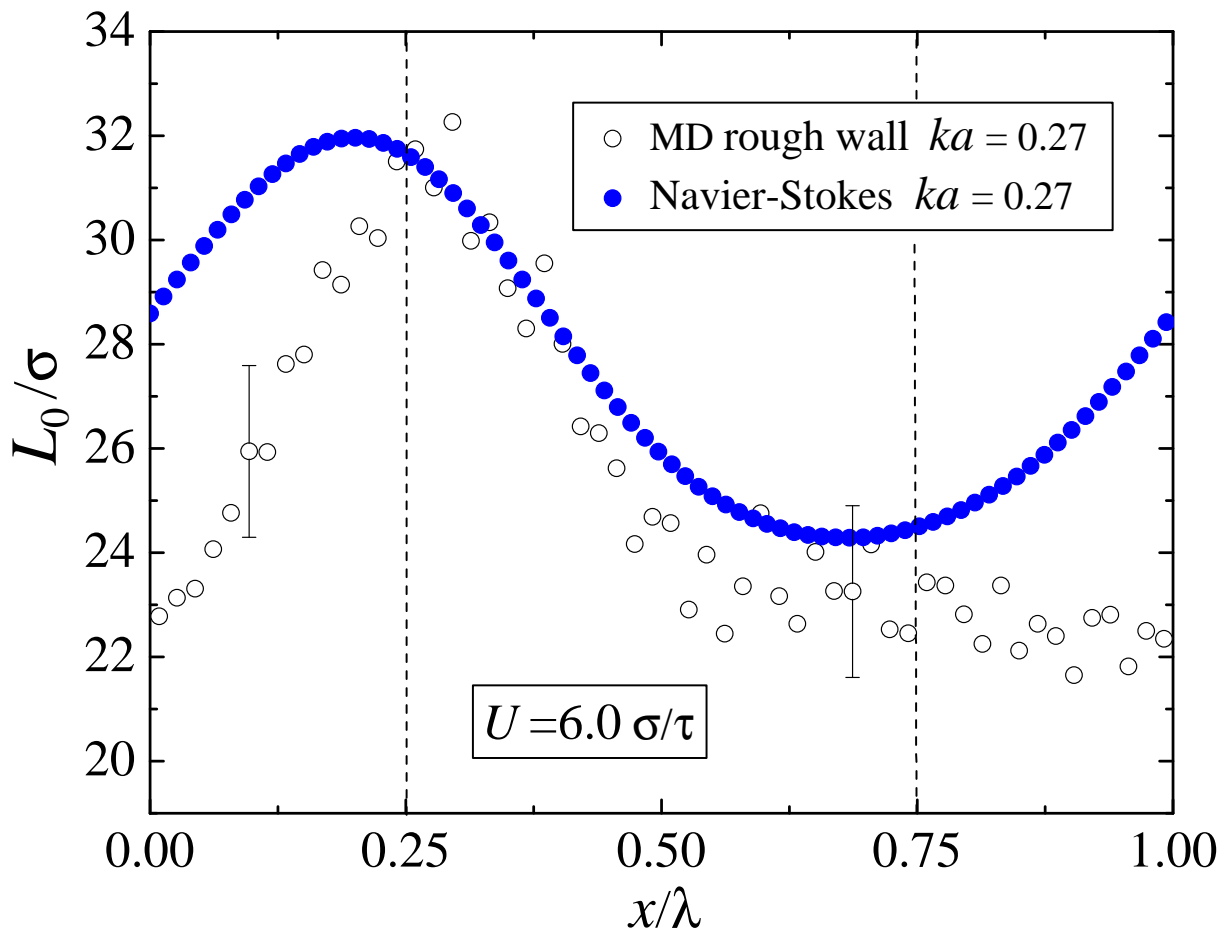


Figure 5.12. The intrinsic slip length along the lower corrugated wall ( $ka = 0.27$ ) for the upper wall speed  $U = 6.0 \sigma/\tau$ . The data are obtained from MD simulations (open symbols) and the solution of the Navier-Stokes equation (filled symbols). The vertical dashed lines denote the position of the crest ( $x/\lambda = 0.25$ ) and the bottom of the valley ( $x/\lambda = 0.75$ ).

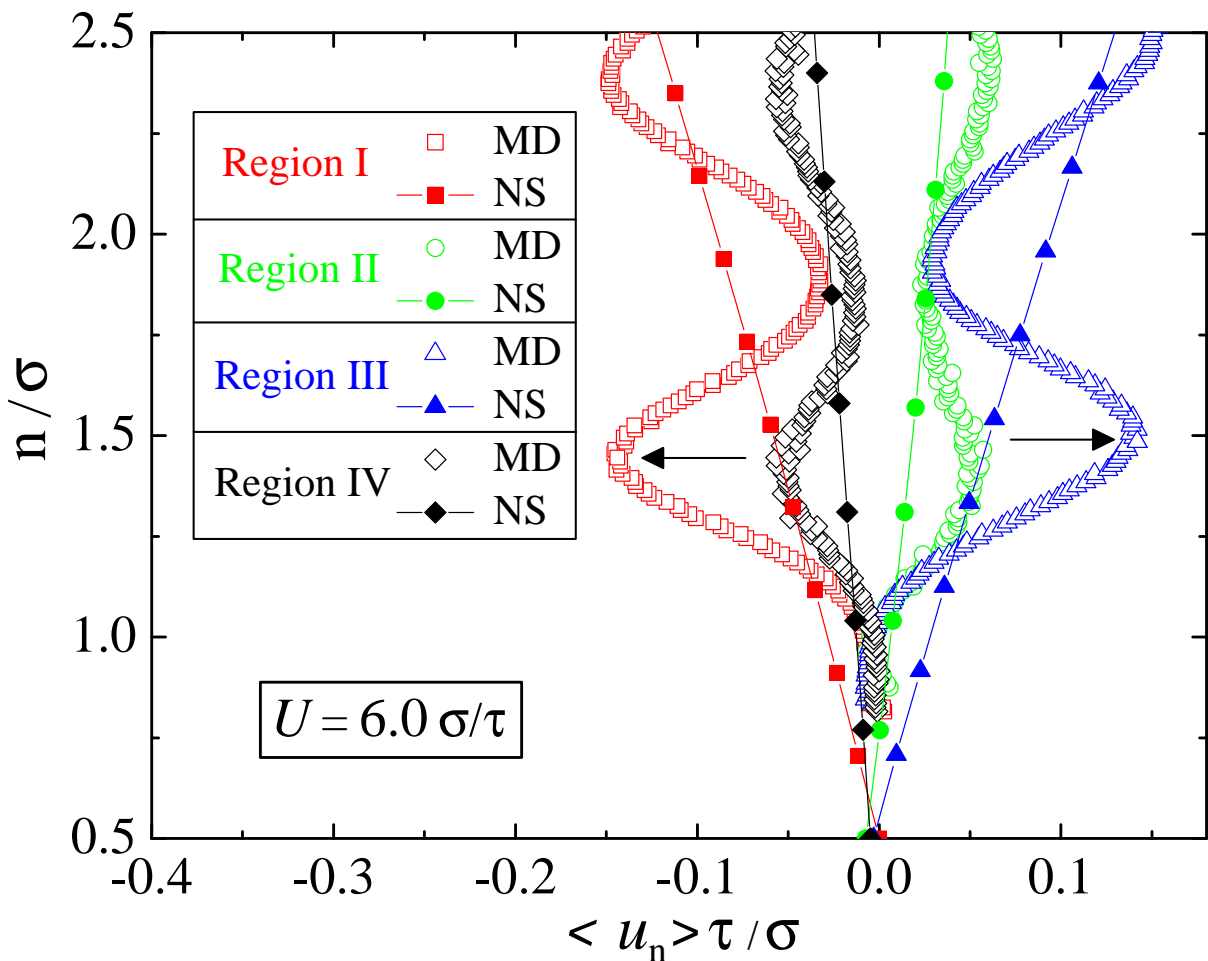


Figure 5.13. Averaged normal velocity profiles inside regions I-IV obtained from MD simulations (open symbols) and the solution of the Navier-Stokes equation (filled symbols). The upper wall speed is  $U = 6.0 \sigma/\tau$ . The horizontal arrows indicate the location of the minima in density profiles between the first and second fluid layers in regions I and III.

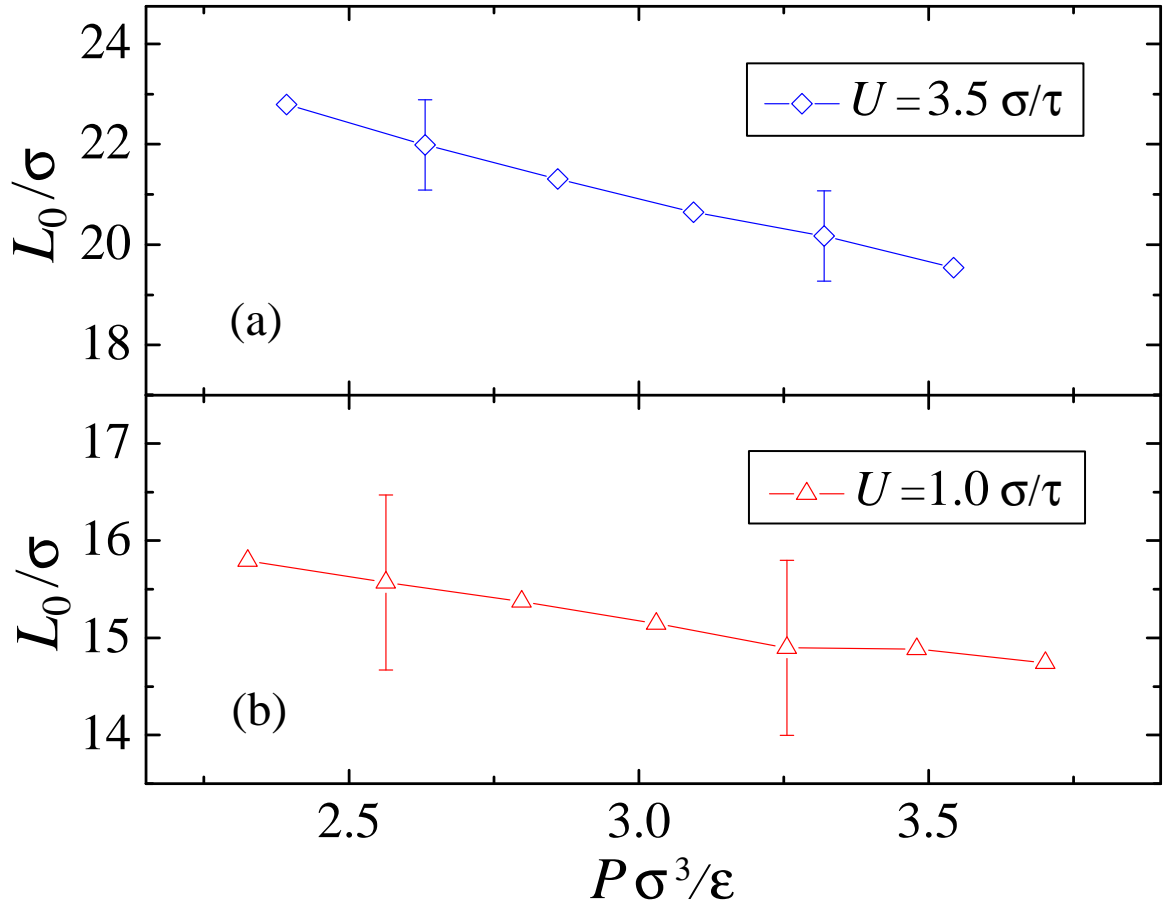


Figure 5.14. The intrinsic slip length  $L_0/\sigma$  as a function of the bulk pressure  $P$  (in units of  $\epsilon/\sigma^3$ ) in the cell with flat upper and lower walls. The temperature of the Langevin thermostat is varied in the range  $1.1 \leq T k_B/\epsilon \leq 1.35$  for the upper wall speed  $U = 3.5 \sigma/\tau$  (a) and  $1.1 \leq T k_B/\epsilon \leq 1.4$  for  $U = 1.0 \sigma/\tau$  (b).

# CHAPTER 6

## Slip boundary conditions for the moving contact line in molecular dynamics and continuum simulations

### 6.1 Introduction

The problem of contact line motion, which involves flow of two immiscible viscous fluids in contact with a solid substrate, has captivated a lot of attention because of its fundamental difficulties and important applications including droplet spreading, spray painting, lubrication, and coating [134, 135].

In wetting problems, the line of contact of the fluid/fluid interface with the solid wall is called the contact line. In the absence of the fluid flow relative to the solid wall, the fluid/fluid interface forms an angle with the solid wall, called the static contact angle  $\theta_s$ , which is determined by the balance of the surface tensions between three media. In the presence of flow, the shape of the fluid/fluid interface near the wall becomes deformed and it is described by the dynamic contact angle  $\theta_d$ . The deformation of the interface depends on the flow fields near the contact line, surface tensions, and energy dissipation at the contact line.

The analytical calculation of flow fields and motion of the contact line with no-slip boundary condition along the solid surface leads to a stress singularity and infinite viscous dissipa-

tion near the contact line [136, 137]. Due to multi-scale nature of the moving contact line problem and breakdown of the local hydrodynamics near the contact point, the problem has inspired many theoretical/numerical studies over the last 30 years [62, 137, 138, 141, 144]. On the other hand, experimental studies are limited to measuring a macroscopic contact angle, known also as an apparent contact angle  $\theta_a$ , which is accessible at a distance  $R$  (order of microns) from the surface. When the shape of the fluid/fluid interface is deformed on a molecular distance from the wall, the static contact angle  $\theta_s$  and dynamic contact angle  $\theta_d$  are distinguishable while  $\theta_a$  depends on the value of  $R$ .

Most of analytical and numerical solutions of the moving contact line problem were performed based on the fact that the far field solution of the problem is almost insensitive to the exact dynamics of the contact line close to wall [138]. One of the possibilities to remove the singularity at the contact line is to replace the no-slip boundary condition with slip BC via the Navier model. Some of the challenges in applying the slip models near the fluid/solid interface include a correct specification of the region near the contact line where the boundary slip must be applied, the magnitude of the slip length, and the shape of the fluid/fluid interface.

The molecular dynamics (MD) simulations have been only recently used to study the moving contact line problem [20, 130, 131, 139, 140, 141, 142, 143, 144, 145]. One of the advantages of the MD method is that it offers a detailed information about microscopic flow structure near the contact line without any assumptions about boundary conditions or constitutive relations. Thus, an accurate physical description of the flow fields and motion of the contact line can be obtained from MD simulations, which in turn might help to develop models for characterizing the flow behavior in continuum modeling.

In this chapter, the moving contact line problem is studied using a combined approach of molecular dynamics and continuum simulations. First, MD simulations are carried out to resolve the flow fields in the vicinity of the moving contact line on the molecular scale and to establish a relation between the interfacial shear stresses and slip length as a function of the distance from the contact line. This is done by extracting the velocity profiles and the shear and normal stress tensors at the fluid/solid interface. Second, in the presence of shear flow, the shape of the fluid/fluid interface is accurately resolved using MD simulations. In

the next step, the boundary conditions near the moving contact line extracted from MD simulations are implemented as input conditions in the continuum solution of the Navier-Stokes equation (using the finite difference/particle tracking methods) to reproduce velocity profiles and the shape of the fluid/fluid interface.

The rest of this chapter is organized as follows. The details of MD simulations, equilibration procedure, careful evaluation of normal stresses near the solid substrate, averaging velocity profiles are presented in the Sec. 6.2. The continuum model and comparative analysis are described in Sec. 6.3. A brief summary is given in the last section.

## 6.2 Molecular dynamics (MD) simulations

### 6.2.1 Equilibrium case

The system consists of two immiscible fluids confined between flat walls. The initial configuration of the atoms is presented in Fig. 6.3. Each of two solid walls is modeled as two layers of *FCC* lattice in [111] direction. The number of fluid monomers in fluid 1 and 2 are fixed to  $N_{f_1} = 18900$  and  $N_{f_2} = 18900$ , respectively. The total number of wall atoms is set to  $N_w = 10600$ . The MD simulations were performed at a constant fluid density ( $\rho = 0.81 \sigma^{-3}$ ) ensemble, while the wall density is set to  $\rho_w = 1.86 \sigma^{-3}$  to allow a partial slip flow along the walls in each single fluid phase. The thermostat temperature is set to  $T = 1.1 \varepsilon/k_B$ , where  $k_B$  is the Boltzmann constant. The system size in the  $\hat{x}$  and  $\hat{y}$  directions is  $L_x = 241.87 \sigma$  and  $L_y = 7.90 \sigma$ . The relative distance between the walls is fixed to  $L_z = 25.41 \sigma$  in the  $\hat{z}$  direction. Periodic boundary conditions were applied along the  $\hat{x}$  and  $\hat{y}$  directions.

The fluid monomers interact through the truncated pairwise Lennard-Jones (*LJ*) potential

$$V_{LJ}(r) = 4\varepsilon \left[ \left( \frac{\sigma}{r} \right)^{12} - \delta \left( \frac{\sigma}{r} \right)^6 \right], \quad (6.1)$$

where  $\varepsilon$  is the energy scale and  $\sigma$  is the length scale of the fluid phase. The cutoff radius for the *LJ* potential is set to  $r_c = 2.5 \sigma$  for the fluid/fluid and wall/fluid interactions. For the contact line problem, the *LJ* potential is modified by adding a parameter  $\delta$  in the attractive part of the potential. For fluid 1/fluid 1, fluid 2/fluid 2, and wall/fluid interactions  $\delta = 1$ . However, for immiscible fluids (fluid 1/fluid 2),  $\delta = -1$  and the *LJ* potential only consists

of the repulsive term. In Fig. 6.4 the *LJ* potential is plotted as a function of the distance between two monomers for different values of  $\delta$ . It is clear from Fig. 6.4 that for all values of  $r/\sigma$  when  $\delta = -1$  the potential is repulsive. Throughout the simulations the interaction energies between the fluids and walls are the same ( $\varepsilon_{f1w} = \varepsilon_{f2w}$ ).

For a system with stationary walls, after an equilibration period of about  $2 \times 10^4 \tau$ , the snapshot of fluid molecules of both phases and the shape of the fluid/fluid interface are presented in Fig. 6.5. The fluid/fluid interface is almost a straight line and the static contact angle is  $\theta_s \approx 90$ . This value is in agreement with the angle predicted by the Young's equation  $\gamma_{f1w} + \gamma \cos\theta_s = \gamma_{f2w}$ , when  $\gamma_{f1w} = \gamma_{f2w}$ .

The fluid properties in equilibrium case are studied by computing the density and the normal stress distributions inside the fluid domain. First, the fluid density is averaged in bins measuring  $50\sigma \times 7.90\sigma \times 0.01\sigma$  in the  $\hat{x}$ ,  $\hat{y}$ , and  $\hat{z}$  directions in fluid 1 away from the contact line, respectively. The density profile along the  $\hat{z}$  direction is shown in Fig. 6.6(a). In Fig. 6.6(b) the fluid density is averaged in bins inside the bulk region with dimensions  $0.1\sigma \times 7.90\sigma \times 5\sigma$  in the  $\hat{x}$ ,  $\hat{y}$ , and  $\hat{z}$  directions, respectively. The density profiles are plotted along the channel in the  $\hat{x}$  direction. In both cases the density in the bulk region is  $0.81\sigma^{-3}$ . In Fig. 6.6(a) pronounced oscillations in the density profile are due to the layering of the fluid molecules near the walls. The fluid densities are reduced in Fig. 6.6(b) for both fluids as they get closer to the fluid/fluid interface region. The location of the contact line is estimated from the intersection of two density profiles. The width of the interface is approximately  $5\sigma$ .

In addition to the fluid densities, calculating the normal stresses provides an insight into the fluid characteristic near the fluid/fluid or fluid/solid interfaces. Estimating the stresses correctly is a difficult task even in the equilibrium case. Equilibrium simulations can provide an opportunity to check whether our numerical algorithm for the stress calculation is correct and, as a result, the surface tension is computed accurately. As discussed in previous chapters, the Irving-Kirkwood relation is used to compute normal and shear stresses [58]. However, in our previous studies the stresses were only estimated in the bulk region to compute the fluid viscosity [32, 93, 146]. In this chapter, the algorithm for computing stresses near the interfaces is modified. If we assume that any two monomers are connected

through an imaginary line, while the stress is calculated from the combination of kinetic and potential energies between the two monomers, the stress associated with each pair should be partitioned in proportion to the fraction of the line segment between them that lies in each spatial bin [147]. In this study the imaginary line between any two monomers is divided into 100 segments regardless of the distance between the monomers.

The results for  $\tau_{xx}$ ,  $\tau_{yy}$ , and  $\tau_{zz}$  normal stresses in the  $\hat{x}$ ,  $\hat{y}$ , and  $\hat{z}$  directions, are plotted in Fig. 6.7. The legends show the values of normal stresses in units of  $\varepsilon/\sigma^3$ . As it is required by the conservation of the momentum, the component of pressure tensor normal to any interface is constant across that interface. Therefore, the stress  $\tau_{xx}$  is constant across the fluid/fluid interface ( $\hat{x}$  direction) and  $\tau_{zz}$  is constant across the fluid/wall interface ( $\hat{z}$  direction). This also indicates that the modified stress algorithm is accurate and it can be used for further analysis, in particular, the evaluation of stresses in a shear flow. The next step is to calculate the surface tension of the fluid/fluid interface

$$\gamma = \int (\tau_{\perp} - \tau_{\parallel}) dx, \quad (6.2)$$

where  $\tau_{\perp}$  and  $\tau_{\parallel}$  are the normal stresses perpendicular and parallel to the interface, respectively. The value of the surface tension calculated from Eq. (6.2) is about  $\gamma = 3.7 \pm 0.2\varepsilon\sigma^{-2}$ , which agrees well with previous studies for similar flow conditions [141, 144].

Fig. 6.8(a) shows an enlarged view of an equilibrated system near the contact line. The depletion region of fluid monomers near the fluid/fluid interface approximately defines the location of the contact line. This is also consistent with the density reduction in each fluid phase close to the interface in Fig. 6.6(b). The arrows indicate the direction of the tangential forces  $F_x$  from the solid wall applied on each fluid phase at the fluid/solid interface near the contact line. The distribution of the tangential force per unit area is defined as the shear stress  $\tau_{xz}(x)$ . In Fig. 6.8(b), far away from the contact line region, the shear stress vanishes as expected in the equilibrium case. However, the net tangential force on the left and right sides of the contact line becomes negative and positive, respectively. The finite value of the tangential force is due to the repulsive interaction between fluid monomers that belong to different fluid phases.

### 6.2.2 Shear flow

In this section, the effects of shear flow on the moving contact line, the contact angle, and velocity profiles are presented. The shear flow is induced by translating the upper and lower walls in opposite directions while the center of mass of the fluid phases remains in the center of the channel. The configuration of monomers for the selected upper/lower wall speeds is plotted in Fig. 6.9. As the wall velocity  $U$  increases, the fluid/fluid interface remains straight and the contact angle, measured in the advancing fluid, becomes larger. The values of the contact angle as a function of the fluid velocity are shown in Fig. 6.10. For the velocities considered in the present study, the contact angle increases linearly from  $\theta_s = 90^\circ$  when  $U = 0$  to  $\theta_d = 115^\circ$  when  $U = 0.1\sigma/\tau$ . However, at higher velocities,  $U \gtrsim 0.12\sigma/\tau$ , the fluid/fluid interface undergoes an unsteady motion and breaks up, while the contact angle varies significantly (not shown).

For  $U = 0.1\sigma/\tau$ , the configuration of fluid monomers near the contact line region is shown in Fig. 6.11 (top). The flow behavior in this system is studied by averaging the instantaneous velocities of fluid monomers in small spatial bins over a long period of time. The average velocity vectors are estimated inside bins measuring  $1.0\sigma \times 7.90\sigma \times 0.9\sigma$  in the  $\hat{x}$ ,  $\hat{y}$ , and  $\hat{z}$  directions, respectively. An example of the averaged velocity vectors are plotted in Fig. 6.11 (bottom). The direction of vectors indicates the presence of circulation zones, which are centered in the bulk region of each fluid phase while rotating in a clockwise direction. The fluid flow cannot penetrate the fluid/fluid interface, and therefore, it is forced to adjust its direction and move parallel to the interface.

Inspired by the detailed resolution of the velocity profiles inside the fluid domain, the slip velocities can also be calculated near the fluid/solid interface. Fig. 6.12 shows the slip velocity of the first fluid layer averaged separately in each fluid phase. Due to weak wall/fluid interaction energy and incommensurable wall/fluid densities, a finite value of the slip velocity is observed far away from the contact line. In each fluid phase (indicated by symbols in Fig. 6.12), the slip velocity increases near the contact line and approaches the wall speed. However, the combined effect of slip flows from two fluids (shown by the dashed line) results in the peak of the slip velocity which is smaller than the wall speed. A

slightly smaller value of the peak in the slip velocity can be explained by the fact that the contact line region is not a line with an infinitesimal thickness but an area expanding about  $5\sigma$  in each fluid (see the density profiles in Fig. 6.6(b) and stress distributions in Fig. 6.8(b)). Moreover, the diffusive motion of the contact line can be another factor attributing to the reduced slip velocity at the contact line.

In Fig. 6.13(a) the slip velocity at the solid/liquid interface is plotted for the selected values of the walls speed  $U = 0.01\sigma/\tau$ ,  $U = 0.05\sigma/\tau$ , and  $U = 0.1\sigma/\tau$ . The slip velocity increases with the wall speed. An important question that needs to be answered for the continuum modeling is what should be the appropriate boundary condition near the contact line and whether the Navier slip law is valid in the region near the contact line. To investigate this issue, the slip length and the friction coefficient away from the contact line in a single fluid phase must be calculated. In Fig. 6.13(b), the velocity profiles in the bulk region away from the fluid/fluid interface are shown as a function of the wall speed. The velocity profiles are linear, and, therefore, the slip length is extracted from the extrapolation of a linear fit to the profiles. The intrinsic slip length for the flow of a single phase is estimated to be  $L_0 = 2.2 \pm 0.5\sigma$ . The fluid viscosity was calculated from the ratio of the bulk shear stress and shear rate away from the contact line  $\tau_{xz}/\dot{\gamma} = \mu = 2.0 \pm 0.2\varepsilon\tau\sigma^{-3}$ . As a result, the friction coefficient at the interface between a single phase fluid and the solid wall is the ratio of the shear viscosity to the slip length, i.e.,  $\beta_{slip} = \mu/L_0 = 0.9$ . These information will be used in the next section as a boundary condition in continuum modeling.

## 6.3 Details of continuum simulations

In moving boundary problems the interface treatment including shape, location, and velocity is highly complicated because the information on the interface need to be computed along with the field equations. Numerous techniques exist for tracking moving interfaces. These techniques can be classified under three main categories a) moving grid (Lagrangian) methods, b) Eulerian methods, and c) combined Lagrangian-Eulerian methods. All these approaches have their relative merits and none of them is superior for all applications.

In this section, the problem of the contact line motion is modeled using a Lagrangian-Eulerian algorithm. The Navier-Stokes (N-S) equations are solved with the finite difference method on a fixed Eulerian grid combined with tracking Lagrangian marker points assigned on the fluid/fluid interface. The N-S equations provide the description of the pressure and velocity distributions in the fluid domain [149]. The marker points determine the time evolution of the fluid/fluid interface [150]. Meanwhile, the molecular dynamics simulations provide correct boundary conditions near the contact line (i.e., the slip length, shear stresses, and friction coefficients).

### 6.3.1 Fixed grid method for immersed objects

This method operates on a fixed Cartesian mesh (Eulerian part) while the fluid/fluid interfaces move through the mesh (Lagrangian part). The advantage of the fixed grid approach is that the grid topology remains simple while large distortions of the interface take place. In the immersed boundary method, originally used by Peskin [148] to model heart flows, the interface can be handled via a set of marker points.

#### Interface

Consider a fluid domain, which is covered with a fixed Cartesian grid. The interface between Fluid 1 and Fluid 2 represented by a curve  $C$ . The grid spacing is  $h$ . The immersed boundary denoted by  $C(t)$  (a curve in 2D case) is represented by  $k$  markers or interfacial points with coordinate  $\vec{x}_k(s)$  with  $k = 1, 2, \dots, K$ . The markers are uniformly distributed along  $C(t)$  at a fraction of the grid spacing,  $0.5 < ds < 1.5h$ . The fluid/fluid interface is parameterized as

a function of the arclength  $s$  by fitting a local cubic polynomial to every four neighboring points. Once the interface position is known, the normal vector and curvature are evaluated and the material properties in each fluid are assigned. The normal vector in  $2D$  is given by

$$n_x = -\frac{y_s}{\sqrt{x_s^2 + y_s^2}} \quad \text{and} \quad n_y = \frac{x_s}{\sqrt{x_s^2 + y_s^2}}, \quad (6.3)$$

where subscript  $s$  denotes  $d/ds$ . The curvature is then obtained by taking the divergent of the normal vector:

$$\kappa = \vec{\nabla} \cdot \vec{n}. \quad (6.4)$$

Knowing the interface location with respect to the grid system, the material properties are assigned in each fluid phase based on a Heaviside step function:

$$\beta = \beta_1 + (\beta_2 - \beta_1)H(\vec{x} - \vec{x}_k), \quad (6.5)$$

where  $\beta$  is the material property such as  $\rho$  density and  $\mu$  shear viscosity. The subscripts 1 and 2 denote Fluid 1 and Fluid 2, respectively. The function  $H(\vec{x} - \vec{x}_k)$  is the discrete Heaviside step function defined as:

$$H(\vec{x} - \vec{x}_k) = \begin{cases} \prod_{m=1}^{\dim} \frac{1}{2} \left( 1 + \frac{(\vec{x}_m - (\vec{x}_m)_k)}{d} + \frac{1}{\pi} \sin \frac{\pi(\vec{x}_m - (\vec{x}_m)_k)}{d} \right) & \text{if } |\vec{x} - \vec{x}_k| \leq d \\ 1 & \text{if } \vec{x} - \vec{x}_k > +d \\ 0 & \text{if } \vec{x} - \vec{x}_k < -d \end{cases}, \quad (6.6)$$

where  $\dim$  is the spatial dimension,  $d = 2h$  with  $h$  is the grid spacing,  $\vec{x}$  is the grid coordinate, and  $\vec{x}_k$  is the interfacial marker coordinate. The Heaviside step function allows a smooth distribution of the material properties over a transition zone  $d$ . The transition zone is twice the grid spacing  $d = 2h$ . Therefore, the interface has the finite thickness  $d$ . Once the material properties are assigned to each fluid, the fluid flow equations can be solved.

### Immersed boundary treatment

The immersed boundary technique facilitates the communication between the moving markers, which represent the interface and the fixed grid. In particular, since the location of the marker points does not coincide with the grid points, the velocity field stored at the cell-center of each grid is interpolated to obtain the velocity of the interface points, and the

interface forces acting on the marker points is distributed to the nearby grid points using a discrete Delta function. The Delta function is given by:

$$\delta(\vec{x} - \vec{x}_k) = \begin{cases} \prod_{m=1}^{\text{dim}} \frac{1}{2d} \left( 1 + \cos \frac{\pi(\vec{x}_m - (\vec{x}_m)_k)}{d} \right) & \text{if } |\vec{x} - \vec{x}_k| \leq d \\ 0 & \text{otherwise} \end{cases}. \quad (6.7)$$

The delta function is the derivative of the Heaviside function and typically spreads over the region of  $4h$ .

Estimation of the force  $\vec{F}$ : The force exerted by the fluid/fluid interface on the flow is added to the momentum equation. The integral of the source terms is expressed as:

$$\vec{F} = \int_{C(t)} \gamma \kappa \hat{n} \delta(\vec{x} - \vec{x}_k) ds, \quad (6.8)$$

where the integral is taken over  $C(t)$ ,  $\gamma$  is the surface tension,  $\kappa$  is the curvature,  $\hat{n}$  is the normal unit vector,  $\delta(\vec{x} - \vec{x}_k)$  is the 'Dirac' Delta function,  $\vec{x}$  gives the location of the grid points,  $\vec{x}_k$  gives the position of the markers as a function of arclength  $s$ . In the discretized form, the force is estimated by:

$$\vec{F}_p = \sum_k \gamma \kappa_k \hat{n}_k \delta(\vec{x} - \vec{x}_k) \Delta s_k, \quad (6.9)$$

The force at the point  $P$ ,  $F_p$ , is evaluated based on the summation of all interfacial forces of the marker points located inside a circle of radius  $2h$  weighted by the Delta function.

Estimation of the interface velocity  $\vec{U}_k$ : The velocity of a marker point or interface velocity denoted by  $\vec{U}_k$  should satisfy the continuity condition. So  $\vec{U}_k$  is:

$$\vec{U}_k = \int_{\Omega} \vec{u} \delta(\vec{x} - \vec{x}_k) d\vec{x}, \quad (6.10)$$

where the integral is over the entire fluid domain  $\Omega$ ,  $\vec{u}$  is the fluid velocity vector, and  $\delta(\vec{x} - \vec{x}_k)$  is the Delta function. In the discretized form, the velocity of the marker point is:

$$\vec{U}_k = \sum_{ij} \vec{u}_{ij} \delta(\vec{x} - \vec{x}_k) h^2, \quad (6.11)$$

where  $h$  is the grid spacing,  $i$  and  $j$  are the grid indices and  $\vec{u}$  is the fluid velocity. The velocity at the  $k^{th}$  marker,  $\vec{U}_k$ , is the sum of the fluid velocity of the grid points located inside a circle of radius  $2h$ , weighted by the Delta function.

The interface velocity  $\vec{U}_k$  is by definition the time derivative of the marker point position:

$$\vec{U}_k = \frac{\partial \vec{x}}{\partial t}. \quad (6.12)$$

Therefore, the interface is advected as:

$$\vec{x}_k^{n+1} = \vec{x}_k^n + \Delta t(\vec{U}_k^n). \quad (6.13)$$

The dynamics of two immiscible fluids in a channel is governed by the incompressible Navier-Stokes equations given below

$$\nabla \cdot \mathbf{u} = 0, \quad (6.14)$$

$$\frac{\partial(\rho\mathbf{u})}{\partial t} + \nabla \cdot (\mathbf{u}\rho\mathbf{u}) = -\nabla p + \mu\nabla^2\mathbf{u} + \mathbf{F}. \quad (6.15)$$

In these equations  $\mathbf{u}$  is the fluid velocity vector,  $p$  the pressure,  $\mathbf{F}$  the body force,  $\mu$  the dynamic viscosity of fluid,  $\rho$  the density of fluid, and  $t$  time. The properties are constant in each fluid.

The Navier-Stokes equations are solved using the projection method on fixed Cartesian grids. The projection method is divided into three steps:

Step1: Solve the momentum equations without pressure. Evaluation of the intermediate velocities  $\tilde{u}_x$  and  $\tilde{u}_z$  for a two dimensional problem:

$$\left( \frac{\tilde{\mathbf{u}} - \mathbf{u}^n}{\Delta t} \right) + \left( \frac{3(\mathbf{u} \cdot \nabla \mathbf{u})^n - (\mathbf{u} \cdot \nabla \mathbf{u})^{n-1}}{2} \right) = \frac{\nu \nabla^2 \mathbf{u}^n - \nu \nabla^2 \tilde{\mathbf{u}}}{2} + \mathbf{F}, \quad (6.16)$$

where  $n$  is the time step level and  $F$  is the source term.

The pressure equation is derived by assuming that the velocity satisfies the continuity equation at  $n + 1$  time step level.

Step 2: The following equation is solved for the pressure

$$\nabla \cdot \mathbf{u}^{n+1} = 0 \Rightarrow \nabla \cdot \left( \frac{1}{\rho} \nabla p^{n+1} \right) = \frac{1}{\Delta t} \nabla \cdot \tilde{\mathbf{u}}. \quad (6.17)$$

Step 3: Combining the velocity and pressure information: Finally, the correction step is done as follows

$$\mathbf{u}^{n+1} = \tilde{\mathbf{u}} - \Delta t \left( \frac{1}{\rho} \nabla p^{n+1} \right). \quad (6.18)$$

### 6.3.2 Continuum Results

All variables in continuum simulations are normalized by the  $LJ$  length  $\sigma$ , time  $\tau$ , and energy  $\varepsilon$  scales. The cell dimensions are set to  $L_x = 100$  and  $L_z = 25$  in the  $\hat{x}$  and  $\hat{z}$  directions, respectively. The system setup is designed to mimic the MD simulations with only one fluid/fluid interface for simplicity. The schematic picture of the system is shown in Fig. 6.14 (top).

The upper and lower walls are moving in the opposite directions with velocity  $U$ . At the inlet and outlet it is assumed that the flow enters the system parallel to the walls  $u_z|_{inlet} = 0$  and  $\frac{\partial u_x}{\partial x}|_{inlet} = 0$ . In Fig. 6.14 (top) the red circles represent the initial location of the Lagrangian marker points. The total number of the marker points is set to  $N_p = 30$  to ensure an accurate resolution of the fluid/fluid interface with respect to the number of grids in the  $\hat{z}$  direction ( $N_z = 25$ ). The motion of these marker points is governed by Eq. (6.13). Far away from the contact line, along the green line in the Fig. 6.14, the slip velocity  $u_{slip}$  is calculated using the Navier slip condition with  $\beta_{slip} = 0.9$  and  $\mu = 2.0$  extracted from the MD simulations. At the contact lines indicated by the blue circles in the schematic picture, the velocity  $u_{contact}$  is estimated from the following equation

$$u_{contact} = \gamma(\cos(\theta_s) - \cos(\theta)) / \beta_{CL}, \quad (6.19)$$

where  $\beta_{CL}$  is the friction coefficient at the contact line,  $\gamma = 3.7$  the surface tension, and  $\theta_s = 90^\circ$  the static contact angle. The value of  $\beta_{CL} = 10.5$  is selected by trial and error so that the contact angle  $\theta = \theta_d$  in the converged solution stays within an error bar of about 5 degrees from the dynamic contact angle predicated by the MD simulations. Applying the correct boundary condition for the rest of the domain (blue lines of in Fig. 6.14 (top)) is challenging. In this region neither the far-field Navier condition nor the contact point dynamics can be applied. Therefore, motivated by the shape of the slip velocity profiles from the MD simulations (see Fig. 6.13(a)), a Delta function similar to Eq. (6.7) with the maximum value of  $u_{contact}$  and a minimum value of  $u_{slip}$  is used. The schematic shape of velocity distribution is shown in Fig. 6.14 (bottom). The values of the  $u_{contact}$  and  $u_{slip}$  vary during the numerical iterations based on the temporary contact angle and the local shear rate until the solution converges.

The velocity vectors and the streamlines are shown in Fig. 6.15 for  $U = 0.01$ ,  $U = 0.05$ , and  $U = 0.1$ . The streamline directions indicate that the fluid can not penetrate into the contact region, and, therefore, a circulation zone is formed in each side of the contact line, which is shown by a red line. The dynamic contact angle as a function of the wall speed is plotted in Fig. 6.16 and the results are compared with MD simulations. The dynamic contact angle in the advancing fluid phase increases with increasing wall speed. As discussed earlier in Sec. 6.2 and shown in the Fig. 6.16, the value of the friction coefficient  $\beta_{CL}$  was chosen to keep the contact angle extracted from the Navier-Stokes solution within an error bar of about  $5^\circ$  from the MD results.

The slip velocity profiles from the Navier-Stokes solution are plotted in Fig. 6.17 by symbols and compared with MD results (dashed lines) for the selected wall speeds. The continuum results successfully reproduce the slip velocity profiles away from the contact line. The results show qualitative agreement between the shape of the profiles near the contact line. Note that one of the differences between the MD and continuum results is that the slip velocity profile from N-S solution is narrower near the contact region. This discrepancy can be in part attributed to an ambiguity in defining the width of the Delta function Eq. (6.7) in the contact region shown in Fig. 6.14 (bottom). It is not clear at present whether the region near the contact line should be about  $3 - 5\sigma$  (as deduced from the density profiles and shear stress distribution) or even about  $10\sigma$  (the width of slip velocity profiles).

## 6.4 Conclusions

The problem of moving contact line between two immiscible fluids on a smooth surface is studied using molecular dynamics (MD) and continuum simulations. The flow boundary conditions near the moving contact line extracted from MD simulations and applied in the continuum solution of the Navier-Stokes equation to reproduce velocity profiles and the shape of the fluid/fluid interface. The algorithm based on the Irving-Kirkwood relation for stress calculation provides an accurate description of shear stresses near fluid/fluid and fluid/solid interfaces. With increasing wall speed, the contact angle increases and the slip velocity near the contact line is significantly larger than in shear flow of a single fluid

phase. By implementing the slip boundary condition extracted from MD simulations, the continuum method successfully reproduces the flow pattern and velocity profiles.

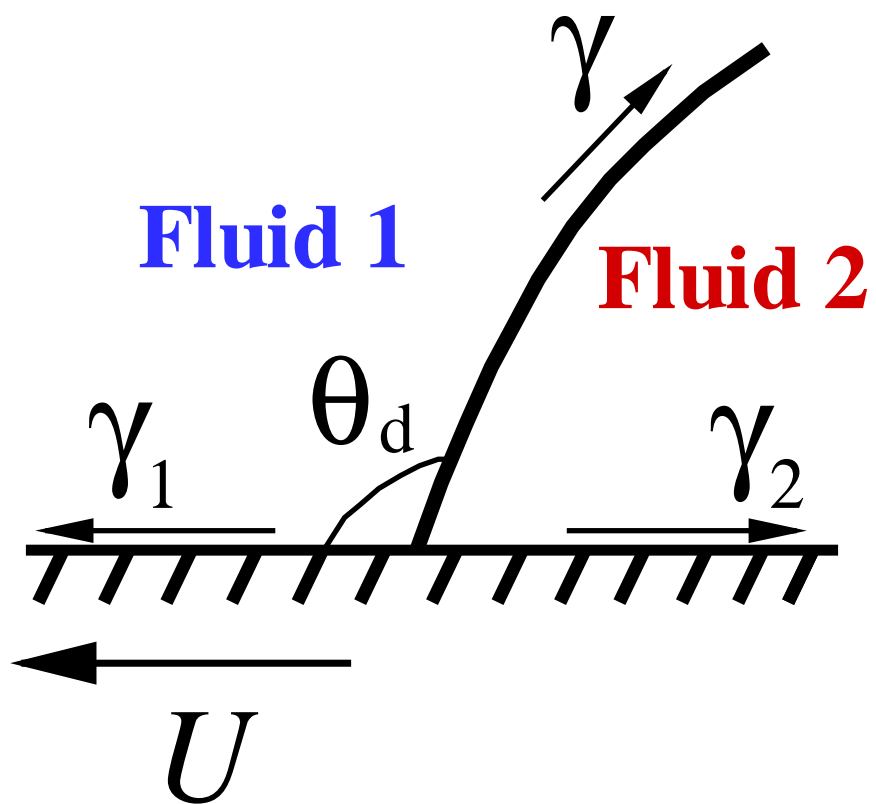
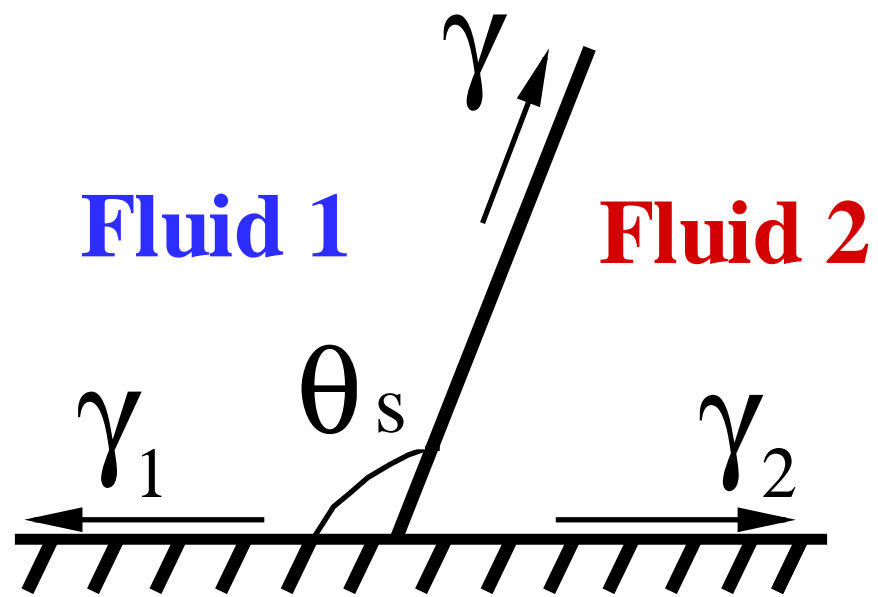


Figure 6.1. The schematic representation of the contact line and the shape of the fluid/fluid interface for the static (left) and dynamic (right) cases.

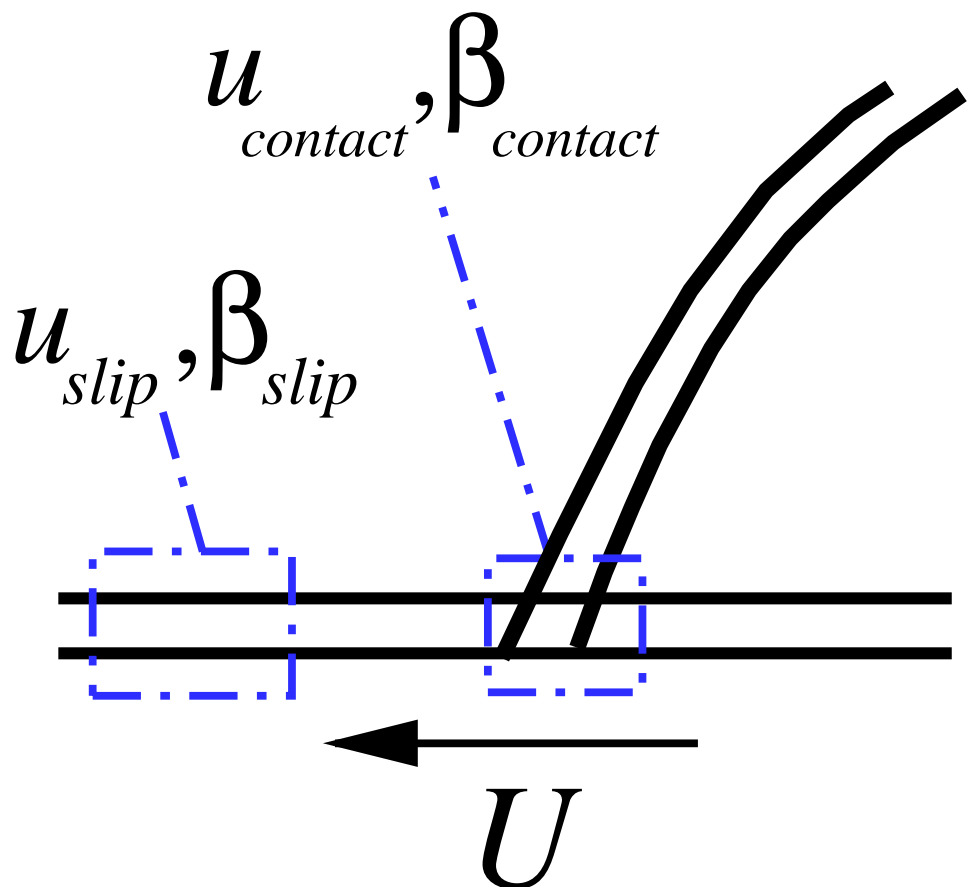


Figure 6.2. The schematic picture of the moving contact line problem where the slip velocity and the friction coefficient far from the contact line are denoted by  $u_{slip}$  and  $\beta_{slip}$  and in the contact region by  $u_{contact}$  and  $\beta_{contact}$ .

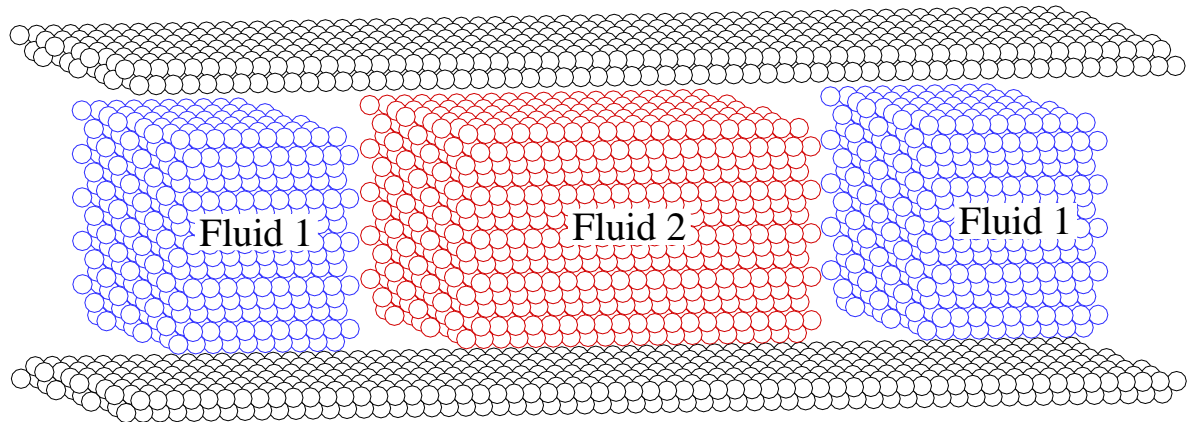


Figure 6.3. Initial arrangement of fluid molecules and wall atoms in the system that consists of two immiscible fluids confined between flat walls.

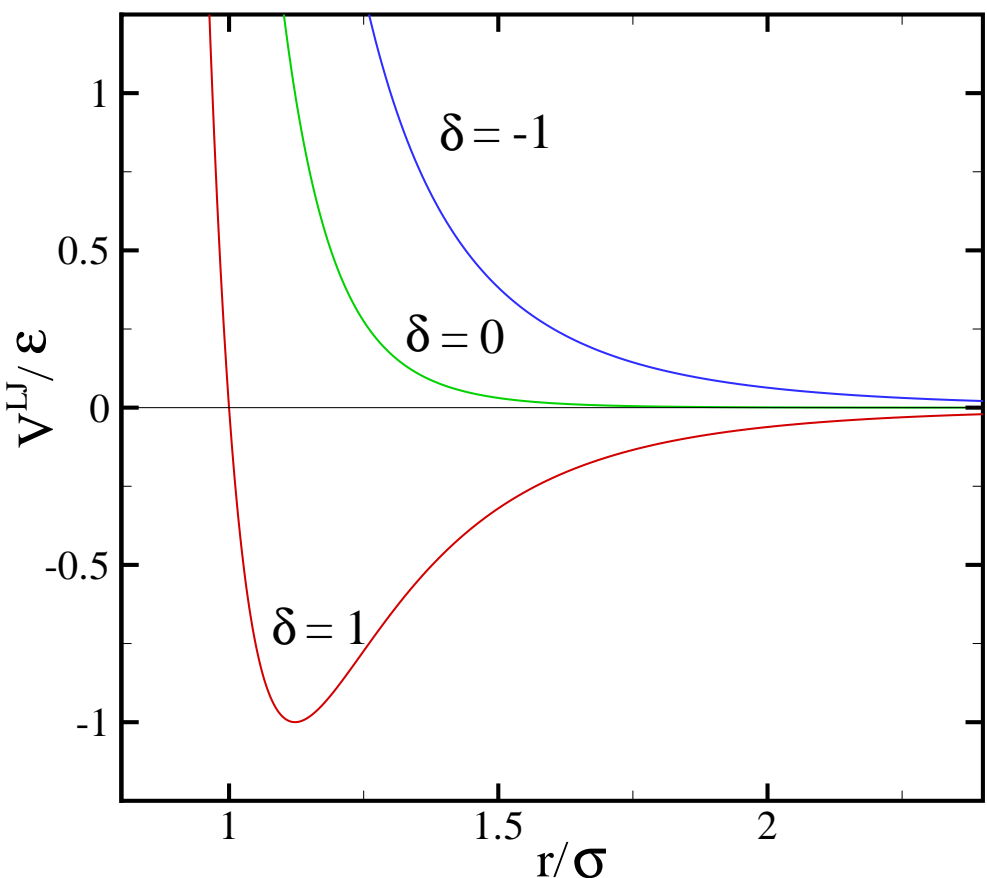


Figure 6.4. The modified Lennard-Jones potential Eq. (6.1) as a function of monomer/monomer distance for different values of the parameter  $\delta$ .

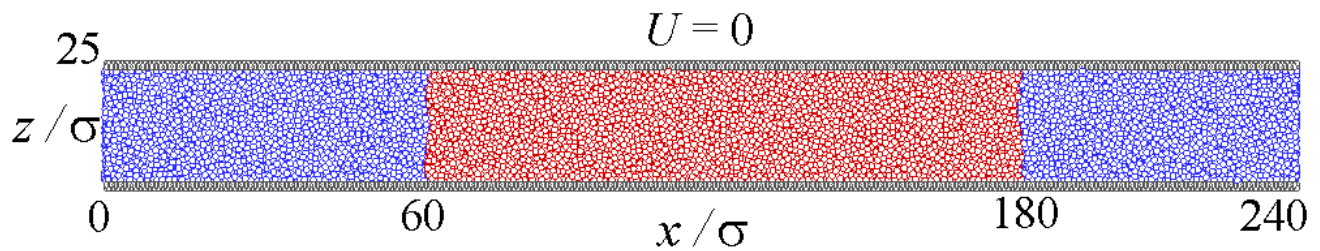


Figure 6.5. A snapshot of an equilibrated system with two immiscible fluids when both walls are at rest.

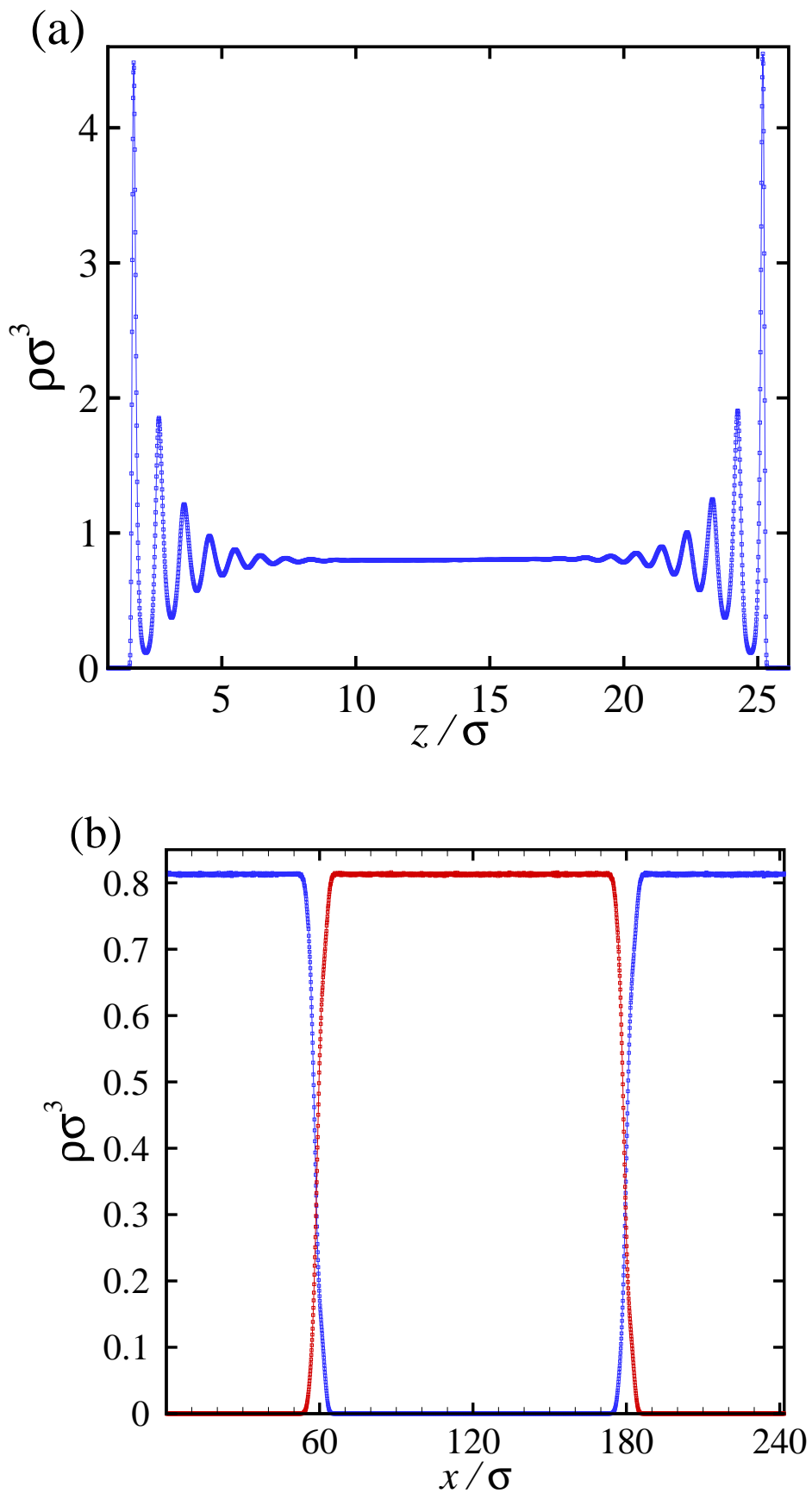


Figure 6.6. The averaged density profiles for fluid 1 across the channel width in the  $\hat{z}$  direction (a) and density profiles for fluids 1 and 2 parallel to the walls in the  $\hat{x}$  direction (b).

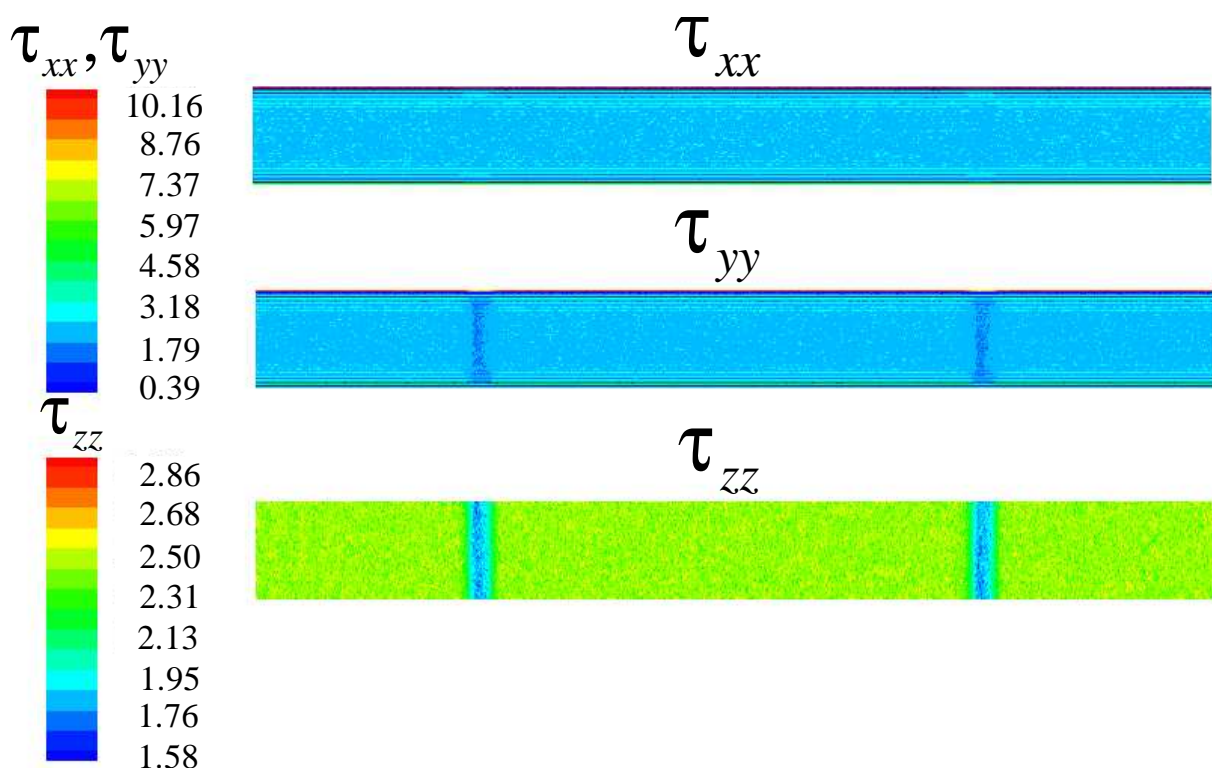


Figure 6.7. The normal stress distributions in the  $\hat{x}$ ,  $\hat{y}$ , and  $\hat{z}$  directions in equilibrium case ( $U = 0$ ) calculated from the Irving-Kirkwood relation. The normal stresses are measured in units of  $\varepsilon/\sigma^3$ .

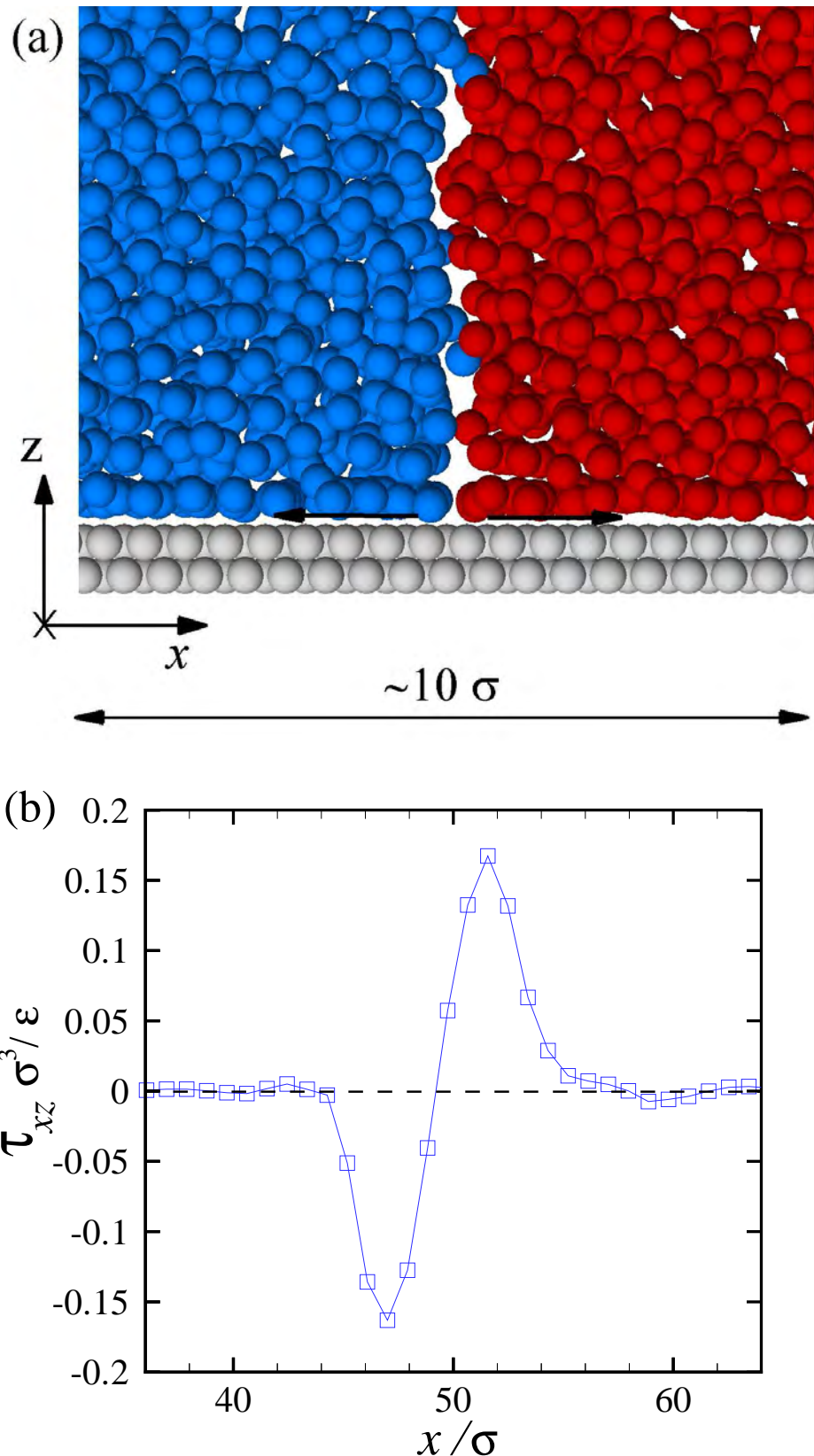


Figure 6.8. (a) The snapshot of the fluid molecules near the solid wall within  $5\sigma$  from the contact line at equilibrium. The horizontal arrows near the contact line indicate the direction of the tangential forces on each fluid. (b) The shear stress distribution  $\tau_{xz}(x)$  along the wall as a function of the distance from the contact line.

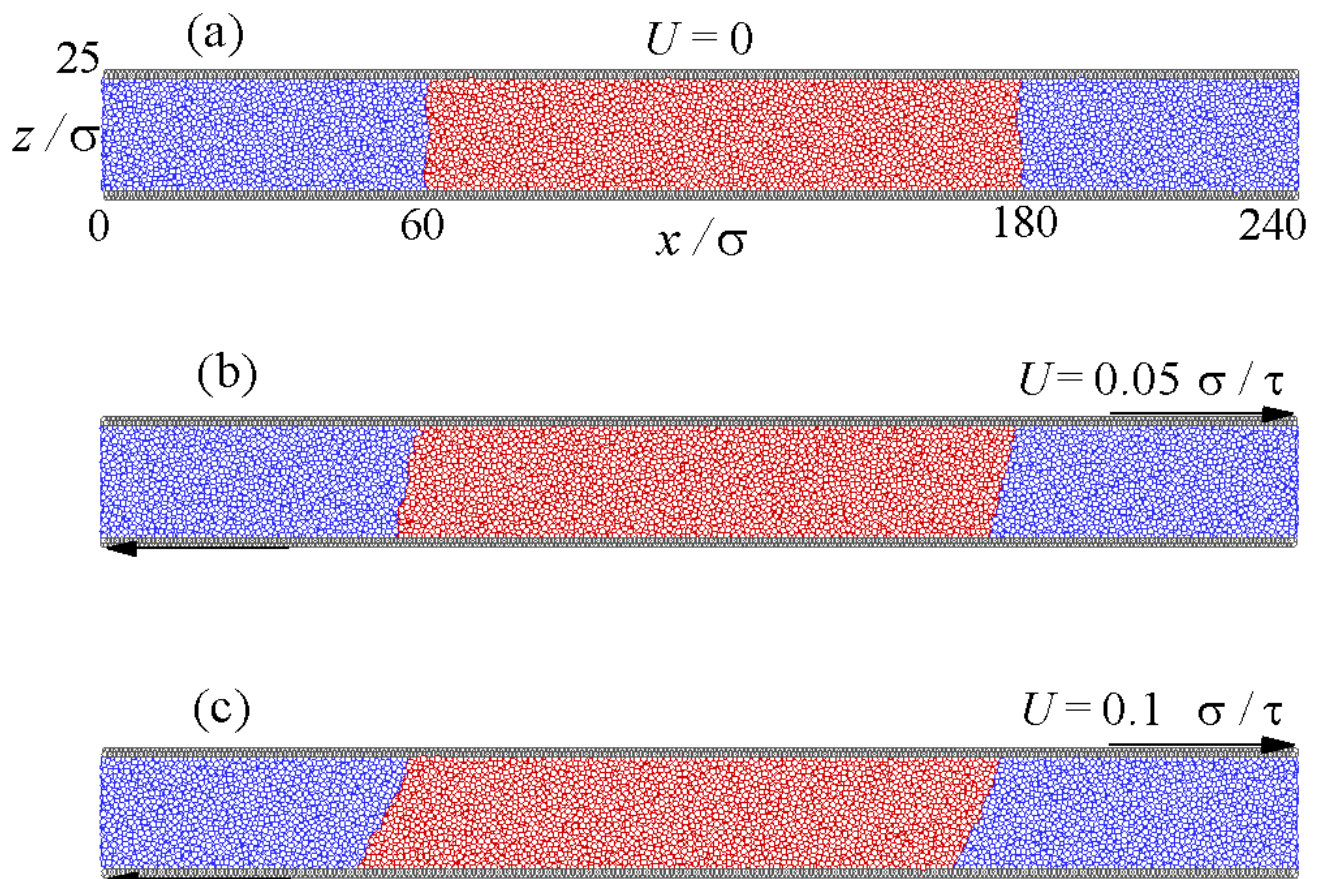


Figure 6.9. The shape of the fluid/fluid interfaces as a function of the wall speeds for (a)  $U = 0$ , (b)  $U = 0.05 \sigma / \tau$ , and (c)  $U = 0.1 \sigma / \tau$ .

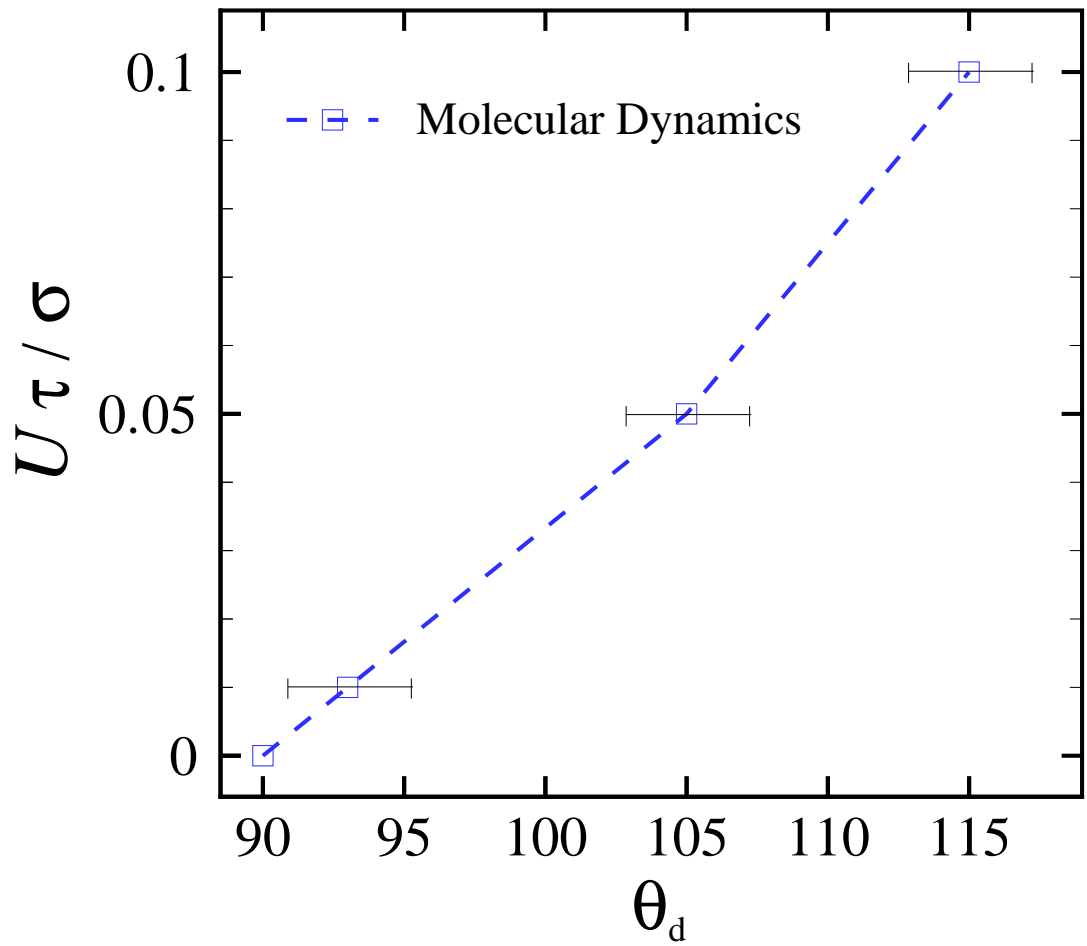


Figure 6.10. The contact angle averaged in two fluid phases is plotted as a function of the wall speeds  $U$ .

$$U = 0.1 \sigma/\tau$$

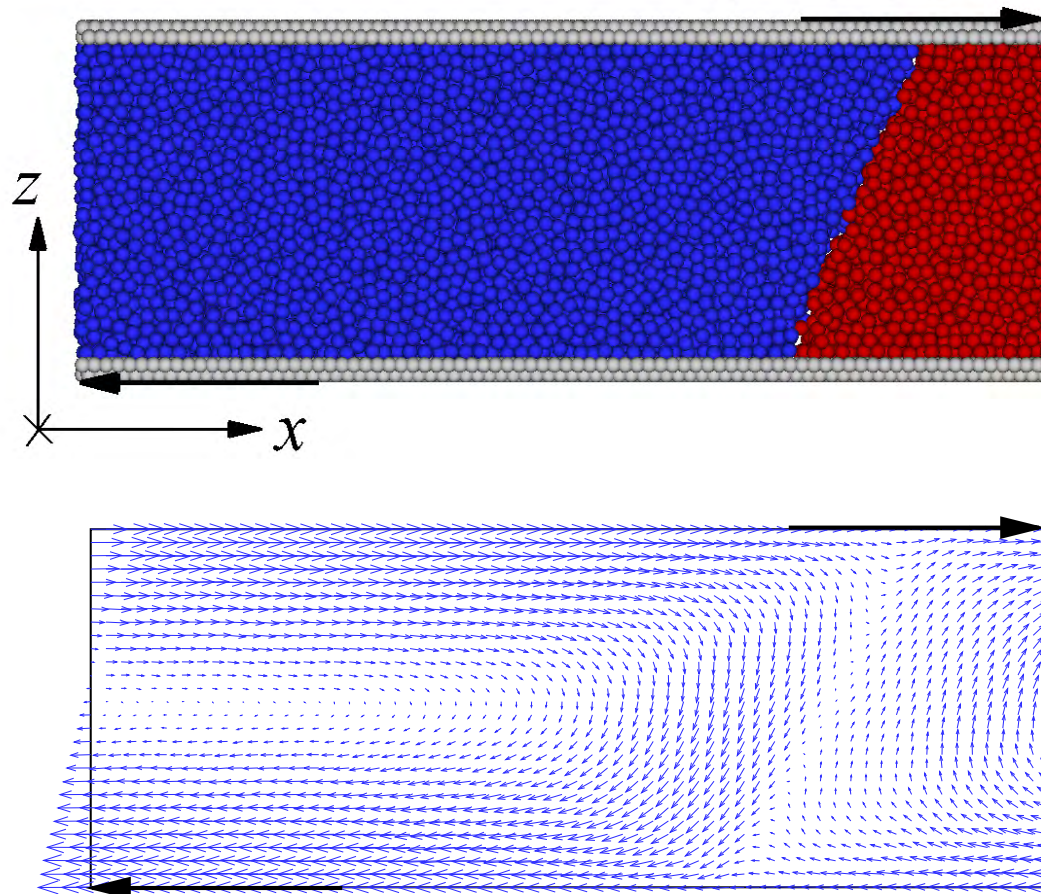


Figure 6.11. The snapshot of the system near the contact line for  $U = 0.1 \sigma/\tau$  (top), the averaged velocity vectors (bottom) obtained from MD simulations.

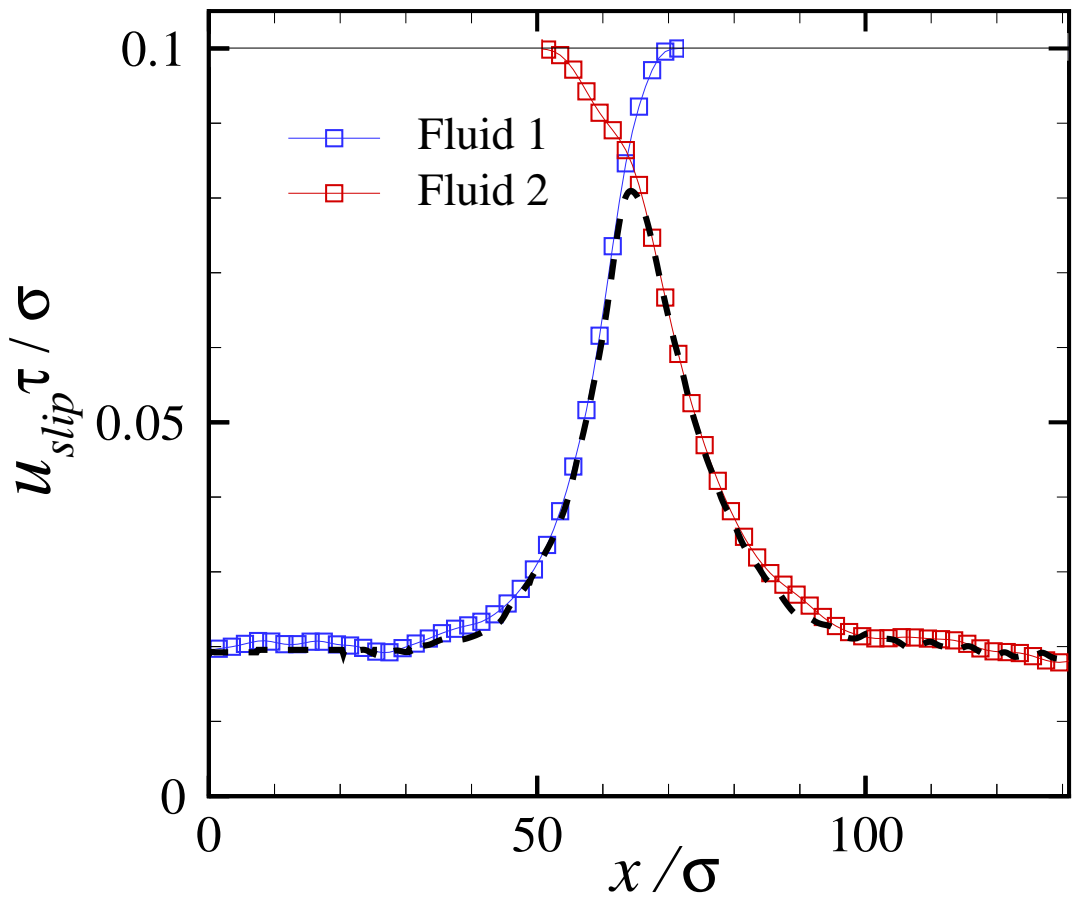


Figure 6.12. The slip velocity of the first fluid layer for upper and lower wall speeds  $U = 0.1 \sigma/\tau$ . The velocity profiles are averaged separately in each fluid phase as shown by symbols. The dashed line is the slip velocity computed regardless of the fluid type. The black solid is a guide for the eye.

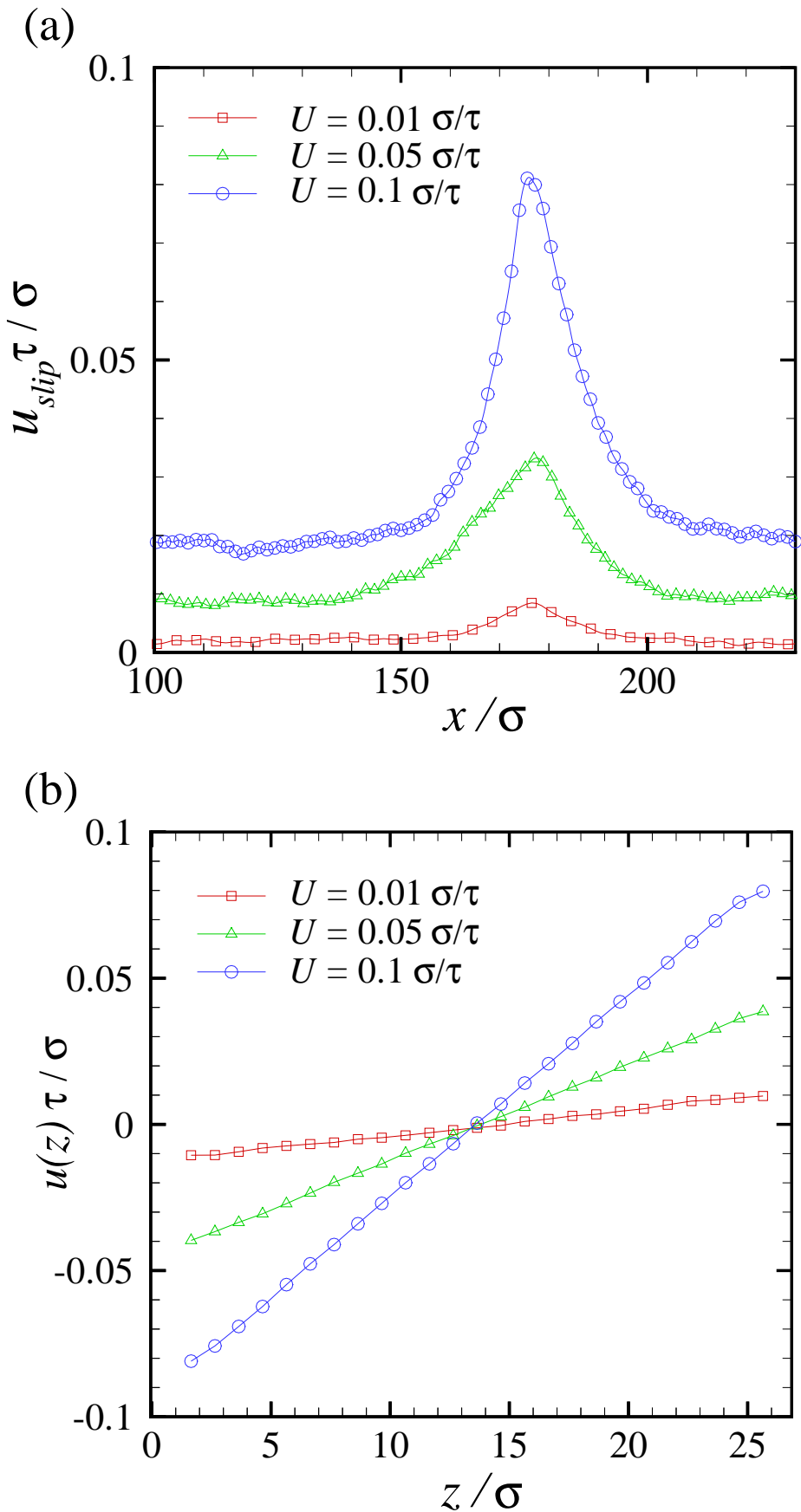


Figure 6.13. (a) The slip velocity in the first fluid layer as a function of upper/lower wall speeds. (b) The velocity profiles across the channel far from the contact lines in the  $\hat{z}$  direction as a function of the upper/lower wall speeds.

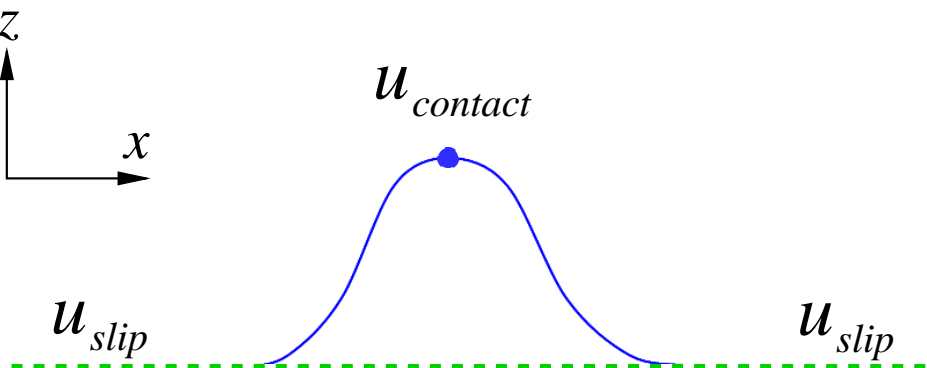
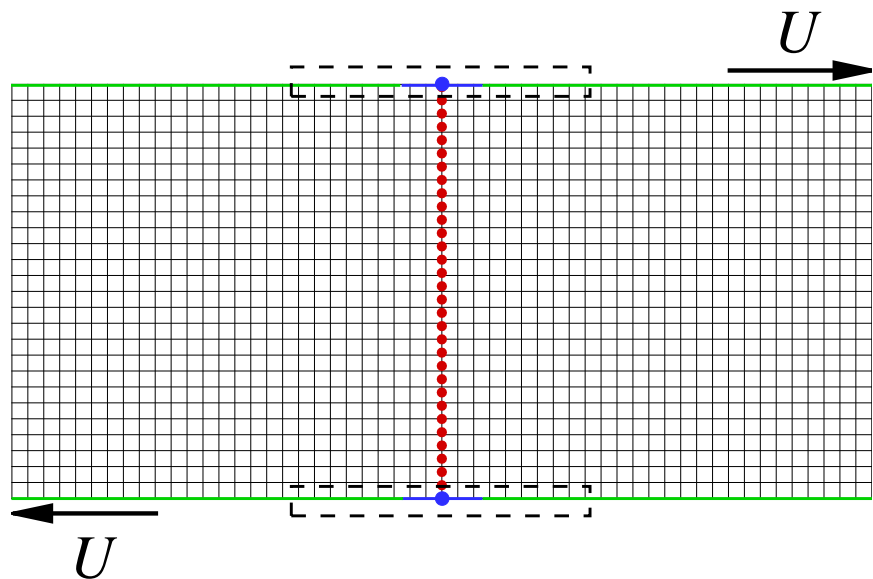


Figure 6.14. The setup of the continuum simulations where the black solid lines show the fixed Cartesian grids, the red circles are the initial position of the marker points, and the blue circles are the initial location of the contact points. The boundary conditions are applied along the green regions away from the contact point and along blue regions close to the contact point (top). The schematic velocity profile in the bottom figure shows an enlarged view of the velocity profile inside top figure's dashed-boxes.

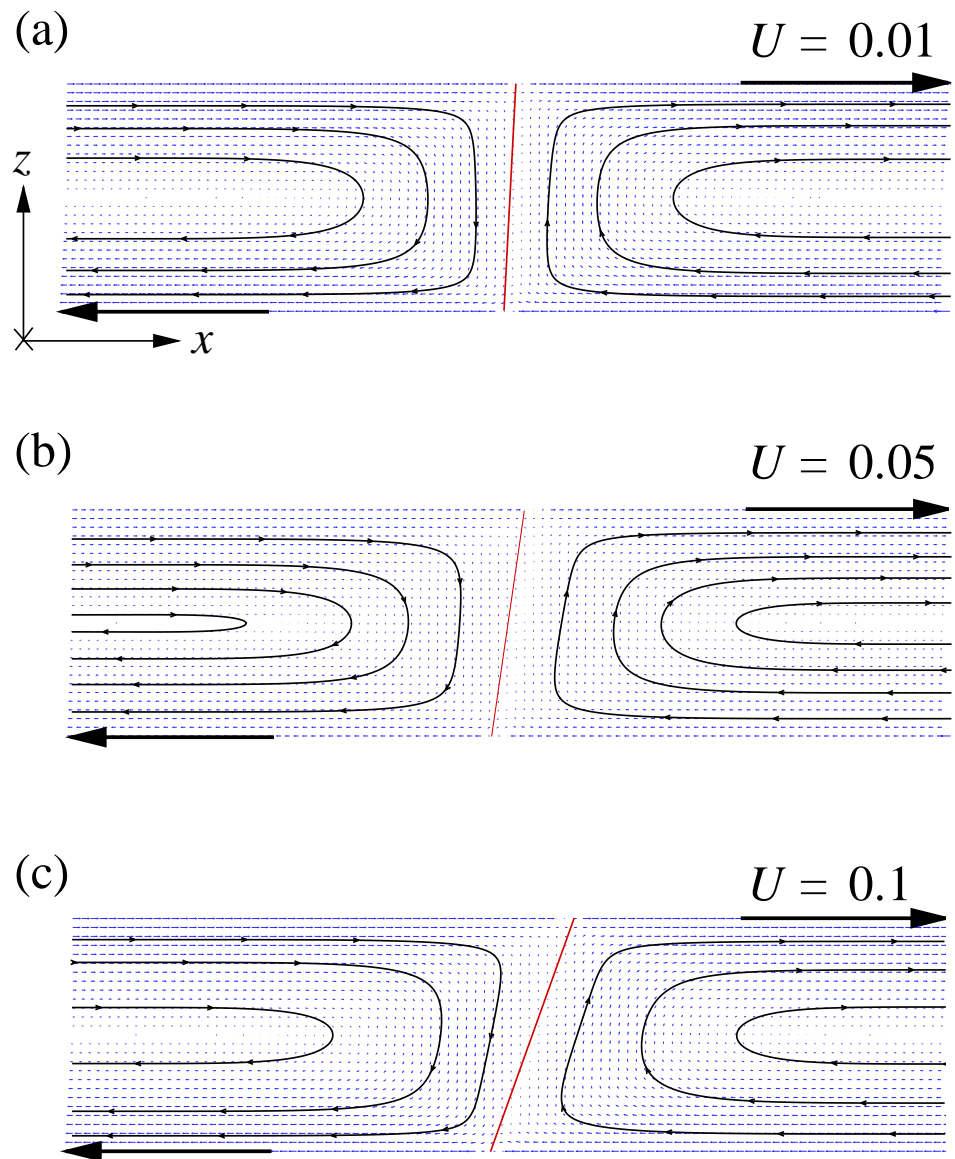


Figure 6.15. The results from the Navier-Stokes solution of the moving contact line as a function of upper/lower wall speeds  $U = 0.01$  (a),  $U = 0.05$  (b), and  $U = 0.1$  (c). The velocity vectors are shown by blue arrows, streamlines by black lines, and fluid/fluid interfaces by red lines.

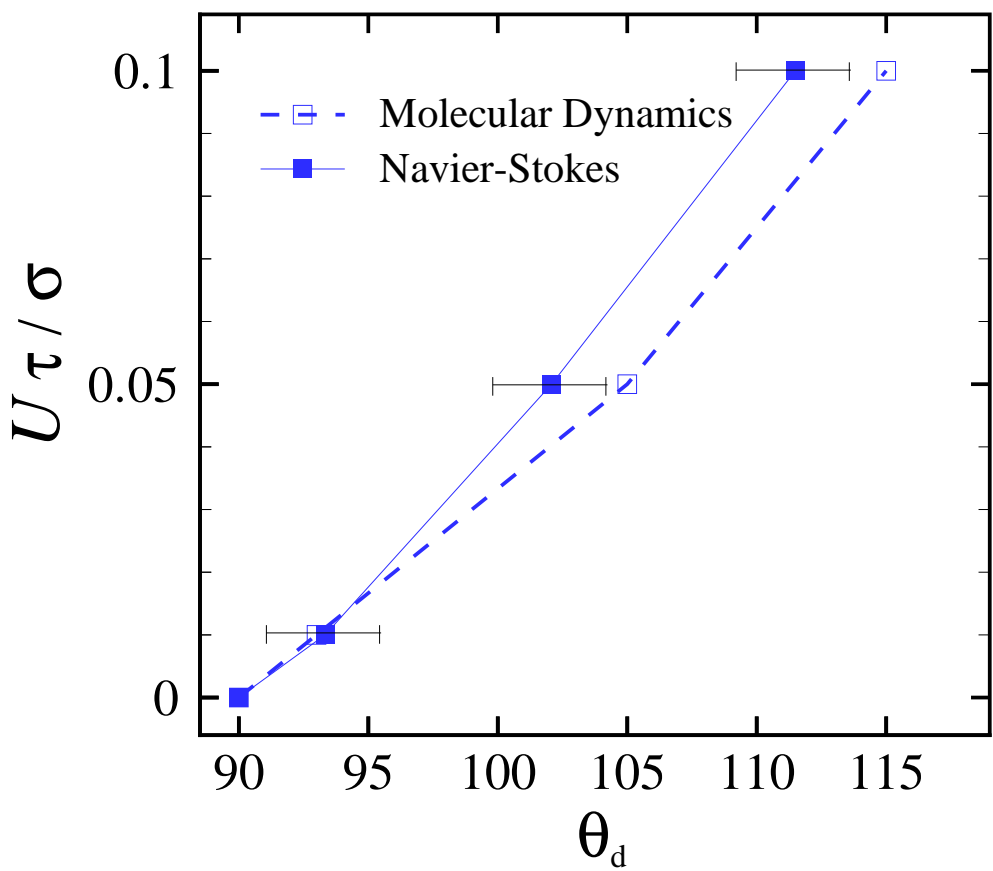


Figure 6.16. The filled symbols represent the contact angle extracted from the Navier-Stokes solution as a function of upper/lower wall speeds. The open symbols are the results from the molecular dynamics simulations. Solid and dashed lines are a guide for the eye.

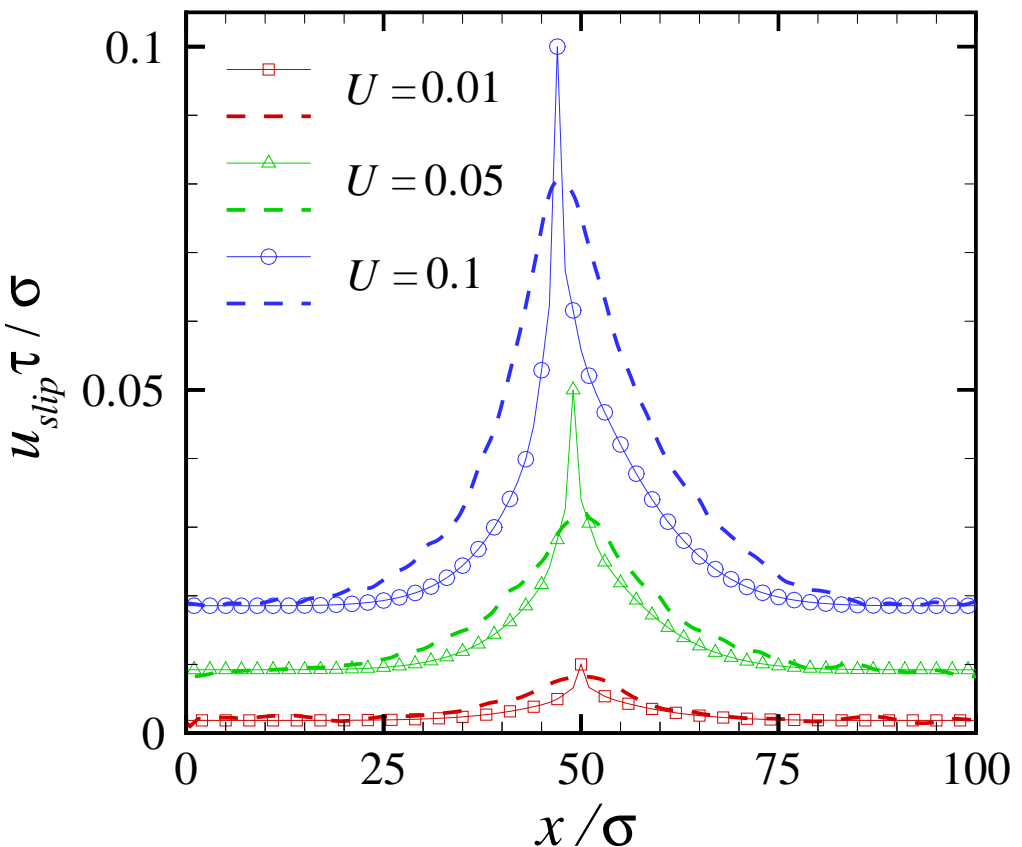


Figure 6.17. The symbols and solid lines show the slip velocities near the moving contact line obtained from the Navier-Stokes solution. The dashed lines are the slip velocities from molecular dynamics simulations in the first fluid layer as a function of upper/lower wall speeds.

## BIBLIOGRAPHY

- [1] G. Karniadakis, A. Beskok, and N. Aluru, *Microflows and nanoflows: Fundamentals and simulation* (Springer, New York, 2005).
- [2] H. A. Stone, A. D. Stroock, and A. Ajdari, “Engineering flows in small devices: Microfluidics toward a lab-on-a-chip,” *Annu. Rev. Fluid Mech.* **36**, 381 (2004).
- [3] A. A. Darhuber and S. M. Troian, “Principles of microfluidic actuation by modulation of surface stresses,” *Annu. Rev. Fluid Mech.* **37**, 425 (2005).
- [4] C. Neto, D. R. Evans, E. Bonaccurso, H. J. Butt, and V. S. J. Craig, “Boundary slip in Newtonian liquids: A review of experimental studies,” *Rep. Prog. Phys.* **68**, 2859 (2005).
- [5] N. V. Churaev, V. D. Sobolev, and A. N. Somov, “Slippage of liquids over lyophobic solid-surfaces,” *J. Colloid Interface Sci.* **97**, 574 (1984).
- [6] C. Cottin-Bizonne, S. Jurine, J. Baudry, J. Crassous, F. Restagno, and É. Charlaix, “Nanorheology: An investigation of the boundary condition at hydrophobic and hydrophilic interfaces,” *Eur. Phys. J. E* **9**, 47 (2002).
- [7] L. Joly, C. Ybert, and L. Bocquet, “Probing the nanohydrodynamics at liquid-solid interfaces using thermal motion,” *Phys. Rev. Lett.* **96**, 046101 (2006).
- [8] T. Schmatko, H. Hervet, and L. Leger, “Friction and slip at simple fluid-solid interfaces: The roles of the molecular shape and the solid-liquid interaction,” *Phys. Rev. Lett.* **94**, 244501 (2005).
- [9] R. Pit, H. Hervet, and L. Leger, “Direct experimental evidence of slip in hexadecane: Solid interfaces,” *Phys. Rev. Lett.* **85**, 980 (2000).
- [10] Y. Zhu and S. Granick, “Limits of the hydrodynamic no-slip boundary condition,” *Phys. Rev. Lett.* **88**, 106102 (2002).
- [11] E. Bonaccurso, H. J. Butt, and V. S. J. Craig, “Surface roughness and hydrodynamic boundary slip of a newtonian fluid in a completely wetting system,” *Phys. Rev. Lett.* **90**, 144501 (2003).
- [12] J. Sanchez-Reyes and L. A. Archer, “Interfacial slip violations in polymer solutions: Role of microscale surface roughness,” *Langmuir* **19**, 3304 (2003).
- [13] T. Schmatko, H. Hervet, and L. Leger, “Effect of nanometric-scale roughness on slip at the wall of simple fluids,” *Langmuir* **22**, 6843 (2006).
- [14] O. I. Vinogradova and G. E. Yakubov, “Surface roughness and hydrodynamic boundary conditions,” *Phys. Rev. E* **73**, 045302(R) (2006).
- [15] K. B. Migler, H. Hervet, and L. Leger, “Slip transition of a polymer melt under shear stress,” *Phys. Rev. Lett.* **70**, 287 (1993).

- [16] R. G. Horn, O. I. Vinogradova, M. E. Mackay, and N. Phan-Thien, "Hydrodynamic slippage inferred from thin film drainage measurements in a solution of nonadsorbing polymer," *J. Chem. Phys.* **112**, 6424 (2000).
- [17] Y. Zhu and S. Granick, "Rate-dependent slip of Newtonian liquid at smooth surfaces," *Phys. Rev. Lett.* **87**, 096105 (2001).
- [18] V. S. J. Craig, C. Neto, and D. R. M. Williams, "Shear-dependent boundary Slip in an aqueous Newtonian liquid," *Phys. Rev. Lett.* **87**, 054504 (2001).
- [19] C. H. Choi, K. J. A. Westin, and K. S. Breuer, "Apparent slip flows in hydrophilic and hydrophobic microchannels," *Phys. Fluids* **15**, 2897 (2003).
- [20] J. Koplik, J. R. Banavar, and J. F. Willemsen, "Molecular dynamics of fluid flow at solid interfaces," *Phys. Fluids A* **1**, 781 (1989).
- [21] P. A. Thompson and M. O. Robbins, "Shear flow near solids: Epitaxial order and flow boundary conditions," *Phys. Rev. A* **41**, 6830 (1990).
- [22] P. A. Thompson, M. O. Robbins, and G. S. Grest, "Structure and shear response in nanometer thick films," *Israel Journal of Chemistry* **35**, 93 (1995).
- [23] P. A. Thompson and S. M. Troian, "A general boundary condition for liquid flow at solid surfaces," *Nature (London)* **389**, 360 (1997).
- [24] A. Jabbarzadeh, J. D. Atkinson, and R. I. Tanner, "Wall slip in the molecular dynamics simulation of thin films of hexadecane," *J. Chem. Phys.* **110**, 2612 (1999).
- [25] J.-L. Barrat and L. Bocquet, "Large slip effect at a nonwetting fluid-solid interface," *Phys. Rev. Lett.* **82**, 4671 (1999).
- [26] M. Cieplak, J. Koplik, J. R. Banavar, "Boundary conditions at a fluid-solid interface," *Phys. Rev. Lett.* **86**, 803 (2001).
- [27] N. V. Priezjev and S. M. Troian, "Molecular origin and dynamic behavior of slip in sheared polymer films," *Phys. Rev. Lett.* **92**, 018302 (2004).
- [28] T. M. Galea and P. Attard, "Molecular dynamics study of the effect of atomic roughness on the slip length at the fluid-solid boundary during shear flow," *Langmuir* **20**, 3477 (2004).
- [29] N. V. Priezjev, "Rate-dependent slip boundary conditions for simple fluids," *Phys. Rev. E* **75**, 051605 (2007).
- [30] R. Khare, J. J. de Pablo, and A. Yethiraj, "Rheology of confined polymer melt," *Macromolecules* **29**, 7910 (1996).
- [31] A. Koike and M. Yoneya, "Chain length effects on frictional behavior of confined ultrathin films of linear alkanes under shear," *J. Phys. Chem. B* **102**, 3669 (1998).

- [32] A. Niavarani and N. V. Priezjev, “Slip boundary conditions for shear flow of polymer melts past atomically flat surfaces,” *Phys. Rev. E* **77**, 041606 (2008).
- [33] J. P. Gao, W. D. Luedtke, and U. Landman, “Structures, solvation forces and shear of molecular films in a rough nano-confinement,” *Tribol. Lett.* **9**, 3 (2000).
- [34] A. Jabbarzadeh, J. D. Atkinson, and R. I. Tanner, “Effect of the wall roughness on slip and rheological properties of hexadecane in molecular dynamics simulation of Couette shear flow between two sinusoidal walls,” *Phys. Rev. E* **61**, 690 (2000).
- [35] N. V. Priezjev and S. M. Troian, “Influence of periodic wall roughness on the slip behaviour at liquid/solid interfaces: Molecular-scale simulations versus continuum predictions,” *J. Fluid Mech.* **554**, 25 (2006).
- [36] C. Kunert and J. Harting, “Roughness induced boundary slip in microchannel flows,” *Phys. Rev. Lett.* **99**, 176001 (2007).
- [37] N. V. Priezjev, “Effect of surface roughness on rate-dependent slip in simple fluids,” *J. Chem. Phys.* **127**, 144708 (2007).
- [38] E. Lauga and H. A. Stone, “Effective slip in pressure-driven Stokes flow,” *J. Fluid Mech.* **489**, 55 (2003).
- [39] S. C. Hendy, M. Jasperse, and J. Burnell, “Effect of patterned slip on micro- and nanofluidic flows,” *Phys. Rev. E* **72**, 016303 (2005).
- [40] N. V. Priezjev, A. A. Darhuber, and S. M. Troian, “Slip behavior in liquid films on surfaces of patterned wettability: Comparison between continuum and molecular dynamics simulations,” *Phys. Rev. E* **71**, 041608 (2005).
- [41] T. Qian, X. P. Wang, and P. Sheng, “Hydrodynamic slip boundary condition at chemically patterned surfaces: A continuum deduction from molecular dynamics,” *Phys. Rev. E* **72**, 022501 (2005).
- [42] S. C. Hendy and N. J. Lund, “Effective slip boundary conditions for flows over nanoscale chemical heterogeneities,” *Phys. Rev. E* **76**, 066313 (2007).
- [43] S. Richardson, “On the no-slip boundary condition,” *J. Fluid Mech.* **59**, 707 (1973).
- [44] C. Cottin-Bizonne, J.-L. Barrat, L. Bocquet, and É. Charlaix, “Low-friction flows of liquid at nanopatterned interfaces,” *Nature Mat.* **2**, 237 (2003).
- [45] C. Cottin-Bizonne, C. Barentin, É. Charlaix, L. Bocquet, and J.-L. Barrat, “Dynamics of simple liquids at heterogeneous surfaces: Molecular-dynamics simulations and hydrodynamic description,” *Eur. Phys. J. E* **15**, 427 (2004).
- [46] M. Sbragaglia, R. Benzi, L. Biferale, S. Succi, and F. Toschi, “Surface roughness-hydrophobicity coupling in microchannel and nanochannel flows,” *Phys. Rev. Lett.* **97**, 204503 (2006).

- [47] M. Sbragaglia and A. Prosperetti, “A note on the effective slip properties for microchannel flows with ultrahydrophobic surfaces,” *Phys. Fluids* **19**, 043603 (2007).
- [48] J. Ou, B. Perot, and J. P. Rothstein, “Laminar drag reduction in microchannels using ultrahydrophobic surfaces,” *Phys. Fluids* **16**, 4635 (2004).
- [49] C. H. Choi and C. J. Kim, “Large slip of aqueous liquid flow over a nanoengineered superhydrophobic surface,” *Phys. Rev. Lett.* **96**, 066001 (2006).
- [50] P. Joseph, C. Cottin-Bizonne, J.-M. Benoit, C. Ybert, C. Journet, P. Tabeling, and L. Bocquet, “Slippage of water past superhydrophobic carbon nanotube forests in microchannels,” *Phys. Rev. Lett.* **97**, 156104 (2006).
- [51] D. Einzel, P. Panzer, and M. Liu, “Boundary condition for fluid flow: Curved or rough surfaces,” *Phys. Rev. Lett.* **64**, 2269 (1990).
- [52] P. Panzer, M. Liu, and D. Einzel, “The effects of boundary curvature on hydrodynamic fluid flow: Calculation of slip lengths,” *Int. J. Mod. Phys. B* **6**, 3251 (1992)
- [53] K. Kremer and G. S. Grest, “Dynamics of entangled linear polymer melts: A molecular dynamics simulation,” *J. Chem. Phys.* **92**, 5057 (1990).
- [54] G. S. Grest and K. Kremer, “Molecular-dynamics simulation for polymers in the presence of a heat bath,” *Phys. Rev. A* **33**, 3628 (1986).
- [55] J. P. Boon and S. Yip, *Molecular Hydrodynamics* (McGraw-Hill, New York, 1980).
- [56] M. P. Allen and D. J. Tildesley, *Computer Simulation of Liquids* (Clarendon, Oxford, 1987).
- [57] J. C. Heinrich and D. W. Pepper, *Intermediate Finite Element Method: Fluid Flow and Heat Transfer Applications* (Taylor and Francis, Philadelphia, 1999).
- [58] J. H. Irving and J. G. Kirkwood, “The statistical mechanical theory of transport processes. IV. The equations of hydrodynamics,” *J. Chem. Phys.* **18**, 817 (1950).
- [59] R. B. Bird, C. F. Curtiss, R. C. Armstrong, and O. Hassager, *Dynamics of Polymeric Liquids* 2nd ed. (Wiley, New York, 1987).
- [60] Z. Xu, J. J. de Pablo, and S. Kim, “Transport properties of polymer melts from non-equilibrium molecular dynamics,” *J. Chem. Phys.* **102**, 5836 (1995).
- [61] J. T. Bosko, B. D. Todd, and R. J. Sadus, “Viscoelastic properties of denrimers in the melt from nonequilibrium molecular dynamics,” *J. Chem. Phys.* **121**, 12050 (2004).
- [62] L. M. Hocking, “A moving fluid interface on a rough surface,” *J. Fluid Mech.* **76**, 801 (1976).
- [63] E. O. Tuck and A. Kouzoubov, “A laminar roughness boundary condition,” *J. Fluid Mech.* **300**, 59 (1995).

- [64] T. Aoyagi, J. Takimoto, and M. Doi, “Molecular study of polymer melt confined between walls,” *J. Chem. Phys.* **115**, 552 (2001).
- [65] I. Bitsanis and G. Hadzioannou, “Molecular-dynamics simulations of the structure and dynamics of confined polymer melts,” *J. Chem. Phys.* **92**, 3827 (1990).
- [66] S. J. Plimpton, *J. Comp. Phys.* **117**, 1 (1995); see also URL <http://lammps.sandia.gov>.
- [67] L. Bocquet and J.-L. Barrat, “Flow boundary conditions from nano- to micro-scales,” *Soft Matter* **3**, 685 (2007).
- [68] V. Mhetar and L. A. Archer, “Slip in entangled polymer solutions,” *Macromolecules* **31**, 6639 (1998).
- [69] K. M. Awati, Y. Park, E. Weisser, and M. E. Mackay, “Wall slip and shear stresses of polymer melts at high shear rates without pressure and viscous heating effects,” *J. Non-Newton. Fluid Mech.* **89**, 117 (2000).
- [70] X. Zhou, D. Andrienko, L. Delle Site, and K. Kremer, “Flow boundary conditions for chain-end adsorbing polymer blends,” *J. Chem. Phys.* **123**, 104904 (2005).
- [71] C. Pastorino, K. Binder, T. Kreer, and M. Muller, “Static and dynamic properties of the interface between a polymer brush and a melt of identical chains,” *J. Chem. Phys.* **124**, 064902 (2006).
- [72] S. Barsky and M. O. Robbins, “Molecular dynamics study of slip at the interface between immiscible polymers,” *Phys. Rev. E* **63**, 021801 (2001).
- [73] M. Tsige and G. S. Grest, “Molecular dynamics simulation of solvent-polymer interdiffusion: Fickian diffusion,” *J. Chem. Phys.* **120**, 2989 (2004).
- [74] J. L. Barrat and J. P. Hansen, *Basic concepts for simple and complex liquids* (Cambridge University Press, Cambridge, 2003).
- [75] J. N. Israelachvili, *Intermolecular and Surface Forces*, 2nd ed. (Academic Press, San Diego, 1992).
- [76] M. O. Robbins, “Fluid dynamics: All stressed out,” *Nature (London)* **389**, 331 (1997).
- [77] Z. Xu, R. Khare, J. J. de Pablo, and S. Kim, “On the calculation of transport properties of polymer melts from nonequilibrium molecular dynamics,” *J. Chem. Phys.* **106**, 8285 (1997).
- [78] E. D. Smith, M. O. Robbins, and M. Cieplak, “Friction on adsorbed monolayers,” *Phys. Rev. B* **54**, 8252 (1996).
- [79] M. S. Tomassone, J. B. Sokoloff, A. Widom, J. Krim, “Dominance of phonon friction for a xenon film on a silver (111) surface,” *Phys. Rev. Lett.* **79**, 4798 (1997).
- [80] C. Pastorino, T. Kreer, M. Muller, and K. Binder, “Comparison of dissipative particle dynamics and Langevin thermostats for out-of-equilibrium simulations of polymeric systems,” *Phys. Rev. E* **76**, 026706 (2007).

- [81] D. J. Beebe, G. A. Mensing, and G. M. Walker, "Physics and applications of microfluidics in biology," *Annu. Rev. Biomed. Eng.* **4**, 261 (2002).
- [82] T. M. Squires and S. R. Quake, "Microfluidics: Fluid physics at the nanoliter scale," *Rev. Mod. Phys.* **77**, 977 (2005).
- [83] V. Mengeaud, J. Josserand, and H. H. Girault, "Mixing processes in a zigzag microchannel: Finite element simulations and optical study," *Anal. Chem.* **74**, 4279 (2002).
- [84] A. Gigras and S. Pushpavanam, "Early induction of secondary vortices for micromixing enhancement," *Microfluid. Nanofluid.* **5**, 89 (2008).
- [85] H. M. Metwally and R. M. Manglik, "Enhanced heat transfer due to curvature-induced lateral vortices in laminar flows in sinusoidal corrugated-plate channels," *Int. J. Heat Mass Transfer* **47**, 2283 (2004).
- [86] P. E. Geyer, N. R. Rosagutti, D. F. Fletcher, and B. S. Haynes, "Thermohydraulics of square-section microchannels following a serpentine path," *Microfluid. Nanofluid.* **2**, 195 (2006).
- [87] N. R. Rosagutti, D. F. Fletcher, and B. S. Haynes, "Low-Reynolds number heat transfer enhancement in sinusoidal channels," *Chem. Eng. Sci.* **62**, 694 (2007).
- [88] J. H. Forrester and D. F. Young, "Flow through a converging-diverging tube and its implications in occlusive vascular disease. 1. Theoretical development," *J. Biomech.* **3**, 297 (1970).
- [89] D. M. Wootton and D. N. Ku, "Fluid mechanics of vascular systems, diseases, and thrombosis," *Annu. Rev. Biomed. Eng.* **1**, 299 (1999).
- [90] S. A. Berger and L. D. Jou, "Flows in stenotic vessels," *Annu. Rev. Fluid Mech.* **32**, 347 (2000).
- [91] C. Cottin-Bizonne, B. Cross, A. Steinberger, and E. Charlaix, "Boundary slip on smooth hydrophobic surfaces: Intrinsic effects and possible artifacts," *Phys. Rev. Lett.* **94**, 056102 (2005).
- [92] V. P. Sokhan, D. Nicholson, and N. Quirke, "Fluid flow in nanopores: An examination of hydrodynamic boundary conditions," *J. Chem. Phys.* **115**, 3878 (2001).
- [93] A. Niavarani and N. V. Priezjev, "Rheological study of polymer flow past rough surfaces with slip boundary conditions," *J. Chem. Phys.* **129**, 144902 (2008).
- [94] K. M. Jansons, "Determination of the macroscopic (partial) slip boundary condition for a viscous flow over a randomly rough surface with a perfect slip microscopic boundary condition," *Phys. Fluids* **31**, 15 (1988).
- [95] M. J. Miksis and S. H. Davis, "Slip over rough and coated surfaces," *J. Fluid Mech.* **273**, 125 (1994).

- [96] K. Sarkar and A. Prosperetti, “Effective boundary conditions for Stokes flow over a rough surface,” *J. Fluid Mech.* **316**, 223 (1996).
- [97] C. Y. Wang, “Flow over a surface with parallel grooves,” *Phys. Fluids* **15**, 1114 (2003).
- [98] N. Lecoq, R. Anthore, B. Cichocki, P. Szymczak, and F. Feuillebois, “Drag force on a sphere moving towards a corrugated wall,” *J. Fluid Mech.* **513**, 247 (2004).
- [99] J. C. F. Chow and K. Soda, “Laminar flow in tubes with constriction,” *Phys. Fluids* **15**, 1700 (1972).
- [100] G. L. Bordner, “Nonlinear analysis of laminar boundary layer flow over a periodic wavy surface,” *Phys. Fluids* **21**, 1471 (1978).
- [101] S. Taneda, “Visualization of separating Stokes flows,” *J. Phys. Soc. Jpn.* **46**, 1935 (1979).
- [102] I. Sobey, “On flow through furrowed channels. Part 1. Calculated flow patterns,” *J. Fluid Mech.* **96**, 1 (1980).
- [103] T. Nishimura, Y. Ohori, and Y. Kawamura, “Flow characteristics in a channel with symmetric wavy wall for steady flow,” *J. Chem. Eng. Japan* **17**, 466 (1984).
- [104] S. Tsangaris and D. Potamitis, “On laminar small Reynolds-number flow over wavy walls,” *Acta Mechanica* **61**, 109 (1986).
- [105] G. Leneweit and D. Auerbach, “Detachment phenomena in low Reynolds number flows through sinusoidally constricted tubes,” *J. Fluid Mech.* **387**, 129 (1999).
- [106] H. Zhou, R. J. Martinuzzi, R. E. Khayat, A. G. Straatman, and E. Abu-Ramadan, “Influence of wall shape on vortex formation in modulated channel flow,” *Phys. Fluids* **15**, 3114 (2003).
- [107] C. Pozrikidis, “Creeping flow in two-dimensional channels,” *J. Fluid Mech.* **180**, 495 (1987).
- [108] M. Scholle, A. Wierschem, and N. Aksel, “Creeping films with vortices over strongly undulated bottoms,” *Acta Mechanica* **168**, 167 (2004).
- [109] J. C. Heinrich and R. S. Marshall, “Viscous incompressible flow by a penalty function finite element method,” *Computers and Fluids* **9**, 73 (1981).
- [110] T. J. R. Hughes, W. K. Liu, and A. Brooks, “Finite element analysis of incompressible viscous flows by the penalty function formulation,” *J. Comp. Phys.* **30**, 1 (1979).
- [111] T. B. Benjamin, “Shearing flow over a wavy boundary,” *J. Fluid Mech.* **6**, 161 (1959).
- [112] F. Pan and A. Acrivos, “Steady flows in rectangular cavities,” *J. Fluid Mech.* **28**, 643 (1967).
- [113] H. K. Moffatt, “Viscous and resistive eddies near a sharp corner,” *J. Fluid Mech.* **18**, 1 (1964).

- [114] H. Schlichting and K. Gersten, *Boundary-Layer Theory* (Springer, Berlin, 2000).
- [115] P. Koumoutsakos, “Multiscale flow simulations using particles,” *Annu. Rev. Fluid Mech.* **37**, 457 (2005).
- [116] D. A. Nield and A. Bejan, *Convection in Porous Media* (Springer, New York, 2006).
- [117] J. Baudry, E. Charlaix, A. Tonck, and D. Mazuyer, “Experimental evidence for a large slip effect at a nonwetting fluid-solid interface,” *Langmuir* **17**, 5232 (2001).
- [118] Y. Zhu and S. Granick, “No-slip boundary condition switches to partial slip when fluid contains surfactant,” *Langmuir* **18**, 10058 (2002).
- [119] U. Ulmanella and C.-M. Ho, “Molecular effects on boundary condition in micro/nanoliquid flows,” *Phys. Fluids* **20**, 101512 (2008).
- [120] U. Heinbuch and J. Fischer, “Liquid flow in pores: Slip, no-slip, or multilayer sticking,” *Phys. Rev. A* **40**, 1144 (1989).
- [121] J.-L. Barrat and L. Bocquet, “Influence of wetting properties on hydrodynamic boundary conditions at a fluid/solid interface,” *Faraday Discuss.* **112**, 119 (1999).
- [122] S. C. Yang and L. B. Fang, “Effect of surface roughness on slip flows in hydrophobic and hydrophylic microchannels by molecular dynamics simulation,” *Molecular Simulation* **31**, 971 (2005).
- [123] A. Martini, H. Y. Hsu, N. A. Patankar, and S. Lichter, “Slip at high shear rates,” *Phys. Rev. Lett.* **100**, 206001 (2008).
- [124] N. V. Priezjev, “Shear rate threshold for the boundary slip in dense polymer films,” *Phys. Rev. E* **80**, 031608 (2009).
- [125] S. T. O’Connell and P. A. Thompson, “Molecular dynamics-continuum hybrid computations: A tool for studying complex fluid flows,” *Phys. Rev. E* **52**, R5792 (1995).
- [126] E. G. Flekkøy, G. Wagner, and J. Feder, “Hybrid model for combined particle and continuum dynamics,” *Europhys. Lett.* **52**, 271 (2000).
- [127] X. B. Nie, S. Y. Chen, W. E, and M. O. Robbins, “A continuum and molecular dynamics hybrid method for micro- and nano-fluid flow,” *J. Fluid Mech.* **500**, 55 (2004).
- [128] Q. Li and G.-W. He, “An atomistic-continuum hybrid simulation of fluid flows over superhydrophobic surfaces,” *Biomicrofluidics* **3**, 022409 (2009).
- [129] X. B. Nie, S. Y. Chen, and M. O. Robbins, “Hybrid continuum-atomistic simulation of singular corner flow,” *Phys. Fluids* **16**, 3579 (2004).
- [130] N. G. Hadjiconstantinou, “Hybrid atomistic-continuum formulations and the moving contact-line problem,” *J. Comput. Phys.* **154**, 245 (1999).
- [131] W. Q. Ren and W. E, “Heterogeneous multiscale method for the modeling of complex fluids and microfluidics,” *J. Comput. Phys.* **204**, 1 (2005).

- [132] A. Niavarani and N. V. Priezjev, “The effective slip length and vortex formation in laminar flow over a rough surface,” *Phys. Fluids* **21**, 052105 (2009).
- [133] W. Shyy, H.S. Udaykumar, M. M. Rao, and R. W. Smith, *Computational Fluid Dynamics with Moving Boundaries* (Dover Publications, Inc., New York, 1996).
- [134] G. de Gennes, “Wetting: Statics and dynamics,” *Rev. Mod. Phys.* **57**, 827 (1985).
- [135] A. L. Yarin, “Drop impact dynamics: Splashing, spreading, receding, bouncing,” *Annu. Rev. Fluid Mech.* **38**, 159 (2006).
- [136] C. Huh and L. E. Scriven, “Hydrodynamic model of steady movement of a solid/liquid/fluid contact line,” *J. Colloid Interface Sci.* **35**, 85 (1971).
- [137] E. B. Dussan V., “On the spreading of liquids on solid surfaces: Static and dynamic contact lines,” *Annu. Rev. Fluid Mech.* **11**, 371 (1979).
- [138] R. G. Cox, “The dynamics of the spreading of liquids on a solid surface. Part 1. Viscous flow,” *J. Fluid Mech.* **168**, 169 (1986).
- [139] J. Koplik, J. R. Banavar, and J. F. Willemsen, “Molecular dynamics of Poiseuille flow and moving contact lines,” *Phys. Rev. Lett.* **60**, 1282 (1988).
- [140] P. A. Thompson and M. O. Robbins, “Simulations of contact-line motion: Slip and the dynamic contact angle,” *Phys. Rev. Lett.* **63**, 766 (1989).
- [141] P. A. Thompson, W. B. Brinckerhoff and M. O. Robbins, “Microscopic studies of static and dynamic contact angles,” *J. Adhesion Science and Technology* **7**, 535 (1993).
- [142] N. G. Hadjicostantinou, “Combining atomistic and continuum simulations of contact-line motion,” *Phys. Rev. E* **59**, 2475 (1999).
- [143] T. Qian, X. P. Wang, and P. Sheng, “Molecular scale contact line hydrodynamics of immiscible flows,” *Phys. Rev. E* **68**, 016306 (2003).
- [144] W. Ren and W. E, “Boundary conditions for the moving contact line problem,” *Phys. Fluids* **19**, 022101 (2007).
- [145] T. Ito, Y. Hirata, and Y. Kukita, “Fluid epitaxialization effect on velocity dependence of dynamic contact angle on molecular scale,” *J. Chem. Phys.* **132**, 054702 (2010).
- [146] A. Niavarani and N. V. Priezjev, “Modeling the combined effect of surface roughness and shear rate on slip flow of simple fluids,” *Phys. Rev. E* **81**, 011606 (2010).
- [147] C. Denniston and M. O. Robbins, “Mapping molecular models to continuum theories for partially miscible fluids,” *Phys. Rev. E* **69**, 021505 (2004).
- [148] C. S. Peskin, “Numerical analysis of blood flow in the heart,” *J. Comput. Phys.* **25**, 220 (1977).

- [149] M. Griebel, T. Dornseifer, and T. Neunhoeffer, *Numerical simulation in fluid dynamics: A practical introduction* (Society for industrial and applied mathematics, Philadelphia, 1998).
- [150] W. Shyy, M. Francois, H. Udaykumar, N. N'dri, and R. Tran-son-tay, “Moving boundaries in micro-scale biofluid dynamics,” *Appl. Mech. Rev.* **54**, 405 (2001).